DOTTORATO DI RICERCA IN CHIMICA

Convenzione tra
UNIVERSITÀ DEGLI STUDI DI TRIESTE
e
UNIVERSITÀ CA' FOSCARI DI VENEZIA

CICLO XXX

TITOLO DELLA TESI

APPLYING CARBON DOTS: ENHANCEMENT IN WATER OXIDATION SYSTEMS AND IN NANOMEDICINE

Settore scientifico-disciplinare:
CHIM/02

DOTTORANDO
ENRICO PONTOGLIO

COORDINATORE
PROF. MAURO STENER
Mauro Stener

SUPERVISORE DI TESI
PROF. ALVISE BENEDETTI

ANNO ACCADEMICO 2016/2017

"Necessity is the mother of invention."

Plato

Contents

Abstract

Since their first application, nanotechnologies have been capable to produce improvements and revolutionary results in many technological and industrial branches: medicine, transport, food security, environmental management and many others. Among these, nanotechnologies have proved their potential in medicine and in the treatment of polluted water. Nano-medicine made available increasing numbers of personalized and selective diagnostic methods and therapies. Nano-systems produced also more efficient purification processes for the treatment of polluted water. Thanks to the results obtained so far, these research fields are particularly significant and highly valued in the scientific world.

With this in mind, the present thesis focused on assessing the application of Carbon Dots (CDs). CDs are nano-sized carbon particles, with dimensions between 1 and 10 nm. Since their discovery, they have proven their potential in countless fields. Here, CDs were evaluated for the treatment of polluted water and for their potential application in nano-medicine. In particular, their reduced toxicity makes them the ideal candidate for drug delivery purposes. In addition to this, their peculiar nature allows their employment as charge delocalizers and photosensitizers, implementing the properties of established water purification systems. Among these systems, TiO_2 is, up to now, one of the most powerful material. When excited by the correct wavelength, TiO_2 can react with the water absorbed on its surface and produce highly oxidative radicals. Radicals that are capable to decompose water pollutants.

In this study, CDs were synthesized from different precursors, and they were characterized. The samples with the most promising properties were selected and applied for the production of a TiO_2-based high-performance photocatalytic material, capable of purifying polluted waters by exploiting solar light. This study pointed out also how the formation of sub-products during the CDs synthesis may be the responsible for CDs cytotoxicity. The research demonstrated, moreover, that CDs cytotoxicity was not related to the toxicity of the starting reagents. The class of CDs, synthesized with citric acid and diethylenetriamine, displayed the best properties for advanced TiO_2 oxidation systems and the lowest cytotoxicity. Additionally, a TiO_2-based photocatalytic system was also applied for water purification, exploiting the use of solar

radiation. An enhanced photocatalytic material was produced by loading TiO_2 particles with CDs into. In order to preserve the CDs properties within the system, a hydrothermal process, with mild thermal treatments, was developed and evaluated.

In conclusion, we obtained a material which may be used to treat polluted water by exploiting the solar radiation. This material may represent the starting point for advanced water purification systems in developed and developing countries.

1-Introduction

1.1-Nanotechnologies impact

The main goal of technological development is the production of new technologies to improve our life quality. Nanotechnology is referred to the manipulation of matter on an atomic, molecular, and supramolecular scale. On a quantitative basis, it is commonly considered as the manipulation of matter with at least one dimension sized from 1 to 100 nanometers. The impact of nanotechnologies in our everyday life is high, even though we are commonly unaware of it. Electronics, pharmaceutics and agriculture are just few of the fields in which nanotechnologies are present and active. For this reason, the design of new technologies has to pay attention to its entire lifecycle and to the respective environmental interactions. Electronic waste, such as old computers and other out-of-date electronics, as well as pharmaceutical and chemical waste can be heavily polluting. The effects on human health can be critical, and the danger of contamination exponentially increase in nanotechnology. In fact, the dimensions and the typical high surface-to-volume ratio of nano-based materials make them particularly reactive and invasive for living organisms, since they can easily bypass the cellular membranes and accumulate in the living tissues.

However, nanotechnologies are also promising for the realization of innovative drug delivery systems, nanomachines, high efficiency photocatalysts and other systems with many other applications.

1.2- Carbon Dots applications

Carbon based nanomaterials are a big family that relevantly increased its numbers since the discovery of carbon nanotubes, fullerenes, and many others carbon nanoallotropes. As reported in Fig.1 this family groups 4 different systems characterized by their dimension: materials with 2 and 3 dimensions such as multilayer graphitic nanosheets, graphene, and graphene nanoribbons, one-dimension carbon systems based on nanomaterials like nanotubes and nanofibers and finally, zero dimension nano-allotropes composed by fullerenes, nanodiamonds, graphene quantum dots and carbon quantum dots (Fig.1).

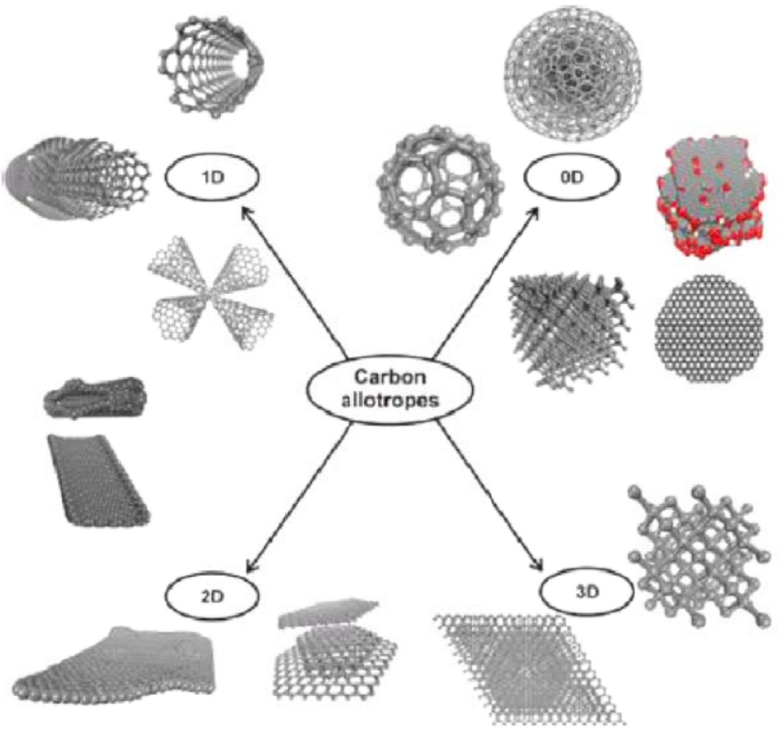

Figure 1: Nano-sized carbon allotropes in 0, 1, 2, and 3 dimensions (Chem Rev 115 (2015) 4744-4822).

Carbon dots (CDs) is a recent family of materials in the nanosystems universe. Since their discovery in 2004, they have attracted great attention due to their physical and chemical properties and their versatility in a wide range of applications. CDs synthesis is usually simple and relatively cheap; they generally are nontoxic, their size ranges between 1-10 nm and they have highly functionalized surfaces. Thanks to their optical properties, they are employed as photosensitizers to enhance dielectric absorbance, while their low toxicity allows their use in the bio imaging field.

Thanks to the presence of sp^2 carbon in their core[1], CDs can be used also as charge delocalizers in semiconductors in order to reduce the effect of photo-generated electron-hole couples recombination on efficiency. Moreover, doping of these nanoparticles with heteroatoms introduce intra gap levels in their bandgap and adapt their energetic properties to the chemical environment related to composite systems. Thanks to their luminescence quenching effect due to the photo-generated charge, CDs can be used for the detection of metal ions in polluted water. Finally, CDs can efficiently load drug molecules by electrostatic interactions, and release these molecules delivering them through tissues and membranes.

As usual, the discovery of a new material goes hand in hand with the exploration of its applications in different fields. Indeed, literature, focused on application of CDs in different fields, increases with articles proposing new synthesis processes or explanation of the nature of CDs properties.

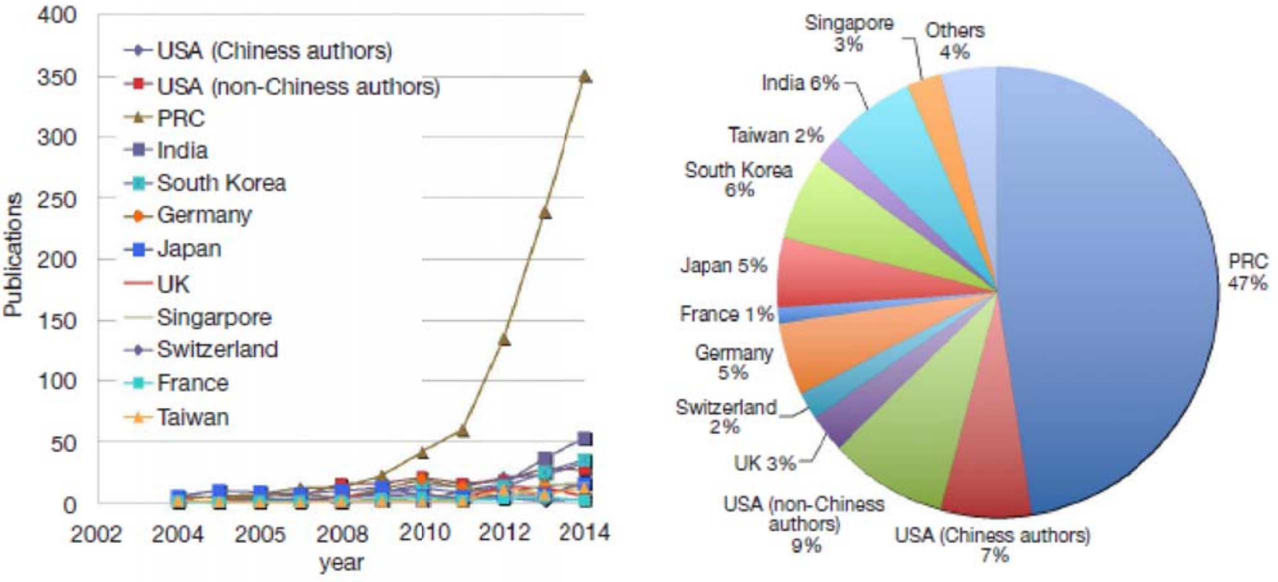

Figure 2: Yearly publications on CDs and their nanocomposites by countries during 2004-2014 (left), and share of publications on CDs and their nanocomposites by countries during 2004-2014[2] *(right).*

Since their first discovery, CDs attracted attentions by researchers of every country. As clearly showed in Fig.2, Chinese researchers contributed the most to the comprehension, development and application of CDs. Despite the exponential increase of interest, the development of new CDs applications is often preferred to CDs properties and phenomena comprehension. As reported above, CDs are typically considered nontoxic. Thanks to this property, CDs shows promising application in the medicine field. Human cancer outbreak is a hopelessly growing phenomenon involving every one of us. From these considerations, emerges the stringent necessity to find solutions mitigating this problem. Nowadays, many efforts are spent on chemotherapeutic drugs development and many progresses have been achieved increasing their selectivity and their efficacy. Despite that, chemotherapy still has many secondary effects. The intensity of them is obviously due to the drug toxicity, but also to the free drug concentration in the body. One of the most common method to solve this problem is to deliver the drug directly to the cancer cells. In the field of drug delivery, carbon nanomaterials have gained considerable attention as nano-carriers due to their surface area, enhanced cellular uptake, and easy conjugation with therapeutics molecules. Their synthesis is cheap and green as their purification, since they do not necessarily require toxic reagents. Thanks to their size, CDs can easily pass through the cell membranes.

1.3- Titanium dioxide and applications

As stated by Islam et al.[3], TiO_2 is one of the most extensively studied semiconductor photocatalysts. Its wide use is due to its capabilities able to overcome the worldwide energy shortage as well as counteract issues of climate change and environmental contamination. Since the first report of its use, for hydrogen generation via the photocatalytic decomposition of water by Fujishima and Honda[4], TiO_2 has attracted significant interest as a photocatalyst, due to its favorable band edge positions, which are well-matched with the redox potentials of water, CO_2, and a variety of organic compounds. These unique properties have enabled TiO_2 to be utilized in a wide range of applications, including solar energy conversion, antimicrobial and self-cleaning surfaces, paint whiteners, ceramics, textiles, personal care products, and environmental catalysis. Like many semiconductors, the photoactivity of TiO_2 originates from its ability to absorb light with greater energy than its band gap, which generates electrons and holes as charge carriers by promoting electrons from the valence band to the conduction band. This photocatalytic process involves a series of physical processes including light absorption, charge separation, charge migration, charge recombination, and surface redox reactions. The photo-generated charges can recombine and release their energy as light and heat, or these excited charges may reach the surface of titania and participate in reactions. The excited electrons have the potential to reduce oxygen molecules in producing superoxide radicals that are very reactive and participate in different reactions. On the other hand, in electrochemical process, if they reach the electrolyte interface either at titania or at a counter electrode, holes are able to oxidize water to produce reactive hydroxyl radicals. Despite many attractive features of TiO_2, the major challenges of its applications under natural solar light are its innate inability to absorb visible light, a high rate of photo-generated charge carrier recombination, and a low interfacial charge transfer rate of photo-generated charge carriers[3].

1.4- Enhanced photocatalytic material for wastewater treatment

The attention on the consumer goods full cycle, from their production to their management as waste material, impose more attention on: i) pollution administration, ii) their managements and iii) their costs. Waste treatment is a wide field that comprise solid waste, recycling, management of soil and air pollution. Nevertheless, one of the most important aspect concerns the treatment of wastewater and polluted water. Water is both the most important natural resource for life and the most efficient system to spread pollution. Rains can extract pollution and clean the air, while water of rivers and canals can spread out pollution from contaminated sites to groundwater and cultivated soils. Moreover, water is one of the most used natural goods for agricultural and industrial processes, and for many companies and production plants is the most expensive waste to consider.

Pollution dispersed in water involves both inorganic and organic chemical compounds, which are, generally, toxic with a lifetime of several years. The persistence of these compounds, in water as well as in soil, generates problems during clean-up processes. Most of the remediation processes provide to remove and transfer the pollutant in another place. So, in many cases of soil and water remediation, the storage of the high concentrated toxic materials extracted during the remediation process could generate additional problems.

Therefore, as well as reducing pollution production, wastewater treatment and water sanitization are still the most important solution to contrast pollution efficiently.

In the last decades, several water purification methods and sewage disposals are developed. Among these, most propose to collect pollutants removing them from water, whereas only few processes are able to convert pollutants in something less dangerous. Biological oxidation and anaerobic digestion used in lagooning processes are commonly used as secondary treatment and to tear down NH_3, N and S based compounds and phosphates. These systems reproduces water natural cleaning cycle, but requires great spaces, long time and, often, they are not able to act on Permanent Organic Pollutants (POPs) as hexaclorobenzene, insecticides, polychlorinated biphenyls and dioxins. Electro-flotation permits to electro induced organic compounds oxidation and metals reduction, and is capable to remove the smallest solid suspension thanks to micro bubbles production[5]. This system permits to reuse directly the just treated water, but it requires great amount of energy. Among these processes, Advanced Oxidation Processes (AOPs) seems to be the most promising way to treat water at accessible times and costs and, at the same time, to treat POPs. AOPs use strong and reactive oxidants as hydroxyl radicals to treat wastewater, which oxidize pollution obtaining CO_2 and H_2O. Produced radicals can theoretically oxidize any organic compound present in water, bacteria included. In order to produce a high concentration of hydroxyl radicals, ozone, hydrogen peroxide and oxygen are usually added into the treating system, but also strong UV light and photocatalytic materials as titanium dioxide.

One of the most AOPs challenging aspect is the possibility to use it directly for water sanitization.

In everyday applications, as reported above, AOPs include also the use of ozone, H_2O_2 and/or UV-light. Several methods have been developed[6,7] to produce radical species, which can be grouped in two main categories: non-photochemical and photochemical methods. The former one includes the methods that generate radicals without light energy. They involve reaction with ozone, hydrogen peroxide and catalysts. The latter one uses UV lamps to activate the process. Indeed, there is a problem related to the fact that conventional oxidation processes cannot oxidize some stable organic pollutant. Often the intermediate product remaining in the system may be as toxic as or more toxic than the initial compound. In these cases, supplemental oxidation processes can be applied using UV radiation. The use of UV light increases oxidation power and, as it is showed in Tab.1, the highest oxidative power can be reached with radicals, produced by the photo excitation of a semiconductor as TiO_2.

Table 1: Relative oxidation power of some oxidizing species[6]

Oxidizing species	**Relative oxidation power**
Chlorine	1,00
Hypochlorous acid	1,10
Permanganate	1,24
Hydrogen peroxide	1,31
Ozone	1,52
Atomic oxygen	1,78
Hydroxyl radical	2,05
Positively charged hole on titanium dioxide, TiO_2^+	**2,35**

AOP's can be used also for mild water treatment, such as water sanification and antimicrobial maintenance for drinkable water distribution. Today in the world, 2,5 billion people lives without a basic water sanification. Water sanification is not only a common problem for poor and developing countries, but also for the rich part of the world, where drinkable water distribution is still inefficient and potentially dangerous[8]. The most common system to contrast bacteria proliferation in drinkable water is the addition of low concentration of sodium hypochlorite to the aqueduct. Water sanification with sodium hypochlorite involves poison substances. Important studies refer that rats supplied with water containing NaClO evidenced no cancer development, even though, high NaClO doses (1,6 mg/Kg) increase the amount of sperm-head abnormalities in male rats[6]. Aware of these problems, application of advanced oxidation processes can offer an alternative to the sodium hypochlorite. The highly active radical species produced from activate photocatalysts, can easily destroy microorganisms and prevent their proliferation during water distribution. Due to the problem's complexity, the study and application of TiO_2 based processes for the wastewater treatment and sanitization of drinkable water can be considered as a hot theme. Indeed this research-work aims to developing TiO_2 based wastewater treatment working under solar radiation. Today AOPs are not widely applied, and the use of reagents and UV lamp make these systems expensive, especially in developing countries.

AOPs with radiation and activated TiO_2 are potentially the cheapest systems: they do not strictly require additional reagents as H_2O_2 and, with an appropriate doping, they became a photocatalytic material able to absorb visible light from solar radiation. The part of this study concerning AOPs is focused in increasing visible absorption, developing a hybrid system in order to produce better photocatalytic performances under visible light. The development of a solar light sensitive photoactive material may be useful even for less stressed situation, as drinkable water treatment, supplying an alternative to water sanification with sodium hypochlorite.

Here, CDs can play a central role in improving photocatalytic activity and the efficiency of the wastewater treatment, that may also be more eco-friendly and safer. Nitrogen-doped-titania is an active and robust photocatalyst, with the property to be activated also by solar light. Un-doped titania can be activated only in the near-UV region, and the solar radiation does not possess enough UV light for large scale wastewater treatment. Using a photocatalyst activated mostly under solar radiation, allows developing photochemical AOPs based on renewable energy resources. In the photocatalyst used in this research, carbon dots are loaded as charge delocalizers in order to reduce electron-hole recombination and enhance the photocatalytic activity. Usually CDs are loaded on the surface of photocatalyst by impregnation. While in other processes, CDs are directly synthesized on photocatalytic material surface.

1.5- Objectives and summary of the research

In the thesis, as reported in Fig.3, we have investigated the CDs properties for fine applications such as drug delivery and photocatalytic enhancers. Then, for a possible environmental application, we studied the properties of doped titanium dioxide materials for wastewater purification, under solar radiation. Finally, we combined our findings on these topics to study the synthesis of an innovative materials which combines CDs and doped titanium dioxide properties, able to be used in developing countries.

As exposed in the paragraph 1.4, AOP's are one of the few waste water treatments able to remove and at the same time to degrade pollutants. Among the different treatments, TiO_2 based processes are the most performing AOP's. Despite that, TiO_2 is activated only under UV light radiation, and at the same time, it suffers of recombination processes which reduce its photocatalytic activity.

The main objective of the thesis is to improve TiO_2 photocatalytic activity in order to produce more performing AOP's. We tried to reach this objective in two different ways:

- Improving the efficiency of the radical species production thanks to the reduction of the charge recombination processes. At this purpose we studied the carbon dots (CDs) loading on TiO_2.
- Enlarging the range of TiO_2activation ability from the UV light to the visible radiation. At this purpose we tried to produce nitrogen doped TiO_2 ($NTiO_2$) to be used as photocatalytic material for CDs loading.

Another objective of this thesis has concerned the study of CDs viability for nanomedicine. This aspect was studied considering the cytotoxicity of the synthesized CDs in relation with the toxicity of the used reagents.

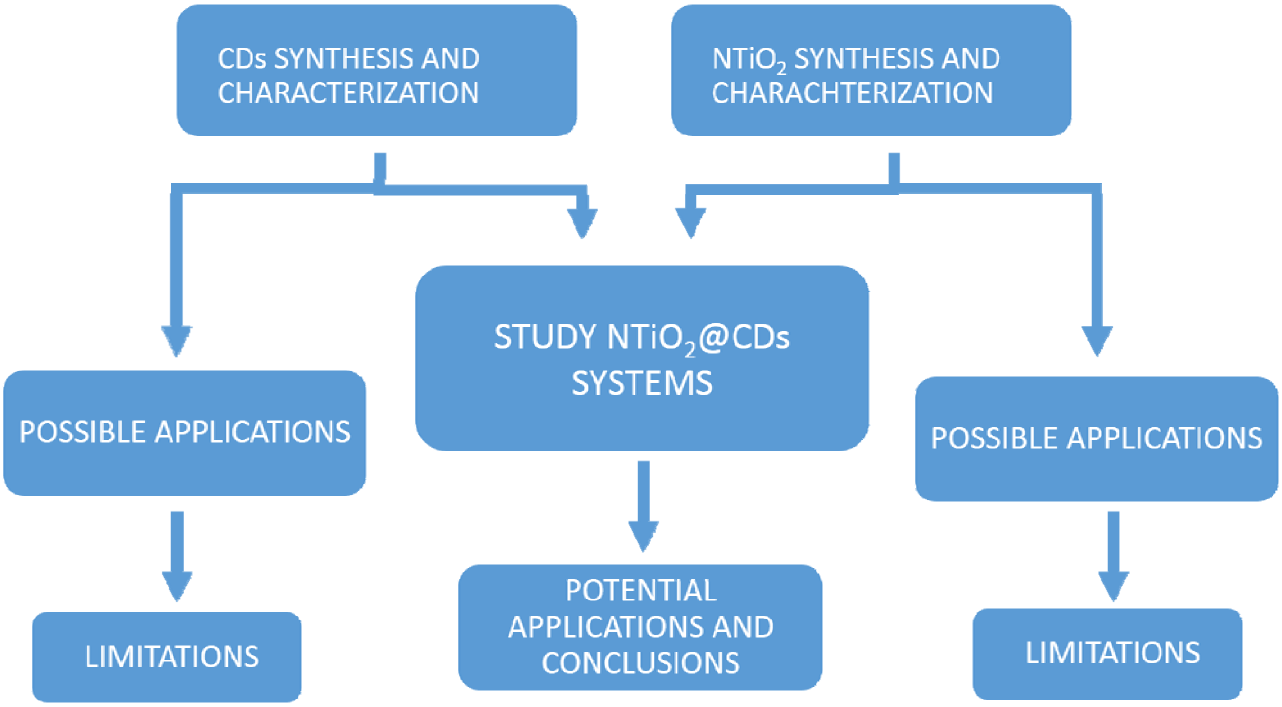

Figure 3: scheme of the research topic investigated in this work.

2-General and Theoretical aspects

2.1-Carbon Dots

2.1.1-Synthesis

Carbon Dots can be produced by different methods with both "bottom-up" and "top-down" approaches. The former starts processing organic molecules producing carbon based nanoparticles after their condensation and dehydration. Top down processes operate directly on carbon- or graphite-based bulk materials.

Generally, bottom-up processes produce amorphous CDs (with small carbon sp^2 domains embedded in an amorphous carbon sp^3 matrix), while top-down processes produce crystalline graphitic nanoparticles[9]. Most top-down methods require special and expensive equipment or complicated synthesis procedures. Typically, these methods produce particles characterized by a dispersed size distribution and low quantum yield. Bottom-up approaches, based on carbonization of organic precursors via thermal treatment, produce particles with more homogeneous sizes and morphology. Independently from the synthesis approach, sometimes it is necessary to perform an additional passivation step in order to obtain suitable optical properties. Last but not least, bottom-up processes seems to be more cost effective in yield and quality[10] with respect to the top-down ones.

Bottom up

In these processes the main carbon source typically is an organic molecule, e.g. glucose, fructose, citric acid, etc. These molecules are then dehydrated and condensed. Nitrogen source such as urea, amines, amino acids and other heteroatoms can be mixed with the organic molecules before the reaction in order to produce co-doped systems with specific properties. Hydrothermal synthesis is the most diffuse bottom-up process used to produce CDs[11,12,13,14,15,16,17,18,19]. Other documented processes are raw[20,21] and microwave[22] assisted pyrolysis of the precursors, electrochemically induced[23,24] carbonization, and plasma treatment[25,26,27] (where the energy of plasma induces carbonization of the precursor solution). Some studies propose also the precursors treatment by ultrasonication[28,29]. Other research foresee to produce CDs with reverse micelles[30] systems. There exist several other bottom-up processes[31,32,33] using also nano-sized porous structure templates, CDs can be synthesized by calcination of porous silica nanoparticles (SiNPs) impregnated with CDs precursor and annealed in order to obtain CDs with size comparable with SiNPs pores[34].

Tipically, hydrothermal processes are used for CDs production.

Hydrothermal processes allow the production of CDs from a wide range of starting materials[15,16,17,18,19]. Carbohydrates, organic compounds, and natural products can be successfully used to produce carbon nanoparticles with fine optical properties. Despite this widespread diffusion, the formation mechanism presented in literature is complicated and generally not completely understood. For example, even the treatment of simple organic compounds, such as sucrose, generates complicated processes to achieve the CDs formation. Sahu and coworkers[17] tried to describe the CDs formation when hydrothermally treated sucrose undergoes hydrolysis to form glucose and fructose. Although glucose isomerizes to form fructose, dehydration and decomposition of fructose/glucose give rise to different soluble products such as furfural compounds, several organic acids such as acetic, lactic, propionic, levulinic and formic acids, aldehydes and phenols. The polymerization and condensation of these products results in the formation of soluble polymers. Aromatization and formation of aromatic clusters take place via aldol condensation, cycle-addition and a hydroxyl-methyl mediated furan resin condensation. When concentration of aromatic clusters reaches a critical super-saturation point, nucleation takes place and carbon dots are formed.

Some works report easier processes using citric acid and amines. Probably, the use of precursor with known reactivity allows the description of the formation and the composition of intermediates before CDs formation. For example, the use of citric acid and amines produce fluorophores[35,36] as intermediate compound before the CDs growth.

Therefore, bottom-up approaches and in particular hydrothermal synthesis, allow producing particular types of carbon nanoparticles by the aggregation of fluorophores[37,38]. As deepened in the following paragraphs, these CDs have special optical properties, as the independence of the luminescence from the excitation wavelength and the red edge effect.

Top down

The first reported top-down method used an arc discharge to purify soot derived from SWCNTs to produce CDs[39]. Xu et al. started oxidizing soot with HNO_3. The sediment, extracted by NaOH solution, resulted in a stable black suspension. Finally, the suspension was further separated by gel electrophoresis into SWCNTs, short tubular carbons, and a new material called C-dots.

Using top-down approaches, carbon systems such as soot, graphite, fibers, graphene, graphene oxide, and nanotubes are chemically, or electrochemically reduced in smaller parts to produce nano-sized particles. Top-down processes are based on exfoliation and oxidation of bulk materials. For this purpose, solvo-thermal processes are usually involved in these processes. However, also hydrothermal treatments can be used to exfoliate bulk materials in graphite flakes or in graphene[40,41,42] sheets. The oxidation of the graphene to cut sp^2 sheets into smaller fragments is another investigated method to obtain Graphene Quantum Dots (GQDs)[43,44]. Conversely, the direct oxidation of bulk graphite with electro-induced exfoliation processes is also possible[45]. In this case, two graphite rods immersed in water are used as cathode and anode. When the right potential is applied, a great number of radical ions are formed by oxygen reduction. The formation of these highly active species on the graphite surface allows the oxidation and removal of nano-sized graphite sheets forming a stable suspension in water.

After the exfoliation process, the fragmentation can be achieved by further oxidation of the exfoliated material. For this purpose, several strong processes can be used, such as pyrolysis, sulpho-nitric and nitric acid reflux or even photo-Fenton reactions[46].

The oxidation process often is so strong that the resulting products require further treatments to acquire the desired properties. Usually, a reduction step with $NaBH_4$ and hydroxylamine can recover the nanoparticles sp^2 backbone[47,48, 49,50,44,50].

Clearly, the production of carbon nanoparticles starts from expensive materials as graphene and carbon nanotubes, however it can push for the research and development of new and cheaper productions[51,52].

2.1.2-Optical properties

Photoluminescence:

Luminescence usually defines a low temperature light emission. Luminescence can be due to chemical reaction, electrical energy or subatomic changes. Photoluminescence (PL) is a process caused by the absorption of an electromagnetic radiation. PL starts with photo excitation, followed by various relaxation processes followed by the emission of another photon. Relaxation processes consume part of the energy of the absorbed photon, so the emitted photons are usually less energetic than the absorbed ones. PL in carbon dots is not yet well understood, also because of the numerous processes involved in it: CDs are a complex system that undergoes different photoluminescence processes depending on the synthesis process.

Mechanisms

Photoluminescence is one of the most fascinating features of CDs, both for fundamental understanding and practical applications. Despite its relevance, the complete photoluminescence process in CDs is still not completely understood due to the different contributions from: CDs dimension, surface functionalization, oxidation level, and synthesis route. Both CDs surface and core play an important role on the PL behavior and on the CDs response to excitation light. The PL properties can also depend on the excitation wavelength and the pH of the CDs solution. This dependence and how the red shift emission is influenced by the solution pH is still matter of debate.

CDs consist in a “muffin like” structure, where carbon sp^2nano-domains are embedded in oxygen rich sp^3 matrix. An accepted CDs description defines that sp^2nano-domains have suitable band gap and can emit light thanks to electron-hole recombination with radiative processes. Furthermore, sp^3 carbon matrix is rich in oxygenated chemical groups and can interact with sp^2 domains producing charges[33,53,54,55,55,31,56].

Recent literature shows that quantum confinement effect, zigzag effect and surface traps are the processes at the base of the photoluminescence mechanism of action in carbon nanoparticles.

Quantum confinement effect:

When a nano object have a size comparable with the Compton wavelength ($2{,}426\times 10^{-12}$ m), its energy levels change from continuous to discrete configurations. The gap between the bands increases, and the produced emission is more energetic (Fig. 4A)[32,57,58] with an inverse proportionality to the nano object size. This phenomenon called quantum confinement effect is evident in Fig.4B, where a series of CDs suspension with different sizes are showed under UV light: when the CDs sizes are higher the emission shifts from blue to orange[23].

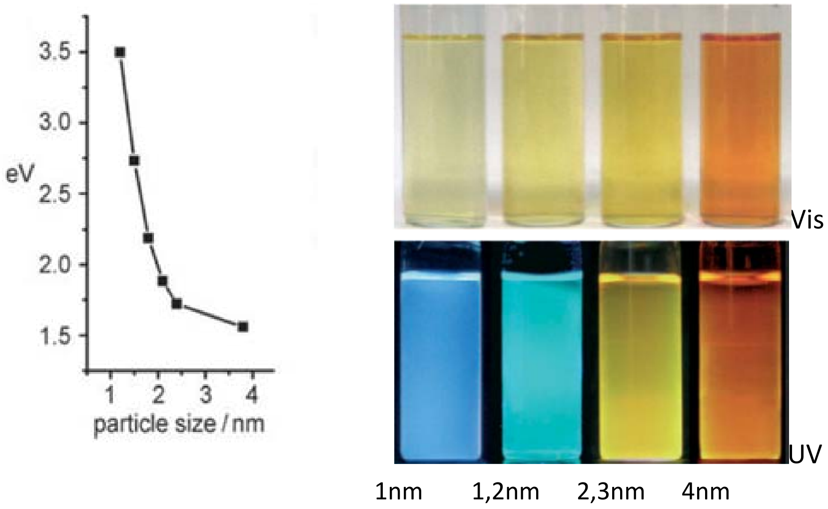

Figure4:Suspensions of CDs with different size. A) Bandgap dimension Vs particle size. The plot shows the dependence of the bandgap from the particle size. B) Photoluminescence emission at higher wavelenghts are recorded for CDs with highersizes (Angew.Chem. Int. Ed. 49, 2010 pp. 4430).

At the present, also the role of quantum confinement effect as contribution in CDs luminescence is not completely clear. Recently, Bhattacharya et al. showed a strong correlation between luminescence and size distribution, and suggested that the excitation wavelenght (λ_{ex}) dependence of CDs on PL arises from the inhomogeneous size distribution rather than to the distribution of different surface traps[59]. Obviously, CDs photoluminescence is related to the quantum confinement effect, but there are other phenomena giving a contribution that has more influence on it.

Zigzag effect:

Zigzag effect is a phenomenon ascribed only to highly sp^2 graphitic ordered graphene quantum dots. The edge of these highly ordered materials possesses several ground state carbene (hybridized sp^2) triplets and ground state carbyne (hybridized sp) singlets[60,61].

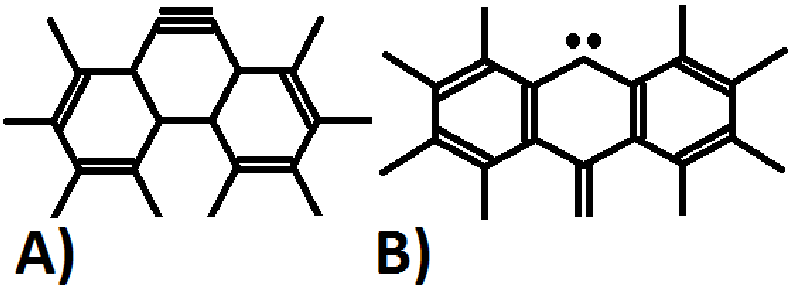

Figure 5: Suggested chemical nature of the edge sites in GQDs. A) Carbyne armchair site and B) Carbene zigzag site.

The carbenes triplets (Fig. 5 A and B) that can be found on the GQDs edges have two singly occupied orbitals (σ and π). Thanks to the UV absorption, electronic transition between these two orbitals generate photoluminescence[40].

Therefore, luminescence in GQDs is generally due to the σ and π carbine triplet electronic transitions to the ground state respectively[62].

Surface traps and surface state:

CDs have a high degree of surface functionalization. Therefore, the presence of specific chemical groups on the CDs surface can influence optical properties by arising several energy levels that may result in a series of surface defects. Moreover, an higher number of surface oxidation levels can results as a consequence of more surface defects[63], thus optical properties such as the shape of the absorption and emission spectra, the maximum absorption wavelength and the quantum yield are strongly correlated to the CDs synthesis method and the parameters involved. In particular, the production of functional groups on the surface (mostly carbonyl and carboxylic groups) allows adsorbed energy to relax with radiative processes[64].

Some examples of CDs oxidation or reduction prove the strong relationship between photoluminescence and functional groups. Tan et al. observed that the CDs luminescence changes with a redshift emission after oxidation with strong UV exposure. This was correlated to a greater C-O-C and C=O amount on the surface[65]. Meanwhile, Zheng et al. reduced green luminescent CDs with sodium borohydride, who selectively reduces carbonyl and epoxy moieties to hydroxyl groups without interacting with C=C and COOH[66]. After the reduction step, they noted blue-shifted PL and a 10-fold increase in QY. They also observed a decrease of sp^2 C=C moiety and an increase of carbonyl surface functionalization, so they correlated the blue-shift emission and the greater quantum yield to the hydroxyl groups electron-donor characteristic. Both the research groups agreed that PL arise from surface traps: change of the surface traps directly causes optical properties variations. Finally, it is possible to state that CDs photoluminescence originates from oxygen-rich surfaces.

In CDs there is a synergic interaction between sp^2 and sp^3 domains. The sp^3 domains convert the energy transmitted from the sp^2 domains into light, resulting in photoluminescence.

Once cleared the general relationship between photoluminescence and surface functionalization, it is necessary to correlate specific functional groups to their possible optical properties. The studies reported above showed that carbonyl groups produce more energetic luminescence, related to a blue shift of the emission, while ethers and carboxyl groups produce less energetic emission.

However, how can we define the dependence or independence of the luminescence from the excitation wavelength?

Surface groups such as C-O, C=O and O=C-OH can introduce trapping states with different energy levels, making CDs able to emit light with photoluminescence depending from the excitation light wavelength[66,1].This can explain why many CDs systems show an excitation-dependent luminescence.

This phenomenon produces a redshift of the emission spectra in response to the wavelength increase of the excitation light, and could arise from multi-chromophoric units. Fig.6 shows a typical effect of this phenomenon.

In turn, multi-chromophoric units can be related to a different conjugation[67,68]of the CDs or to different chemical groups on the surface[33,]. Wen et al.[33]found two overlapped spectral bands: their experiments showed that an “intrinsic” band originates from the isolated sp^2 nano-domains, while an “extrinsic” band is related to surface states. Ultrafast photoluminescence experiments revealed that excited electrons, produced by the photon absorption, are trapped into the surface states. Successively, surface states emit down-converted light.

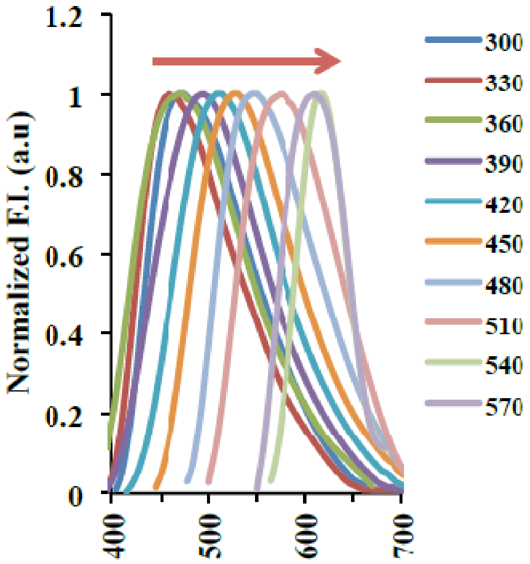

Figure6: Excitation wavelength dependence of the photoluminescence in CDs synthesized via hydrothermal treatment of black tea, (Bayda et al[69]). Legend reports the tested excitation wavelengths.

Das et al.[70] illustrated the process with a similar concept, describing the excitation energy transfer from the core to lower energy sites, where energy states can be associated to the surface state of the particle.

Many groups tried to explain the relation between red shifting and the coexistence of surface states with different oxidation states[71,72,73]. However, this does not justify the redshift of the emission caused by the excitation light wavelength (λ_{ex}). Indeed, even if the energetic levels of the bonding could be involved in radiative processes (surface traps), they are not homogenously distributed, consequently the continuity of the “broadening” cannot be explained. In addition to this, surface states cannot justify the recurring dependence to the pH. Kan and coworkers justified λ_{ex} dependence, pH dependence, and the redshift continuity with the red edge excitation shift (REES)[74]. REES is a shift of the maximum fluorescence wavelength caused by a shift in the excitation wavelength toward the red edge of the absorption band. This effect is mostly observed with polar fluorophores in particular media such as very viscous solutions or condensed phases[75].

CDs usually show a broadened shape emission, characteristic of systems composed by organic fluorophores which show similar unresolved emission and enlarged to less energetic frequencies. The same PL characteristics are found in aromatic fluorophores, embedded in viscous media. These effects depend on the existence of excited state and on their interaction with the environment. This is correlated to their slow relaxation rate. The intermolecular interactions allow for electron-transfer along several ways and for the generation of wide and continuous emission spectra, typical of the REES. The shape and the position of the spectra is related to the specific functional group constituting the fluorophore, and the pH variation of the environment can affect the protonation degree of the functional group[76].

In a system mostly related to functional groups, solvation dynamics of polar solvents strongly contribute to smooth the discrete emission of the surface traps.

As previously reported, CDs surface groups are related to the reagent used during the synthesis. If nitrogen containing organic compounds are used as precursors to synthesize CDs, it is possible to introduce amino groups on the surface state and to drastically change the respective PL behavior. This phenomenon is particularly evident when short chain molecules are used. If oxygen based surface state causes the excitation-dependent PL production, amino-based molecule scan passivate the surface state. In this case, the energy derived from the recombination allows the sp^2 domains to directly emit their energy[77].

Latest studies demonstrated that fluorescence of nitrogen-based doped CDs, synthesized with citric acid, originates from organic fluorophores[35]. Shi and coworkers proved that organic fluorophores are the origin of CDs luminescence, in particular for CDs with high quantum yield. Starting from the same precursors, they synthesized organic fluorophores5-oxo-3,5-dihydro-2*H*-thiazolo [3,2-*a*] pyridine-3,7-dicarboxylic acid (TPDCA) and 5-oxo-3,5-dihydro-2*H*-thiazolo [3,2-*a*] pyridine-7-carboxylic acid(TPCA) (Fig.7) and nitrogen-sulfur co-doped CDs (NSCDs). The authors observed that, since NSCDs are constituted by TPDCA and TPCA, these materials showed the same UV-Vis absorption, excitation, emission photoluminescence, QY, lifetime, and excitation independent emission.

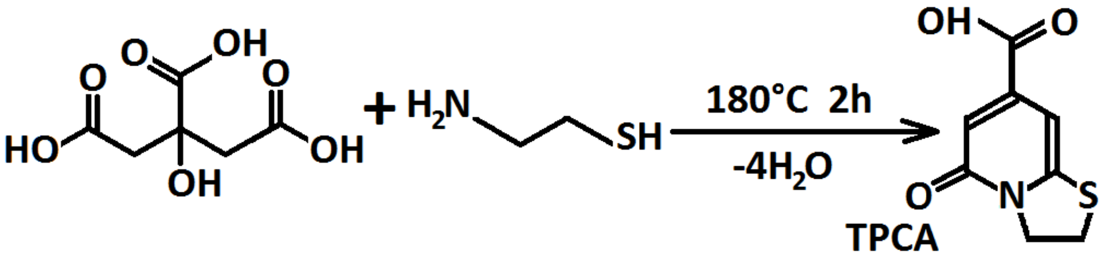

Figure 7: synthesis of TPCA from the same precursors used to synthesize nitrogen and sulphur co-doped CDs.

A recent study have showed that the emission of an isolated carbon dot is asymmetric and broader in the red region, proving the existence of a relaxing process[78].

CDs photoluminescence derives also from surface state interactions with carbonaceous core. The core adsorbs light depending on its bandgap and, once excited, it produces electron-hole couples while surface states delocalize electrons, emitting light through radiative processes. Radiative processes emit luminescence at wavelength depending on the energy lost during the electron transfer, and on the energy bonding of surface states.

It is possible to assume that photoluminescence of CDs, produced via bottom-up synthesis, derives from the presence of organic fluorophores that compose the CDs structure. Moreover, some optical properties such as pH-dependent luminescence and the continuous red shifting trend caused by λ_{ex} dependence, can be explained by the intrinsic interactions of coagulate organic fluorophores.

Before concluding this paragraph, another phenomenon observed on CDs photoluminescence has to be considered: the increase of PL intensity when the surface polarity increases. When polarity and PL intensity increase, also λ_{ex} dependence increases[79]. Studies revealed that electron donor functional groups, such as amine, influence luminescence and PL lifetime, also when λ_{ex}

dependence emission derives from other functional groups such as CO and COOH. Electron donor functional groups can boost the electronic cloud around the bond and enhance the number of electron at the excited level. Consequently, electron donor groups can enhance the number of radiative events, increasing the lifetime and the PL intensity. Moreover, for highly-functionalized surfaces, objects such as CDs permit to increase the odd-to-transfer electrons from the level of a functional group to another. Since each electronic transition causes an energy loss, the photon emission at a greater wavelength is more probable[80,33].

In conclusion, bottom-up synthesized CDs are composed by sp^2nano-domains embedded in amorphous sp^3 matrix. They possess high surface functionalization that is translated in surface traps and they show a continuous emission. This type of CDs adsorbs light from the sp^2nano-domains that transfers excited electrons to the amorphous sp^3 surface, rich of energy traps. The produced photoluminescence is related to λ_{ex} and pH, with a similar behavior to high-density clusters of organic fluorophores. Moreover, some recent studies found that some organic fluorophores can be synthesized in the same condition used to synthesize CDs. Therefore, it is possible that this type of carbon dots is constituted by organic fluorophores which define the respective optical properties.

Passivation effect

Passivation with organic compounds allows tuning of the surface functionalization and the optical properties, including also the λ_{ex} dependence of the photoluminescence.Sachdev[81] et al. passivated chitosan based CDs with polyethyleneimmine (PEI) and polyethyleneglycol (PEG), producing batches with different optical properties. However, both the batches presented photoluminescence λ_{ex} dependence[82].

In order to obtain λ_{ex} independence, Li and coworkers[83] completely passivated the CDs surface with amino groups. The surface resulted very homogeneous and only one electron transition and emission was allowed, conferring the independence of the luminescence from the exciting wavelength (Fig.8).

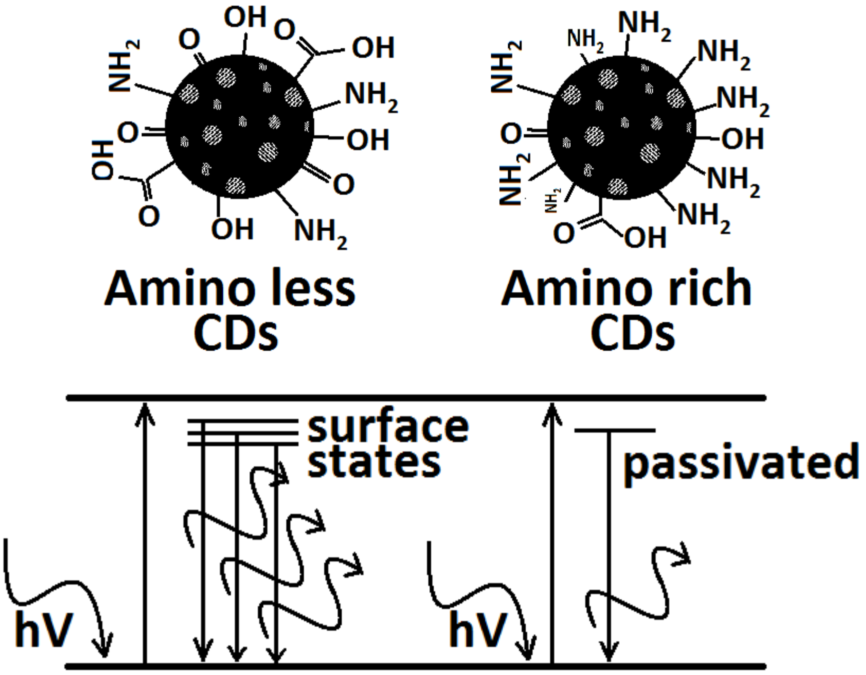

Figure 8: effect of complete surface passivation with amine. Photoluminescence independence from the excitation wavelength was due to the removal of surface states with passivation.

Photoluminescence up-conversion

A particular optical property, commonly cited as an excellent peculiarity of the carbon dots, is the up-conversion of fluorescence (UPCL)[84,85,86,87,88,89].

UPCL is an anti-Stokes emission, in which the sequential absorption of two or more photons leads to the emission of light at shorter wavelength than the excitation wavelength[90,91].

Usually, up-conversion photoluminescence is a phenomenon strictly related to the presence of meta-stable levels between the main levels of the material that can be populated by photons. Moreover, the lifetime of the population of the levels must be long enough for further photon adsorption in order to populate the higher levels. These properties are typical of some elements and some organic compounds[92,93,94,95], and the discovery of new materials with up-conversion properties could be very interesting. In the last years a great debate was opened on the existence of CDs up-conversion and, while some research groups sustain carbon dots present this peculiar property, others attribute these results to forgetfulness during the experimental setup that produce effects that can be confused with up-conversion photoluminescence. The up-conversion

PL in CDs could be due to the excitation of second order diffraction light from the monocromator of the spectrofluorimeter[37].

Despite all, to understand how carbon dots can produce up-converted photoluminescence it is necessary to understand the possible processes at the base of this phenomenon. With this aim, some of the most important up-conversion processes are described below.

Excited state absorption

In excited state absorption (Fig.9A), the system absorbs a photon with energy Φ_1 equal (resonant) to the transition 1-2, promoting a charge to level 2. When the first transition allows the occupation of the intermediate level, another photon with energy Φ_2, resonant with the transition 2-3 can be adsorbed. Finally, the relaxation of this system can emit one photon with energy equal or a bit lower than $\Phi_1 + \Phi_2$. If $\Phi_1 = \Phi_2$, the pumping source can be the same for both the1-2 and 2-3 transitions, while if $\Phi_1 \neq \Phi_2$ different pumping sources will be necessary.

Processes where energy transfer can follow excited state absorption

Energy transfer is a process of energy transport from a donor at an excited state to an acceptor at its ground state. Depending on both donor and acceptor electronic configurations and energetic states, it is possible to obtain several processes that induce up-conversion photoluminescence.

The process exposed in Fig.9B happens when a conventional energy transfer is followed by an excited state absorption. This second phenomenon promotes the charge from the second to the third excited state. At the end, the emission produced from the final relaxation of the system produces a photon with a higher energy than that one of the two adsorbed photons.

Another energy transfer process is called successive energy transfer. In this process, showed in Fig. 9 C, the photons are adsorbed only by the sensitizer. In this case, the activator can receive different charges from two different excited sensitizers. This double absorption allows the charges promotion to the third excited state, and in this case, the relaxation of charges from the third state can produce photons at higher energy than the absorbed one.

In Fig.9D a cross relaxation up-conversion is schematized. Energy transfer occurs between two identical objects. In this case, incident Φ is absorbed by the sensitizer and by the activator, leading both of the two objects in their excited state 2. Then, energy transfer between them promotes the activator in its state 3 while the sensitizer goes down to lower energy states.

In cooperative sensitization showed in Fig.9E, two sensitizers cooperate to excite the same activator. In this case, two photons are transferred to the activator, which reaches a higher excited state.

Between other non-linear optical properties, the multi-photon absorption process is cited as one of the most common pumping process in carbon dots up-conversion phenomenon.

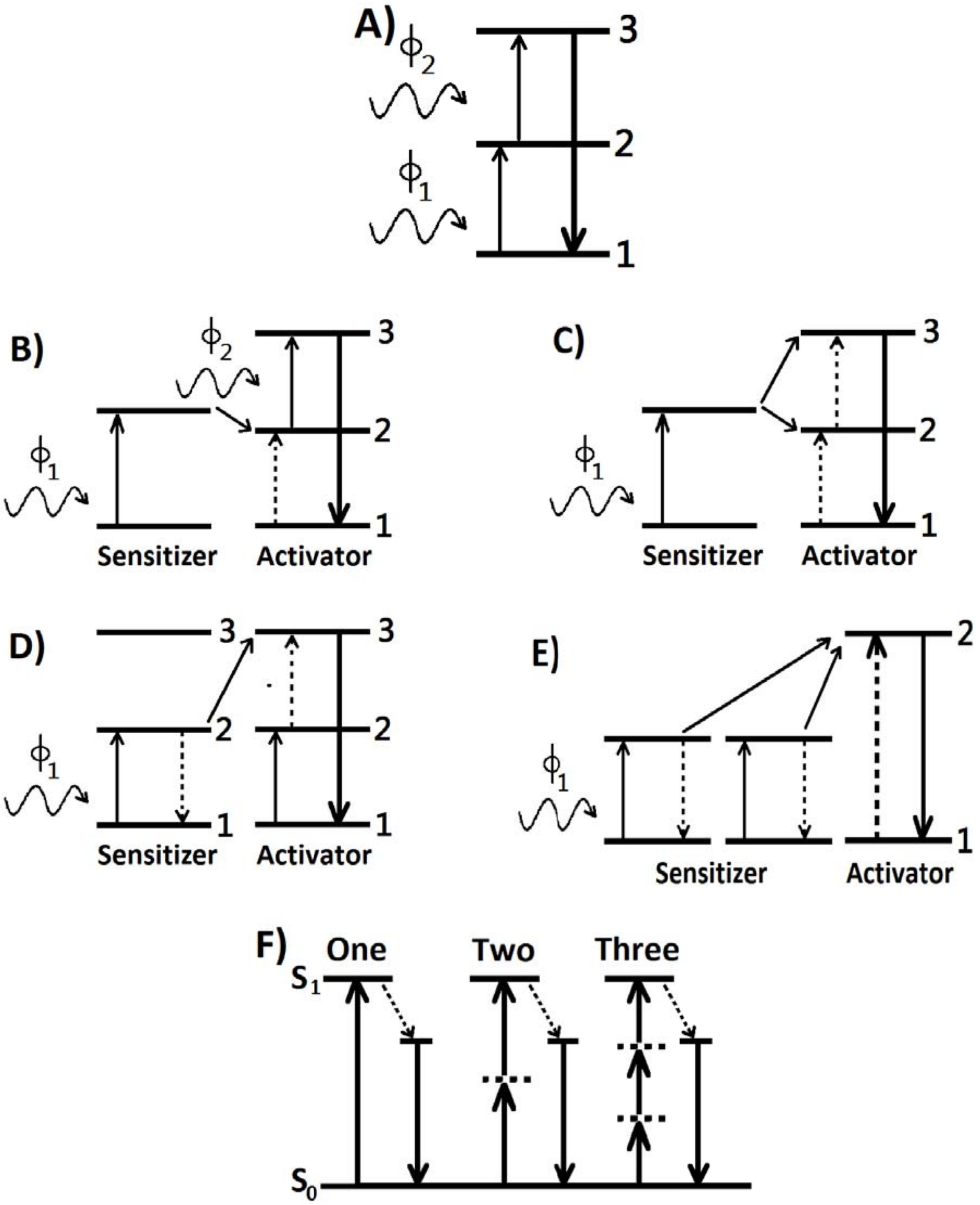

Figure 9: possible processes ruling the up-conversion phenomenon in photoluminescence materials. A) Excited state absorption; B) Energy transfer followed by energy state absorption; C) Successive energy transfer; D) Cross relaxation up-conversion; E) Up-conversion from cooperative sensitization and F) Multi photon absorption.

Multiphoton absorption (Fig.9F) is a process that occurs through the simultaneous absorption of two or more photons. The simultaneous absorption can occur via virtual levels, which significantly reduces the lifetime of the excited states. Since absorption rate of the material is proportional to the optical density of the incident light, multiphoton absorption does not need real levels, but just enough photon density. Considering the high pumping rate needed, this process can be only generated by high-energy sources as high frequency pulsed lasers.

On the basis of the processes exposed above, the production of up-converted emission by carbon dots with low carbon-based crystallinity seem very difficult. Up-conversion processes arise from well-defined energy structures. The electronic conformation of carbon dots is not so ordered and it makes difficult to obtain UPCL phenomena, even though some important articles report relevant experimental evidences in this sense[72,89,96,23,97,98,99,43]. Since we encountered problems reproducing some of the experimental results reported in literature, we tried to understand the real origin of the phenomena. In the next chapters, we will present our results which confirm the up-conversion fluorescence originates by the leakage from the second diffraction of the incident light on the monocromator. In fact, counterfeit up-conversion phenomena can be eliminated using an appropriate long pass filter able to block the excitation shorter wavelength light; even though Gan et al. shows that there is a co-existence both the two Up-conversion PL and second order diffraction light[100].

We also proved that within our amorphous carbon dots, up-conversion fluorescence (UPCL) derives from down-conversion of photoluminescence (PL) produced by the light component derived from the spectrofluorimeter grating monocromator second order diffraction component. In fact, the phenomena can be eliminated by using a long pass filter blocking the second harmonic leakage, or using a monochromatic light source to excite the samples[75,101,102].

Quantum Yield

The CDs quantum yield (QY) was calculated by comparing the integrated PL intensities and absorbance values of the samples (exited at 360 nm), using quinine sulphate dissolved in H_2SO_4 0,5 M as the standard (QY = 55%). The use of quinine sulphate in acidic media is widely recommended as a standard for static fluorescence[103].This because its absorption maximum peaks is at a wavelength very close to CDs maximum absorbance. The similarity of their maximum absorbance guarantees the avoidance of errors caused by intensity fluctuations in the emission of the instrument lamp.

The relative QY,ϕ, can be calculated using equation (1), where ***Grad*** is the gradient obtained from the integrated fluorescence intensity as a function of absorbance and ***n*** is the solvent refractive index. The subscript ***R*** represents the reference fluorophore with known QY.

$$\phi = \phi_R \left(\frac{Grad}{Grad_R}\right)\left(\frac{n^2}{n_R^2}\right) \qquad (1)$$

In order to minimize re-absorption effects, absorbance in the 1 cm fluorescence cuvette was kept lower than 0.05 Abs by using an excitation wavelength of 360 nm.

QY differences between amino-functionalized CDs and raw CDs can be explained by the presence of amino-based groups. Since electron-donating groups can enhance the conjugation degree of conjugated systems, this is expected to increase the transition probability from the ground state to the lowest excited state of the CDs band gap, contributing to a higher quantum yield[83].

2.1.3-Doping CDs

As reported in literature, one of the most important aspects related to CDs, is their capability to be doped with heteroatoms in order to adapt their properties to the need. In bottom-up approaches, CDs doping is performed adding a molecule that contains the heteroatom during the synthesis, i.e., it is possible to produce nitrogen doped CDs using urea[104,105], amines[12,106,107] and ammonia[108,109,110], while aminoacids[111,112] are used to produce co-doped CDs. Nitrogen heteroatoms can be added also using different compounds, as ammonium citrate[113], sodium alginate[114], polyethylenimmine[115], and Trizma®[116].

Moreover, other heteroatoms can be loaded or used as co-dopants. Nitrogen and phosphorus[117,118,], nitrogen and boron[119,120], and nitrogen and sulphur[121,122] co-doped CDs are synthesized using several molecules. For example, Barman et al.[123] produced co-doped CDs by bottom-up hydrothermal treatment of citric acid, using diethylentriamine as nitrogen source, boric acid as boron source and phosphoric acid as phosphor source. During the synthesis, the molecules containing the heteroatom can interact with the carbon source and embed the dopant in the carbonaceous matrix. In spite of the simplicity of the doping process, during the synthesis of our co-doped samples it was difficult to synthesize batches doped with small inorganic compounds, such as phosphoric acid and boric acid. The best approach is to consider the heteroatoms containing organic compounds, which can be able to react with the carbon source, instead small inorganic molecule. Indeed, when we used mercaptosuccinic acid as source of sulphur, the doping was performed without problems.

Effect of the CDs doping

In addition to passivation processes, CDs properties can be changed also introducing new heteroatoms in the carbon based backbone.

For example, the increase of nitrogen content in N doped CDs allows a quantum yield increase. Wang et al.[124] found that QY was correlated to conjugated π domains of C=N. Therefore, QY and photo stability under UV light exposure are enhanced by the increase of amine content in N-CDs synthesis. Carbon dots doping causes the insertion of new elements in the carbonaceous matrix introducing new bonding and new functional groups. This feature affects the energy levels and the new intra-gap layers that can be used to change some CDs properties.

The effect of doping can be particularly effective when CDs are used in charge transfer.

The production of new intra-gap layers can be used to tune the energy level position in comparison with other materials, for example with photocatalysis.

At this purpose, Han et al.[125] produced nitrogen, phosphor, boron and Sulphur-doped and co-doped CDs by combustion flame technique. They used their CDs without any other catalyst, enhance oxygen reduction reaction (ORR). CDs showed different photocatalytic performances to reduce oxygen. Finally they noted that N,B co-doped CDs presented good activity, with electron transfer number[126] close to the Pt one. In this case, the particular disposition of the intra-gap layers, produced by the doping with nitrogen and boron, allowed a good electron transfer process capable to reduce oxygen.

Barman et al.[123] studied the photo-physical properties of nitrogen, phosphor and boron co-doped CDs and the influence of the dopants on the electron-hole transfer process. They studied the effect of the doping with nickel(II)phtalocyanine attached on CDs surface. By studying the radiative decay rate and the average decay time, they observed different behavior in NP-CDs and NB-CDs. Indeed, the first sample accelerates electron transfer from CDs to the phtalocyanine, while the boron slows down the electron transfer and promotes holes transfer. In conclusion they understood that the doping of different heteroatom, as showed in Fig.10, confers CDs p-type (Fig.10A) or n-type (Fig.10B)behavior.

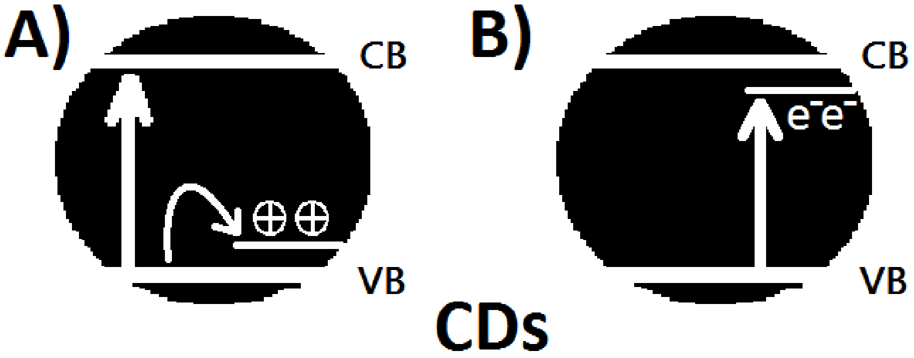

Figure 10: Representation of CDs doped with heteroatoms able to confer N-type or P-type behavior. In A) heteroatoms like boron introduce intra-gap layer on the valence band, allowing the promotion of holes on the new layer and holes transfer. In B) the introduction of intra-gap layer under the conduction band promotes the charge transfer of the photo generated electrons.

2.2- Titanium Dioxide

2.2.1-History of Titania

Studies and application on titanium dioxide cover approximately one century.

Over the past century an extensive research has been conducted to understand titanium dioxide properties and unveil its possible applications.

In 1921, Renz published some preliminary observations in a paper concerning the interaction between titania and light. His work focused on the partial reduction of TiO_2 into Ti_2O_3 and TiO when irradiated with sunlight in presence of an organic compound[127].

Furthermore, thanks to its wide application as pigment for external murals, de-cohesion and pulverization of the surfaces exposed to sunlight was observed. These phenomena induced Goodeve and Kitchener, in 1938, to presume that TiO_2 could act as a catalyst increasing photo-oxidation of the wall paint's organic component[128].

Despite the captivating properties of TiO_2, the interest of the scientific community remains mostly focused on zinc oxide because of its higher photocatalytic activity. In 1953 the reaction mechanism of ZnO was explained for the first time, showing its capability to oxidize organic compounds and reducing atmospheric oxygen. M. C. Markham described the involvement of radical species in the photo oxidation process[129]. During that period, her work was focused on the development of several typologies of photo-assisted fuel cells, by employing various metal oxides. Then, Markham discovered that the more active zinc oxide underwent fast photo corrosion, while titanium dioxide appeared to be more resistant. These findings reignited the interest of the scientists on TiO_2.

In 1958, while studying the oxygen absorbance on TiO_2, Kennedy observed that the produced electrons were transferred to the oxygen only after the photo excitation and that oxygen was reduced before being absorbed on titania's surface. In the same publication, he observed that when oxygen was absorbed, titania was able to decompose a sacrificial dye such as methylene blue or methyl orange[130].

In 1964, Kato studied titanium dioxide' ability to oxidize alcohols, producing hydrogen peroxide. He found out that various types of titania had different photocatalytic activities. Moreover, he also observed that anatase powders were more active than the rutile powders[131].

One year later, Mc Lintock stated for the first time that, thanks to the conversion of superoxide ion to oxygen[132], it was possible to oxidize organic compounds to CO_2 and H_2O.

During the end of 1971s, Fujishima found out that photo-activated titania evolved oxygen at different potential from the thermodynamic expectation, because the photo excitation process converted the photon energy into chemical energy with little loss[4].

In 1972, Fushijima and Honda published their famous paper on simultaneous oxygen and hydrogen production from titania using a photo electrochemical cell. Thanks to the solar energy conversion implication[133], photoelectrochemistry started to receive much wider attention.

In 1977, Bard and coworkers proposed that TiO_2could be used for water purification via photocatalityc decomposition of pollutants[134].

They also expanded the research to a long list of inorganic and organic species and suggested that photocatalysis could be a useful approach to both environmental and photo-assisted organic synthesis. They proposed that each irradiated semiconductor particle could be considered as a photo electrochemistry cell, where both photo-assisted oxidation and dark reduction take place[135].

After several years of research, photocatalysis grew as a well-known technology for both selective and unselective oxidation of organic compounds for water purification[136,137,138].

However, the main drawback of this application is the necessity to employ powerful UV light sources to treat organic pollutants in wastewater. In the early 1990s, it was clear that the amount of UV light present in natural light was insufficient to produce passive purification processes without special light sources. Therefore, it was unavoidable to shift the focus to less energy-demanding technologies, such as passive self-cleaning and self-sterilizing surfaces. Despite the problems related to the low activity, the concern on this socially relevant application pushed the scientists to develop new systems coated with TiO_2 films. At the same time, with the aim to produce more versatile materials able to be activated in visible light, several doping approaches were developed. Metal doping, non-metal doping and oxygen-deficient titania were developed in order to reduce the titania bandgap. Alternatively to the bandgap reduction, the addition of photosensitizers able to transfer adsorbed energy to titania was also developed.

In the last twenty years, the application of charge delocalizers with the purpose of reducing electron-hole recombination was also developed. At this purpose, cases of production and development of titania based hybrid materials in combination with metal nanoparticles, metal nanowires, carbon nanotubes, graphene sheets and carbon dots, increased in literature. Both titania doping system and titania based hybrid materials have been used in this work in the attempt to produce a versatile material for wastewater treatment under visible light. However, before discuss those aspects, a short digression on chemical, physical, and electrochemical properties of Titania is reported below.

Crystal structures of titanium dioxide

Titanium dioxide exists with three different crystal structures: Rutile, Anatase and Brookite. Rutile and Anatase phases possesses photocatalytic activity. Just recently[139], Brookite began to be considered a good material for photocatalysis. On the other way, despite Rutile possesses smaller bandgap than Anatase and Brookite, it shows smaller photocatalytic activity due to the less amount of oxygen defects. Since the thesis is focused on the application of Anatase as photocatalyst for wastewater treatment, this paragraph describe only this phase. Three different facets mainly describes anatase: {101}, {001} and {100}. The first two planes have low surface energy, for this reason they are common in natural crystalline materials[140]. In anatase nano crystals, the face {101} is the most prevalent (Fig.11).

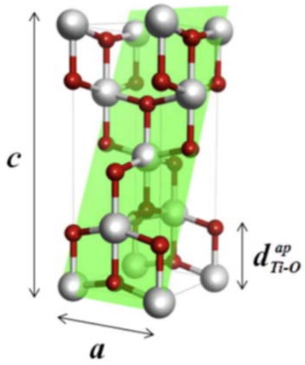

Figure 11: (101) anatase face, from Chemical Physics Letters 577 (2013) 114-120

Electronic structure: valence band and conduction band

Electrons in free and isolated atoms occupy well-defined energy levels, while atoms in solids are commonly disposed in periodic, regular and tridimensional organization. During the formation of the solid, valence electrons of the external orbitals start to interact with each other, starting to split the spin or to shift energy. When the number of atoms increases, an increasing number of orbitals shifts at higher and lower energy. Shifted orbitals move close each other and produce two distinct bands: the valence and the conduction bands. Whichever is the orbitals involved in the formation of the chemical bond, the energy gap between the bands is related to the inter-atomic distances. The bandgap defines the energy required to promote an electron from the valence band to the conduction band.

According to the characteristics of the bandgap as the disposition of the valence and conduction bands, the materials can be grouped into three different categories: metals, semiconductors and dielectrics materials.

In metals (Fig.12A) the valence and conduction bands are overlapped. Since externals orbital attract electrons with weaker forces than the others orbitals, their electrons can be easily transferred. Therefore, few energy is required to move electrons through the net of atoms in the metal solid. This high electron mobility expresses one of the most important features of metals: the high electrical conductivity.

In semiconductors (Fig.12B), the valence and conduction bands are separated by a discrete amount of energy. In metals, some electrons occupy the conduction band, but in semiconductors conduction band is completely unoccupied, because all electrons occupy the valence band. When the semiconductor receives enough energy to fill the gap, electron starts to be promoted to the conduction band. This electron movement results in a flux of current.

Finally, in dielectric materials (Fig.12C), the valence and conduction bands are well separated and it is very difficult to promote an electron from the valence band to the conduction band.

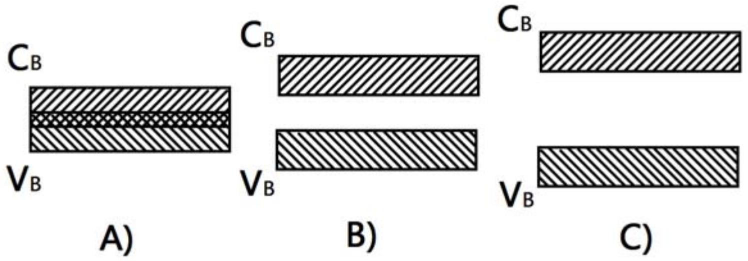

Figure 12: representation of valence and conduction band in A) metals, B) semiconductors and C) dielectric materials.

In semiconductors, an electron promotion to the conduction band leaves a positive charged vacancy on the valence band, usually called “hole”. The necessary energy to promote electrons can derived by heat, chemical energy or light. Depending on the type of the carried charges (electrons or holes), semiconductors can be grouped into two distinct categories: n-type and p-type semiconductors, in which electrons and holes respectively are the principal carried charges. Fermi level is another important parameter, useful to define the behavior of n- and p- type of semiconductors. It is defined as the energy level at which the probability of occupation by an electron is 0,5. For example, in a pure silicon based semiconductor the Fermi level lies at half energy of the bandgap. For a n-type semiconductor the Fermi level lies just below the conduction band, meanwhile for a p-type material it lies just above the valence band.

Titanium dioxide is a semiconductor with a bandgap depending on the considered crystalline phase. In anatase, bandgap is defined by the 3d band of Ti^{3+} (valence band) and the 2p band of O (conduction band). Oxygen in the lattice also defines photocatalytic properties of the semiconductor. Its behavior derives from the presence of some oxygen vacancy in the crystal lattice, that permits to redistribute free electrons from Ti^{3+} at the edge of the defect. This concentration of negative charges generates the n-type behavior of the anatase.

If in rutile, the presence of oxygen vacancies permits to electrons of the neighbor Ti^{3+} atoms to re-occupy their respective 3d orbitals, in anatase, a “split geometry” takes place where an oxygen atom near the vacancy is attracted in it and partially shifted from its position. This partial migration of the oxygen generates two zones where titanium atoms possess greater electrons concentration. The first zone is defined by the Ti^{3+} atoms near the vacancy, whereas the second zone identifies with the space produced by the partial shift of the second oxygen[141].

2.2.2-Photo-electrochemical properties of titania

The main property of titanium dioxide and of other semiconductors is the capability to adsorb thermic or light radiation to produce pairs of electron-hole. If the semiconductor is in contact with another material, as described below, it is able to concede electrons or holes. In this way, if the oxidation potential of the material is greater than the energy of the valence band, the hole transfer is allowed and the material can be oxidized. Conversely, when reduction potential of the material is less energetic than the conduction band, the semiconductor can transfer electrons and reduce the material. Therefore, the generation of electron-hole pairs can promote photo-catalyzed reaction. When titania is irradiated in presence of water, electron-hole pairs can react with water to produce high reactive species able to oxidize a wide range of organic pollutants[142,143].

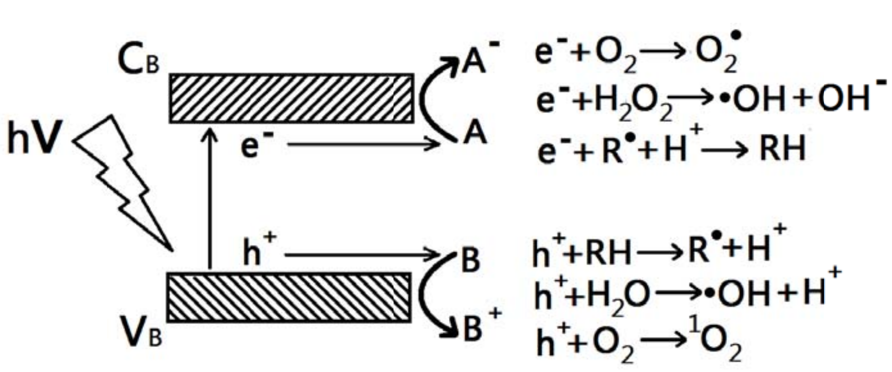

Figure 13: Electrons and holes reactions with water can produce several reactive species useful for wastewater treatment.

In the Fig.13 water photochemistry in rutile and anatase are summarized. All these highly reactive radicals can be generated thanks to the titania bandgap configuration. It is important to note that anatase can include in its bandgap the potential of important reversible reaction concerning water and radicals production. As it is possible to notice in Fig.14, the energy of anatase conduction band (E_{CB}) is higher than the reversible hydrogen potential at all pH values. The energy of anatase valence band (E_{VB}) is positive enough to oxidize water at all pH. At the same time, E_{CB} is sufficiently negative to reduce molecular oxygen into superoxide radical anion, while the E_{VB} is enough positive to produce hydroxyl radicals and hydroxide anions. Another important aspect is that the E_{VB} is sufficiently positive to permit the direct hole-mediated oxidation of organic compounds adsorbed on the surface[144].

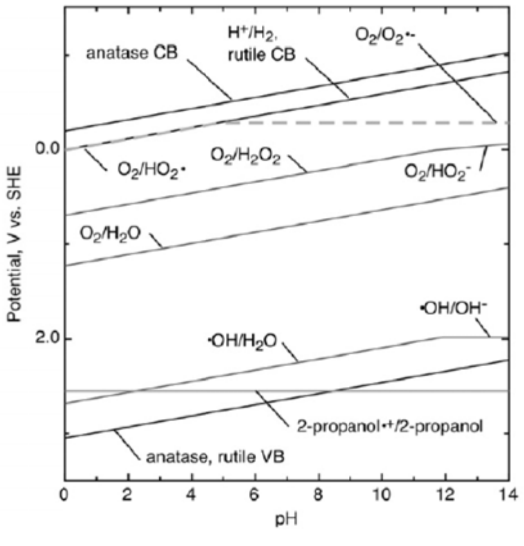

Figure 14: Scheme of potentials representing all the potential involved in water reaction, inscribed into the energy bandgap of anatase and rutile as function of pH.

If the potential of the anatase is well defined, it is more difficult to show how TiO_2 is able to carry the photo generated electron-hole pair with small number of recombination events. In order to explain this peculiarity, Fushishima et al. proposed a model where titanium dioxide is able to trap electrons in restricted areas of its surface, with a consequent local increase of electrical conductivity[144]. Therefore, when the first electron is trapped on the surface, it generates a more conductive domains that can simplify the direction of a second electron to the same area. These small areas are able to act as "conductive wire", and they could start from the surface to develop in the bulk of the material. If electrons are channeled in this way, the localization in these domains should protect them from recombination with holes. The electron trapping occurs with the reduction of a proton adsorbed on the surface in an atom of hydrogen, who is electrochemically inserted on the semiconductor surface (Fig.15 A). As studied by Colón et al.[145], the insertion of hydrogen atoms is theoretically confirmed by an increase of the volume. To further contrast recombination, hole-trapping agent can be inserted as interstitial hydrogen on the surface leaving electrons. The "conductive wire" is usually contrasted by recombination and by the presence of adsorbed oxygen. When oxygen is adsorbed on the surface, it can be reduced to superoxide or hydrogen peroxide by the migrating electrons (Fig.15 B): in this case the photocatalysis takes place. In the meanwhile, trapped holes on the surface can oxidize adsorbed water in hydroxyl radicals and superoxide anion radicals (Fig.15 C).

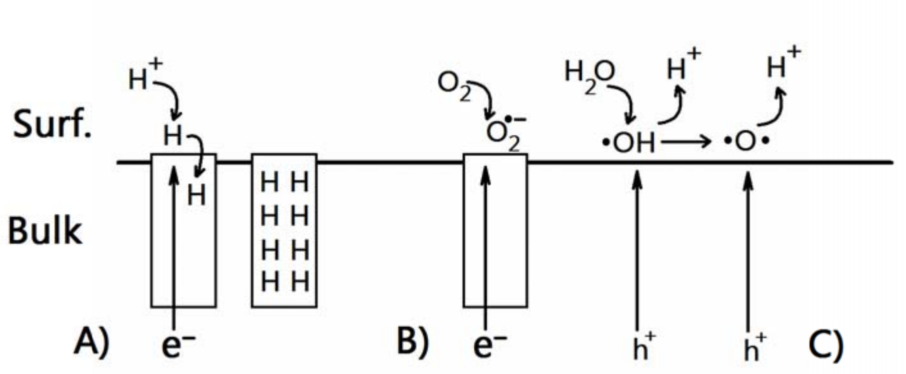

Figure 15: combined oxidative-reductive model for the photo-induced hydrophilic effect, in which oxidizing and reducing regions are formed spontaneously. In the absence of oxygen, protons are reduced to produce hydrogen insertion (A); in presence of oxygen, they are reduced to hydroxyl and superoxide radicals (B); in (C) the oxidation region formed in contrast to the hydrogen insertion area. At the same time, all the active products produced on the titania surface contribute to increase the wettability of the titania surface, producing the photo-induced hydrophilic effect.

Lifetime of the processes related to electron-hole pair

When TiO_2 adsorbs a photon with equal or greater energy to its bandgap, electron-hole couples are generated. After generation, charges are separated in free electrons and holes that migrate to the particle surface until its capture. On the photocatalyst surface, trapped charges can react with adsorbed electron acceptor or electron donors. The processes with the trapped charges and these materials can occur after charge transfer, especially when these materials are strongly adsorbed on the surface.

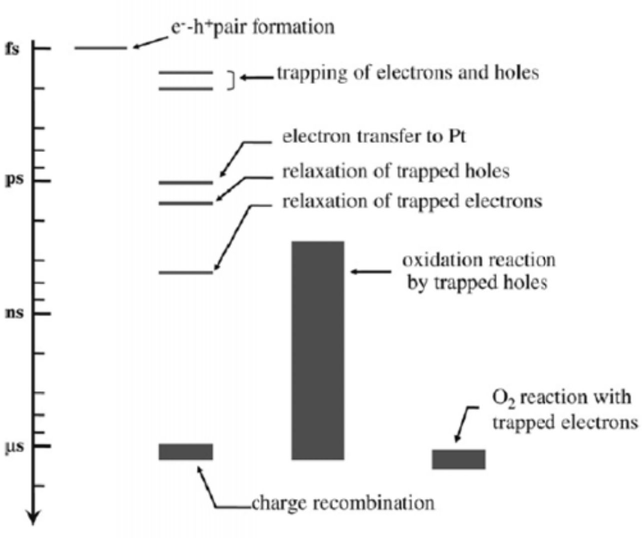

Figure16: time scale of the most important processes involving electron-hole pairs in photocatalysis[139].

There are not only surface processes involving electron-hole pair. The two free charges can also be trapped into bulk trapping sites and recombine, releasing heat and reducing titania efficiency. Titania can be used as photocatalyst because processes such as electron-hole pair generation, migration, trapping and reaction are usually faster than charge recombination (Fig.16). Therefore, the addition of charge delocalizers can improve charge separation and contrast recombination effect. Usually wide ranges of compounds are added to allow charge separation to increase efficiency, such as metal nanoparticles and carbon based nanomaterials. In this study, the addition of carbon dots is strictly connected with this practice.

Active species formation

Titanium dioxide is an excellent photocatalyst under different points of view: it is cheap and widely present in nature. Moreover, titania possesses good chemical stability against corrosion[133] and its bandgap is in a position between water oxidation and water reduction potentials.

As seen before, several reversible reactions involving water to produce radicals can be developed thanks to its bandgap position. The most important reaction are:

$$TiO_2 + h\nu \rightarrow e^- + h^+ \qquad (2)$$

$$h\nu\, e^- + h^+ \rightarrow heat \qquad (3)$$

$$H_2O + 2H^+ \rightarrow \frac{1}{2}O_2 + 2H^+ \qquad (4)$$

$$2H^+ + 2e^- \rightarrow H_2 \qquad (5)$$

$$O_2 + e^- \rightarrow \bullet O_2^- \qquad (6)$$

$$2\bullet O_2^- + H_2O \rightarrow OH_2\bullet + OH^- \qquad (7)$$

$$OH^- + h^+ \rightarrow OH\bullet \qquad (8)$$

The reaction (2) represents electron-hole pair generation from the adsorption of one photon by titanium dioxide, while the reaction (3) represents the recombination between the photo-generated charges. In order to guarantee the development of the reaction (4-8), it is necessary to minimize or to suppress the reaction (3). The reaction (4) describes oxidation of water by two holes to produce molecular oxygen and two hydrogen cations; meanwhile the reaction (5) describes the reduction of two H^+ into elemental hydrogen. Reaction (6) illustrates oxygen reduction into superoxide radical anion, while reaction (7) illustrates the interaction of water with two superoxide radical anions to produce hydroperoxy radicals and hydroxyl anions. Finally, reaction (8) shows the oxidation of a hydroxyl into hydroxide radical.

To fully understand the titania potentiality as photocatalyst for wastewater treatment, it is necessary to study the oxidizing and reducing species produced on the surface, as well as their roles in the photo assisted process of the pollutants mineralization.

The main oxidizing species produced on titania surface include: holes, hydroxyl radicals, superoxide radicals anions and singlet oxygen; while oxygen and hydrogen peroxide are involved in the photocatalytic oxidation processes, with indirect mechanisms.

Holes

Holes are the first oxidizing specie in the photocatalytic process, since they can directly react with pollutants adsorbed on titania surface. Moreover, they can react with water and with hydroxyl radicals to produce other active species. As it is showed in Fig. 6, holes are usually trapped in few picoseconds on the surface of photocatalyst; this indicates a high trapping rate and high concentration of holes on the surface. Yoshihara et al.[146] describe two kinds of trapped holes: deep holes and shallow holes. Shallow trapped holes can be thermally excited and they show a comparable reactivity and mobility with free holes. These holes reacts rapidly with chemisorbed substances. On the contrary, deeply trapped holes usually possess less oxidizing potentials[147] and, due to their localized nature, they prefer to react with more mobile physisorbed substances.

Hydroxyl radicals

Another subject playing an important role in initiating oxidation reactions is the •OH radical. •OH is produced by oxidation of hydroxyl anion on the surface or adsorbed water and it is particularly active towards substances weakly adsorbed on TiO_2 surface. However, after the research published by Ishibashi et al., the role of •OH radicals lost importance as active species. The authors found out that hydroxyl radicals are produced with three orders of magnitude smaller than trapped holes[148]. Moreover, •OH produces an indirect oxidation, while holes and many other substances act with direct oxidation[149,150]. Often the oxidation of adsorbed compounds can be produced easier by the direct oxidation than the indirect oxidation. In these cases, the role of hydroxyl radicals can be outclassed by the other species.

For example methanol oxidation could be initiated by holes (11) (12) instead of •OH radicals (9) (10)[151]:

$$CH_3OH + \bullet OH \rightarrow \bullet CH_2OH + H_2O \qquad (9)$$

$$\bullet CH_2OH \rightarrow HCHO + H^+ + e^- \qquad (10)$$

The oxidation initiated by holes:

$$CH_3OH + h^+ \rightarrow CH_3OH^+ \rightarrow \bullet CH_2OH + H^+ \qquad (11)$$

$$\bullet CH_2OH \rightarrow HCHO + H^+ + e^- \qquad (12)$$

As for methanol, many other adsorbed materials can be oxidized by holes instead of •OH radicals. This fact suggests the relative importance of this specie and the indirect oxidation process in comparison with holes and direct processes.

The proper origin of •OH could also be another aspect to be investigated. Fujishima et al.[144] report a series of publication showing that •OH is generated by the oxidation of water or hydroxide ion with photo-generated holes[152]. Nakato and co-workers[153] proposed an alternative reaction (13), showed below, in which •OH are produced by a nucleophilic attack of water on a hole trapped under the TiO_2 surface.

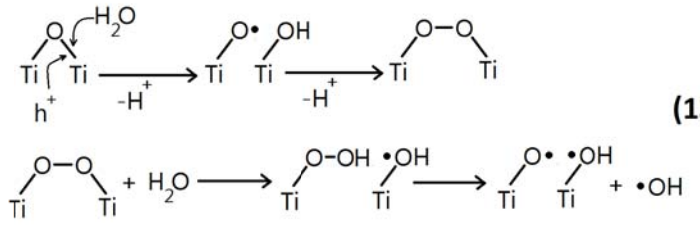

(13)

Moreover, on titania surface, different processes involving H_2O_2 produced by reduction of oxygen (14) or by disproportion of superoxide anions (15), can produce ●OH radicals (16-18):

$$O_2 + 2e^- + 2H^+ \rightarrow H_2O_2 \qquad (14)$$

$$\bullet O_2^- + \bullet O_2^- + 2H^+ \rightarrow H_2O_2 + O_2 \qquad (15)$$

$$H_2O_2 + e^- \rightarrow \bullet OH + OH^- \qquad (16)$$

$$H_2O_2 + \bullet O_2^- \rightarrow \bullet OH + OH^- + O_2 \qquad (17)$$

$$H_2O_2 + h\nu \rightarrow 2\bullet OH \qquad (18)$$

Singlet oxygen $^1O_2$

Even if not reported before, singlet oxygen is an important reactive specie also used as reagent in organic synthesis. Its formation was predicted in 1981 by Munumera et al.[154], but only 23 years later Nosaka et al.[155] for the first time reported the detection of $^1O_2$ on irradiated TiO_2 surface. They propose that singlet oxygen derives from the oxidation of $\bullet O_2^-$ with holes (19):

$$\bullet O_2^- + h^+ \rightarrow {}^1O_2 \qquad (19)$$

An experiment focused on the generation of singlet oxygen by anatase or rutile particles dispersed in solvents, corroborates the thesis of Nosaka: the addition of superoxide dismutase in the system caused the complete suppression of $^1O_2$. This result suggests that $^1O_2$ arises from the oxidation of $\bullet O_2^-$.[156] Moreover, observation of short lifetime from 2,0 to 2,5 µs[151], and the oxidation of materials only adsorbed on TiO_2 surface, propose that singlet oxygen mainly lies on the TiO_2 surface.

Molecular Oxygen O_2

Molecular oxygen is directly dissolved in the wastewater and participates in the reaction, accelerating the mineralization of organic pollutants. O_2 also plays an important role in many other aspects of the TiO_2 photocatalysis, such as it can capture the photo-generated electrons and suppress molecular recombination, but in TiO_2 nanoparticles is able also to improve stimulated charge separation[157]. Indeed, more holes can be trapped on particles surface in presence of oxygen.

Another aspect described before concerns the oxygen contribution to active oxygen species generation. Superoxide anion radical and hydrogen peroxide are the two main products of TiO_2 photocatalysis and are fundamental for the production of other active species such as ●OH and $^1O_2$.

If oxygen contributes to active species formation, it can also directly act as oxidizer of organic pollutants. It is proposed that mineralization of organic pollutants is mostly mediated by molecular oxygen. If holes can initiate the oxidation, oxygen can react with the formation of organoperoxy radicals (ROO●) with the consequent degradation and mineralization of the organic material. Its role in the formation of organoperoxy radicals is corroborated by similar conclusion obtained from photo electrochemical studies[158,159] and isotope studies[160].

Another important role of the oxygen is the maintenance of the stoichiometry of TiO_2. Indeed, oxygen atoms of TiO_2 lattice can be lost during the activation. On the photocatalyst surface, high concentration of trapped holes could break oxygen bonded on the edge of the material changing the oxygen content on the surface. Moreover, it was noticed that during the degradation of adsorbed organic compounds as acetic acid, photocatalyst lose oxygen[161]. In O_2 deficient conditions, oxygen atoms on the edge are lost with a change of the stoichiometry and with a reduction of the photocatalytic. Thus, presence of O_2in the system can contrast the depletion of the element from the photocatalyst and the maintenance of its properties.

2.2.3-Widening the titania absorption window: the doping effect

Anatase is one of the most promising photocatalyst for wastewater treatment thanks to its bandgap values, its resistance to the corrosion and the cheap cost. Anatase possesses a band gap of 3,2 eV, and electrons start to be promoted to the conduction band with a wavelength of 387 nm[162]. The solar radiation transmitted through the atmosphere is composed by 95% of visible and infrared radiation and only 5% from UV region (Fig.17), thus the most part of the solar radiation is useless for titania.

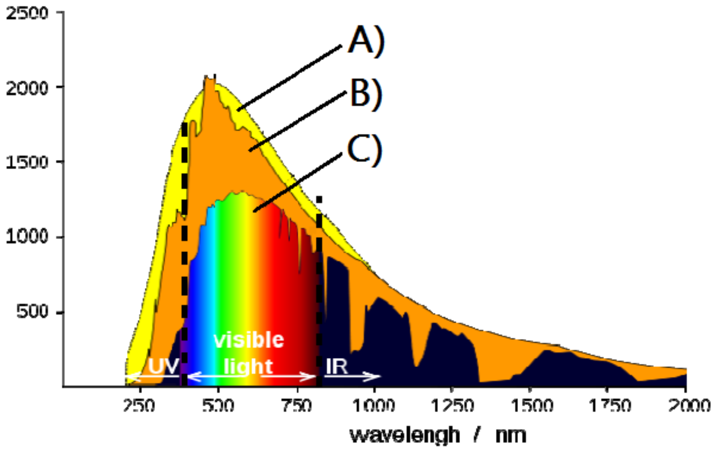

Figure 17: Solar spectrum A) 5778K black body radiation; B) solar radiation before the atmospheric adsorption C) solar radiation at the level of the sea.

Many publications report the possibility to tune the anatase crystal structure in order to improve its interaction with solar light[163,164]. It is possible to modify the structure following three different approaches: 1)the first concerns the introduction of metal or non-metal heteroatoms into the crystal lattice[136,165,3] in order to insert new intra-gap band levels to reduce titania bandgap; 2)the second considers the synthesis of oxygen-deficient titania[166,167]; 3) the third uses dyes or other semiconductors that, thanks to energy transfer processes[168,169,170,171], can activate the photocatalyst.

A wide range of transition metals can be introduced into the lattice as heteroatoms, as V[172], Cr[173], Mn[174], Fe[175], Co[176], Ni[177], Cu[178], Zn[179], Y[180], Zr[181], Pd[182], Ag[183], Cd[184], W[185], Pt[186], which have been successfully added as dopant to reduce titania bandgap. The method is usually conducted through various processes: via sol-gel[187], wet impregnation of TiO_2 with metal precursors solutions[188], hydrothermal processes[189], chemical vapor deposition[190] (CVD), ion assisted sputtering[191] and W/O microemulsion[192].

After several years of systematic research, the doping of transition metals solved some problem related to the use of suspensions of titania particles in wastewater treatment. For example, the use of Fe or Fe and Co can lend ferromagnetic properties to titania nanoparticles partially solving the problem to rescue the photocatalyst from the wastewater treatment reactor[193].

Despite some possible improvements, the fine-tuning of the doping with transition metals is still an unsolved problem. Indeed, high percentages of doped cations can induce recombination with a strong decrease of the photocatalytic activity of the materials. In alternative to the metals, the addition of heteroatoms such as C[194,195,196,197], S[198,199], N[200,201,163,202], F[203,204]and others[205,206,207] can reduce the bandgap and can extend the adsorption on visible light range. For the purpose of this study, we considered the nitrogen doped titania as starting material. This well-known compound may facilitate to focus on the problems deriving from the interaction of the loaded carbon dots and the photocatalyst. .

Nitrogen doped titania

During the synthesis of titania with $TiCl_4$ in presence of NH_4OH, Sato[208] observed the production of NH_4Cl. He noted that impurities of the salt, during the annealing process, produces a photocatalytic material able to absorb in visible light. Since this first report, nitrogen doped titanium dioxide was widely studied and the role of nitrogen in crystal lattice was clarified.

In 2001 Asahi et al.[209]suggested that nitrogen introduces the N 2p level on the O 2p valence band and N 2p level produces a bandgap narrowing, improving its photocatalytic activity in the visible range. Despite the increase of nitrogen content, the N 2p level remain localized. Lin et al.[164] calculated that even for high nitrogen concentration as 12,5%, the level is always localized slightly above the top of the O 2p valence band.

Since the discovery of this effect, several methods able to insert nitrogen into the lattice were proposed: i) sol-gel synthesis[200,201,210,211,212], ii) chemical treatments of TiO_2[202,213,214], iii) oxidation of titanium nitride[215,216], iv) ion implantation[217,218] and v) magnetron sputtering[219,220].

Regardless the synthesis, the nature of the doping nitrogen in the lattice determines photocatalyst properties. Nitrogen can remain simply trapped in the matrix as nitrogen oxide or can occupy defined sites in the lattice. Furthermore, it can be trapped into the lattice as: nitrogen oxide or chemically bonded with titanium and/or oxygen as interstitial and substitutional nitrogen. Concerning the second case, interstitial or substitutional doping nitrogen need some further explanations. As showed in Fig.18A, substitutional nitrogen is bonded with titanium atoms in a regular lattice site, while in Fig. 18B an interstitial nitrogen is directly bonded to a lattice oxygen.

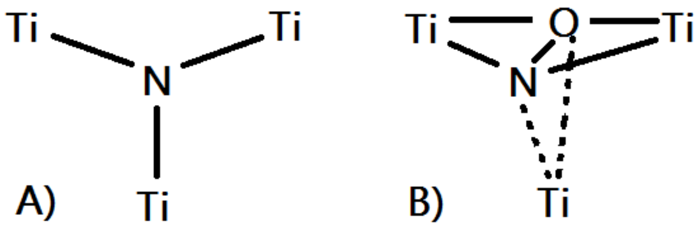

Figure 18: Schematic draw for A) substitutional and B) interstitial nitrogen doped anatase[221].

The process of nitrogen intercalation in titania crystal lattice is still not well understood. Nitrogen species are embedded into the matrix while, during the crystallization process, nitrogen is intercalated to dope the lattice. As showed in Fig.19, Kuroda et al.[222], for samples treated under NH_3 atmosphere, proposed a model to describe the intercalation process of nitrogen during the annealing. When the bridging OH condense, ammonia reacts with the five coordinate Ti to form Ti-NH_2. In a second time, during the annealing process, part of the bonded species are incorporated in the lattice through the condensation and dehydration of OH groups. Finally, thanks to the higher temperatures of the annealing process, the material dehydrates to form an anatase phase doped with nitrogen.

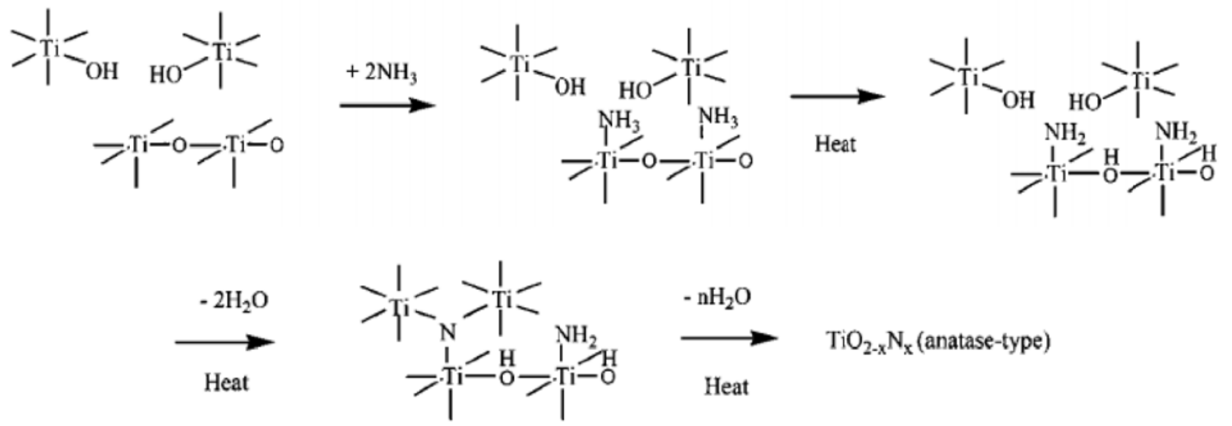

Figure 19: process proposed by Kuroda et al. of the intercalation of nitrogen species and the titania doping with nitrogen.

Unfortunately, the similar radius of oxygen and nitrogen atoms produces crystal lattice distortions that are impossible to detect by XRD measurements, in fact, no differences are detectable in XRD[223] patterns of doped and un-doped titania.

Despite the common origin, substitutional and interstitial nitrogen possess different energies and two different positions in the bandgap. Di Valentin et al.[221] calculated that the N 2p level of the substitutional nitrogen lies on the valence band, while the N-O level of the interstitial nitrogen is more energetic and shows a level in a more energetic part of the bandgap. Therefore, thanks to its position on the valence band, substitutional nitrogen is the real cause of the bandgap reduction, which permits the use of visible light for photocatalysis.

Once defined the origin of nitrogen doping species in titania crystal lattice, it is necessary to define their role in photocatalytic activity. In the past, the researchers working on this field were divided on the role of nitrogen in reducing the bandgap. Some authors attributed the adsorption in the visible range to the localized impurities, while the moiety of the titania without doping was able only to adsorb UV light.

Today is clear that the oxygen substitution with nitrogen makes the photocatalyst able to interact with the visible light, but is also evident that nitrogen atoms are localized in the lattice. Consequently, the localized nature of the doping centers generates holes with very low mobility. This property was noted by Nakamura et al.[224] who showed nitrogen doped titania able to degrade a sacrificial dye only with processes involving intermediate species, while the direct oxidation operated by holes is totally missing.

In 2005, Livraghi et al.[225] explained theoretically the behavior of nitrogen doped titania; they studied their results obtained by magnetic resonance spectroscopy (EPR) and their theoretical model was confirmed. Usually, the anatase oxygen vacancies are characterized by two exceeding electrons which cause the reduction of the neighbor Ti^{4+} in to Ti^{3+}. EPR is able to detect the electron localized in 3d level of Ti^{3+}.

From the Livraghi et al.[225] study emerged the existence of nitrogen species strictly bonded to the TiO_2 lattice. Depending on the interaction with oxygen vacancies (Ti^{3+}), these species generate doubly occupied or singly occupied electronic states. Doubly occupied states generate diamagnetic species (Nb^-), while singly occupied states generate paramagnetic species (Nb●). This feature derives from the interaction of nitrogen with the oxygen vacancy, independently from their substitutional and interstitial position.

Livraghi found that one of the two configuration is more stable because the electron that lies on Ti^{+3}3d level can be transferred to the N 2p level. As it is showed in Fig.20A, the electron transfer produces the oxidation of Ti^{3+} in to Ti^{4+} and the Nb● paramagnetic center recombines in a Nb^- diamagnetic one. This phenomenon was associated to a diminution of oxygen vacancies after nitrogen doping of TiO_2. Once nitrogen doped titania is excited by visible light radiation (Fig.20B), electrons in diamagnetic centers are promoted to the Ti^{3+} 3d level, making the backward travel and producing paramagnetic centers. This passage locks the photo-generated holes in the paramagnetic centers, enabling the direct oxidation nitrogen doped TiO_2 to be absorbed on TiO_2 surface. In this process if holes are locked in the doping centers, electrons are free to react; as the case of the reduction of O2 into ●O_2^- superoxide anion.

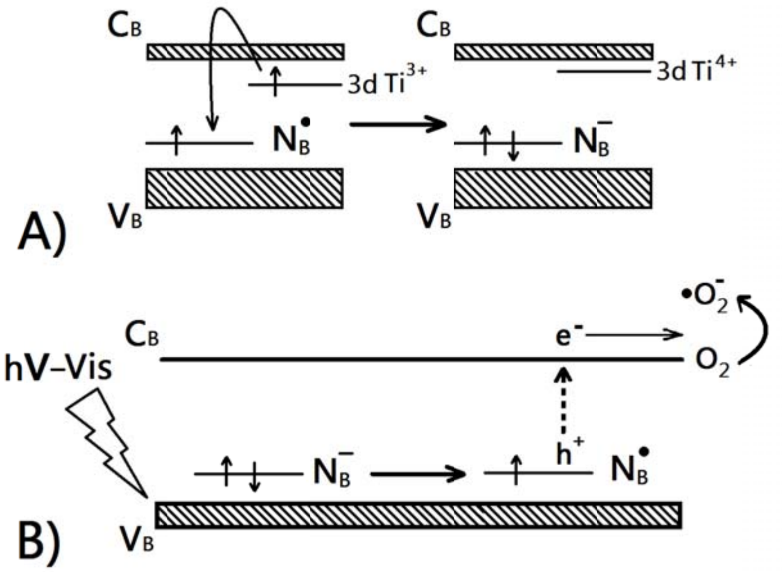

Figure 20: A) Electronic band structure modification resulting from the interactions between paramagnetic levels and oxygen vacancy and B) Livraghi et al. proposed mechanism for the process by visible light activation of the nitrogen doped NTiO$_2$.

Thanks to the work of Livraghi et al.[225], is it possible to assert that the activity derived from the holes in the nitrogen doped titania is limited to the doping centers. In this condition, the photocatalytic material is deprived of one of its most powerful oxidizing species. Despite that, the ability to use visible portion of the spectrum, associated with the less amount of the free holes, can increase the generation of free electrons and reduce the recombination.

In conclusion, doping titania with nitrogen generates a versatile photocatalyst interacting with the visible portion of the solar spectrum. Although, this enhancement is mitigated by the lower mobility of some active species able to reduce the photocatalytic activity.

Synthesis of nitrogen doped titania: state of the art

Since the first nitrogen-doped TiO$_2$ synthesis performed in 1986 by Sato[208], many efficient nitrogen-doped titania under solar radiation were studied. The great attention paid on this system developed many syntheses, with different scalability opportunities; all of these syntheses can be divided into two main categories: dry methods and wet methods. Since in this study we adopted a particular wet process called gel-sol process, the latter will be described in a dedicated paragraph.

Dry processes

The most common dry process uses annealing treatments of titanium oxide or other titanium-based precursors in specific atmosphere. For example, it is possible to synthesize nitrogen-doped titania through oxidizing titanium nitride (TiN) in O_2 atmosphere by annealing[226], at 550°C. In the same reference, nitrogen-doped anatase is produced by annealing undoped TiO_2 in NH_3\Ar atmosphere at 600°C. Further studies showed that when gaseous NH_3 is used, it possible to tune the amount of N in $TiO_{2-x}N_x$ changing the annealing temperature from 550° to 600°C[227].

At these temperatures, NH_3 gas is both a nitrogen source and a powerful reducing agent, because at 550°C it decomposes in N_2 and H_2. So, when TiO_2 is treated at the right temperature in NH_3 atmosphere, the sample is doped and reduced at the same time[228].

Annealing in NH_3 atmosphere is used also to directly treat titanium isopropoxyde[229] (TIP,) and $Ti(OH)_4$[230]. In order to produce $TiO_{2-x}N_x$, titanium-based alcoholates are also annealed in presence of urea[231]. Another synthesis is based on mechano-chemical methods. In these processes, nitrogen sources like urea and hexamethylenetetramine are ground with TiO_2 into a ball mill. Energy applied during the milling allows nitrogen intercalation in the lattice. Moreover, these methods are very energetic and they can convert anatase into rutile phase. Unluckily, mechano-chemical processes permit to dope TiO_2, but annealing at 400° C is required to remove residual organic substances and clean the compound[232,233].

Another dry process is the application of DC reactive magneton sputtering, where a nitrogen-containing plasma can implant nitrogen atoms in TiO_2 crystal lattice[219]. This technique is particularly versatile to dope thin film and TiO_2 layers, even on non-flat and complex surfaces.

Wet processes

Sol-gel synthesis is the most widely used process to synthesize nitrogen-doped titanium dioxide.

Sol-gel is a technique able to produce ceramic and glass materials that involves the transition of a colloidal solution (sol) into a solid phase (gel)[234].

A sol is a stable suspension of colloidal amorphous or crystalline particles in a liquid. Thanks to aggregation and covalent bonding between the sol particles it is possible to form a gel.

A gel consists of a three-dimensionally continuous and porous solid network. In particular situations, when a solvent submerges a gel, the system is commonly called wet gel. In most sol–gel systems for the synthesis of oxide materials, gelation is due to the formation of covalent bonds between the sol particles. Gel formation can be reversible when other types of bond are involved, such as van der Waals forces or hydrogen bonds. The structure of a gel network largely depends on the size and shape of the sol particles.

As for silica, the sol-gel synthesis of metal oxides involves the metal center with oxo (M-O-M) or hydroxo (M-OH-M) links until the generation of metal-oxo or metal-hydroxo polymer suspension.

Consequently, the sol evolves toward the formation of a gel system containing both solid and liquid phases with morphologies that can change from continuous network to discrete particles.

Finally, a thermal treatment is necessary in order to favor further poly-condensation and to enhance the mechanical properties and structural stability until final sintering and densification.

This versatile technology is reliable at low temperature and permits to control the composition of the final material on molecular scale. In fact, even small quantities of dopants, such as organic dyes and rare earth elements, can be introduced in the sol and uniformly dispersed in the final product[235,236].

In addition, thanks to the use of high purity reagents it is possible to synthesize materials with complex composition[237,238]. Sol-gel process also allows to produce systems of nanoparticles[239,240,131], with well-defined porosity and surface area, as well as thin film coatings[241,242,243,244].

Usually, starting products used in the sol preparations are inorganic metal salts or organic compounds like metal alcoholates, which form the sol thanks to hydrolysis and polycondensation reactions.

Though silicon-based material production is the most famous and used sol-gel system and can be usually taken as an example, there are some highly relevant differences among silicon and transition metals in sol-gel chemistry. The first difference that influences the reactivity is that other metals are more sensitive to nucleophilic attack thanks to their greater Lewis acidity.

Another difference deals with coordination number. Silicon coordination number and valence is 4, while titanium is coordinated by other six atoms. The increase of the coordination number is due to the interaction with nucleophilic entities in the systems. Therefore, hydrolysis makes the water molecules that coordinate the Ti more acid than the non-coordinated water. This peculiarity allows to produce oxides or hydroxides depending on pH changes.

As in case of silica-based sol-gel processes, transition metals M-OH groups derive from M-OR hydrolysis. Due to the higher Lewis acidity of metal alkoxides, nucleophilic attack on Ti is easier and hydrolysis rate is strongly increased. For this reason hydrolysis rate of $Ti(OR)_4$ is about 10^5 times faster than $Si(OR)_4$ with the same substituent[245]. Thanks to their high reactivity, in order to obtain gels instead of precipitate, alkoxytitanates hydrolysis must be moderated, while the reactivity of alkoxysilanes has to be promoted by acid or basis catalysts. Acidic or basic conditions can be used in a sol-gel reaction to enhance respectively the kinetics of the hydrolysis step or the kinetics of the condensation step.

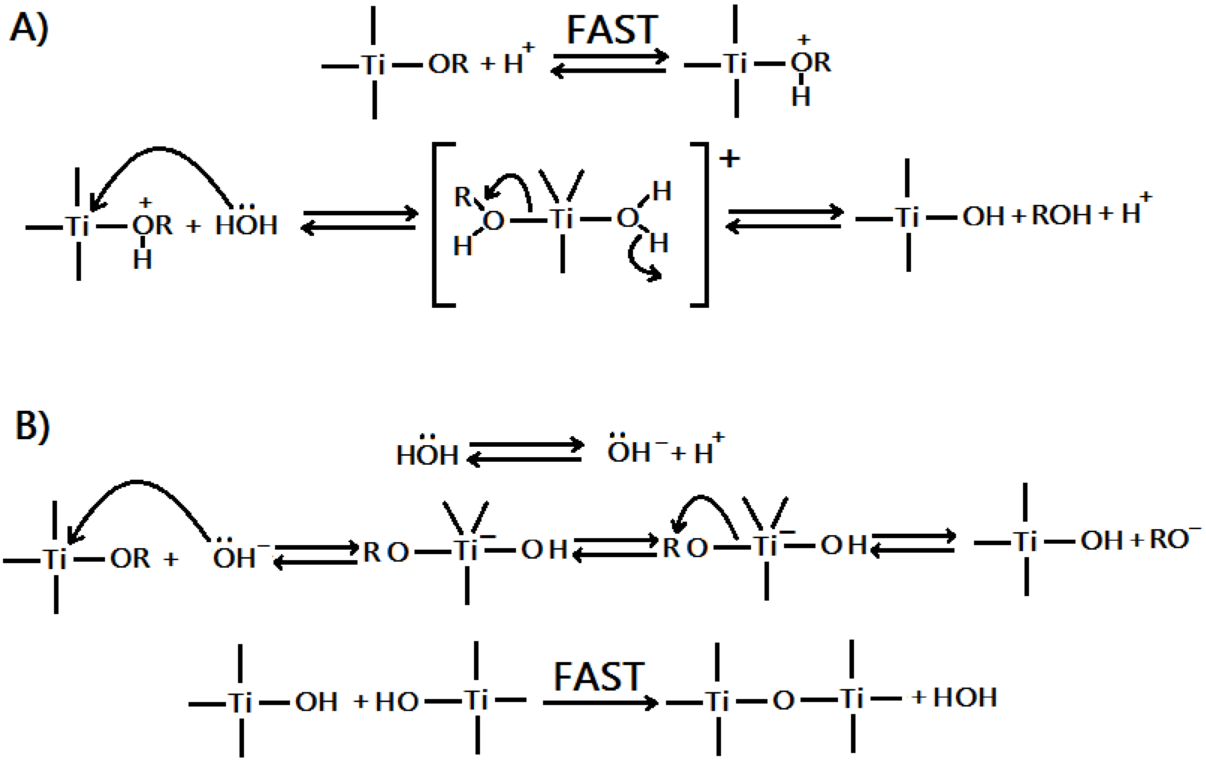

Figure 21: Hydrolysis and condensation reactions of titanium alkoxide into titanium oxide. The reaction A shows the process conducted in acidic condition, where the hydrolysis step is faster than the condensation. The reaction B shows the process conducted in basic condition, where the condensation process is faster than the hydrolysis.

It is well known that in sol-gel processes, as it is showed in Fig.21A, acidic conditions promote positive charges on precursors and their hydrolysis in SN2 type reaction with water. The great avaibility of hydrolyzed precursor allows to produce bulk materials. When the sol-gel reaction is conducted in basic catalyzed conditions (Fig.21B), condensation is faster than hydrolysis, resulting in highly condensed species that can agglomerate into nanoparticles.

Sol-gel processes are also able to produce doped materials, like nitrogen-doped compounds. So nitrogen-doped titanium dioxide can be synthesized adding to the system defined nitrogen sources. Despite the high reactivity permits to avoid using acid or basis to promote hydrolysis and polycondensation, basic compounds like ammonium hydroxide and other amines like diethylamine[246], etilendiamine[247], triethylamine[248] and triethanolamine[249] are used to dope titania with nitrogen.

Acid-catalyzed sol-gel processes, too, can produce $TiO_{2-x}N_x$. Colloidal suspension of nitrogen-doped TiO_2 can be produced in H_2O adjusted with HNO_3[250]. Nitric acid is commonly used as hydrolysis catalyst and to increase crystallization of metal oxides, but at greater concentration can be used to efficaciously dope titania[212].

High temperature annealing step is mandatory to obtain crystalline $TiO_{2-x}N_x$ materials, even when synthesis concerns sol-gel methods[211,212,202,42,200]. Like the nitrogen content[227], the crystallinity degree is important and defines the photocatalityc power.

As reported in paragraph 1.5, the aim of this research concerns the synthesis of a system composed by crystalline nitrogen-doped titanium dioxide loaded with carbon nanoparticle. Since heat treatments higher than 300°C can oxidize carbon nanoparticles until complete combustion, it is necessary to find a method to produce a crystalline N_2-doped TiO_2 without the use of high temperature annealing. In fact, if combustion occurs, carbon may intercalate into crystal lattice acting as co-dopant in previously doped $TiO_{2-x}N_x$ and change the bandgap due to the introduction of carbon related intragap bands. In consequence, an alternative method to produce anatase phase without annealing, called Gel-Sol method is applied. Despite gel-sol method is a wet process like the sol-gel, it is described in a dedicate paragraph.

Gel-Sol method

Gel-sol is a wet process that permits to obtain particles and nanoparticles of metal oxides starting from gel phase[251].

In a gel sol method, metal precursor is hydrolyzed in a metal hydroxide and then aged to obtain the gel phase. Subsequently, the gel is aged and treated in autoclave at well-defined temperatures and pH. During the hydrothermal treatment, the gel is solubilized in an intermediate compound, which can change depending to the pH of the system. When the intermediate saturates the sol, it starts to condense and to rearrange in a crystalline oxides with a well-defined crystalline phase. Gel-sol method is a versatile system developed in 1993 by Sugimoto et al.[252] to study the formation mechanism of crystalline Fe_2O_3 from condensed ferric hydroxide gel; subsequently they continued their studies applying gel-sol method to titanium dioxide.

Temperature used in Sugimoto works to produce crystalline anatase do not reach high enough values to degrade the carbon-based nanoparticles used to prepare nitrogen-doped titania loaded with carbon dots. In a typical gel-sol process to obtain undoped titanium dioxide, $Ti(OH)_4$ is produced by hydrolyzing titanium alcoholates in water. After the collection and the washing steps, the gel pH is adjusted with $HClO_4$ and NaOH at well defined ionic strength. Once the pH has been checked, hydrothermal process is done at 100°C for 24 hours.

Depending on the system pH, during the hydrothermal process the concentration of $Ti(OH)_2^{2+}$ and $Ti(OH)_3^+$ in equilibrium with $Ti(OH)_4$ changes, with consequences on the treatment yield (Fig.22). Sugimoto found that the precursor complex able to produce anatase TiO_2 is $Ti(OH)_3^+$.[253].

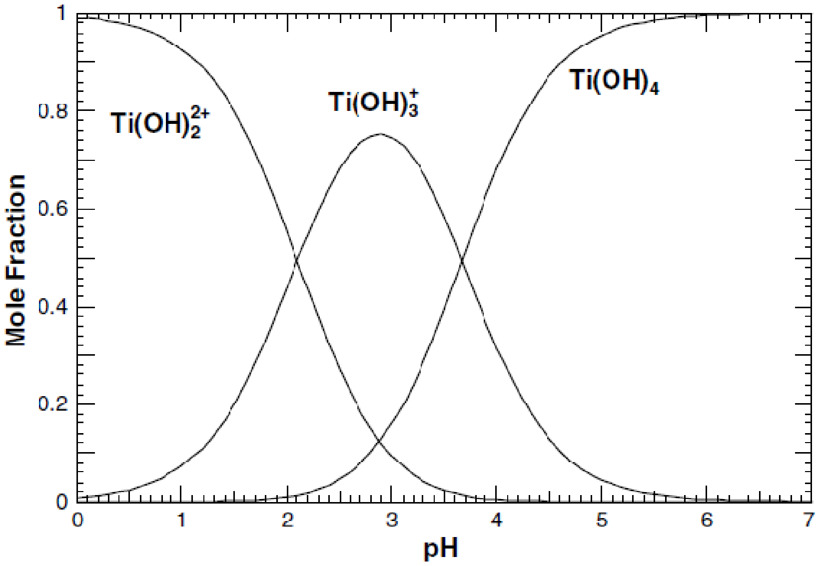

Figure 22: mole fractions of $Ti(OH)_2^{+2}$, $Ti(OH)^{+3}$, and $Ti(OH)_4$ complexes as a function of pH at 25°C and ionic strength 0.1.

After the hydrothermal process, Sugimoto et al[252], proposed to wash with a 2M HNO_3 solution in order to remove un-reacted titanium hydroxide. For our samples, we changed this passage washing with H_2O because we noted by X-ray diffraction that a lot of amorphous material was still present despite the acid washing.

For our purposes, we adopted the technique developed by Sugimoto et. al. to produce $TiO_{2-x}N_x$ anatase. Instead of un-doped $Ti(OH)_4$, we started from a nitrogen-containing titanium-based gel. Moreover, treatment parameters proposed by the study of Sugimoto[254,255,255] were changed. The amount of treated gel, ionic strength, temperature and treatment time were changed in order to obtain the maximum of anatase $TiO_{2-x}N_x$.

2.3- Enhanced photocatalytic materials

CDs interaction with other materials

Thanks to their composition and structure, CDs possess fine properties that can used for several applications. Indeed, CDs can delocalize or supply easily electric charges in other materials and they can be used as photosensitizers or as charge delocalizers.

Due to their sp^2 nanoclusters embedded into carbon sp^3 matrix, CDs possess a bandgap. Depending on the position of its bandgap with respect to the band structure of another material, CDs can transfer or receive electrons or positive charges. When the CDs can transfer charges to another material, it acts as a photosensitizer (Fig.23B); on the other hand when it receives charges it is usually referred as a charge delocalizer (Fig.23C).

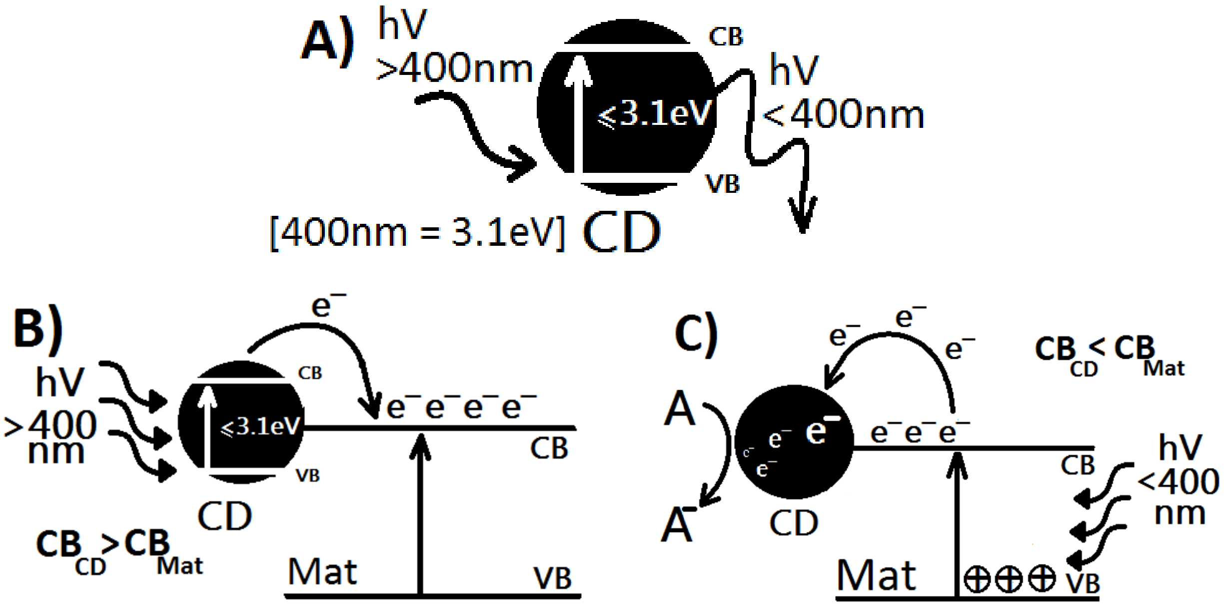

Figure23: A) free CDs are able to photoluminescence in relation to their band structure and their surface functionalization. When CDs are put in relationship with other materials, they can manage energy depending on the nature of the neighbor material: B) example of energy transfer from CDs to other materials (sensitization) and C) example of energy transfer from other materials to CDs (charge delocalization).

If considered as separated systems, CDs can absorb light depending to their band structure and produce photoluminescence in accordance with their bandgap and surface functionalization (Fig.23A). When CDs are in contact with other materials, they can show different behaviors. CDs can act as photosensitizers or can delocalize charges from the host material, and the position of the respective bandgap can influence the CDs behavior. When CDs possess larger conduction band than the host material, they can transfer photo-generated electrons (Fig.23B), while if CB is less energetic in CDs than in the host material, negative charges can be recovered by CDs and delocalized (Fig.23B). Since the discovery of these properties, applications using them made CDs very popular. CDs photoluminescence has been applied in biological imaging[256] and lighting technology[257,258,259]. Charge delocalization has been applied in sensing of metal ions in solution, due the quenching effect of the photoluminescence derived from the delocalization[260]. Both the sensitizing effect and the charge delocalization are successfully used in photocatalysis, for water purification[261,262,263], hydrogen production[264,265] and energy production in solar cells[266,267].

The versatility of CDs was improved thanks to the ability of the scientist to tune their electronic structure. The CD doping with several elements permitted to manage their bandgap and to fine adapt them in order to use their properties with a wide range of materials.

CDs interaction with titania

As reported above, titanium dioxide can improve its photocatalytic performance also in the visible light region if it is doped with transition metals or nonmetals heteroatoms. However, this approach does not consider the negative effect of the electron-hole couple recombination. At this purpose TiO_2 can be loaded with a wide range of different materials[268,269,270]many of which are based on carbon materials like nanotubes[271,272,273], carbon fibers[272], reduced graphene[274,275,276,277] and carbonaceous composites[278,279,277]. Since their discovery in 2004, CDs have been added to the list of systems used to enhance photocatalyst properties.

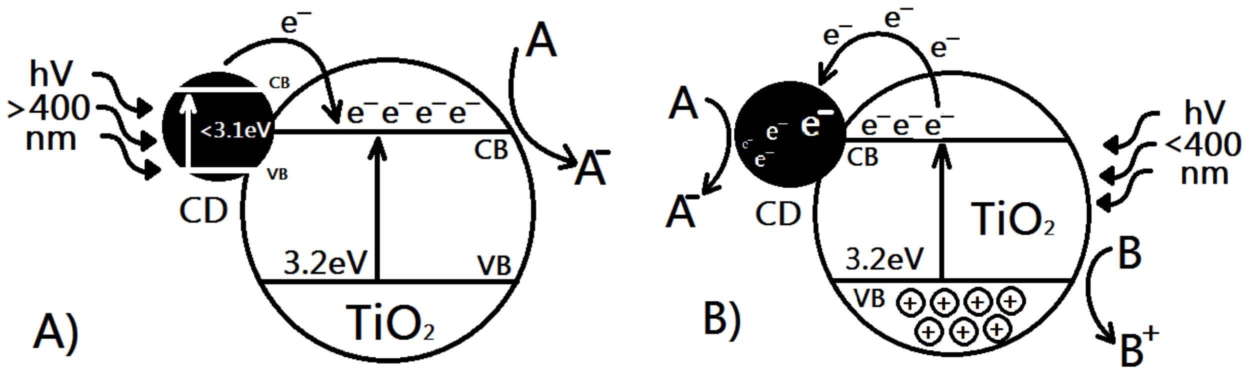

Figure 24: A) electron transfer from carbon dots and titania: in this case CDs can act as photosensitizers. B) electron transfer from titania to carbon dots: in this case CDs act as charge delocalizers.

As represented in Fig.24A, electron transfer can occur in a system where two conditions are satisfied. The first condition is represented by a system where CDs, able to absorb in the visible range, are coupled with titanium dioxide, and where CDs conduction band lies in a more energetic position in comparison of TiO_2 bandgap. In this case, CDs can act as photosensitizers, pumping generated electron to TiO_2 after absorption in visible light range. Here, the electrons injected in the conduction band can reduce compounds adsorbed on the titania surface. In a second situation, as presented in f Fig.24B, TiO_2 conduction band can be higher than the CD conduction band, and photo-generated electrons can be transferred to CDs, which act as charge delocalizers. Once received the electrons, CDs can further provide charges reducing materials dispersed in the system, while the produced holes can oxidize compounds adsorbed on TiO_2 surface.

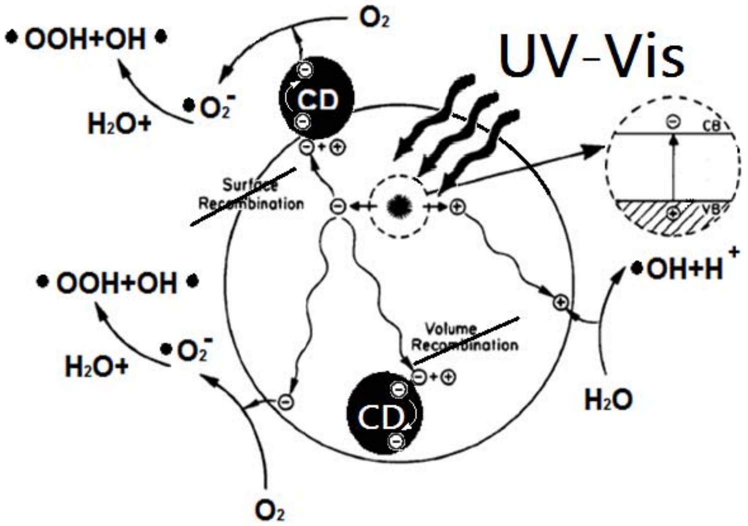

Figure 25: Draw representing the charge delocalization effect of CDs in TiO_2 and $NTiO_2$ systems. Depending on the position into the photocatalyst system, CDs can delocalize the charge and avoid volume recombination or transfer the electron to an adsorbed material (e.g. H_2O).

In Conclusion, the addition of CDs should contrast volume and surface recombination (Fig.25) thanks to electron delocalization. Delocalized electrons can be used to reduce reagents adsorbed on CD surface, while the free ones can react directly from the TiO_2 surface. In the meanwhile, produced holes can react on TiO_2 surface, oxidizing reagents adsorbed on the surface.

3- Materials and methods

3.1- Hydrothermal processes

Hydrothermal synthesis includes the various techniques of crystallizing substances using high-temperature aqueous solutions and high vapor pressures; it is also known as "hydrothermal method". This method can be defined as a synthesis of single crystals that depends on the solubility of minerals in hot water under high pressure. The crystal growth is performed in an apparatus consisting of a steel pressure vessel called autoclave, in which a nutrient is supplied along with water. The method is also suitable for growing large quantities of good-quality crystals, while maintaining control over their composition. Disadvantages are the need of expensive autoclaves, and the impossibility of observing the process of the crystal growing.

A custom-made teflon-lined autoclave is used to produce CDs with hydrothermal synthesis and to treat amorphous TiO_2-based samples.

3.2- Carbon dots

3.2.1- Synthesis

All the aqueous solutions were prepared using de-ionized water (<2µS/cm). Glucose [CAS 50-99-7], Citric acid [CAS 77-92-9], Urea [CAS 57-13-6], Ethylenediamine [CAS 107-15-3], Diethylamine [CAS 111-40-0], Triethylenetetramine [CAS 112-24-3], Boric acid [CAS 10043-35-3], Phosphoric acid [CAS 7664-38-2], Sodium Hydroxide [CAS 1310-73-2], Magnesium Sulfate (anhydrous) [CAS 7487-88-9], Ethanol [CAS 64-17-5] and Acetone [CAS 67-64-1], was purchased by Sigma Aldrich and used as received. Ammonia solution (30%) was purchased by Carlo Erba and used as received. Graphite rods was purchased by TAAB .

3.2.1.1: Upconversion study samples

CD_A*[280]*:

CDs_A was synthesized by mixing 3wt % of glucose dissolved in aqueous ammonia (30%) at room temperature. After the solution become homogenous, it was heated at a constant temperature of 180°C for 4 hours. During the process, because of CDs formation, solution color changed from transparent to pale yellow. The solution was cooled down to room temperature and centrifuged at 13000 rpm for 40 min to remove larger particles. Solution was finally dried to remove all excess of ammonia. The dried sample was re-dispersed in distilled water to form a 0,5 mg/ml solution.

CD_B*[29]*:

CDs_B was synthesized dissolving 9,007g of glucose in 50ml of deionized water to form a 1mol/L clear solution. 2g NaOH was dissolved in 50ml of distilled water to form a 1mol/l clear solution, then was added to the solution of glucose and mixed for 10 min. The mixed solution was treated by an ultrasonic wave (150 W, 40 KHz) for 1 hour. The crude sample obtained from glucose/NaOH was adjusted to pH 7 with HCl. After that, the crude brown solution was dialyzed with semipermeable membrane (MWCO 3000 KDa) to remove any impurities. The dried sample was re-dispersed in distilled water to form a 0,5 mg/ml solution.

CD_C*[85]*:

CDs_C was synthesized adding 1 g of glucose and 0.1 g of NaOH in 15 mL water under stirring. The solution was then transferred into a 60 mL Teflon-lined stainless-steel autoclave and was heated at a constant temperature of 160°C for 4 h. The resulting solution was cooled at room temperature and suspension containing CDs was obtained after centrifugation at 13000 rpm for 40 min. To purify, this solution was heated at 100°C to allow the residual sodium hydroxide to dissolve out, and dialysis treatment using a semipermeable membrane (MWCO 3 KDa) was performed. The solution was dried under vacuum, and CDs sample was finally dispersed in de-ionized water in the form of a 0,5 mg/ml solution.

CD_D:

CDs_D was synthesized dissolving 1,5 g of glucose in to 0, 4ml of NH_3 25% and 14,6ml of H_2O under stirring. The solution was transferred into a 60 mL Teflon-lined stainless-steel autoclave and heated at a constant temperature for 4 h at 160° C. The resulting solution was cooled at room temperature and the surnatant solution, obtained after centrifugation at 13000 rpm for 40 min was collected. To purify, this solution was heated at 100°C to allow the evaporation of the NH_3. The dried sample was finally kept in de-ionized water in the form of a 0,5mg/ml solution.

CD_E*[23]*:

The electrolyte of the electrochemical process was produced by mixing ethanol 99,5% with 0.4 g of NaOH. By using graphite rods (diameter about 0.5 cm) as both anode and cathode, we have synthesized CDs imposing 190 $mAcm^2$ current intensity. The raw CDs solution was treated by adding a suitable amount of $MgSO_4$ (5–7 wt%), stirred for 20 min, and then stored for 24 h to remove the salts and water. After that, sample was centrifuged at 13000 rpm for 40 min, dried and dispersed in distilled water in the form of a 0, 5 mg/ml solution.

3.2.1.2: Preliminary synthesis of codoped NCDs

Citric acid was dissolved in the corresponding nitrogen source with molar ratio of 1:4. The mixture was transferred in a teflon-lined autoclave and treated at 170°C for 1h. Nitrogen doped and co-doped CDs were synthesized with excess of nitrogen source. In each co-doped batch, citric acid, nitrogen source and co-doping source, were respectively used with molar ratio 1 : 4 : 0,2. [123]

An alternative purification was performed because dialysis process did not properly purify the samples, which passed through the membrane along with the un-reacted material. Therefore, the sample was dried in rotavapor and washed three times with acetone and ethanol respectively. For each washing step, centrifugation at 13000 rpm for 10 min permitted to collect all not solubilized sample. A final step considered to suspend CDs in water and collect supernatant after centrifugation at 13000 rpm for 10 min. In this way, the unstable material in water was wasted. Finally, only the supernatant fraction was collected and the suspension was dried in rotavapor and stored in vacuum overnight.

Nitrogen doped and co-doped CDs were synthesized working with amine excess. Description of synthesized samples in Tab.2.

Table 2: description of nitrogen co-doped carbon dots samples. For each sample nitrogen source and co-doping source is described.

Sample	Amine source	Co-dopant source
N_CDs	**DIETHYLENTRIAMINE**	//
N_P_CDs	II	P ACID
N_B_CDs	II	B ACID
N_S_CDs	II	MERCAPTOSUCCINIC ACID

3.2.1.3: Synthesis of codoped NCDs with different nitrogen sources

In these synthesis, we increased the amount of citric acid with respect to nitrogen source. In order to maintain the adequate doping, the ratio between citric acid and co-doping source remained unchanged. Moreover, water was added to the system.

Each 1.11 mol of water, 10.5 mmol of citric acid and 6.25 mmol of corresponding nitrogen source, were mixed. The mixture was transferred in a teflon-lined autoclave at 200°C for 5h. When co-doped samples were required, 2mmol of phosphoric acid, boric acid or mercaptosuccinic acid were added with the previous molar ratio.

Once cooled, sample was dried in rotavapor and it washed three times with acetone and ethanol respectively. After each washing step, samples were centrifuged at 13000 rpm for 10 min, and surnatant was discharged. A final step foresaw the suspension of CDs in water and the collection of supernatant after centrifugation at 20000g/min for 10 min. In this way, all the unstable material in water was collected and wasted. Finally, only the water soluble fraction was collected. The suspension was dried in rotavapor and stored in vacuum overnight. Once dried, samples was stored in dry atmosphere to avoid water adsorption.

Groups of samples were synthesized using urea, ethylendiamine, diethylentriamine, triethylentetramine as nitrogen source.

The use of different nitrogen-based precursors permitted to study possible relationships between nitrogen source molecular weight (MW) and CDs size. In addition, the use of different precursors with different hazard grade permitted to study possible relationships between these toxic materials and CDs cytotoxicity. In the Tab.3, all the synthesized samples were described, with their nitrogen source and co-doping source.

Table 3: Presentation of nitrogen co-doped carbon dots samples synthesized in presence of water. For each sample nitrogen source and co-doping source is described.

Sample	Amine source	Co-dopant source
Urea_NCDs	**UREA**	//
Urea_NPCDs	**II**	P ACID
Urea_NBCDs	**II**	B ACID
Urea_NSCDs	**II**	MERCAPTOSUCCINIC ACID
ETIDI_NCDs	**ETHYLENDIAMINE**	//
ETIDI_NPCDs	**II**	P ACID
ETIDI_NBCDs	**II**	B ACID
ETIDI_NSCDs	**II**	MERCAPTOSUCCINIC

		ACID
DETA_NCDs	**DIETHYLENTRIAMINE**	//
DETA_NPCDs	**II**	P ACID
DETA_NBCDs	**II**	B ACID
DETA_NSCDs	**II**	MERCAPTOSUCCINIC ACID
TRITETRA-NCDs	**TRIETHYLENTETRAMINE**	//
TRITETRA-NPCDs	**II**	P ACID
TRITETRA-NBCDs	**II**	B ACID
TRITETRA-NSCDs	**II**	MERCAPTOSUCCINIC ACID

Sample purification was performed by repeated washing with solvents. CDs can be easily suspended in water but not in less polar solvents, as methanol or ethanol, while washing with acetone can remove not hydro-soluble moieties. As last purification step, CDs were suspended in water and centrifuged, in order to waste all not suspended materials. After drying step, samples were stored as solids until the characterization.

3.3- Titanium Dioxide

All the reactions and hydrothermal treatments were performed in milliQ water. As Titanium precursor, Ti(IV)isopropoxide was purchased from Sigma Aldrich [CAS: 546-68-9]. To avoid contamination and increase the reproducibility, trace analysis Nitric acid 69% was used and purchased from Sigma Aldrich, [CAS:7697-37-2]. To prepare the treating solution of hydrothermal processes, Sodium Hydroxide was purchased from Sigma Aldrich [CAS 1310-73-2], while Perchloric acid 70% was purchased from Carlo Erba[CAS 7601-90-3].

3.3.1- Synthesis of $NTiO_2$

All the samples containing TiO2 can summarized as follows:

- TiO_2Comm., P25, TiO_2 ann. and $NTiO_2$ ann. were used as reference materials. These samples have been treated at high temperature
- S_1, S_2 and B_1 were synthesized, in order to define the right hydrothermal treatment to stabilize anatase without annealing processes. Samples S_1 and S_2 reproduced hydrothermal treatment of undoped TiO_2, while sample B_1 reproduced the hydrothermal treatment of a nitrogen doped TiO_2.
- The sample W_1 was used to study amorphous nitrogen doped titania. In particular, the samples was analyzed to study the CDs addition protocol during the production of the amorphous $NTiO_2$.

- Samples WS_1 and WS_2 were synthesized in order to study the best host for the CDs.
- TiO_2@CDs based samples were used as comparison for samples loaded with CDs.

Working with new compounds requires reference materials in order to compare the properties of the new samples with known reference systems. For this purpose, the cited work of Di Valentin et al.[221] offered a selection of good references. In the paper, the authors deeply characterized the role of nitrogen in nitrogen doped titanium dioxide, and furnished good explanations for behavior shown by our nitrogen doped titania. Moreover, the several annealing processes, presented in the paper, could be used to highlight differences with the hydrothermal treatments described in this thesis. In addition to the samples prepared according to the Di Valentin's recipes, it was necessary to compare the properties of our samples with some other accepted reference systems such as a commercial TiO_2 anatase purchased by Sigma-Aldrich and a commercial Degussa P25.

TiO_2Anatase (TiO$_2$ Comm.)

It was a commercial titanium oxide nanopowder purchased by Sigma-Aldrich, with a particles average size of 25nm. This product is commercialized as CAS 1317-70-0.

In this work, this sample was labeled as TiO_2 Comm.

Degussa P25 (P25)

Degussa P25 was a titania photocatalyst widely used, thanks to its relatively high activity, in many photocatalytic reaction systems. P25 was used as standard titania photocatalyst.

In this work this sample was labeled as P25.

Un-doped Titania (TiO_2ann.)

The anatase TiO_2 reference was synthesized by the sol-gel method still proposed by Di Valentin et al.[281]. This sample was synthesized following the recipe of the paper, but without the addition of ammonium chloride added to the synthesis as nitrogen source. Sol-gel TiO_2 sample was prepared mixing a solution of titanium (IV) isopropoxide in isopropyl alcohol with some ml of milliQ water. The system was aged 15h in order to obtain the complete hydrolysis of the Ti precursor and dried in oven at 80°C. The dried gel was annealed at 500°C for 1h.

In this work this sample was labeled as TiO_2 ann.

Nitrogen-doped titania: ($NTiO_2$ann.)

Anatase nitrogen doped titania reference sample was synthesized by the same sol-gel process described by Di Valentin et al[281] and described in the previous paragraph, but using ammonium chloride, which was added to the synthesis as nitrogen source. Sol-gel $NTiO_2$ sample was prepared mixing a solution of titanium (IV) isopropoxide in isopropyl alcohol and adding to the solution some ml of milliQ water. The system was aged 15h in order to obtain the complete hydrolysis of the Ti precursor and dried in oven at 80°C. The dried gel was annealed at 500°C for 1h.

In this work this sample was labeled as $NTiO_2$ ann.

The reference samples purchased or synthesized from selected literature are summarized in Tab.4.

Table 4: Reference samples, commercial references as TiO_2comm. and P25 were purchased, so the treating parameters are unknown

Sample	Treating parameters	Structural properties
TiO_2 ann.	505°C x 2h	Anatase - bulk
$NTiO_2$ ann.	505°C x 2h	Anatase - bulk
TiO_2comm	unknown	Anatase- nanosized
P25	unknown	unknown

The next section describes the synthesis of the samples containing a stabilized anatase phase without the use of annealing processes. The sample B_1 proposes a synthesis of nitrogen doped TiO_2, while the samples S_1 and S_2 propose samples of undoped TiO_2. These samples are summarized in Tab.5.

B_1 synthesis

The synthesis of the sample B_1 was based on the paper written by Bao et al.[246]The authors presented one pot synthesis to prepare nitrogen doped crystalline titanium dioxide. The proposed synthesis was able to satisfy both the necessity to produce nitrogen doped and anatase titania phase using hydrothermal treatment. For this reason, this procedure was studied with the others to produce crystalline material.

First, 6.8 ml of Titanium tetrabutoxide and 10 ml of Ethanol were mixed with stirring for 30 min to form solution A. Secondly, 5 ml of Etilamine, 10 ml of milliQ water and 10 ml of Ethanol were mixed with stirring for 10 min to form solution B. Then, solution A was added drop-wise into solution B under vigorous stirring. The resulting mixture was transferred into a 120ml Teflon-lined stainless-steel autoclave and heated at 150°C for 8 h. Finally, the obtained white precipitate was washed with H_2O and EtOH several times, and dried at 80°C for 8 h in vacuum.

In this work this sample was labeled as B_1

S_1 synthesis

The synthesis of the sample S_1 was taken from the work of Sugimoto et al[253]. The authors proposed a procedure to produce crystalline undoped TiO_2. The adopted synthesis followed the prescription of the paper working at pH condition indicated as the best to obtain anatase phase. 2,96ml of Ti(IV)isopropoxide was added to a 40ml of solution 0,1M of $HClO_4$. The pH of the solution was adjusted to 3 with solutions of NaOH and $HClO_4$ 0,1M. The system was maintained under stirring for 120 minutes at room temperature to stabilize the pH and to obtain complete hydrolysis and condensation of the gel. Finally, the formed gel was stored in an autoclave at 100°C for 24h. After the treatment, the autoclave was cooled at room temperature and the powder was washed three times with milliQ water and dried in oven at 80°C.

In this work this sample was labeled as S_1

S_2 synthesis

The synthesis of the sample S_2 was referred to another paper of Sugimoto et al.[255] concerning the study of undoped anatase production made with the use of amines as shape control agents and through hydrothermal route. Also in this case, synthesis was performed following the prescription of the paper and working at pH condition indicated as the best to obtain anatase phase.

First a stock solution was prepared mixing Titanium (IV) isopropoxide with triethanolamine at molar ratio of 1:2 respectively, in order to produce Ti^{4+} compound stable at room temperature. The solution was diluted with the addition of milliQ water to make an aqueous stock solution of 0,5 mol/L in Ti^{4+}.

10 ml of the stock solution were mixed with additional 10ml of milliQ water, placed into a screw-capped Pyrex bottle, and aged at 100°C for 24 h in order to obtain the gel. Finally, the resulting highly viscous gel was transferred to Teflon-lined autoclave and aged at 140°C for 72h to nucleate and grow titania particles.

The final product was washed three times with milliQ water and dried in oven at 80°C overnight.

Table 5: Samples studied to define the best hydrothermal process to stabilize anatase phase. For each sample treating parameters, structural properties and chemical formula are reported.

Sample	Treating parameters	Structural properties	Material

S_1	20°Cx 2h + 100°C x 24h	Anatase - microsized	TiO_2
S_2	100°Cx24h + 140°Cx72h	Anatase - nanosized	TiO_2
B_1	150°C x 8h	Anatase - nanosized	$NTiO_2$

Synthesis of the amorphous $NTiO_2$

W_1 sample represented the amorphous nitrogen doped TiO_2 to treat with the selected hydrothermal process. WS_1 was obtained after hydrothermal treatment of W_1 sample. WS_2 was obtained with optimized hydrothermal process, and corresponded to the best sample obtained.

W_1 synthesis

WS_1 synthesis was produced starting from the study proposed by Wang et al.[282] The procedure was adapted to insert CDs suspension during the synthesis.

W_1 synthesis was represented in Fig.26. Titanium (IV) isopropoxide (TIP) (3,2ml) was added drop wise into a solution made by 15 ml of milliQ water and 4ml on concentrated HNO_3 under continuous stirring. After hydrolysis, condensation and dissolution of TIP other 4ml of concentrated HNO_3 was added. These additional 4ml could be used to introduce CDs in the system, using a suspension of the required amount of CDs in concentrated HNO_3. After 30 min stirring ammonia solution was added drop-wise to the system until the complete precipitation of an orange slurry. The orange precipitate was filtered and washed with 400ml of milliQ water in order to remove all the salt produced by the neutralization and all the ammonia in excess. In order to remove all the water the sample was dried in oven at 80°C.

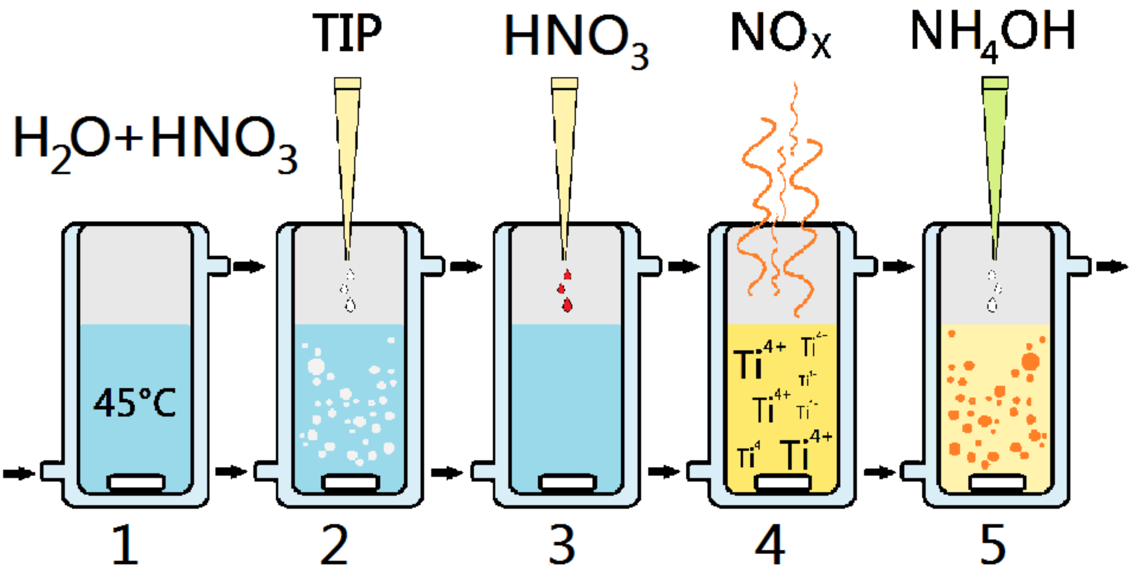

Figure 26: scheme for the production of the W1. Once synthesized, the amorphous material was treated in to solvothermal process in order to obtain crystalline photoactive material.

WS_1 synthesis

This sample was synthesized following the procedure reported in W_1 synthesis, followed by the hydrothermal treatment proposed for the production of the sample S_1, autoclave at 100°C for 24h.

WS_2 synthesis

This sample was synthesized following the procedure reported in W_1 synthesis. However, the subsequent hydrothermal treatment (proposed for the production of the sample S_1) was optimized to obtain the highest crystallinity grade.

3.4- Enhanced photocatalytic materials

WS_2@CDs synthesis

This sample was synthesized following the procedure of the WS_2 sample with the addition of a suspension of CDs in concentrated HNO_3 (in the step 3 in Fig.26).

In order to verify the optimal CDs concentration, we added NCDs suspensions indicated in Tab.6.

Table 6: reagent amount used to synthesize each sample of nitrogen doped titanium dioxide with different percentages of carbon dots.

Sample	ml TIP	Total ml HNO_3	ml soluz 10mg/ml NCDs	mg NCDs
WS_2	3,2	4 + 4	**0**	**0**
WS_2@**0,01%**	3,2	4 + 4	**0,008**	**0,08**

WS_2@**0,1%**	3,2	4 + 4	**0,08**	**0,8**
WS_2@**1%**	3,2	4 + 4	**0,8**	**8**

TiO_2@CDs synthesis

With the purpose to test an alternative synthesis, we prepared a set of samples of titanium dioxide (TiO_2ann.) loaded with NCDs or NSCDs. The sample preparation protocol was performed by adding 0,8ml of 10mg/ml CDs suspension to a solution of 3,2ml TIP in 3,2ml of isopropyl alcohol. The system was incubated for 15h, in order to obtain the complete hydrolysis of the Ti precursor, and then dried in oven at 80°C. The dried gel was treated with the optimized hydrothermal synthesis used to produce WS_2 sample.

In Tab.7 we showed a scheme of the composition of the TiO_2 samples loaded with NCDs and NSCDs.

Table 7: description of the TiO_2 samples loaded with NCDs and NSCDs.

Type of CDs	NCDs	NSCDs
Doping elements	N	N,S
Sample name	TiO_2@NCDs	TiO_2@NSCDs

3.5- Characterizations

Photoluminescence analysis:

Photoluminescence investigations on nitrogen doped carbon dots and co-doped carbon dots were performed with a Perkin Elmer LS 55 fluorescence spectrophotometer

Upconversion studies:

Upconversion photoluminescence (UPCL) is a fine anti-Stokes emission, where two or more photons are sequentially absorbed inducing emission at shorter wavelenght than the excitation one. UPCL is useful in several different applications, from lighting to bio-imaging and from photovoltaic to nanomedicine. These phenomena are typical for some lanthanide elements and for some quantum dots, and are also often cited in CDs early bibliography.

The study of UPCL phenomena from CDs could be useful for different reason, but the most important for our topic could be the anti-Stokes emission. It can be used to adsorb visible light and re-emit in near UV region, where a photocatalyst as titanium dioxide can be activated. UPCL depends on a well-defined energetic structure, and could be difficult to observe it in a heterogeneous material as CDs, where the high number of surface states could interfere with the process.

UPCL is an uncommon phenomenon, and even in fitted materials needs powerful light sources to be produced. At this purpose powerful photon source, as lasers, are commonly used to induce UPCL. Despite that, several studies on CDs show UPCL using Xenon lamps commonly equipped on spectrofluorimeter. This peculiarity generate several questions, because using a polychromatic source, as a lamp, could introduce light components such as second order of diffraction light. If these components are not properly removed, they could generate some effects that could be mistaken as UPCL.

Indeed, in a common spectrofluorimeter, excitation light is selected thanks to grating monocromator, in which light emission from Xenon lamp is mirrored in different directions. Theoretically, only a well defined range of few nanometers wavelength can be selected by the monocromator; practically, also those lights with a diffraction order equal to a whole number.

$$\theta_m = \arcsin\left(\frac{m\lambda}{d - \sin\theta_i}\right) \qquad (25)$$

When light collides with the grating of a monocromator with an angle of θ_i parallel to the plane wave, the diffracted light can exhibit maximum intensity at angles θ_m defined in formula (25). If λ is the wavelength and *d* is grating spacing, *m* is the integer defining the maxima order of diffraction. Commonly, a spectrofluorimeter selects the first order of maxima diffraction as excitation beam, thanks to its highest intensity. While the chosen wavelength pass, the second and others diffraction orders are selected, contributing with their energies to the sample luminescence (Fig.27A). For this reason, using a long pass filter on the excitation beam permits to stop those contributions of the light source that do not correspond to the selected wavelength (Fig.27B). Considering that light intensity is lower for every diffraction order, we consider the second order of diffraction the real cause of the photoluminescence emission in the sample.

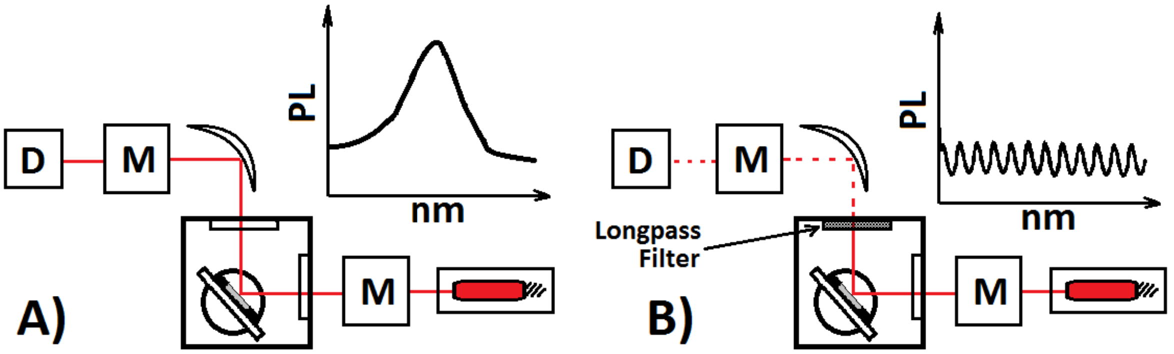

Figure 27: Scheme of the spectrofluorimeter used for second order diffraction detection. A) Here no filters block the leakage of the second order diffraction and that excitation light can activate CDs. B) When long pass filter is used, only the emission generated from the right excitation wavelenght can be detected.

Therefore, UPCL of some CDs proposed in literature was studied. Fluorescence spectra for UPCL investigation were recorded using a spectrofluorimeter Fluorolog-3 (Jobin Yvon), with the excitation source Xenon lamp 450W equipped. The measurements were performed on transparent samples solution, in a front-face setup. Each sample was measured, registering the emission from 300nm to 700nm, and registering excitation at 750nm, 800nm, 850nm, 900nm and 950nm, with and without 715nm long pass filter. The filter application avoided visible light emission. To compare the shape of the measured emission, photoluminescence (PL) was collected by excitement of the samples at the expected second order diffraction: 375nm, 400nm, 425nm, 450nm and 475nm.

Usually, UPCL is studied with high-energy excitation sources as lasers. The laser allowed to pump high flux of photons on the sample and to induce up-conversion phenomena. Experiments and samples taken from the literature were re-proposed (samples CD_A-E) using common Xenon lamp.

Moreover, to unequivocally define UPCL emission of the selected samples, more energetic light sources were used. At this purpose, Diode laser IR single mode CW at 30mW and 980 nm L980P030 and 808 nm L808P030 (Thorlabs) were used as excitation sources to analyze the samples with a monochromatic light source. As represented in Fig.28, in this experiment the sample was enlighted and the emitted light was filtered with long pass filter, in order to avoid leaking contribution. After the long pass filter, the emission was selected by a second monocromator and directed to the detector.

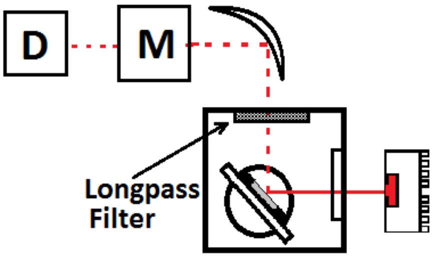

Figure 28: Experiment scheme for the determination of upconversion photoluminescence using high-energy light source.

UPCL was studied pumping in a range from 700nm to 1000nm. In this experiment lasers of 800nm and 980 nm was used.

UV Vis spectrometry:

To determine CDs absorbance spectra, Agilent 8453 was used.

For determination of the concentration of methyl orange solution during photocatalytic activity determination, an Agilent 8453 UV-visible spectrophotometer was used.

UV-Vis spectrometry for reflectance determination:

For reflectance measurements conducted on all photocatalyst samples, a Shimadtzu UV-2401 PC recording spectrophotometer is used. This UV-Vis spectrophotometer is coupled with a Shimadtzu integration sphere mod ISR-240 with internal white standard. It is able to analyze reflectance in a range from 240nm to 800nm. Samples were collected in a sample holder composed by quartz window on a black cap and fitting a window on the integration sphere. To conduct these measurements, was important to pay attention to spread the sample covering all the surface of the sample holder in order to avoid absorption from the black bottom part. An adsorption of light form this part should reduce the maximum of reflectance and should influence the definition of the calculated bandgap.

Determination of the optical bandgap starting to reflectance:

Usually, reflectance measurements are reported in nanometers, while the band gap energy is defined in electronvolts. Therefore, conversion between wavelength (nm) and band gap energy (eV) units is calculated by (20).

$$h\nu\ (eV) = \frac{1239.8\ (eV\ nm)}{\lambda\ (nm)} \qquad (20)$$

In diffuse reflectance measurements the intensity corresponds to reflectance, once obtained the spectrum, conversion in absorbance with Kubelca-Munk formula (21) is needed.

$$Absorbance = \frac{(1-R)^2}{2R} \qquad (21)$$

A detailed band gap analysis needs to plot and fit absorption data, taking in consideration the direct or indirect nature of the bandgap of the semiconductor. Commonly, the absorbance of materials with an absorption coefficient greater than 10^4 cm^{-1} obey the Tauc relation (22).

$$\alpha h\nu \propto (h\nu - Eg)^{\frac{1}{n}} \qquad (22)$$

The symbol *n* take on values of 3, 2, $\frac{2}{3}$or $\frac{1}{2}$ corresponding respectively to indirect forbidden, indirect allowed, direct forbidden and direct allowed transitions. Is widely accepted that TiO_2 anatase possesses indirect allowed transitions. The definition of the energy value of the band gap (eV) is defined by the first electron promoted from the valence band to the conduction band. This first event is graphically obtained calculating the intercept of the Tauc plot with the abscissa axis. To obtain a Tauc plot is necessary to plot the signal as$(h\nu - \mathrm{Eg})^{1/n}$ versus the energy (eV).

Quantum Yield (QY) determination:

The Quantum Yields (QY) was measured using an Infinite M1000Pro, Tecan, excitation wavelength 360nm, emission wavelength range 370-650nm, using Quinine Sulfate as reference. In this work, quantum yield results was calculated using quinine sulfate[283] in 0,5M H_2SO_4 solution (QY 58%). Quantum Yield against Rhodammine 6G (QY 95%) is calculated as follow (23).

$$QY_{Rh} = QY_{Qs}0{,}0551 \qquad (23)$$

Absorbance at the excitation wavelength was optimally kept in between A = 0.02-0.05, in order to avoid inner filter effects and ensure linear response on the intensity. Quinine sulphate was used as reference because its absorbance maximum was close to the CDs absorbance maximum. In this way, possible errors caused by intensity variation in the lamp light spectra could be avoided.

Fourier-transform infrared spectroscopy:

Carbon dots functional groups were determined with a NICOLET NEXUS FTIR coupled with an AVATAR diffuse reflectance accessory. All the spectra were obtained integrating 24 interferograms collected with interval from 600 to 4000cm^{-1}, pass of 4cm-1 on KBr power, and sample mix without any further modifications.

For the determination of the nitrogen content in $NTiO_2$ samples, a spectrophotometer IR Bruker Tensor 27 was used. Spectra were collected with interval from 600 to 4000cm^{-1}. Spectra of each sample was produced integrating 24 interferograms.

Elemental analysis:

For the elemental determination of CHNS in carbon dots, Thermo Fisher Scientific Flash EA 2000 CHNS was used.

For determination of P and B content in carbon dots, Perkin Elmer Optima 4300DV ICP-OES was used.

Atomic force microscope:

In order to determine dimensions of first synthesis carbon dots, AFM Nanoscope IIIa was used.

Scanning electron microscopy:

Scanning electron microscopy (SEM) images were collected with an in-lens detector 5 keV beam energies on a Sigma VP Field Emission SEM (Zeiss, Oberkochen Germany), 1,5 nm resolution. Samples were suspended in ethanol (10-50ug/ml) and briefly ultra-sonicated. Three µl of each suspension were deposited on a silicon wafer substrate mounted with carbon double tape on an aluminum stub, the dried at 70°C for 24h.

Transmission electron microscopy:

CDs TEM images were taken with a JEOL JEM 3010, operating at 300 kV, equipped with ultra-high resolution objective pole pieces (theoretical point resolution = 0.17 nm), a GATAN (Warrendale, PA, USA) Model 794 MultiScan CCD camera. TEM specimens were prepared by ultrasonically dispersing the powdered samples in milliQ water (approximately 10 mg/ mL) and depositing 5–15 µL of the suspension on a holey carbon film grid.

TiO_2 and enhanced photocatalytic materials TEM images were obtained with an electron transmission microscope Jem-1400 (120kV). At this purpose, each sample was dispersed in isopropanol and treated in sonication bath for 30 min. The fine suspension was dropped on copper grids with carbon layer and dried at room temperature for two hours. No staining processes are conducted on samples of this part of the work.

Cytotoxicity studies:

Cytotoxicity was measured on HeLa cells using an Infinite 200 PRO instrument at the CRO of Aviano. Cytotoxicity is evaluated by means of cells counting after incubation with the compound of interest. In our case, we tested CDs concentration ranging from 1,95µg/ml to 1000µg/ml repeating the experiments three times.

In order to evaluate the less detectable cytotoxicity, 1000mg/ml of CDs suspension is chosen as discrimination concentration. Of course, contaminations with so high concentration are impossible in a living organism, but working at maximum concentration allowed to stress the effect of CDs in cells and to obtain clear considerations of CDs effect on living organisms.

Electrophoresis studies:

Electrophoresis can be used to separate carbon dots and to define some of their important properties. Actually, since migration speed of analyzed material is due to its charge and dimension, electrophoresis can informs CDs dimensional distribution and superficial charge. CDs suspension is placed in holes in the middle of the gel, and when potential is applied, they start to migrate. Migration is imposed with a speed in direct proportion to superficial charge and with inverse proportion to particle dimension. The direction of the nanoparticle migration is imposed by the charge of surface functionalization. Nanoparticles with negative surface functionalization migrate to positive electrode and *vice versa*. Moreover, for biological use of electrophoresis is common to dye the sample in the gel with dyes or luminescent materials. Depending on the used dye, UV or visible lamps can be used to check the sample position in the gel. Here, CDs luminescence can be used to detect their position in the gel without any dye process, making easier and faster this step.

In addition, pH of the gel and of the running buffer can be changed, and possible variations in the sample can be correlated to CDs superficial charges change. Therefore, performing electrophoresis at different pH can give additional information concerning CD functionalization.

Smear formation in the gel can derives by the loss of the CDs superficial charge effect. Once masked the effect of the charge, CDs dimension is the only parameter able to condition migration speed. In this case, if the sample is composed by wide size distributed nanoparticles, migration will produce a smear. Bands formation are defined by CDs with similar size and superficial charge that impose similar migration speed.

To perform electrophoresis, a BIO-RAD Sub-Cell GT Agarose gel Electrophoresis system was used, while a Perking Elmer Geliance 600 imaging system was used to collect gel images. All the pictures were collected lighting up the gel with UV lamp.

All electrophoresis were performed on $1\%_W$ Agarose gel. Since the application of high power could warm up and dissolve agarose gel, the electrophoretic system applied was 10W for all the samples. The power was fixed instead of the voltage because different buffers used had different conductibility.

For each sample, a suspension of 10mg/ml was produced, and mixed 1:1 vol. with loading buffer. The loading buffer was made with 1:1 vol. with running buffer and glycerol. In this way, the sample was too thick to do not diffuse in the running buffer.

Running buffer stock solution used for each pH value:

pH4: Na acetate 10x

80ml milliQ water + 9,712g Na acetate, adjusted to pH4 with HCl

pH6: BisTris 10x

80ml milliQ water + 16,740g bistris, adjusted to pH6 with NaOH or HCl

pH8: TBE 10x

250ml milliQ water + 45g tris base, 13,75g Boric acid and 10ml EDTA 0,5M pH8

pH10: CAPS 10X (caps= 3-cyclohexylamino-1propannesulfonic acid)

80ml milliQ water + 17,705g CAPS, adjusted to pH6 with NaOH

Before to use, all the running buffer stock solution was diluted at 1x.

X-ray diffraction:

The microstructure of the samples was studied by means of X-ray powder diffraction (XRPD).

A Bruker D8I-90 with Bragg–Brentano geometry, connected to a highly stabilized generator (40 kV), was used for the Wide-Angle X-Ray Scattering (WAXS) measurements of the sintered specimens.

The definition of the crystallinity of the samples synthesized for the optimization of the hydrothermal treatment and the definition of the parameters for the sample WS_2 was obtained with an X-Pert Powder diffractometer of PAN-alytical. The measurements was conducted using Kα

Cu radiation 1.5419Å. XRD study on WS_2 samples was performed in the X-Ray diffraction laboratories of the Universitad Autonoma de Barcelona during my internship in the research group of the Prof. Xavier Sala Roman.

All measurement was conducted from 10° to 100° integrating 4,5 sec each acquisition point. On XRD patterns, Rietveld analysis was performed order to calculate crystalline phase content and crystallite diameter. On XRD patterns, Rietveld analysis was performed in order to calculate crystalline phase content and crystallite diameter.

Photocatalytic activity studies:

To define the photocatalytic activity of samples, the degradation ability of a solution of methyl orange was studied. The apparatus was composed by a solar lamp of 180W posed in front of a boron silicate beaker covered with a watch-glass (Fig.29). The beaker containing the methyl orange solution was maintained under stirring and positioned at a well defined distance to the lamp in order to obtain a radiation equal to 1sun.

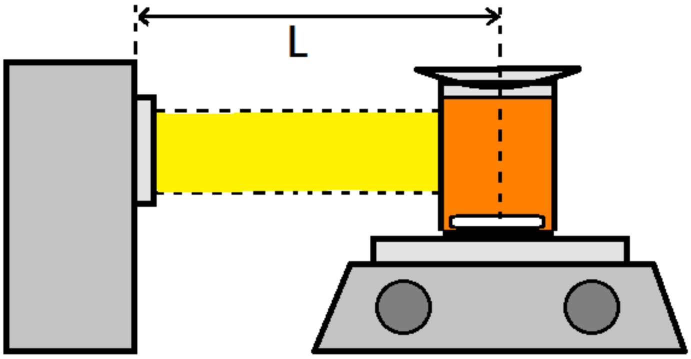

Figure 29: draw of the photocatalytic apparatus used in this work. The length L was defined with a diode, in order to obtain an incident radiation of 1 sun.

First, a stock solution of 5.87 10^{-3}M of methyl orange was produced. Secondly, 0,25ml of stock solution was added in 80ml of milliQ water and positioned under stirring in the photocatalytic apparatus. Third, after the sampling of 3ml of solution to define the zero, 50,0mg of photocatalytic material was added under stirring to the solution, and maintained in the dark for 40min. Dark time permitted to produce an adsorption-desorption equilibrium between the powder and the solution. After 40 min, the system was exposed to the lamp radiation and after 20min, 40min, 60min, 90min, 120min, 180min and 220min 3ml of solution was sampled. Solution sampled was filtered with syringe 0,45um filter and collected in closed vial.

Once the last sampling was taken, UV-Vs were collected to define the intensity at 464nm, corresponding to the maximum wavelength adsorption of methyl orange. After the plot of the intensity at 464nm on a calibration line previously defined, using Lambert-Beer law (24) the concentration of methyl orange for each sampling was calculated.

$$Absorbance = abc \qquad (24)$$

Where:

a: absorptivity of the substance (cm^2/mmol) **b:**optical path (cm) **c:**concentration (mg/ml)

To compare the photocatalytic activity of several materials, the relative concentration $C/C^0$was plotted versus time (min).

4- Results and discussion

The aim of this part of the work was to clarify the CDs behavior, from their synthesis to their characterization, in order to use them for advanced oxidation processes and nano-medicine. These themes were to the center of important studies in the world of the research, and CDs could give important improvements in both of the two fields.

In order to study possible CDs candidates for nano-medicine and advanced oxidation processes applications, several CDs groups were produced by hydrothermal synthesis. Despite other processes, hydrothermal synthesis could be easily controlled, and it guaranteed good reproducibility of the produced materials. For the synthesis, citric acid was generally chosen as carbon source in literature, thus we used this precursor. Conversely, we chosen to test Urea, Ethylendiamine, Diethylentriamine and Triethylenetetramine as nitrogen sources. Finally, nitrogen was chosen as main doping heteroatom to improve photoluminescence due to surface passivation. Surface passivation induced a PL independence from the excitation wavelength, a higher efficiency, and a more efficient charge delocalization processes. The addition of Boron, Phosphor and Sulfur as co-doping elements was performed to test the presence of intra-band layer differences in CDs bandgap and in order to study the respective effect when loaded in $NTiO_2$ in high performance photocatalytic materials. Several groups of doped and co-doped CDs were synthesized via hydrothermal synthesis, using four nitrogen sources and three co-doping sources . These samples are described in Tab.3 in the chapter 3.

As preliminary synthesis and in order to prepare some reference systems, a group of co-doped samples were synthesized using recipes found in literature[29,85,280,284]. Optical and morphological characterization were performed and the synthesis parameters were adjusted to improve the purification procedure. Indeed, purification with dialysis membranes didn't produce good performances. So, synthesis parameters were changed to produce CDs more easy to purify. However, because of the persistence of purification problems, a new procedure was developed and optimized. Therefore, all the synthesized samples were purified and characterized with additional studies, as cytotoxicity and electrophoresis tests at different pH.

The choice to test different nitrogen sources and different co-doping sources allowed to study the effect of the precursors toxicity and the CDs safety. This study produced considerable results on CDs toxicity, which are important to define the real CDs use in nano-medicine applications. The electrophoresis studies at different pH gave interesting qualitative information regarding the nanoparticles distribution with respect to their surface functionalization degree and their size-surface charge relationship.

In Fig. 30 was presented the scheme of the study performed on CDs. First, was performed a preliminary study on CDs UPCL properties. This characterization was useful to study of UPCL in CDs and its possible application to increase photocatalityc activity in enhanced oxidation processes. At this purpose different CDs were purposed from literature, but no upconversion was detected. In consequence, a new approach was explored to enhance photocatalytic activity and CDs were studied to improve charge delocalization in activated titania. At this purpose, CDs were synthesized with several nitrogen and codoping source. CDs were purified, and was performed a deep optical characterization. At the same time, cytotoxicity studies were performed to define CDs safety, while electrophoresis was used to define surface charge and dimension. Finally, the best nitrogen and codopant combination was selected for its loading on photocatalytic systems.

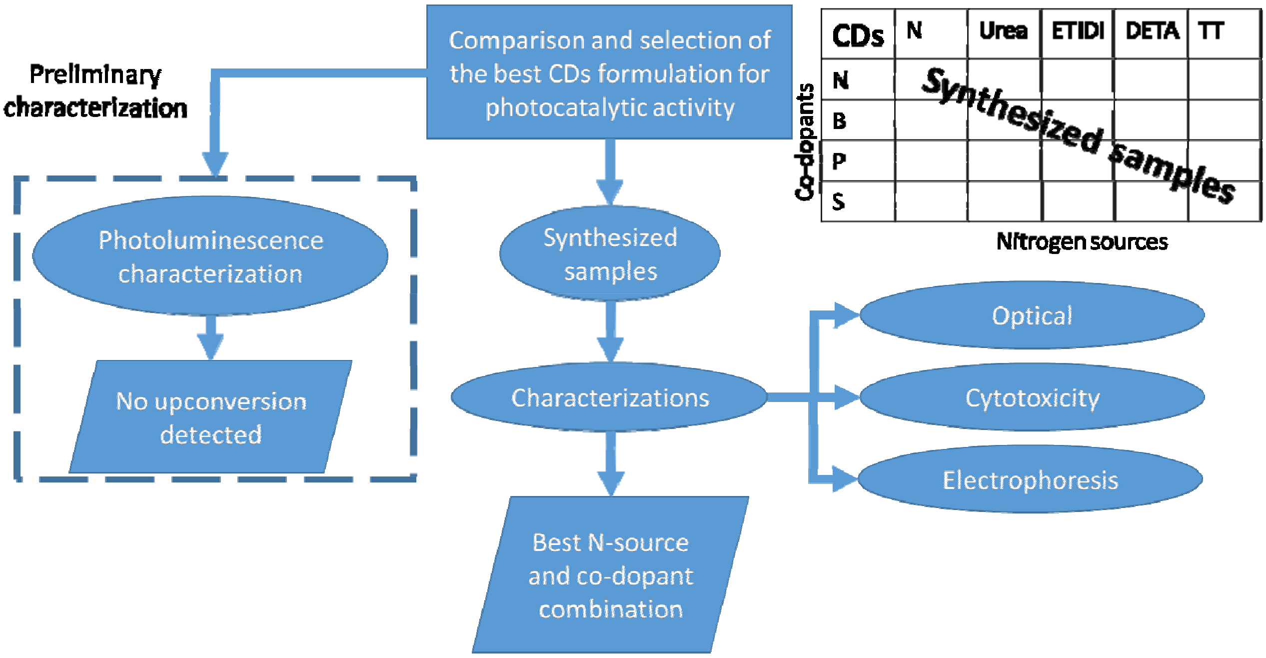

Figure 30: *Scheme of the research topic investigated on CDs .*

4.1.1- Up conversion studies

In this study, samples selected from articles presenting CDs with UPCL properties were selected, synthesized, and optically characterized. At this purpose, CD_A, CD_B, CD_C, CD_D and CD_E were synthesized with bottom-up approach (as described in the paragraph 3.2.1) and the respective UPCL was studied.

We found that up-conversion phenomena can be removed using an appropriate long pass filter able to block the excitation light with shorter wavelengths. In Fig.31A,CD_A photoluminescence spectra, obtained at excitation wavelength ranging from 750nm to 950nm without long-pass filter was described as a function of the emission wavelength. In the inset, we showed the same measurement conducted with the long-pass filter. In Fig.31B, we showed the CD_A luminescence spectra, excited at wavelengths corresponding to the second harmonics.

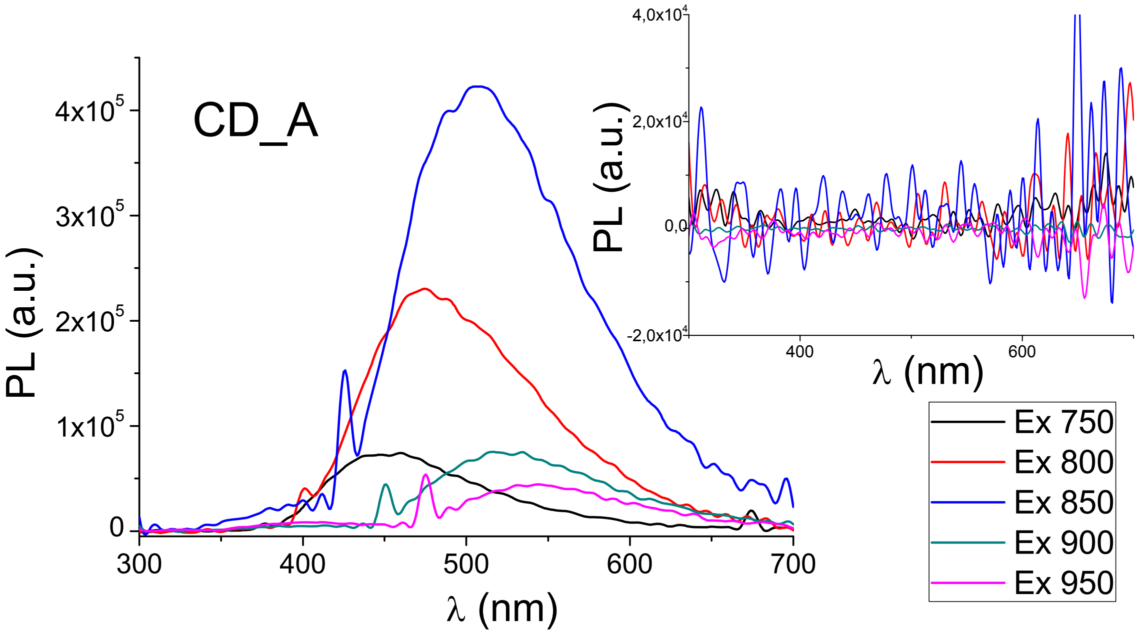

A

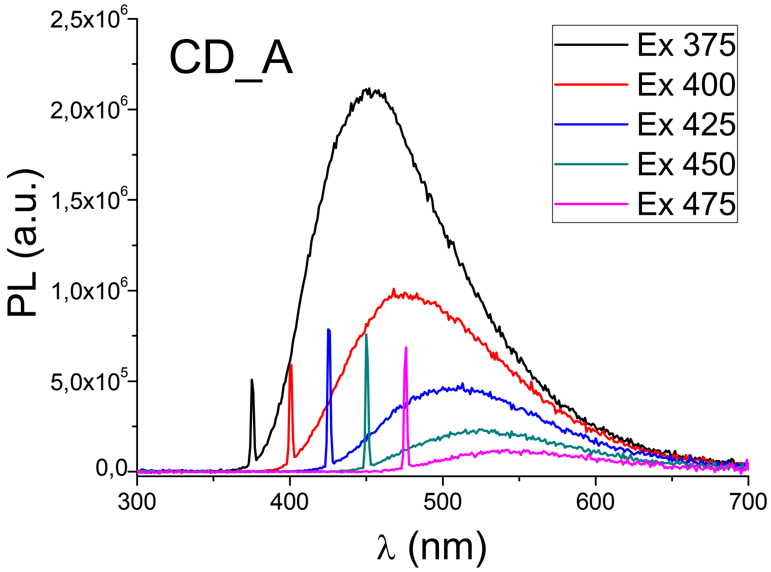

B

Figure 31: A) Photoluminescence spectra of the CD_A sample, produced by the second harmonic grating leaks. In the inset, the same process is excluded by the use of a long pass filter. B) CD_A luminescence spectra, excited at wavelengths corresponding at the second harmonic.

Photoluminescence curves in Fig.31A showed typical CDs emission shape: a broad curve with a tail at greater λ. PL spectra in Fig.31A showed contribution of light of the second order of diffraction. They also were characterized by the presence of small peaks at λ equal to $\frac{1}{2}\lambda_{ex}$. These small peaks were visible at 400nm, 425nm, 450nm and 475nm for spectra obtained at λ_{ex} 800nm, 850nm, 900nm and 950nm, respectively. They represented the leaking light from the excitation source. In the inset of Fig.31A, no photoluminescence was showed due to the use of long-pass filter. In Fig.31B photoluminescence emission obtained at $\frac{1}{2}\lambda_{ex}$ was showed.

Our results confirmed that the fluorescence up-conversion originated by the leakage from the second order diffraction of the incident light on the monochromator.

In comparison to the emission obtained before, these PL showed the same λ_{max}, indicating that the PL arised from the same λ_{ex}. To avoid any contribution in excitation, no filters were used. For this reason, at the beginning of the PL curves, it was possible to note the peak corresponding to the excitation light used to promote the emission. CD_A showed the typical emission dependence from the λ_{ex} of the CDs without passivated surface. This phenomenon is called red edge excitation shift and arises from the intermolecular interaction of the chromophores that constitute the CDs. The detection of light in the region where CDs are commonly excited could justify the emission ($\lambda<450$nm), because that light could be used to excite the material and to produce PL emission.

The real origin of the photoluminescence was unequivocally defined by the application of the long pass filter and not by the production of up-converted emission.

For the remaining samples only PL study conducted at λ_{ex} from 750nm and 950nm were reported, since the other results were exactly the same of the previous ones. The comparison between PL studies conducted with and without long pass filter proved again the real origin of the photoluminescence and excluded the production of up-converted emission. All the other PL studies, conducted on λ_{ex}<450nm are reported in the appendix A.

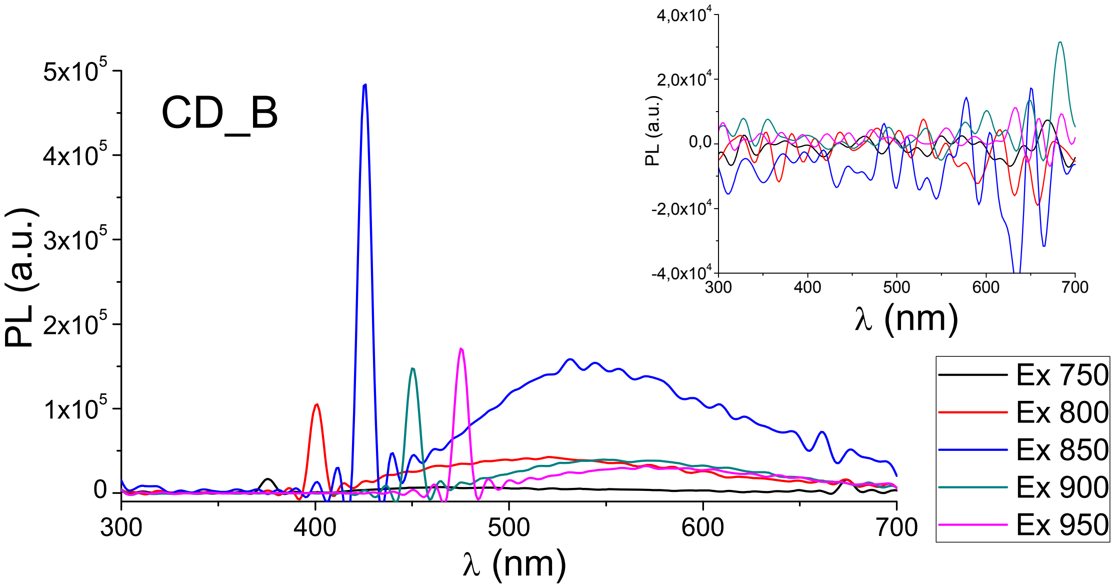

A

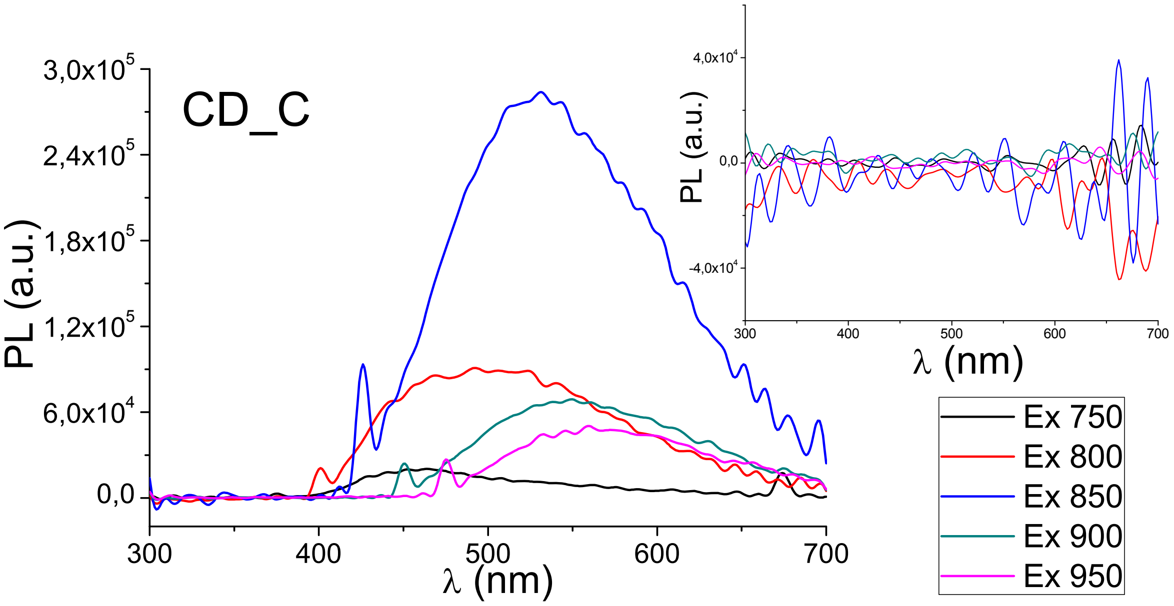

B

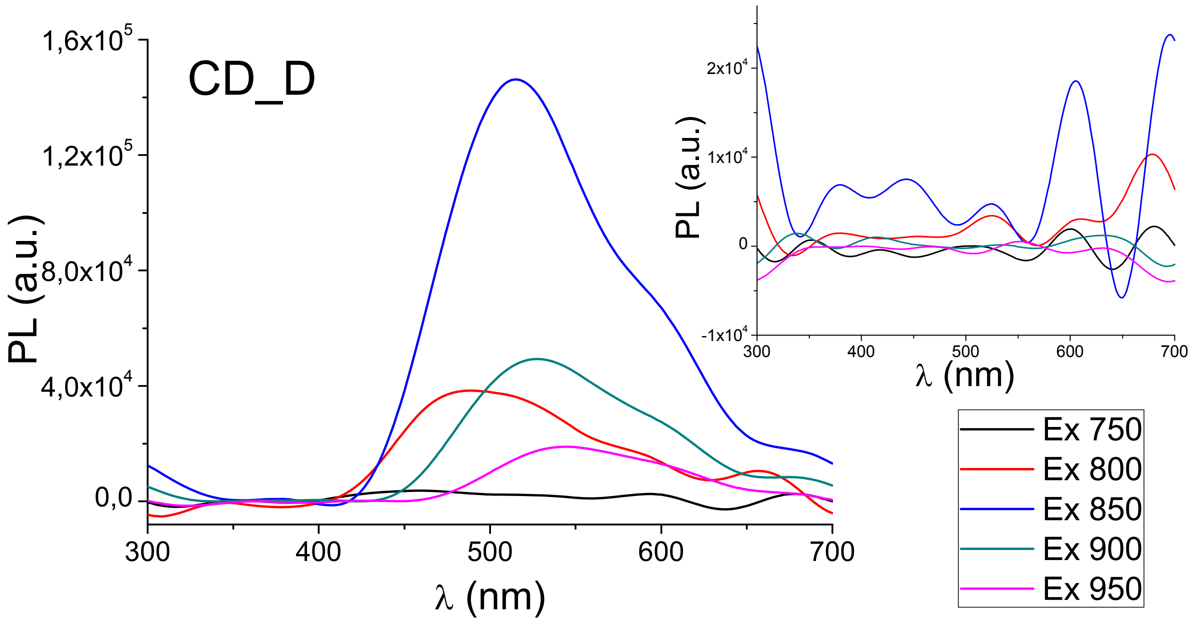

C

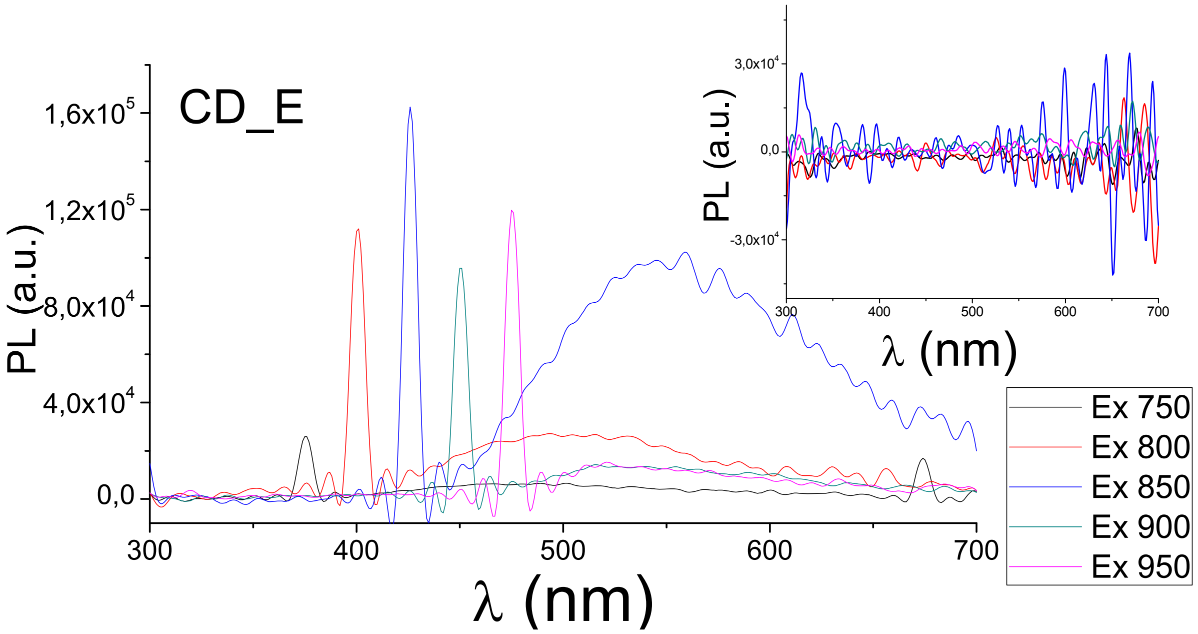

D

Figure 32: PL studies of the spectra produced by the second harmonic grating leaks. In the inset, the same process is excluded by using a long pass filter. A) CD_B; B)CD_C; C)CD_D and D) CD_E samples.

In Fig.32A, CD_B were shown photoluminescence spectra, obtained at excitation wavelengths ranging from 750nm to 950nm, as a function of the emission wavelength, without long-pass filter. In the Fig.32A inset, the PL obtained with long pass filter application were showed. In this case, the second order diffraction peaks were more evident due to the low PL, thus the emission was due to light leaking contribution.

PL in Fig.32B referred to CD_C excited at the same λ_{ex} value. In this case, the second order diffraction peaks were less evident due to high PL. However, also in this case the emission was due to light leaking contribution. PL in Fig.32C referred to CD_D excited with λ_{ex} ranging from 750 nm to 950nm, but the second order diffraction peaks were not detected due to very low PL. PL in Fig.32D referred to CD_D excited with the usual λ_{ex} range. Here, the second order diffraction peaks were evident due to low PL, showing again that the emission was due to light leaking contribution. Despite the different synthesis, all the studied samples showed similar characteristics. In fact, all the samples showed an emission dependence from λ_{ex}. However, their surface functionalization was too inhomogeneous to produce this phenomena, which was unusual for highly passivated carbon dots. All the samples were characterized by the presence of peaks with $\lambda=\frac{1}{2}\lambda_{ex}$, which corresponded to the light leaks detected by the spectrofluorimeter. In all the samples, the contribution of λ_{ex}<450nm light was essential to produce photoluminescence and the second order diffraction leak limitation by longpass filter, completely removed the UPCL effect.

In the previous experiments a Xenon lamp was used. However, high energy light sources are normally used to study UPCL. Therefore, further experiments were performed using high energy lasers to excite our samples. In Fig.33A and B we showed PL spectra recorded from 300nm to 700nm for all the studied samples, excited with 800 nm and 980 nm, respectively.

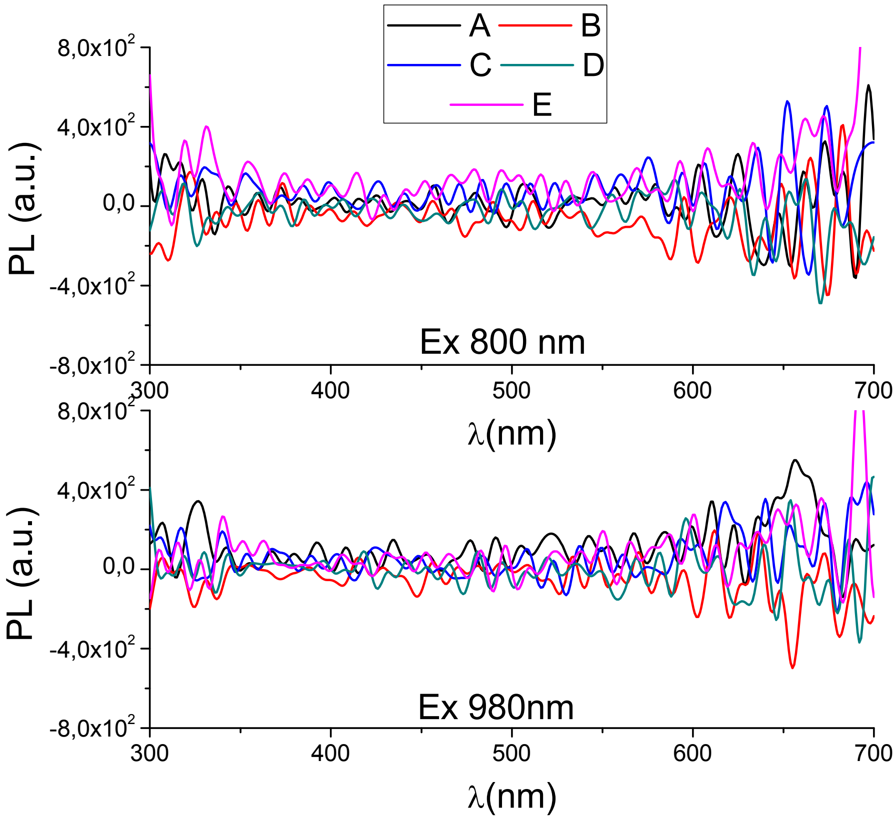

Figure 33: A)PL spectra of the samples CD_A, CD_B, CD_C, CD_D, CD_E excited with monochromatic light source at 800nm. B) PL spectra of the samples CD_A, CD_B, CD_C, CD_D and CD_E excited with monochromatic light source at 980nm.

Both Fig.33A and B didn't show UPCL, despite the high energy supplied to the system. Indeed, the instrument recorded only background signal.

In this study, we proved that five different synthesized CDs didn't present any up-conversion property. The PL observed during the experiments shall not be confused with UPCL, but interpreted as down conversion emission derived from excitation by second order diffracted light. In fact, by using a long pass filter or a monochromatic light source was possible to avoid the phenomena.

4.1.2- Synthesis study of co-doped CDs

In order to produce appropriate materials to use in catalysis and in nanomedicine, the attention is generally focused on the synthesis and characterization of nitrogen doped carbon dots (N_CDs).

Usually, N_CDs have strong passivated surfaces due to the use of high amount of amine for the synthesis. Highly passivated surfaces reduce the surface traps and contrast recombination events that decrease the quantum efficiency. Surface passivation induces PL independence from the λ_{ex}, and higher quantum yield (QY). But higher efficiency implies more efficient charge delocalization processes, which are useful in enhanced photocatalytic systems.

In order to further investigate the CDs potential properties, we decided to dope them with different heteroatoms. In fact, co-doping CDs with phosphor, boron, and sulfur could add intra bandgap layers in order to improve the CDs energy transfer demand in titania@CDs systems. Moreover, the heteroatom doping could have significant effects on cytotoxicity, which was fundamental for their possible use in nanomedicine.

After the reagents definition, a synthesis recipe was selected from literature. All the synthesized samples were purified and optically characterized. Cytotoxicity was evaluated to define the relationships between precursors and CDs toxicity. Electrophoresis at different pH was evaluated to define the CDs surface charge.

Concerning CDs size and shape, several problems emerged from TEM analysis. The weak contrast due the carbon coating of the grid and the low CDs resistance under the beam made these materials difficult to analyze. The first samples were characterized by AFM, and only after several tryouts and experiment we found a way to analyze CDs by TEM.

4.1.2.1-Preliminary CDs study:

The experiments below were performed on the samples synthesized as described in materials and methods (pag. 56).

Optical studies:

In order to study the co-doping effect on the produced CDs optical properties, UV-vis absorbance studies were performed. Right before the tests, all the samples were prepared as a clear 50ug/ml suspension to avoid re-absorption processes and concentration quenching phenomena.

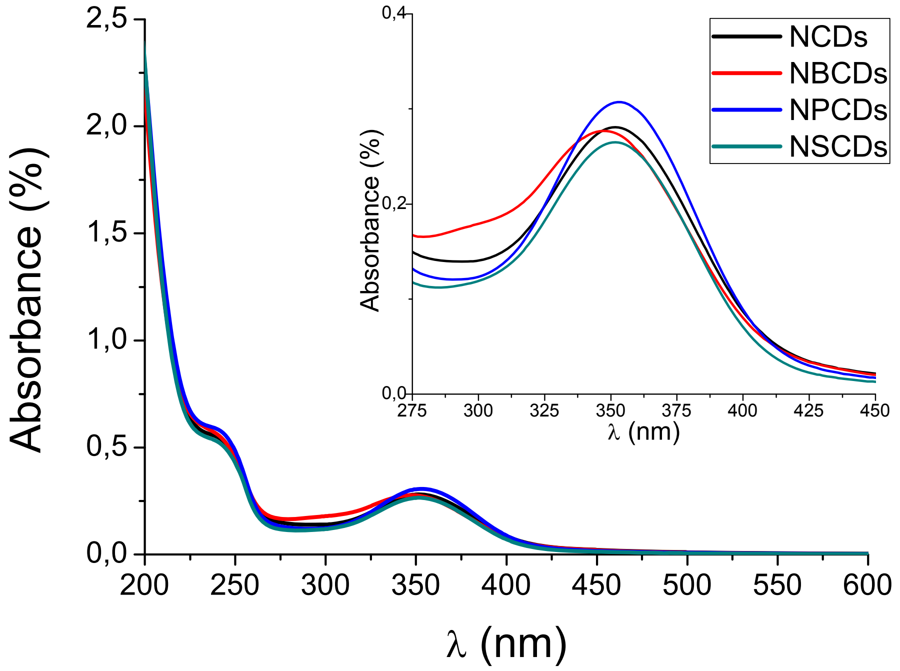

Figure 34: Absorbance spectra of synthesized nitrogen doped and co-doped CDs. The peaks between 275 and 450 nm are reported in the inset.

In all the spectra showed in Fig. 34 two contributes were evident. The shoulder from 229nm to 263nm was related to aromatic π-π* and σ-π* transitions. Usually, this absorption band was produced by saturated compounds containing oxygen, nitrogen or sulfur. Since these samples were nitrogen rich, the main responsible of this absorbance contribution was the C-N bonding of the amidic group. Indeed, the reaction of –COOH groups of the citric acid with $-NH_2$ groups of the diethylentriamine could produce amidic groups.

Another important contribution in the spectra was the peak between 300nm and 450nm, centered at 350nm. Typically, absorption contributes at wavelength greater than 285nm were related to n-π* transitions. As light variation within the NBCDs was the only difference observed between these spectra. This blue shift could be related to the presence of functional groups reducing electronic delocalization.

Photoluminescence characterizations were performed by PL and PLE measurements. The last ones provided information in the λ_{ex} range, while the PL measurements provided information in the emission range. The results are depicted in Fig. 35.

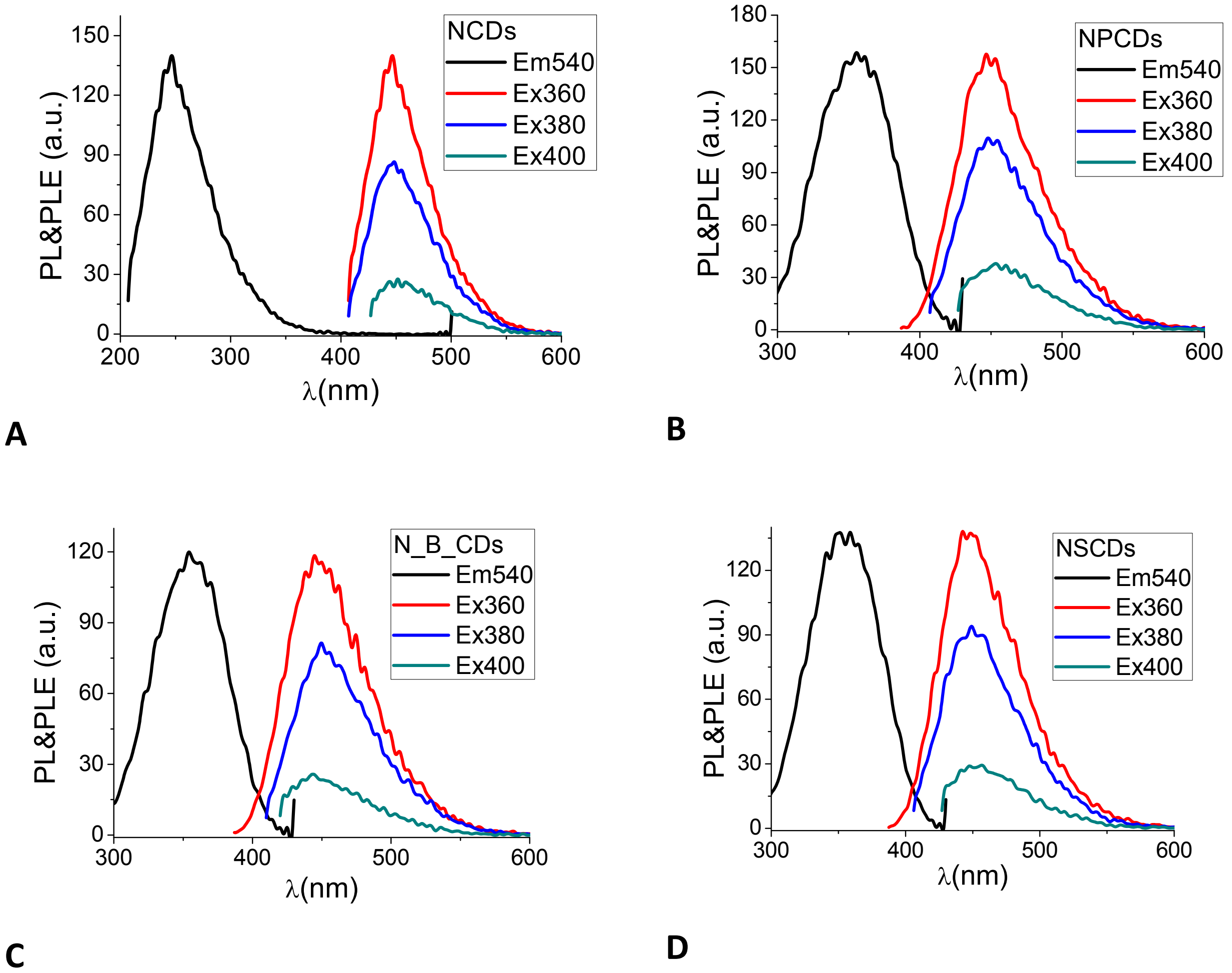

Figure 35:*A)NCDs B) NPCDs C) NBCDs and D) NSCDs PLE recorded at 540nm emission and PL recorded at 360nm, 380 nm and 400nm, respectively.*

Fig.35A showed the photoluminescence study of the NCDs samples. The PLE excitation, and the PL emission λ_{max} were recorded at wavelengths of 245nm and 447 nm, respectively. From the PL and PLE λ_{max} comparison emerged a Stokes shift of 202nm. Fig.35B showed the photoluminescence study of the NPCDs samples. For NPCDs, PLE λ_{max} at 355nm and PL emission λ_{max} at 447nm were recorded, respectively. In this case, the PL and PLE λ_{max} comparison showed a Stokes shift of 92nm. In Fig.35C and 35D the photoluminescence study showed the samples NBCDs an d NSCDs. For both of them the PL and PLE λ_{max} comparison showed a shift of 92nm. Recording the emission at different excitation wavelengths it was possible to confirm the independence of the emission from the λ_{ex}. The PL spectra of the NSCDs sample showed an asymmetric peak, with a tail towards greater wavelengths. The NCDs showed a Stoke shift of 202nm, while the other co-doped CDs showed the same stoke shift of 92nm. This indicated less energy loss in the absorption-emission process, and a more efficient material. Despite these differences, the shapes of PL and PLE were similar, indicating that the synthesis of the four CDs produced systems with similar optical properties. However, all the samples showed photoluminescence independence from the λ_{ex}. This phenomenon could arise from surface passivation due to the high content of amine during CDs synthesis. In fact, amine could passivize the surface, substituting surfaces traps with different energies and homogeneous functionalization with one energy level.

After the optical properties, the different doped CDs were characterized from the morphological and dimensional point of view.

Morphological study

The TEM images production of nitrogen doped and co-doped CDs was complicated due to the low resistance of these objects, which were destroyed under the TEM beam. In addition, the low contrast between carbon coated grid and CDs made their individuation difficult. To bypass these problems, atomic force microscopy (AFM) scans were performed. In order to work on flat substrates, mica layer was employed as support for the CDs. From the AFM images of the samples, it was possible to note particles with a wide size distribution in the range of few nanometers.

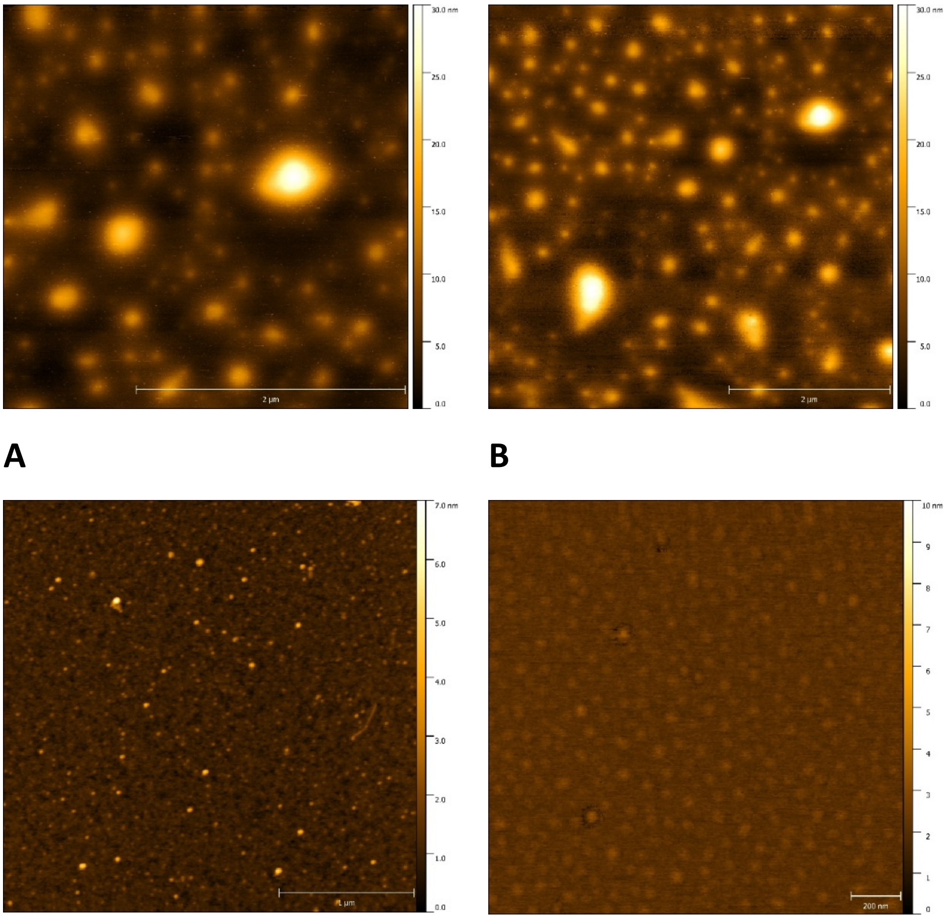

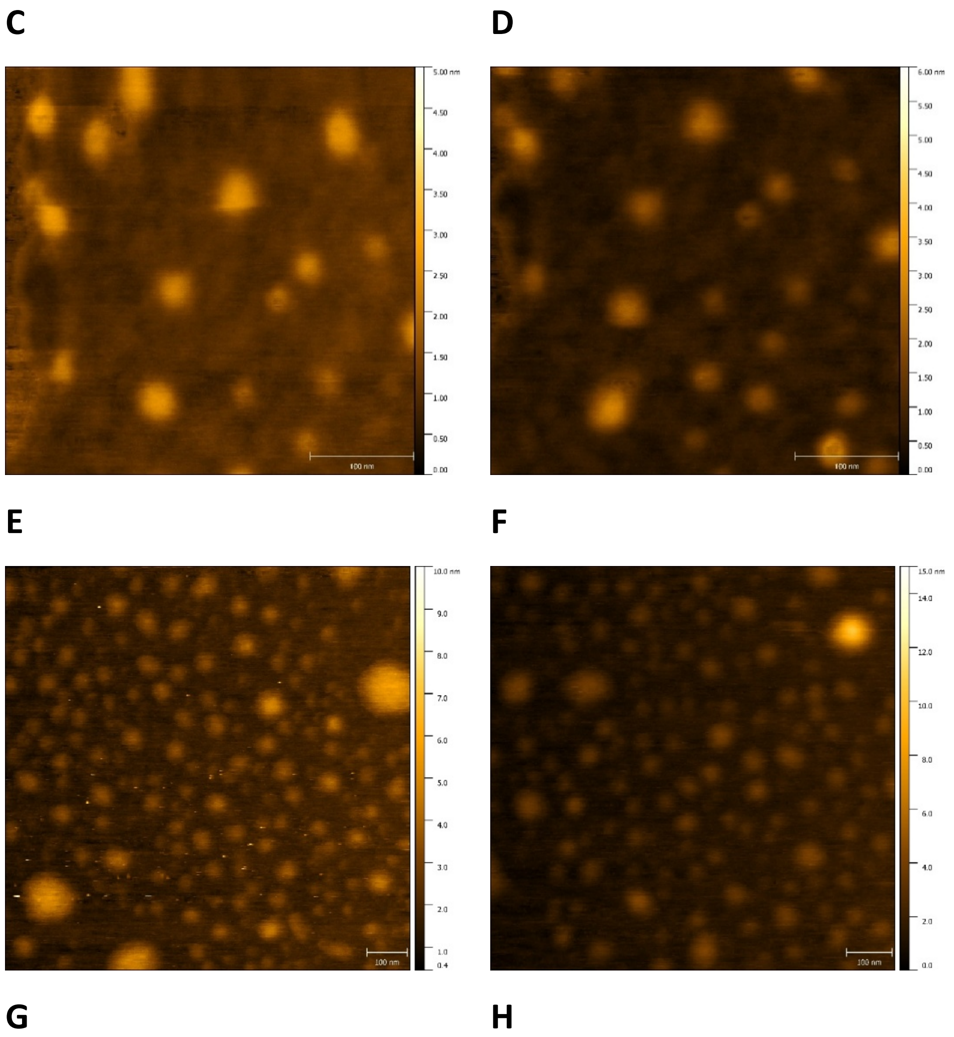

Figure 36: A) and B) AFM images of NCDs. C) and D): AFM images of NBCDs. E) and F): AFM images of NPCDs. G) and H) AFM images of NSCDs. A) and)B show a scale of 2µm; C) shows a scale of 1 µm; D) shows a scale of 200nm, while E) F) G) and H) show a scale of 100nm.

From AFM images of the sample NCDs showed in Fig.36 A and B, is possible to note objects with wide size distribution. Probably, these objects were made by aggregated carbon nanoparticles. From profile studies on smaller objects emerge a population of nanoparticles of 4nm. From the studies on NBCDs showed in Fig.36 C and D, was clear that the sample presented smaller particles than in NCDs sample. Moreover, the sample NBCDs was more homogeneous than the sample NCDs, with a nanoparticles size of 0.6nm. NPCDs AFM images in Fig.36E and F showed similar homogeneity found in NBCDs. Profilometry measurements on NPCDs defined nanoparticles dimension of 0.8nm. Finally, NSCDs images in Fig.36G and H showed a less homogeneous sample, with size of the smaller objects of 1nm.

For a better comparison, all the average sizes are summarized in the Tab.8.

Tab.8: Size dimension of nitrogen doped and co-doped CDs, calculated by profilometry on AFM images

Sample	NCDs	NBCDs	NPCDs	NSCDs
Size (nm)	4nm	0.6nm	0.8nm	1nm

Small dimension defined through AFM measurements could elucidate how dialysis purification was not an appropriate process for the raw samples. In fact, small CDs dimension could filtrate through membrane and get lost in the dialysis solution.

In this chapter, NCDs, NBCDs, NPCDs and NSCDs were synthesized and characterized from optical and morphological point of view. Problems in purification steps obliged to use an alternative purification method. From absorbance analysis, all the samples presented π-π* and σ-π* transitions. All the samples showed n-π* transitions, but probably, for the NBCDs sample, a small blue shift could be ascribed to some functional groups, able to reduce electronic delocalization in NBCDs structure. Checking photoluminescence, NCDs showed Stoke shift of 202nm, while the other co-doped CDs showed the same Stoke shift of 92nm. Despite these differences, shapes of PL and PLE were similar in all the samples, indicating that the four CDs synthesis produce materials with similar optical properties. Furthermore, all the samples showed photoluminescence independence from the λ_{ex}. This phenomenon could arise from surface passivation due the high content of amine during CDs synthesis. Amine could passivize the surface, and substitute surface functionalization with different energies, with a more homogeneous decoration. AFM and profilometry studies showed co-doped CDs sized between 0.8nm and 0.6nm; while doped NCDs showed nanoparticles five times greater than nanoparticles of the other samples. Greater nanoparticle dimensions and wide size distribution could be considered as an indication of sample partial aggregation. The very small size of the four sample permitted to understand why dialysis membrane was and inadequate purification method. In fact, CDs small dimension allowed to pass through membrane and to be lost in the washing solution.

To produce CDs with greater dimensions, synthesis parameters were changed increasing temperature, reaction time and introducing water in the reaction system. These samples were studied in the following paragraph.

4.1.3- Characterization of co-doped CDs with different amines

In this paragraph, CDs with nitrogen source at increasing molecular weight (MW) were studied. Citric acid was used as carbon source, while boric, phosphoric and mercaptosuccinic acids were used as B,P and S co-doping sources. The studied samples were synthesized as reported in Tab.3, paragraph 3.2.1.

Optical studies were performed to define relations with nitrogen source reagents and CDs properties. UV-Vis absorbance was studied to verify its possible variations related to different nitrogen source and different co-doping. PL was studied to verify possible differences between different CDs precursors. In particular, this analysis performed to define the emission dependence from the $\lambda_{ex.}$. Finally, quantum yield (QY) of all synthesized samples was investigated.

Moreover, cytotoxicity study was performed on all synthesized samples. To complete the definition of CDs properties, electrophoresis at different pH was performed. This technique is commonly used in research biology field, but it produced substantial results to study the CDs surface charge and dimensional distribution.

To define synthesis reproducibility, the samples matrix is re-synthesized and QY, Cytotoxicity and electrophoresis at different pH were still compared.

For our purposes, the most important CDs properties were luminescence efficiency and safety.

Luminescence efficiency defined the absence of recombination traps that can reduce the CDs ability to delocalize TiO_2 charges. Cytotoxicity allowed to select safe CDs, and to reduce the danger to work with poisonous nanomaterials. Therefore, to select a defined group of samples to apply in enhanced photocatalytic systems, QY and cytotoxicity were used to select the best group of samples.

As last characterization, elemental analysis was performed on selected samples, in order to verify the right elemental composition and doping.

4.1.3.1-Optical Investigation

Optical studies were performed on NCDs, synthesized with different nitrogen source and on different UREA, ETIDI, DETA and TRITETRA based groups of samples. UV-Vis absorbance was studied to verify possible absorbance variation in relationship with different nitrogen source and different co-doping. PL was studied to verify possible differences due to CDs precursors and to define the emission dependence from the $\lambda_{ex.}$ Finally, QY of all synthesized samples was performed.

As reported in Fig.37, UV-Vis absorbance of nitrogen doped CDs was compared to define differences and relations with nitrogen source reagents at increasing molecular weight.

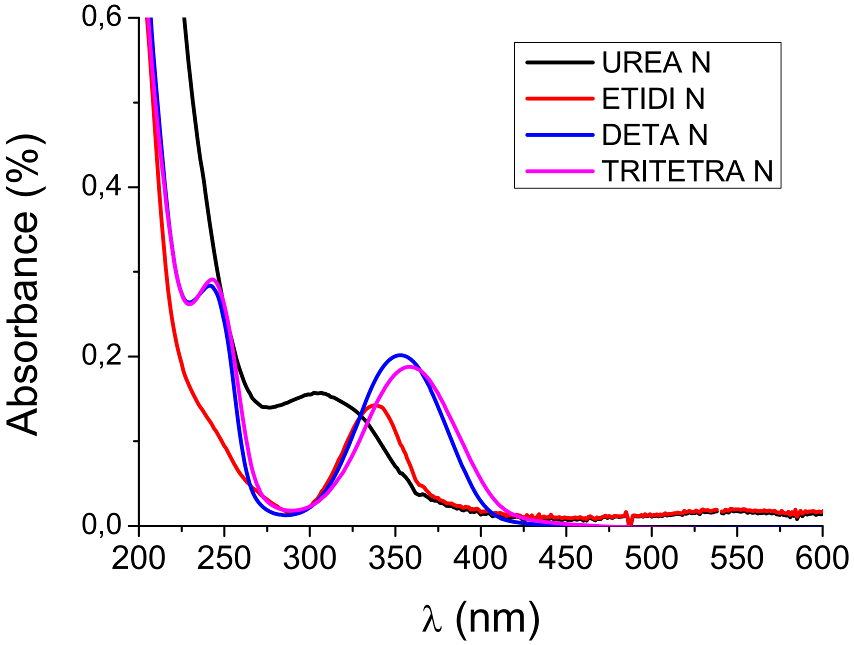

Figure 37: Absorbance of synthesized NCDs, produced with several nitrogen source.

ETIDI_NCDs showed a shoulder at 240nm due to π-π* and σ-π* transition, and an absorption peak of 338nm derived from n-π* transition. DETA_NCDs showed greater absorption at 240nm than ETIDI_NCDs, and an additional contribute at 352nm. If the absorption at 240nm could be related to π-π* and σ-π* transition, contribute at 352nm was referred to n-π*transition. TRITETRA_NCDs showed the same contributions at 240nm than sample DETA_NCDs, and an absorption at 358nm related to n-π*transition. Finally, UREA_NCDs showed a strong absorption near 200nm, that could hide a small contribution at 240nm. The same strong absorption partially covered a peak at 305nm representing n-π* transitions.

From the comparison of the nitrogen doped CDs synthesized with different nitrogen sources, was possible to correlate some aspect with the increase of molecular weight. Increasing molecular weight from ETIDI to TRITETRA, absorbance was increased at 240nm. Another change noted was a redshift of the peak correlated to n-π* transition.

Since all contributes at λ>280n could be referred to n-π* transitions, all the samples could be involved in this comparison. Absorbance redshift could derive by a cyclic compounds iper-conjugation that defined greater electronic delocalization, with consequences on the energy required for the n-π* transitions. Here, redshift of the absorbance was noticeable from UREA_NCDs to TRITETRA_NCDs, with a total shift of 53nm. Therefore, increasing molecular weight precursor, increased the electronic delocalization in NCDs.

In Fig.38, absorbance studies on UREA, ETIDI, DETA and TRITETRA based samples are reported.

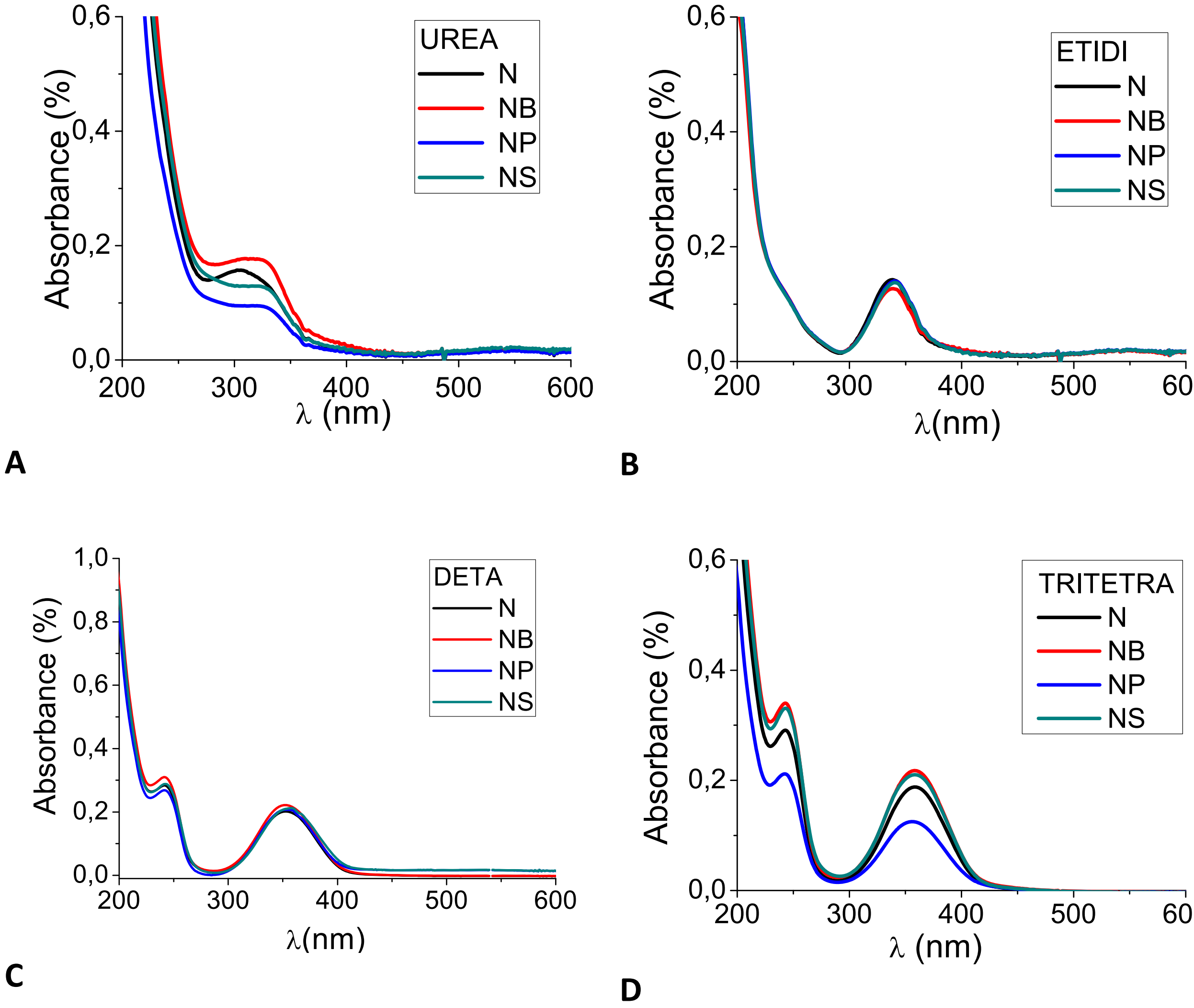

Figure 38: Absorbance comparison of synthesized nitrogen doped B, P and S co-doped CDs produced with A) UREA, B) ETIDI, C) DETA and E) TRITETRA.

From the comparison reported in Fig.38A, UREA based CDs showed one peculiarity. While UREA_NCDs showed a peak at 305nm, all the co-doped samples showed the same absorption shape: a plateau from 275 nm to 336 nm, with an absorption tail until 400 nm. From the comparison of the different ETIDI based CDs presented in Fig.38B, no difference were detected. All ETIDI samples showed an absorption shoulder at 245 nm and a peak at 337 nm. In Fig.38C, all

DETA based samples showed a first peak at 245 nm, while a second peak emerged at 351 nm. In Fig.38D, all TRITETRA samples showed a more intense peak at 245 nm and a second absorption at 358 nm. Increasing MW of the nitrogen source bring an absorbance contribution at 245nm development, and a redshift of the absorbance from 337 nm to 358 nm. The absorption contribute at 240 nm could be related to the increase of aromatic π-π* and σ-π* transition. Absorbance redshift could be due to cyclic compounds iper-conjugation, that defines greater electronic delocalization, with consequences on the energy required for the n-π* transitions.

The co-doping heteroatoms didn't affect absorbance in the UV-Vis region. All the co-doped samples of ETIDI, DETA and TRITETRA based CDs showed two peaks at 240nm and 338nm. The first peak was determined by aromatic π-π* and σ-π* transition, while the second peak was determined by n-π* transition.

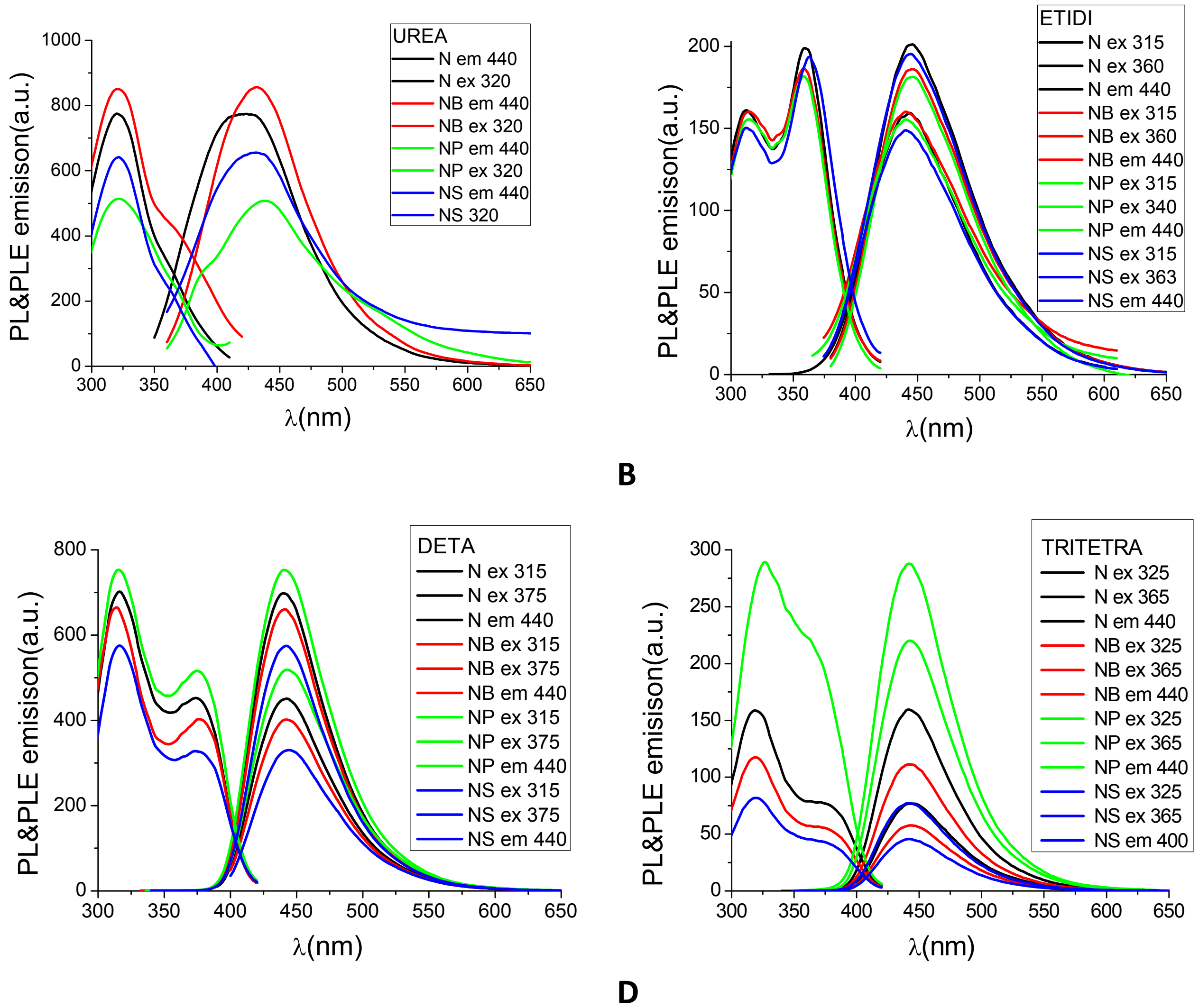

Figure 39: Photoluminescence study of synthesized nitrogen doped and B, P and S co-doped CDs produced with A) UREA, B) ETIDI, C) DETA and E) TRITETRA.

In Fig.39A photoluminescence studies on UREA based CDs are showed. Studying PLE at fixed emission of 440nm, was evident that all the samples presented one excitation peak centered at 365nm. PL studies showed an emission beginning around 360nm and fading close to 575-600nm. The emission range was similar for all the four samples, but the PL λ_{max} was different for NCDs and co-doped CDs. If NCDs emitted at 420nm, NBCDs, NPCDs and NSCDs emitted at 430nm. In Fig.39B studies on ETIDI based samples are showed. Studying PLE at 440nm of ETIDI samples, was evident that all the samples possessed two excitation peaks at 315 and 360nm. PL measurements obtained with both the two λ_{ex} begun around 360nm and faded close to 600nm. In Fig.39C studies on DETA based samples are showed. Form PLE measurements at 440nm, all the samples showed two peaks at 315 and 375nm. In comparison with PLE of ETIDI samples, the intensity of the two peaks were inverted. PL studies, showed the emission beginning around 380nm and fading close to 600nm. In Fig.39D studies on TRITETRA based samples are showed. Studying PLE at emission at 440nm, all the samples showed two peaks at 326 and 360nm.

With exclusion of UREA-based samples, no PL differences were noted. All the PL curves expressed maximum at 440nm. Moreover, no differences were noted in PL curves shape, even setting the excitation at the two different PLE maximum. From the range of λ_{ex} evaluated in this experiment, was noticeable a different behavior in emission dependence from λ_{ex}. In consequence a deeper optical study, focused on the determination of the emission dependence from the λ_{ex} was performed.

In order to determine the emission dependence from the λ_{ex}, PL measurements were recorded with excitation shifts of 10nm in a range of 60 nm. Finally, emission variations were described. In this experiment only NCDs synthesized with different nitrogen source were studied.

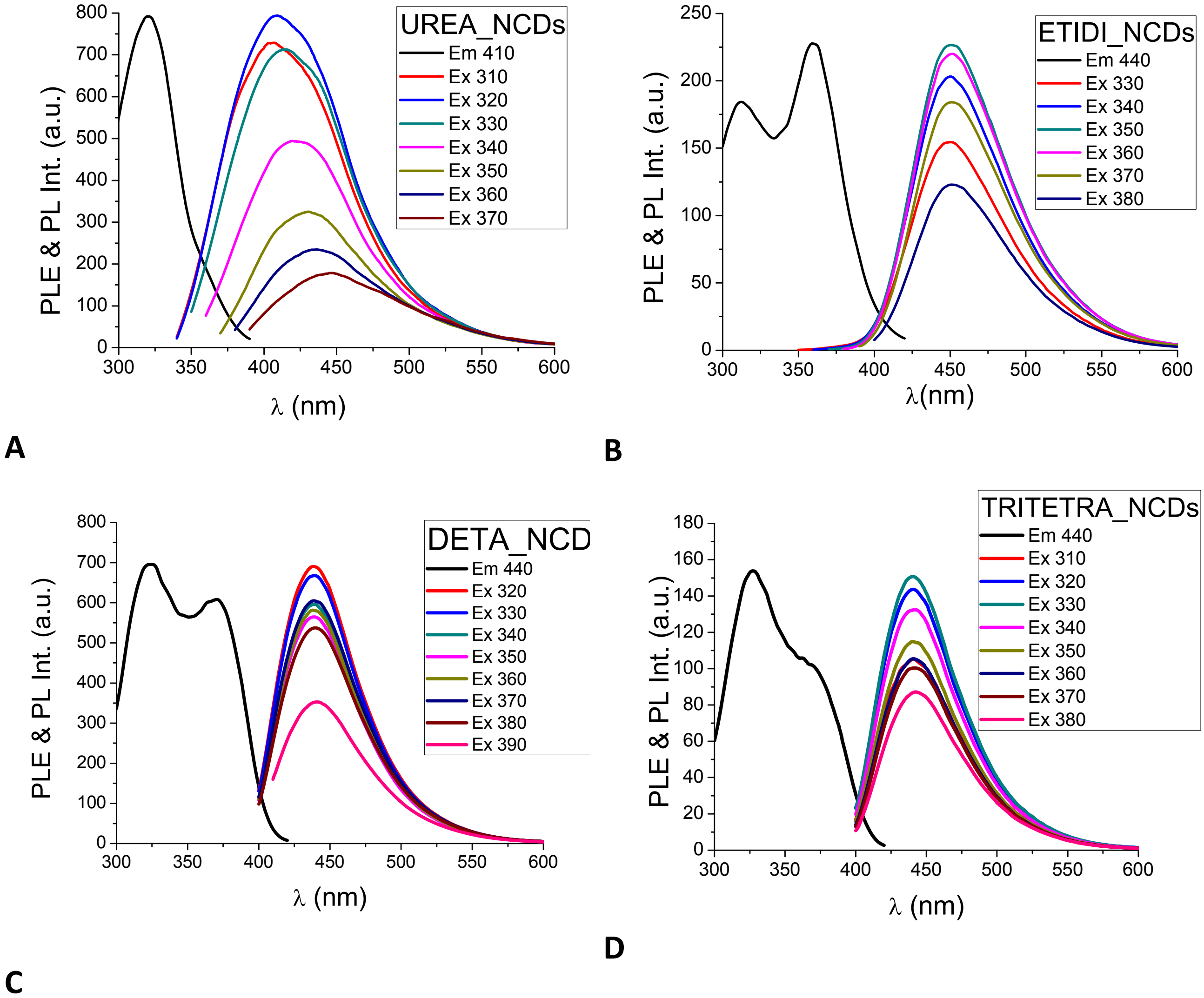

Figure 40: A) PLE and PL studies at different λ_{ex} on the NCDs samples synthesized with UREA B) PLE and PL studies at different λ_{ex}on the NCDs samples synthesized with ETIDI. C) PLE and PL studies at different λ_{ex}on the NCDs samples synthesized with DETA. D) PLE and PL studies at different λ_{ex}on the NCDs samples synthesized with TRITETRA.

In Fig.40A, PLE of UREA_NCDs is reported from 300nm to 370nm. A series of PL were performed from 310nm to 370nm. UREA_NCDs emission shift started at 404nm, at λ_{ex} 310nm, and continued until 445nm at λ_{ex} 370nm. UREA_NCDs expressed a redshift of 40nm. Fig.40B shows, PLE of ETIDI_NCDs from 300nm to 370nm. A series of PL were performed from 330nm to 380nm. Despite the different λ_{ex}, no photoluminescence variation were observed. In Fig.40C, PLE of DETA_NCDs is shown from 300nm to 420nm. A series of PL were performed from 330nm to 380nm. Also in this case, despite the different λ_{ex}, no photoluminescence variations were observed. Fig.40D, shows the PLE of TRITETRA_NCDS from 300nm to 420nm. A series of PL were performed from 330nm to 380nm. Despite the different λ_{ex}, no photoluminescence variation were observed.

From the study of the emission independence from the λ_{ex} was possible to conclude that UREA_NCDs was the only sample that presented this property. Indeed, all the other samples showed PL independence from λ_{ex}. Emission dependence from the excitation wavelength was a typical characteristic of CDs with not passivated surface. Therefore, UREA_NCDs didn't possess concentration of surface nitrogen-based functionalization to avoid emission dependence from λ_{ex}.

Among several measurements for optical properties determination, quantum yield (QY) was undoubtedly one of the most important determination. Since QY was defined with the ratio between absorbed and emitted photons, errors could arise if the excitation lamp can emit an inhomogeneous light in different portion of the spectrum. Therefore, the use of reference materials with absorbance close to the sample could avoid error produced by these conditions. Since Quinine sulphate (QS) absorbed from 320nm to 348nm and CDs samples absorbed from 300nm to 400nm, it represented the best reference material. In a second time, from relative QY calculated on QS (QY 55%), absolute QY was calculated against Rhodammine 6G in ethanol (QY 95%), considered the absolute reference material. In addition, in order to determine QY repeatability, all CDs considered in this study were re-synthesized and their QY was studied. In the plot showed in Fig.41, calculated absolute QY for all the samples and their repeated synthesis are showed.

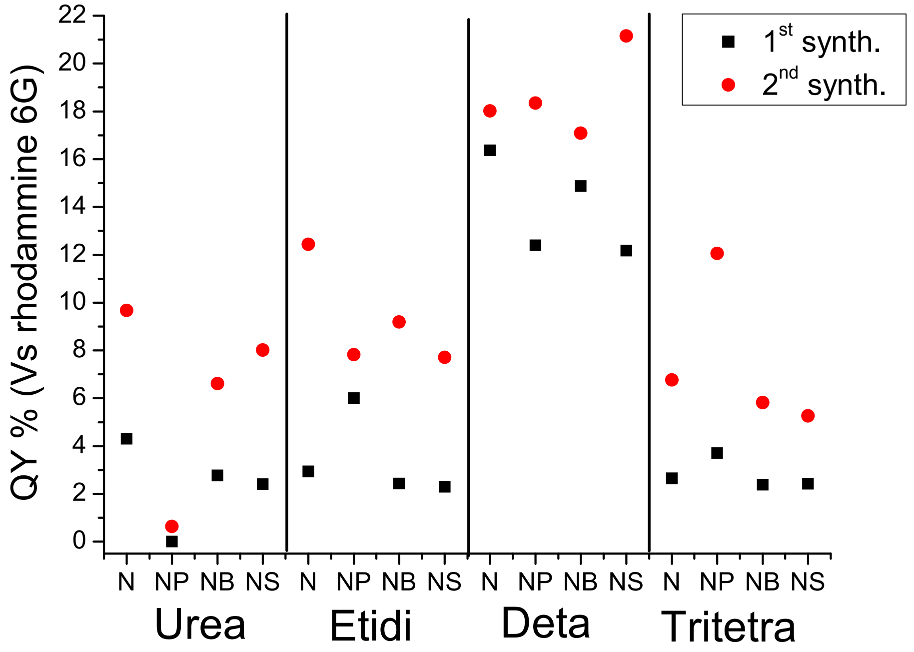

Figure 41: Quantum yield comparison of all the samples produced with different nitrogen source and co-dopant source. Here, in order to check reproducibility, results of two-repeated synthesis are showed.

For easier consideration, calculated QY against QS and Rh6G is showed in the Tab.9.

Table 9: QY values calculated against quinine sulphate solution in 0,5M H_2SO_4 and calculated QY against Rh6G solution in ethanol. Presented values are the mean calculated on the two-repeated synthesis.

Sample	QY QS	QY Rh6G	Sample	QY QS	QY Rh6G
Urea NCDs	12.6±6.9	7±4.2	**DETA NCDs**	31.2±2.1	17.2±1.3
Urea NBCDs	0.5±4.9	0.3±3	**DETA NBCDs**	27.9±2.8	15.4±1.7
Urea NPCDs	8.5±0.8	4.7±0.5	**DETA NPCDs**	29±7.6	16±4.7
Urea NSCDs	9.4±7.2	5.2±4.4	**DETA NSCDs**	30.2±11.5	16.7±7
ETIDI NCDs	13.9±12.2	7.7±7.4	**TRITETRA NCDs**	8.5±5.3	4.7±2.9
ETIDI NBCDs	12.5±8.7	6.9±5.3	**TRITETRA NBCDs**	14.3±4.4	7.9±2.4
ETIDI NCPDs	10.5±12.3	5.8±1.4	**TRITETRA NPCDs**	7.4±10.7	4.1±5.9
ETIDI NSCDs	9.1±6.9	5±4.2	**TRITETRA NSCDs**	6.9±3.6	3.8±2

From the comparison of the plotted QY values, no appreciable variations were noted for samples synthesized with different heteroatoms. Similar considerations could be done for samples synthesized with different nitrogen source. With exclusion of the DETA-based group, all the other samples showed similar QY. This aspect excluded a direct relationship between amine molecular weight and quantum yield. Finally, from the comparison of the plotted quantum yield values, emerged that the QYs of samples from second synthesis were greater than those from the first synthesis, so the parameters relative to the syntheses and the reproducibility of the samples were not completely under control. It was also noticeable that DETA based group showed the highest QY.

To conclude the optical characterization of the four groups of samples, was possible to determine more differences between UREA, ETIDI, DETA and TRITETRA than between different co-doped CDs. Considering absorbance was noticeable that some differences were observed for samples of different groups, while different co-doping didn't produce any change. From the comparison of different groups absorbance, redshift absorption of the peak at λ>300nm was determined, with a shift of 53nm from UREA based samples to TRITETRA based samples. The shift could be due to the cyclic compounds iper-conjugation that defined greater electronic delocalization, with consequences on the energy required for the n-π* transitions. Concerning photoluminescence, the most important difference was the UREA_NCDs excitation dependence from the λ_{ex}, probably derived from a low surface passivation. Finally, from the comparison of the QY, the most efficient material were the DETA based group of samples, with absolute QY close to 20%.

4.1.3.2- Elemental analysis

In this paragraph we report the elemental analysis of some samples in order to correlate nitrogen and codoping CDs content with quantum yield.

To define elemental composition of the synthesized CDs, elemental analysis was performed. At this purpose, two groups of sample were selected. To define the amount of nitrogen content depending to the amine molecular weight, nitrogen-doped samples synthesized with different nitrogen source were studied. Moreover, the second selected group was composed by DETA based samples, because they were selected to be applied in enhanced oxidation photocatalytic materials. Analyzed samples are underlined in the Tab.10.

Table 10: Samples characterized with elemental analysis.

Urea NCDs	ETIDI NCDs	DETA NCDs	TRTETRA NCDs
Urea NBCDs	ETIDI NBCDs	DETA NBCDs	TRTETRA NBCDs
Urea NPCDs	ETIDI NPCDs	DETA NPCDs	TRTETRA NPCDs
Urea NSCDs	ETIDI NSCDs	DETA NSCDs	TRTETRA NSCDs

Fig.42 shows the $\%_w$ elemental composition of NCDs samples prepared with ETIDI, DETA, TRITETRA and UREA groups . From the figure it was possible to compare CDs composition synthesized with different nitrogen sources.

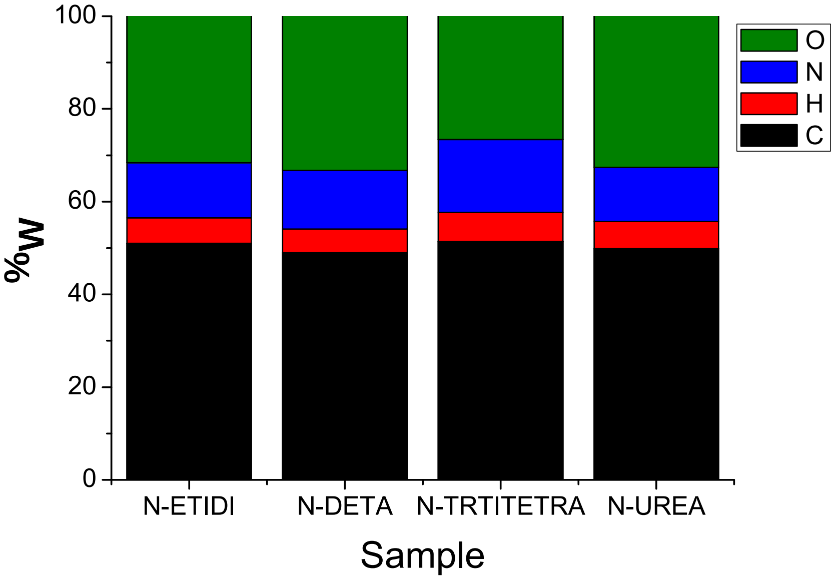

Figure 42: histogram shows elemental composition %w of the nitrogen doped samples of the ETIDI, DETA, TRITETRA and UREA groups.

From the elemental analysis study, was noticeable that samples with similar elemental composition were produced, and particular homogeneity was obtained for the nitrogen and carbon $\%_W$. Despite these samples were synthesized with equal moles of molecules with different MW, carbon percentages were fixed between $51\%_W$ and $49\%_W$, while the nitrogen percentages changed from $11.7\%_W$ and $15.7\%_W$. Similar homogeneities were obtained for hydrogen and oxygen content, where percentages varied from $5.5\%_W$ and $6.3\%_W$ for hydrogen and from $26.6\%_W$ and $33.3\%_W$ for oxygen content. Relating nitrogen elemental percentages and QY, was possible to assume that, for N_CDs, nitrogen content and quantum efficiency were not correlated. In fact, if DETA_NCDs showed the best QY of the nitrogen doped CDs category, the elemental analysis showed no differences composition in comparison with the other samples.

In the Tab.11 is possible to compare theoretic (T) and determined $(D)\%_W$ of the different N_CDs. Theoretic percentage was calculated considering the moles of C, H, N and O of each reagent used in sample synthesis. From the comparison emerged for all the analyzed samples a general loss of oxygen. Oxygen loss, comprised between $10{,}8\%_W$ and $17{,}6\%_W$,was probably due to the condensation of citric acid with the nitrogen source. Moreover, determined hydrogen content was smaller than the theoretical percentage for all the samples synthesized with amines. Also hydrogen loss could be due to the condensation process occurred during CDs synthesis.

Table 11: presentation of the elemental theoretical and the determinate composition of N_CDs synthesized with different nitrogen source.

Sample	**$C\%_w$**		**$H\%_w$**		**$N\%_w$**		**$O\%_w$**	
	T	**D**	**T**	**D**	**T**	**D**	**T**	**D**
UREA_NCDs	37.2	49.9±0.03	4,4	5.8±0.04	11.0	11.7±0.03	47.4	32.6±0.02
ETIDI_NCDs	37.9	51±0.04	5,6	5.5±0.02	7.3	11.9±0.04	49.2	31.6±0.04
DETA_NCDs	39.7	49±0.04	6,3	5.1±0.03	9.9	12.6±0.04	44.1	33.3±0.04
TRTETRA_NCDS	41.2	51.4±0.02	6,8	6.3±0.03	11.9	15.7±0.02	40.1	26.6±0.03

In Fig.43 elemental composition in $\%_w$ of DETA based samples are showed.

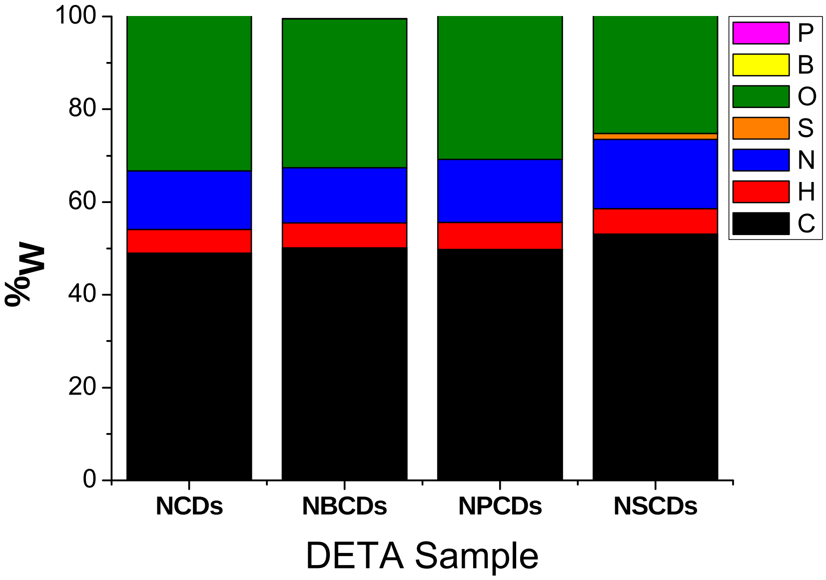

Figure 43: histogram showing elemental composition percentages in weight of the nitrogen doped and B,P,S co-doped DETA samples.

Here, no boron and phosphor were determined in elemental analysis of NBCDs and NPCDs, while 1,3 $\%_w$ of sulphur was detected in NSCDs. Also in this case strong homogeneity in carbon and nitrogen percentages was showed in all the samples. In addition, elemental percentages could be compared with CHNO values of the previous samples. Strong compositional homogeneity was still observed. $N\%_w$ in DETA samples was close to the $N\%_w$ found in samples made with other nitrogen source. Therefore was possible to assume that the higher QY of DETA samples cannot be ascribed to the nitrogen content.

In the Tab.12 is possible to compare the theoretical and the determined percentages of the DETA based CDs. From the comparison of the $\%_w$ of the theoretical calculation and the analytically determination, emerged an oxygen and hydrogen loss. Clearly, O and H loss was due to the condensation processes during the CDs production. Moreover, emerged that no B and P doping took place.

Table12: presentation of the elemental theoretical and the determinate composition of DETA based carbon dots with different doping.

Sample	**C%$_{w}$**		**H%$_{w}$**		**N%$_{w}$**		**O%$_{w}$**		**HETEROATOM%**		**Δ%**
DETA	**T**	**D**	**T**	**D**	**T**	**D**	**T**	**D**	**T**	**D**	**D-T**
NCDs	39.7	49±0.03	6.3	5.1±0.03	9.9	12.6±0.03	44.1	33.3±0.02	-	-	-
NBCDs	37.4	50.1±0.02	6.1	5.4±0.04	9.3	11.9±0.02	46.4	32.6±0.04	0.8	<0.1	0.8
NPCDs	38.7	49.8±0.03	6.1	5.8±0.03	9.2	13.6±0.04	43.7	30.8±0.04	2.3	<0.1	2.3
NSCDS	39.3	53.1±0.04	6.1	5.5±0.02	8.9	14.9±0.04	43.4	25.2±0.03	2.3	1.3	1

We would like to underline that the amount of reagent for CDs co-doping was not high. The used amount of boric acid was enough to load theoretical 0,8%$_{W}$ of B. Despite the low quantity, we maintained the C and B source ratio proposed in the publication used to study co-doped CDs synthesis[123]. Despite the use of $\frac{1}{4}$ of the moles of the prescribed N source increased the amount of the co-doping moles, this was not enough to dope NBCDs with boron. The amount of the used phosphor and sulphur precursors was enough, theoretically, to load 2,3%$_{W}$ of heteroatoms. Despite that, elemental analysis detected 1,3%$_{W}$ of sulphur, and no phosphor was found.

Difference loading yield could be due to the different precursor compatibility with the system. Mercaptosuccinic acid was used as sulphur precursor, while inorganic acids were used as phosphor and boron precursors. Probably inorganic acids were less available as organic molecules to contribute to carbon dots formation, with negative repercussion on co-doping process.

4.1.3.3-Cytotoxicity

In this study, cytotoxicity was considered a propaedeutic step for CDs interaction with living organisms and their application in nanomedicine. For this reason, cytotoxicity was fundamental for the characterization and the application of nanostructured materials as CDs. In fact, the use of toxic precursors as amines at different molecular weight could produce unsafe nanostructured materials. At this purpose, similar consideration could be associated with heteroatoms sources used to synthesize NBCDs, NPCDs and NSCDs. Cytotoxicity was evaluated also to define the real applicability of synthesized materials in nanomedicine. For these considerations, the evaluation of the toxicity was an essential step to base additional measurements on biological compatibility. At this purpose, all the samples produced in this work were involved, and for each samples both of the two-repeated synthesis were tested.

In a typical graph, X axes showed decreasing CDs concentration, while in Y axes cells counts were reported. Similar studies were performed on all the other samples, synthesized with all the possible combinations of nitrogen and co-doping sources. In this paragraph, were discussed only the most representative samples, while the complete cytotoxicity study, performed on all the samples were reported in the appendix A -paragraph 4.1.3.2.

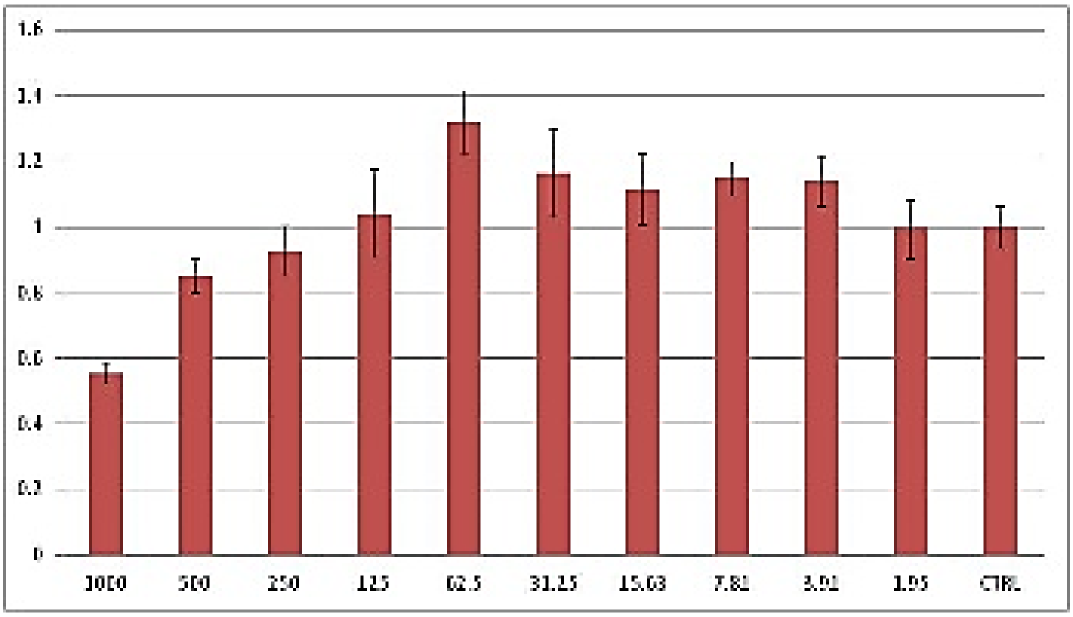

A **UREA_NPCDs#1**

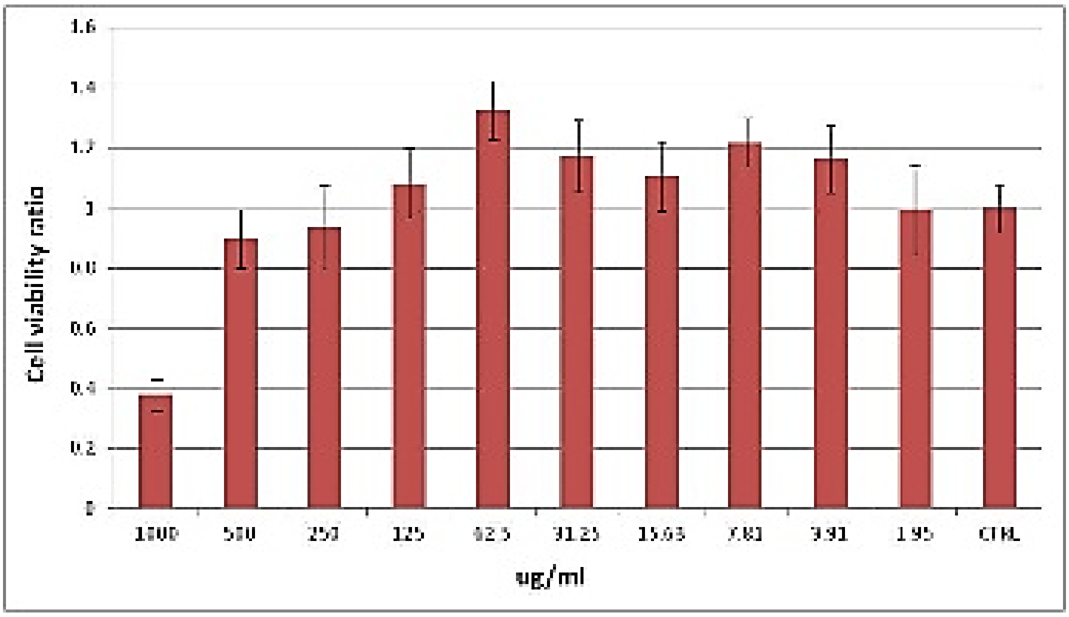

B **UREA_NPCDs#2**

Figure 44: Cytotoxicity determination of the two-repeated synthesis of the samples synthesized with urea as nitrogen source. A)study onUREA_NPCDs#1. B)study onUREA_NPCDs#2. X axes show decreasing CDs concentration (µg/ml), while in Y axes cells viability counts are reported.

In Fig. 44A, UREA_NPCDs#1 cytotoxicity determination is showed. Comparing cell viability at increasing CDs concentration with the control sample (CTRL), good cell viability was exhibited until 1000 µg/ml. At the maximum concentration of CDs, cell viability decreased, showing cytotoxicity. In Fig. 44B,UREA_NPCDs#2 cytotoxicity determination is showed. Also for this sample, good cell viability was exhibited until 1000 µg/ml. From the comparison of the two repeated synthesis emerged good reproducibility.

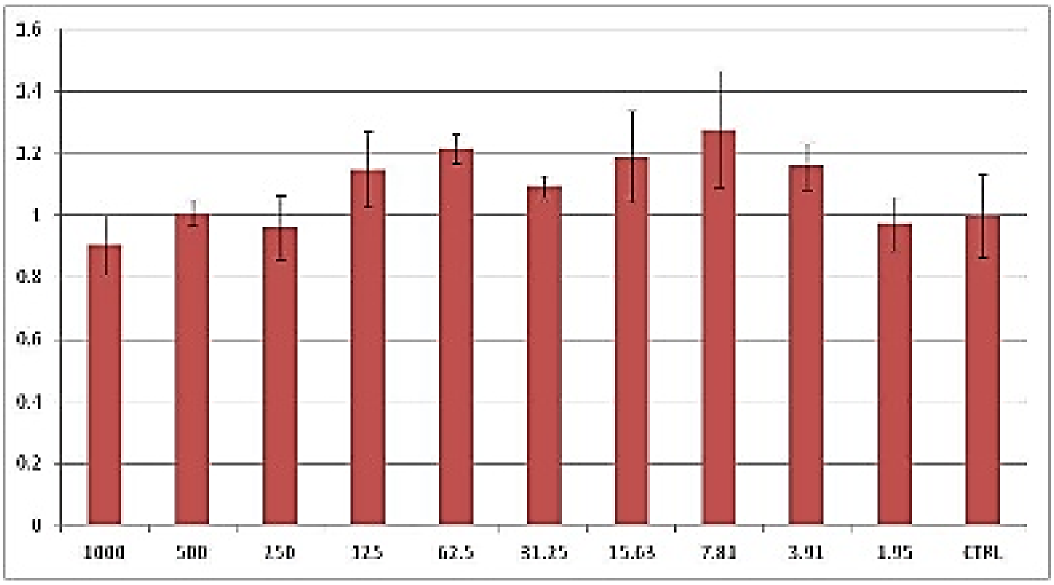

DETA_NPCDs#1

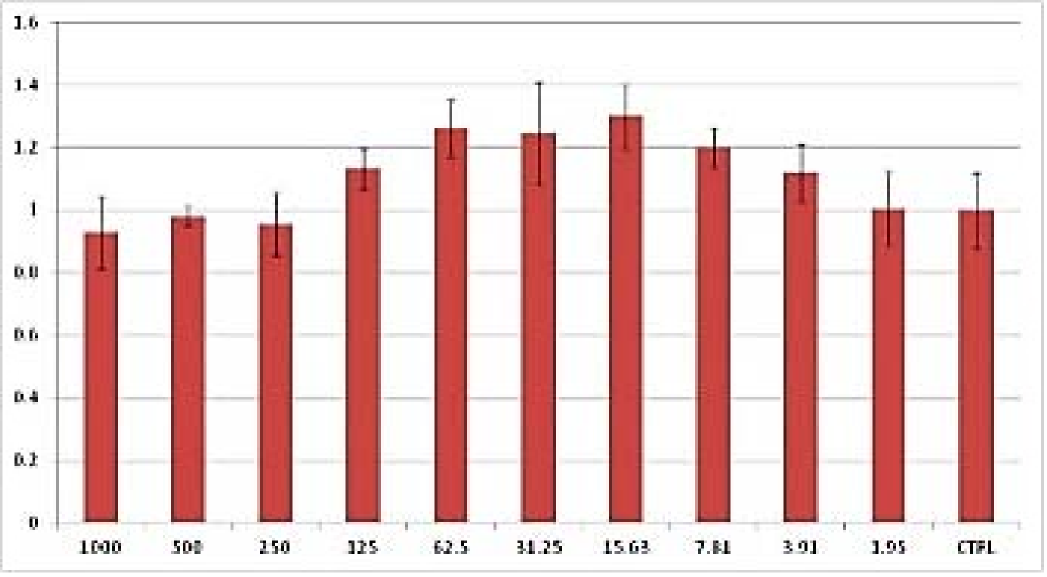

DETA_NPCDs#2

Figure 45: Cytotoxicity determination of the two-repeated synthesis of the samples synthesized with urea as nitrogen source. A) study onDETA_NPCDs#1. B)study onDETA_NPCDs#2. X axes show decreasing CDs concentration (µg/ml), while in Y axes cells viability calculation are reported.

In Fig.45A, DETA_NPCDs#1 cytotoxicity determination is showed. Comparing cell viability at increasing CDs concentration with the CTRL, good cell viability was exhibited even at 1000 µg/ml. In Fig.45B DETA_NPCDs#2 cytotoxicity determination showed similar results, and didn't present cell viability decrease even at maximum CDs concentration. From the comparison of the two repeated samples emerged a good reproducibility.

The cytotoxicity of all the other samples synthesized with the other combinations of nitrogen and co-doping sources was showed in the Tab.13. The yellow label indicated the toxicity of the first synthesis, the orange label indicated the toxicity of the second synthesis, while the brown label indicated if both of the two synthesis produced toxic materials.

Table 13: Summary of the toxicity of the two repeated samples of nitrogen doped and co-doped CDs.

	Urea	ETIDI	DETA	TRITETRA
N	🟫			
N, B	🟫			🟧
N,P	🟫	🟧		🟨
N,S	🟫	🟫	🟫	🟨

🟨 **TOXIC #1**
🟧 **TOXIC #2**
🟫 **TOXIC #1,2**

From toxicity tests made on both of the two repeated synthesis, had arisen a clear relation between some precursors and cytotoxicity. Samples synthesized with urea showed toxicity in each of the two synthesis, while the use of the other nitrogen source didn't influence the safety of the material. Similar consideration can be done concerning the use of mercaptosuccinic acid as sulphur precursor in NSCDs. It was possible that during the hydrothermal synthesis of the UREA based CDs and the production of NSCDs with mercaptosuccinic acid, the reagents could degrade into toxic compounds. These toxic compounds could be joined in the CDs formation, with consequences on safety of the produced nanoparticles. Indeed, mercaptosuccinic acid could be degraded into succinate compounds[285]. For example, sodium succinate is class-2 hazard compound, and similar product embedded into CDs could reduce cell viability. Moreover, in another study high toxicity CDs were synthesized from fructose due the thermal degradation at 100°C of fructose in furan[286].

4.1.3.4-Electrophoresis

In this paragraph, we show the results of electrophoresis study at different pH, conducted on the DETA-based group of sample. Similar studies were performed on all the other samples, synthesized with all the possible combinations of nitrogen and co-doping sources. All the electrophoresis studies performed on these samples were reported in the appendix A - paragraph 4.1.3.3.

Gel holes were loaded with NCDs, NBCDs, NPCDs, NSCDs suspensions. Images of the gels showed CDs migration directed to negative and positive electrode. The loading was repeated for the synthesis #1 and #2. Thanks to this comparison, possible differences in migration speed from a sample to another could be observed, and others differences between first and second synthesis were emphasized.

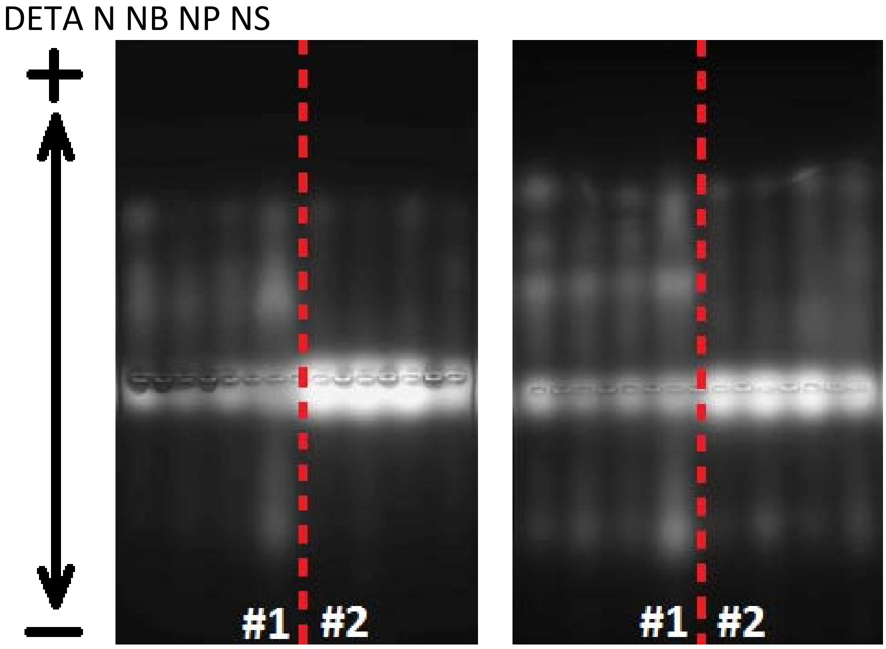

A pH4 **B** pH6

Figure 46A and B: Electrophoresis study at pH 4 and pH6 respectively, performed on repeated synthesis DETA_NCDs, DETA _NBCDs, DETA _NPCDs and DETA _NSCDs.

In Fig.46A, electrophoresis study conducted at pH 4 of the samples DETA_NCDs, DETA _NBCDs, DETA _NPCDs and DETA _NSCDs is showed, while in Fig. 46B, similar study conducted at pH6 on the same samples is presented.

DETA pH4: unlike the other UREA, ETIDI and TRITETRA based samples, DETA based samples showed good resolution at pH4. Despite the presence of smears, one band was easily detectable in the front of the migration of negative charged nanoparticles. Another important aspect was the presence of great CDs portion that, despite acidic pH, possessed zero superficial charge.

DETA pH6: at greater pH, no substantial differences were found in comparison with electrophoresis performed at pH4. In fact, migration speed was not increased and the head of the migration was close to the same position of the electrophoresis at pH4.

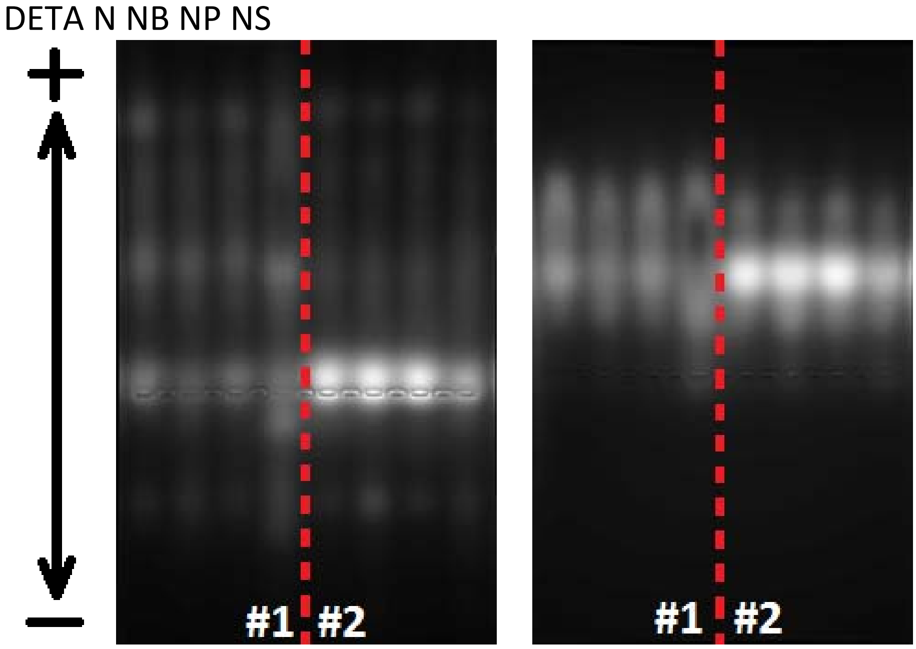

A pH8 **B** pH10

Figure 47 A and B: Electrophoresis gel at pH 8 and pH10 respectively, performed on repeated synthesis of DETA_NCDs, DETA _NBCDs, DETA _NPCDs and DETA _NSCDs.

In Fig.47A, electrophoresis study conducted at pH 8 of the samples DETA_NCDs, DETA _NBCDs, DETA _NPCDs and DETA _NSCDs is showed, while in Fig.47B, similar study conducted at pH10 on the same samples is presented.

DETA pH8: at increased pH, CDs migration speed was increased. However, despite resolution increases, only two bands emerged from the smear. Even at pH8, positive charged CDs were still migrating to negative electrode, while a portion of inert CDs lies in the loading holes.

DETA pH10: also for DETA based samples, high pH values increased negative charges on CDs and increased migration speed to positive pole. Moreover, high pH deprotonated surface charge of the entire sample population, because no luminescence was observed in the loading holes and in the lower part of the gel. In fact, if pH 10 buffer pushed the other CDs outside the gel, it was able to pull out CDs fraction with balanced surface charges from the loading holes, and to attract them to the positive side. At the end of the process these populations were the only still presents in the gel.

From the electrophoresis study at different pH, performed on DETA-based samples, was possible to take some important consideration.

When pH was increased, CDs showed low response to electric field. We supposed that this phenomenon was due to greater functional group density. Supposing that surface functional group were also responsible of luminescence properties of the material, higher density of functional groups could also explain greater quantum yield of DETA-based samples.

It was possible to state that electrophoresis analysis at different pH permitted to identify several different CDs population, and to differentiate them on superficial charge and dimension. In this experiment was observed how CDs migration speed could change with pH values. When pH increased, nanoparticles speed attraction to positive electrode also increased, while the speed attraction to negative charge decreased. This phenomenon could be related to the different deprotonation degree of the functional groups that decorated the surface of the nanoparticle. Greater concentration of negative charges increased CDs response against the electric field, and increased migration speed to the electrode with opposite charge. At the same time, the reduction of positive charges on CDs surface, due to the increased deprotonation of surface functional group, decreased their migration speed to the negative electrode.

In addition, emerged also that when pH increased, some population of CDs reached a charge balance between positive and negative charged surface functional group, becoming inert against the imposed electric field. In this situation inert CDs lied in the loading holes of the gel. Despite that, speed variation related to pH allowed to identify CDs population that at in unique pH could be impossible to determine.

Band definition of different CDs and the comparison of these bands of different samples permitted to define reproducibility of samples of the same synthesis group. If good superimposition of the bands of the CDs samples of the same group indicated good synthesis reproducibility, in the repeated batches (#1 and #2) CDs bands changed. From the comparison of the band of the two #1 and #2 series emerged increasing reproducibility from the UREA group of samples to TRITETRA, and from ETIDI to DETA.

From the comparison of the samples group with different nitrogen source emerged that increasing pH, the migration speed of some group increased slower than others did. This phenomenon could emerge from the different concentration of functional groups on the CDs surfaces. If a defined energy was required to deprotonate one functional group, the energy required to deprotonate a second functional group, close to the first, needed additional energy to contrast the force of the negative charge of the just deprotonated groups. Therefore, required energy was increased when number of deprotonated functional group was increased.

Samples cytotoxicity and quantum yield were used to select the group of samples for the enhanced photocatalytic materials: the CDs loading in TiO_2-based systems. Therefore some characterization, as the morphologic determination were performed on a smaller group of samples. On these considerations, DETA-based samples were chosen for the application with TiO_2 and for further characterizations.

4.1.3.5-TEM imaging

TEM images analysis were performed to determine size and shape of nitrogen doped and co-doped CDs. Considering QY and cytotoxicity results, DETA based samples were selected as the most interesting for further applications . In general, CDs were difficult to be detected by TEM technology due to the very low contrast with the carbon layer of the grid. Therefore, CDs were dropped on the opposite layer of the grid. In this way, copper was the only component of the grid, and CDs were more detectable than when dropped on the carbon layer. Despite the contrast increase, CDs were still difficult to be detected.

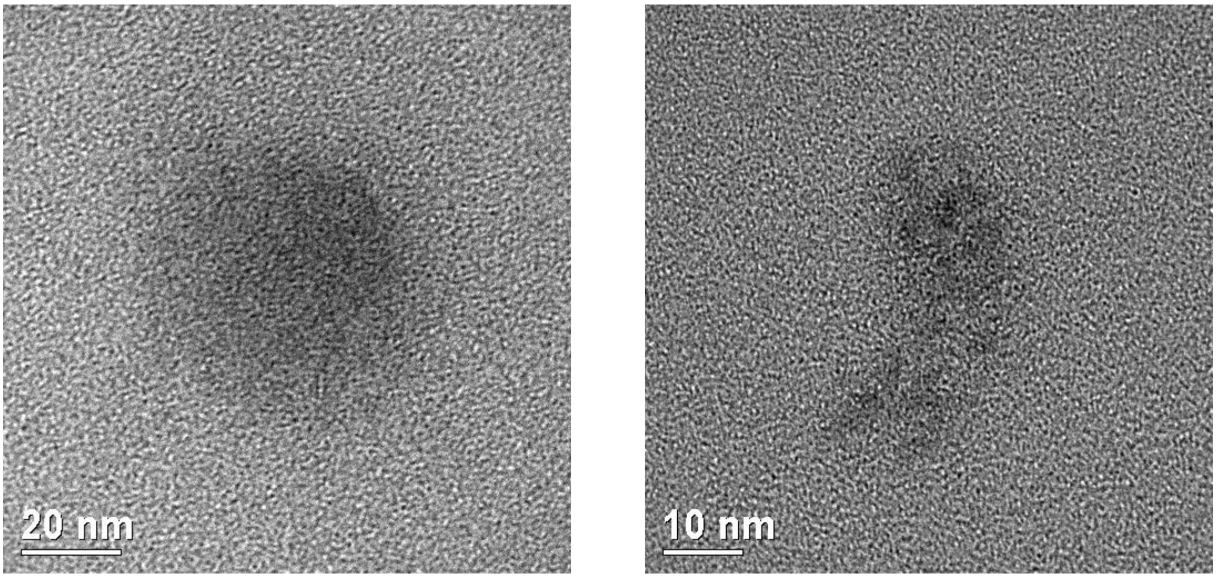

A **B**

Figure 48A and B: TEM images of DETA_NCDs

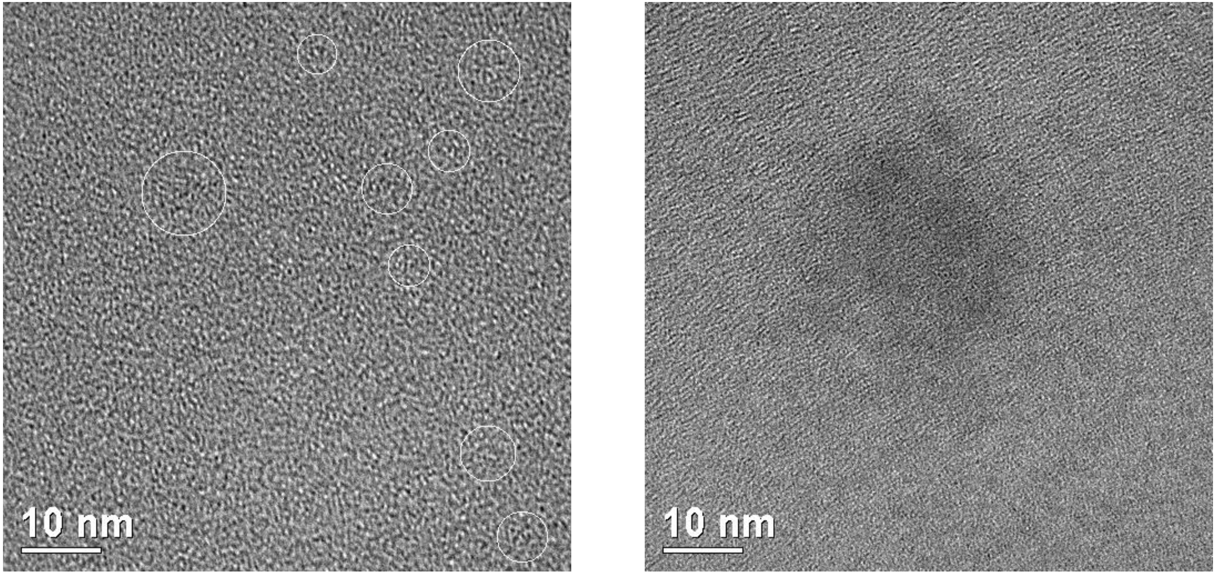

A **B**

Figure 49 A and B: TEM images of DETA_NBCDs

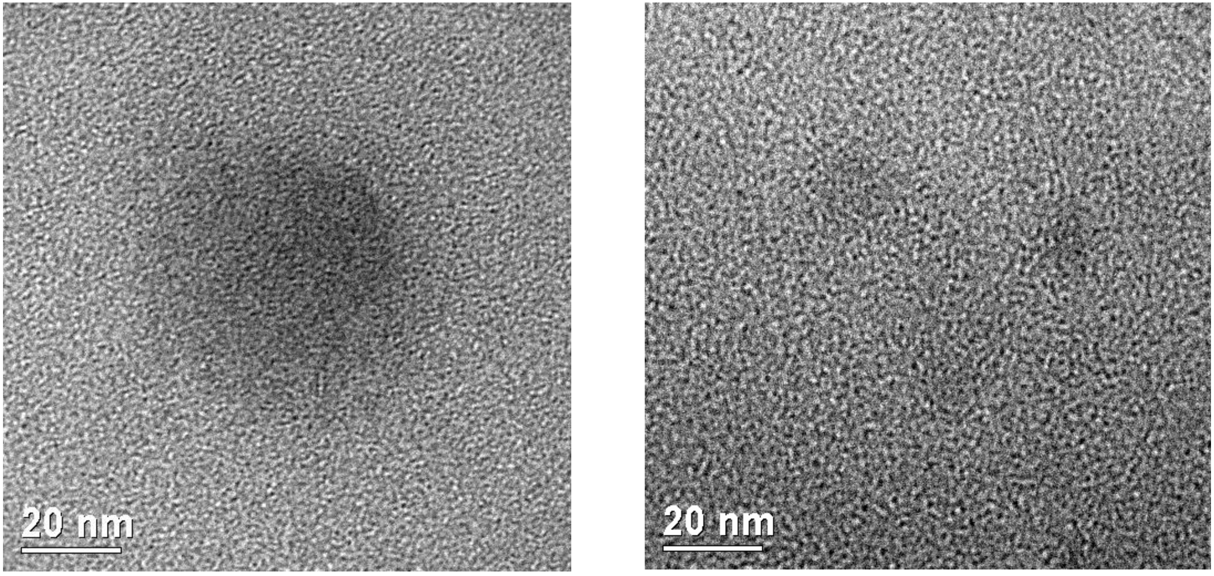

A **B**

Figure 50 A and B: TEM images of DETA_NPCDs

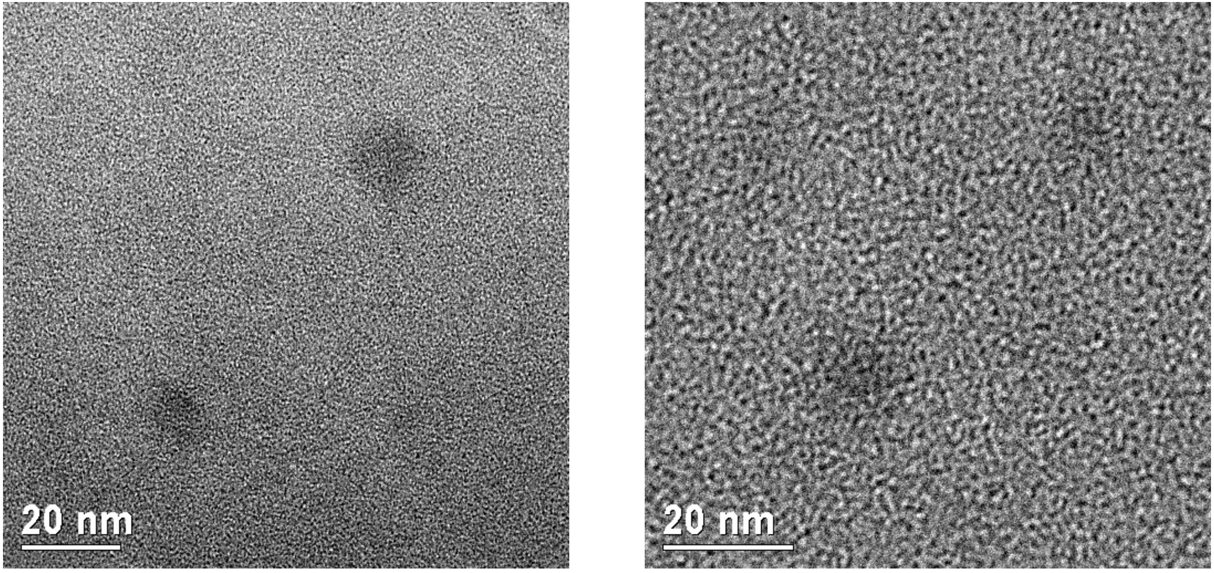

A **B**

Figure 51 A and B: TEM images of DETA_NSCDs

From the comparison of the individuated DETA_NCDs, was possible to define a wide size of particle distribution. If in Fig.48A was represented one CDs of 40nm, in Fig. 48B only small objects with irregular shape and dimension close to 10nm were found. Despite these dimensions were easily detectable with TEM technique, CDs individuation had been long and difficult.

Same problems emerged also for NBCDs detection showed in fig 49A and B. In Fig.49A the presence of CDs was just detectable (for an easier comparison are inscribed in white circles). Here, object individuated in circles had dimension less than 10nm. At the same time, in Fig. 49B, one system similar to that exposed in Fig.48B was showed. Despite the similar size and shape, CDs represented in Fig.49B was less contrasted, and probably thinner than the previous one.

In comparison with NBCDs nanoparticles, NPCDs were more easily detected. Despite that, even this sample presented wide size distribution. In Fig.50A was possible to note CDs with similar dimensions to those reported in the previous figures, while in Fig.50B three CDs, with dimension comprised from 10nm and 20nm were showed. Finally, in DETA_NSCDs, were individuated only small particles. In fact, Fig.51A and Fig.51B showed particles with size close to 10nm.

In conclusion, it had been possible to obtain images of DETA_NCDs and different B, P and S co-doped CDs. To recover CDs images, was spent along search on the loaded grid. Moreover, once CDs were individuated, their low contrast make difficult to obtain good images. From the pictures showed emerged CDs with wide size distribution, with globular shapes and with irregular and frayed edges. Finally, no detected nanoparticles showed visible sp^2 graphitic planes, but only amorphous carbon.

4.1.4- Results

In the whole paragraph 4.1, were shown the results of synthesis, purification and characterization of nitrogen doped and co-doped CDs. The most important aim of this paragraph was to better understand CDs behavior, from their synthesis to their characterization. In second instance, we tried to define CDs best properties in order to apply them in advanced oxidation processes and in nanomedicine. From this perspective, attempts were made to understand if CDs were able to produce UPCL phenomena and how they could be used for these properties. As the founding concerning UPCL enlight, CDs didn't produce UPCL.

At a later stage, to study possible CDs to be applied in enhanced photocatalytic materials, and to verify CDs possible application in nanomedicine, several groups of CDs had been produced via hydrothermal synthesis.

Nitrogen was chosen as main doping heteroatom to improve photoluminescence thanks to surface passivation. The use of nitrogen containing precursors with different toxicity permitted to study the relationship with their toxicity and CDs safe. Usually CDs were considered nontoxic and safe. In this research we stated that the use of nontoxic precursor, like urea, produced toxic CDs, while the use of toxic compounds as ethylenediamine, diethylenediamine and tryethylenetetramine synthesized safety CDs. Moreover, the use of co-doping heteroatoms permitted to study the same phenomenon with other molecules. In this case, the use of mercaptosuccinic acid as sulphur precursor produced CDs with moderate toxicity.

Another aspect analyzed was the variation of the purification procedure. Purification with dialysis membranes was often the only choice to clean CDs. Usually, dialysis membranes required long time treatment and considerable attention to load the sample. The osmotic pressure generated between the inner CDs suspension and the cleaning water could broads pores size or break the membrane. In the specific case of the materials studied in this work, hydrothermal synthesis produced CDs smaller than CDs produced in other ways. Therefore, small CDs could pass through the membrane within impurities and other un-reacted materials. To avoid the sample loss, another purification process was developed. This procedure, based on different chemical affinity, considered repeating washing with solvent at increasing polarity. The use of this process permitted to remove partially reacted materials and to obtain clean samples.

Samples studies were directed to define their possible application in nanomedicine and to increase advanced oxidation processes efficiency. In particular, the analysis on the results of characterization, individuated a small group of samples to apply to photocatalysis.

Considering optical analysis, greatest differences were found in samples synthesized with the different nitrogen precursor. The most important result in absorbance studies was the redshift adsorption at λ>240nm at increasing molecular weight of the nitrogen source. The redshift was due to the cyclic compounds iper-conjugation that defined greater electronic delocalization, with repercussions on the energy required for the n-π^* transitions. Considering photoluminescence, UREA based samples were the only compounds that showed emission dependence from the excitation wavelength. Considering quantum yield, the study showed that DETA-based group of samples were the most efficient material, with absolute QY close to 20%.

Toxicity tests showed clear relation between some precursors and cell viability. UREA-based samples showed discrete toxicity, while other nitrogen source produced safe CDs. Same consideration could be done for mercaptosuccinic acid in NSCDs. Hydrothermal treatment degraded both urea and mercaptosuccinic acid in toxic compounds before CDs formation.

TEM investigation showed how samples are constituted: CDs with wide size distribution, globular shapes and irregular and frayed edges. Moreover, no sp^2 graphitic planes were detected in high-resolution measurements, but only amorphous carbon.

Electrophoresis studies at different pH showed considerable qualitative information, concerning nanoparticles distribution on their size/surface functionalization relationship. CDs were particularly difficult to be characterized with common techniques. Electrophoresis at different pH could become one of the most important measurements, such as TEM imaging, toxicity studies and optical characterizations.

Elemental analysis (EA) identified the effective nitrogen doping and the presence of the other heteroatoms. Despite negative results concerning boron and phosphor co-doping, EA showed independence of $C\%_w$ and $N\%_w$ from the different nitrogen precursors. The use of urea, ethylenediamine, diethylentriamine and triethylentetramine produced CDs with similar composition.

After the characterization of all the samples, it was decided to apply DETA based CDs for the studies on enhanced photocatalytic systems. Their greater quantum efficiency, low toxicity and good reproducibility, make DETA based CDs ideal materials for improvements of advanced oxidation processes, where treated water could transmit and spread these nano materials in the environment. After EA determination, only DETA based NCDs and NSCDs were used for the study of the enhanced photocatalytic material.

4.2- Titanium dioxide

As described in the introduction, one of the aim of this study was to develop an enhanced photocatalytic material able to treat wastewater using solar radiation.

In particular, we studied a process able to obtain the desired crystalline phase (anatase TiO_2 phase) without annealing in order to avoid any deterioration of loaded CDs. The work developed in this part had been summarized in Fig.52. From this perspective, in the aim to produce a crystalline photocatalytic system loaded with CDs, was necessary to find a procedure able to obtain a well-crystallized TiO_2 and to preserve CDs structure. In our research, in order to bypass any thermal treatment, amorphous TiO_2 was previously synthesized and three different hydrothermal treatments were applied to produce crystalline anatase. These processes were selected from literature, reproduced and successively characterized trough XRD studies, morphological studies, bandgap measurements and photocatalytic activity. Properties of the produced samples were compared with respective literature and the selection of the best hydrothermal treatment was used to treat selected amorphous $NTiO_2$. After hydrothermal treatment selection, a study of the correspondent literature based the selection of the amorphous $NTiO_2$ was performed. The amorphous $NTiO_2$ was synthesized and treated with the selected hydrothermal process to obtain crystalline $NTiO_2$ anatase. The new material was characterized with XRD studies to define the crystallinity, while with FTIR was defined the presence of doping nitrogen after the hydrothermal process. Further characterizations were performed with bandgap and photocatalytic activity. On this material, synthesis temperature was studied to enhance nitrogen doping level. After preliminary characterization, the hydrothermal process was optimized in order to improve crystallinity and photocatalytic activity. At this purpose, XRD study, and photocatalytic experiments were performed to define the improvement of material properties . Finally, the best sample with the best crystallinity and photocatalytic activity was selected for the study of enhanced photocatalytic material.

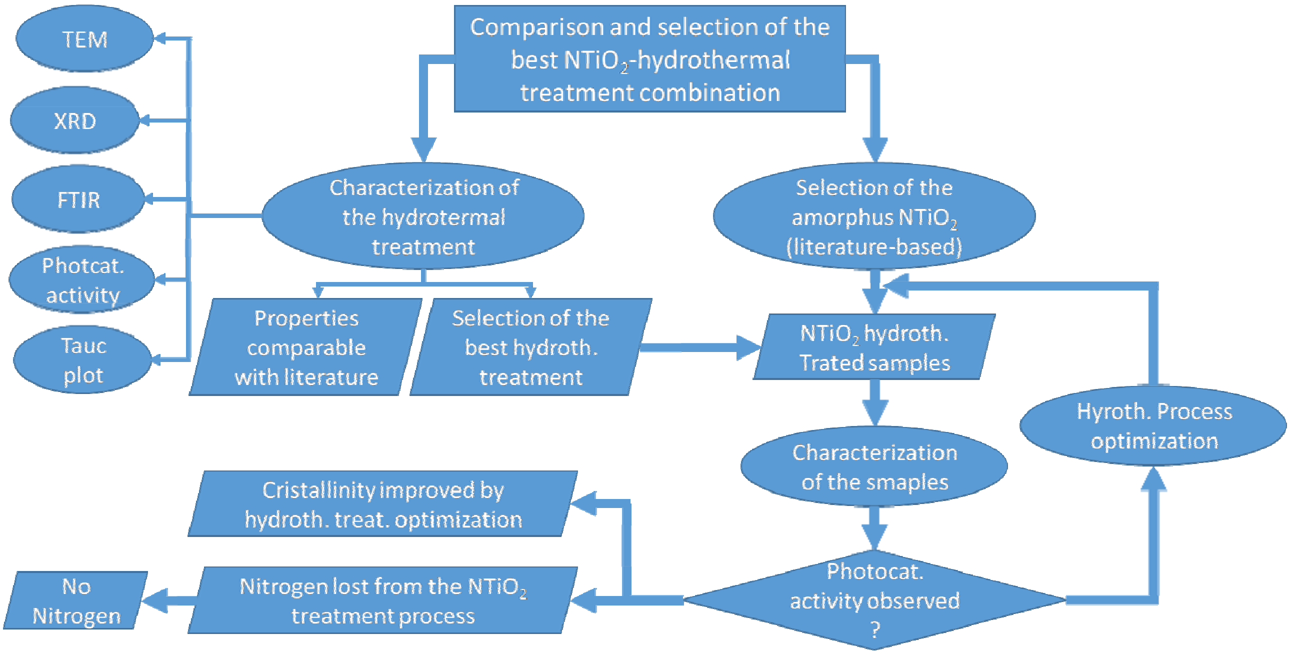

Figure 52: Scheme of the research topic focused on the comparison and selection of the best $NTiO_2$ / hydrothermal treatment combination.

4.2.1-Crystal phase stabilization

In order to produce a crystalline photocatalytic system loaded with carbon dots, was necessary to find a procedure able to obtain a well-crystallized TiO_2 and to preserve CDs structure. In our research, to bypass any annealing treatment, amorphous TiO_2 was previously synthesized and three different hydrothermal treatments were applied to produce crystalline anatase. Selected treatments were already summarized in the paragraph 3.3.1.

To confirm the reproducibility of the three selected methods, XRD diffraction patterns and TEM images of the synthesized materials were compared with the literature results. After that, to study the influence of the synthesis procedure on the final properties, photocatalytic activity and the bandgap of all the samples were measured and compared. This comparison allowed to select samples with the best properties.

In order to check the crystalline phase produced with hydrothermal treatments, XRD analysis were performed.

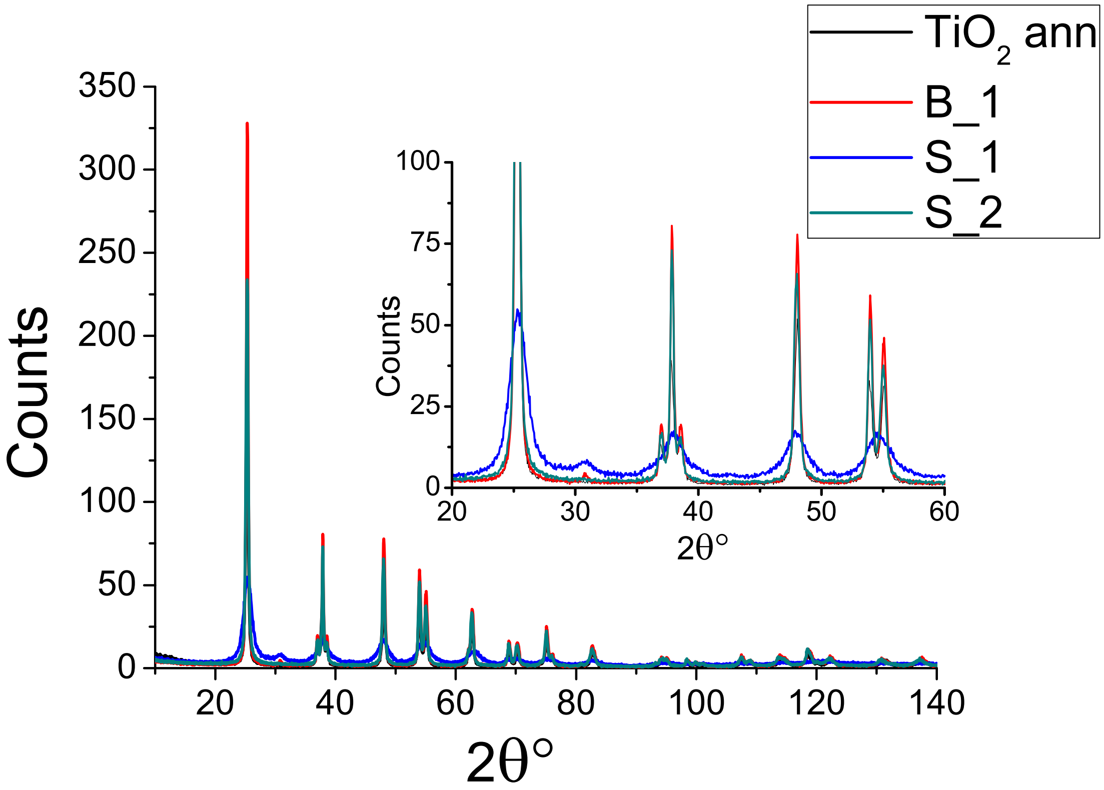

Figure 53: XRD patterns of the samples B_1, S_1 and S_2. The three samples are compared with a reference sample of titania annealed at 500°C for 1h. All the samples show typical anatase patterns but, the sample S_1 also shows a small peak at 30° typical of brookite phase.

In Fig.53 is showed the comparison of XRD pattern, while in Tab.14 are reported the values of calculated phase percentage and crystallite sizes. From XRD studies was possible to assert that all the proposed processes re-arrange amorphous TiO_2 into anatase evidencing the same phase presented in the corresponding literature.

Table14: Phase quantification and crystallite diameter calculated on XRD patterns.

	Anatase %	<L> (nm)	**Brookite %**	<L> (nm)
B_1	99	27	1	nd
S_1	86	4,7	14	2,3
S_2	100	18	-	-
TiO_2 ann.	100	22	-	-

Despite the reproducibility of the majority of the samples, S_1 showed a discrete amount of brookite mixed with anatase phase. In environmental condition, anatase was the most unstable polymorph, but usually was stable in nanoparticles bigger than 14nm[287]; S_1 nanoparticles were smaller than 14nm, and produced a mixture of the two phases. Sample S_2 showed greater anatase amount, but also presented greater crystallite size. Similar results were showed by B_1. Considering crystallites volume and anatase%, the greatest anatase amount was obtained by samples with bigger crystallites. This relationship was in agreement with the study of Zhang et al[287]. S_1 showed the lowest crystallite dimension in comparison with the other samples. In conclusion, considering XRD information, sample S_1 was the best sample because the process could produce the smallest crystallites of the set. So, considering XRD analysis, hydrothermal treatment represented by the sample S_1 could be the best candidate to treat an amorphous $NTiO_2$ loaded with CDs, and to produce enhanced photocatalytic materials.

Once crystalline phase was defined, and the production of anatase with hydrothermal treatment was stated, the samples were morphologically characterized.

Morphological characterization: TEM imaging

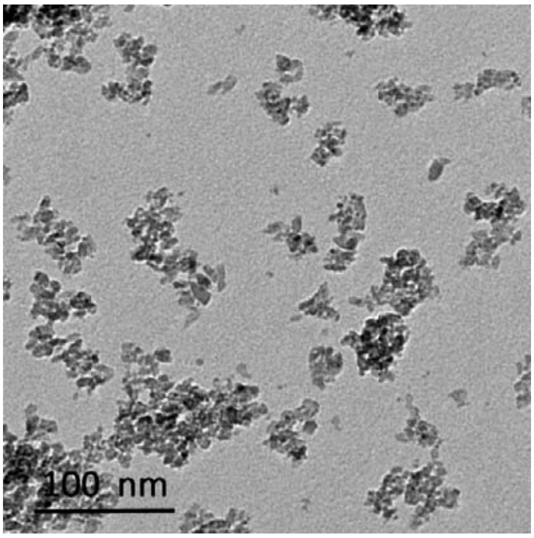

A

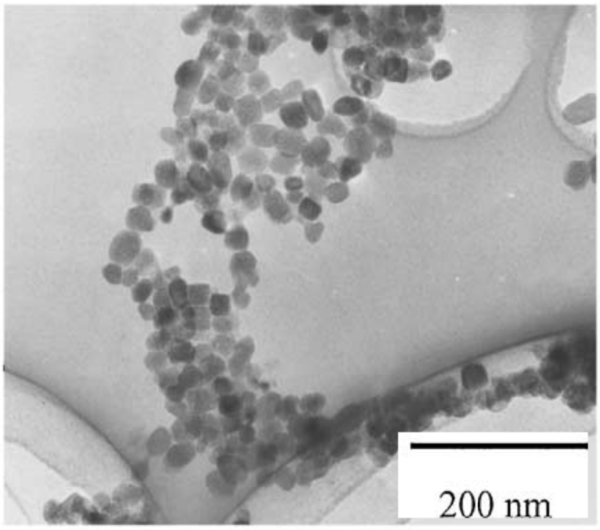

B

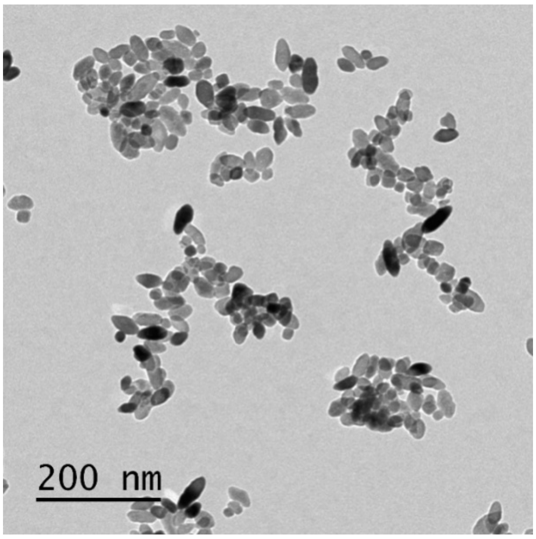

C

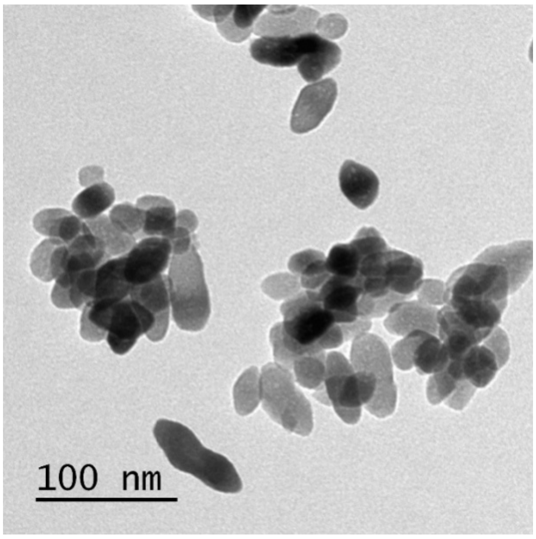

D

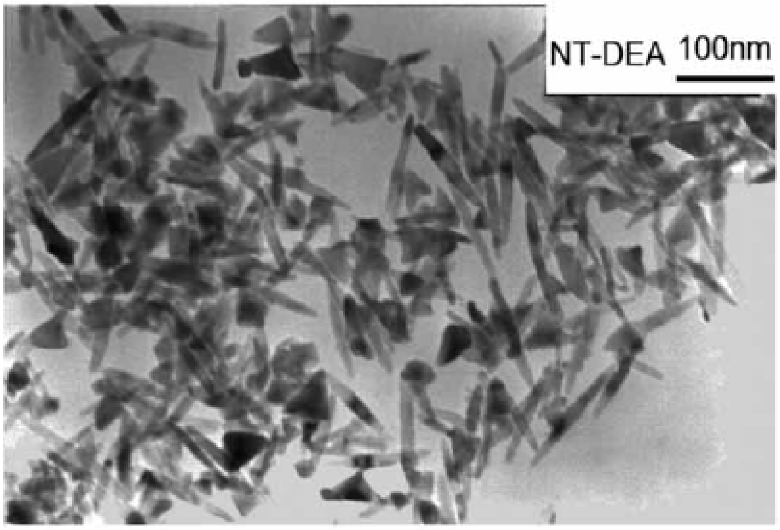

E

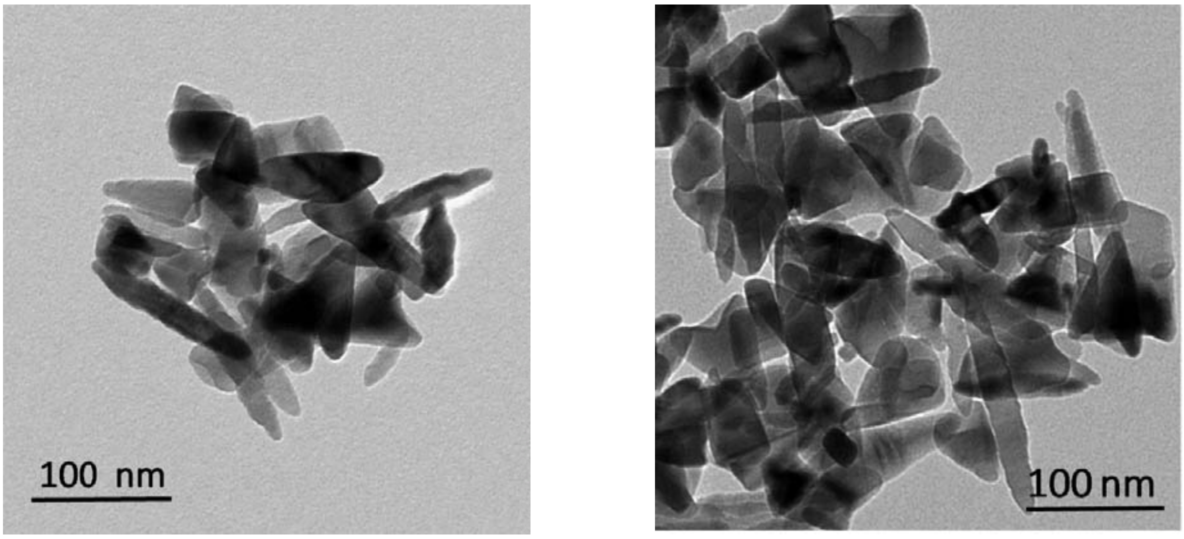

F **G**

Figure 54: Morphological study of the selected hydrothermal processes. The shapes and dimensions of the reproduced samples are compared with measurements reported in the corresponding literature. A) TEM image of the synthesized sample S_1. In the corresponding work of Sugimoto et al. there are no TEM or SEM image to compare with the sample. B) TEM image of TiO_2fromJournal of Colloid and Interface Science 259 (2003) 43–52, where S_2 was studied. C) and D) Tem images of titania nanoparticles of the sample S_2. E) TEM image of $NTiO_2$from Environmental Technology34 (2013) 2939-2949, corresponding to the sample B_1. F) and G) TEM images of the samples B_1 synthesized for the comparison of the treating processes.

TEM of S_1 is showed in Fig.54A. Even if the reference paper didn't report any TEM analysis, the micrographs of S_1 sample could be useful to compare its morphology with the morphology of the other two samples. S_1 was composed by a not aggregate material. The particles detected showed an irregular shape and a size distribution from 6nm to 10nm. In Fig. 54 B) TEM image of the sample S_2 showed nanoparticles of 30 nm with a smooth rhomboidal shape with rounded angles. S_2, showed in Fig.54C and 54D presented bigger particles (80nm), formed by the aggregation of two smaller particles. The S_2 particles were smooth, with blunted angles and, in comparison with the micrographs shown in literature, showed rhomboidal shape. In Fig.54 E) TEM image of sample B_1 showed well-dispersed particles, composed mostly by spindle-like particles with an average length of 100nm and with a small fraction of triangular nanoparticles of 50nm. B_1 showed in Fig. 54 F) and G) still showed spindle-like and triangular nanoparticles of 80nm and of 120nm respectively.

Concerning the comparison with literature, the shape of S_2 and B_1 was very similar even though there were few difference in the size. This could be due to the difficult repeatability that commonly characterize nano materials synthesis. Despite that, the reproducibility could be considered good and satisfactory.

Once morphological comparison was performed, and a good repeatability with the literature was stated, photocatalytic activity was studied.

Photocatalytic Activity:

In order to define the best hydrothermal treatment among S_1, S_2 and B_1 samples, photocatalityc degradation of methyl orange under visible light was compared with reference material such as TiO_2 ann., $NTiO_2$ ann., TiO_2 comm. and P25. The photocatalytic activity is showed in Fig.55.

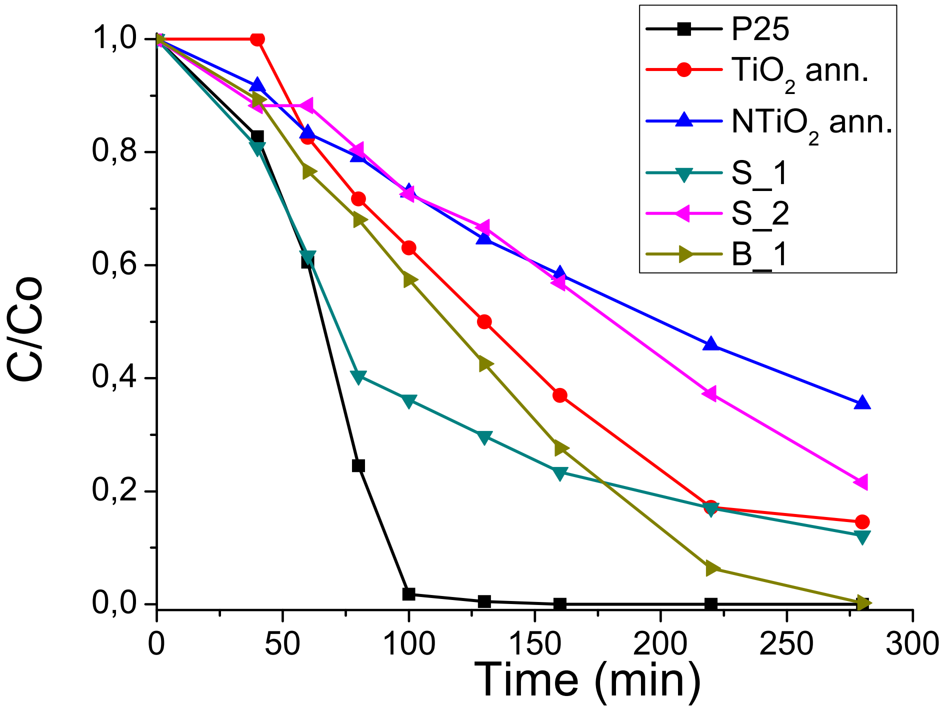

Figure 55: Photocatalityc activity of P25, TiO_2ann., $NTiO_2$ann., B_1, S_1 and S_2

From the comparison of the photocatalytic activity reported in Fig.55, P25 resulted the best systems. Degradation of methyl orange confirmed that annealed samples as TiO_2 ann. and $NTiO_2$ ann. had better activities than the samples treated with hydrothermal processes. Considering only the samples produced by hydrothermal procedure, sample B_1 showed the best activity, while sample S_2 showed the worst activity.

After the definition of the photocatalytic activity, sample bandgap was studied.

Bandgap measurement:

For the determination of the quality of a photocatalyst, bandgap was one of the most important parameter. In Fig.56 and Tab.15 are presented the Tauc plot and the calculated bandgap. Tauc plots and bandgap values of the reference materials were compared with the S_1, S_2 and B_1 samples.

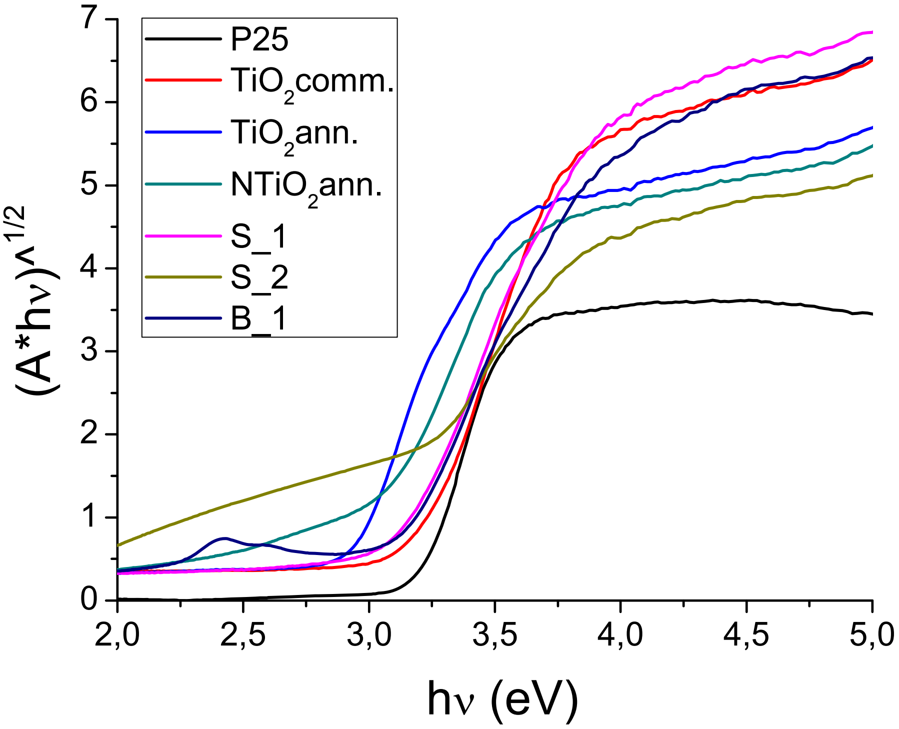

Figure 56: Tauc plot of the reference material and of the synthesized blanks.

For a better comparison, Tab.15 shows bandgap values calculated from the Tauc plot in Fig.57. Considering bandgap values of reference materials, P25 and TiO_2 comm. showed the same value reported in literature. The conformity between literature and experimental results, determined the validity of the bandgap study. TiO_2 ann. and $NTiO_2$ ann. reached similar bandgap values. TiO_2 ann. showed lower bandgap than expected, probably due to a great number of defects that the annealing process didn't removed. Indeed defects could interfere with the bandgap optical determination due to their disposition under the conduction band. The low bandgap value of $NTiO_2$ ann. could arise from the presence of nitrogen doping in the lattice, which could introduce an intragap layer. Considering bandgap values of re-synthesized samples, S_1 and B_1 were similar, while S_2 showed the lowest value. Also for sample S_1 and S_2, the presence of defect not removed by the hydrothermal process could reduce the gap. Both of the nitrogen doping and the presence of defects may reduce B_1 value.

Table 15: Calculated Bandgap values of all the reference and re-synthesized materials.

Sample	P25	TiO_2	TiO_2 ann.	$NTiO_2$ ann.	S_1	S_2	B_1

		comm.					
Bandgap (eV)	3,1	3,2	2,8	2,9	3,0	2,8	3,0

In this study , suitable hydrothermal processes were selected to produce nano-sized anatase. At this purpose three different hydrothermal synthesis were compared from the physical and photocatalytic point of view. Despite the formation of 14% of brookite, the sample S_1 produced smaller nanoparticles than the others. Comparing the bandgap, the most suitable sample to work under solar radiation was the sample S_2, but its photocatalytic activity resulted weaker than the other samples. In conclusion, sample S_1 was chosen as prototype of the hydrothermal synthesis. As demonstrated in the studies on the morphology and on the photocatalytic activity, hydrothermal process proposed through the S_1 sample produced nano-sized and active photocatalytic material. So, this process could perform similar results starting from different amorphous material.

4.2.2 -Crystal phase process optimization

In the last decades, $NTiO_2$ was widely studied and synthesized with several methods[250,288,289,202]. Our aim was to produce an amorphous material doped with nitrogen able to containing, at the same time, the right amount of CDs. Many of the published papers deal with: *i*) annealing processes of amorphous titania oxides in nitrogen rich atmosphere. *ii*) The annealing of amorphous titanium oxide produced in presence of amines. Very few articles foresaw to insert nitrogen during hydrolysis and condensation of the titanium precursor[290,282,246]. According to the last approach and in order to obtain the anatase phase, we had chosen the synthesis proposed by Wang etal.[282]. In this paragraphs synthesis, optimization and characterization of the $NTiO_2$ to host CDs were studied.

To define the best hydrothermal treatment, X-ray diffraction patterns of the treated sample were compared. Moreover, as indicated by Darzi et al.[291], to check the presence of nitrogen in to the crystal lattice FTIR was used.

The synthesized W_1 sample undergone a hydrothermal treatment proposed by the S_1 sample, producing the WS_1 sample.

The XRD patterns reported in Fig.57 showed that all the peaks corresponded to anatase, except a small peak at 30° which corresponded to the main peak of brookite. Therefore, we could conclude that the S_1 hydrothermal treatment on W_1 permitted to obtain crystalline anatase in conditions able to preserve CDs.

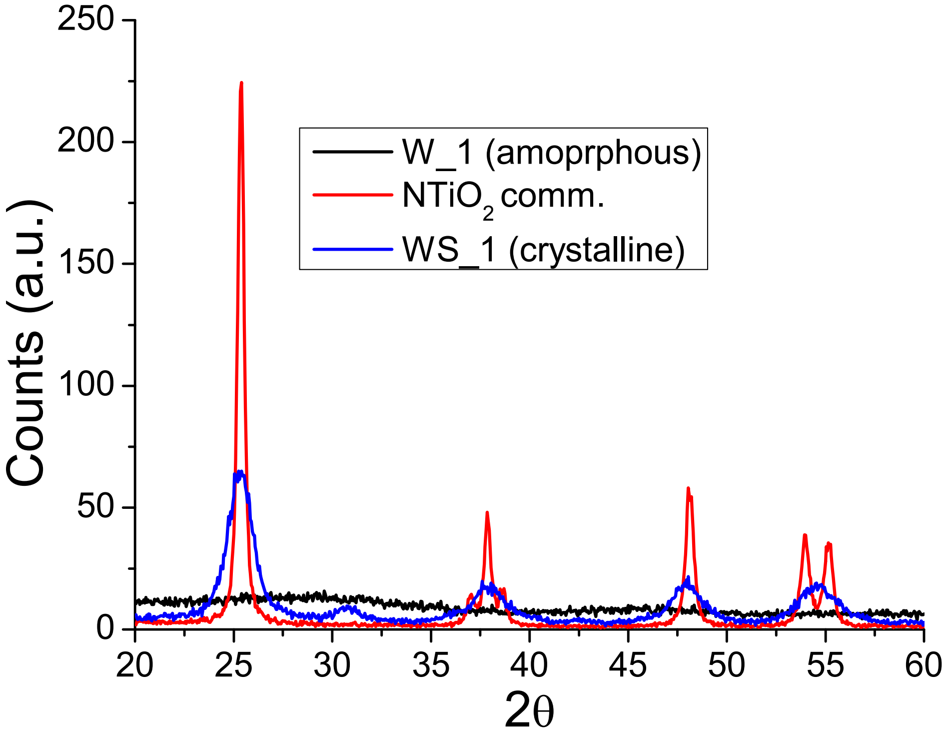

Figure 57: X-Ray diffraction of W_1 and the hydrothermally treated WS_1, compared with the reference NTiO$_2$ ann.

In order to check the presence of nitrogen before and after hydrothermal treatment in Fig. 58,FTIR of sample W_1 and WS_1 were compared. In the 3700cm^{-1}-3000 cm^{-1} region all peaks were assigned to the stretching vibration of water and OH species[292]. The bands for Ti-O and Ti-O-Ti bonds were visible in the 800 cm^{-1} – 400 cm^{-1} area[292,293]. In some publication, where nitrogen doped TiO$_2$ was produced in wet processes, the presence of nitrite and hyponitrite was also evidenced[294]. In our samples, there was no evidence of peaks at 1387 cm^{-1}, 1104 cm^{-1} and 1060 cm^{-1} corresponding to hyponitrite. Similar results were reached for the presence of nitrite at 1450 cm^{-1}, 1260 cm^{-1} and 1160 cm^{-1}. Darzi et al.[294] proposed some FTIR studies of nitrogen doping in TiO$_2$ produced with wet processes. They proposed that peaks comprised between 1500 cm^{-1} and 1250 cm^{-1} could be attributed to the presence of nitrogen embedded in the TiO$_2$ matrix. Both samples, proposed in Fig.59 showed the mentioned peaks. Therefore, the hydrothermal treatment maintained the nitrogen doping in the sample WS_1.

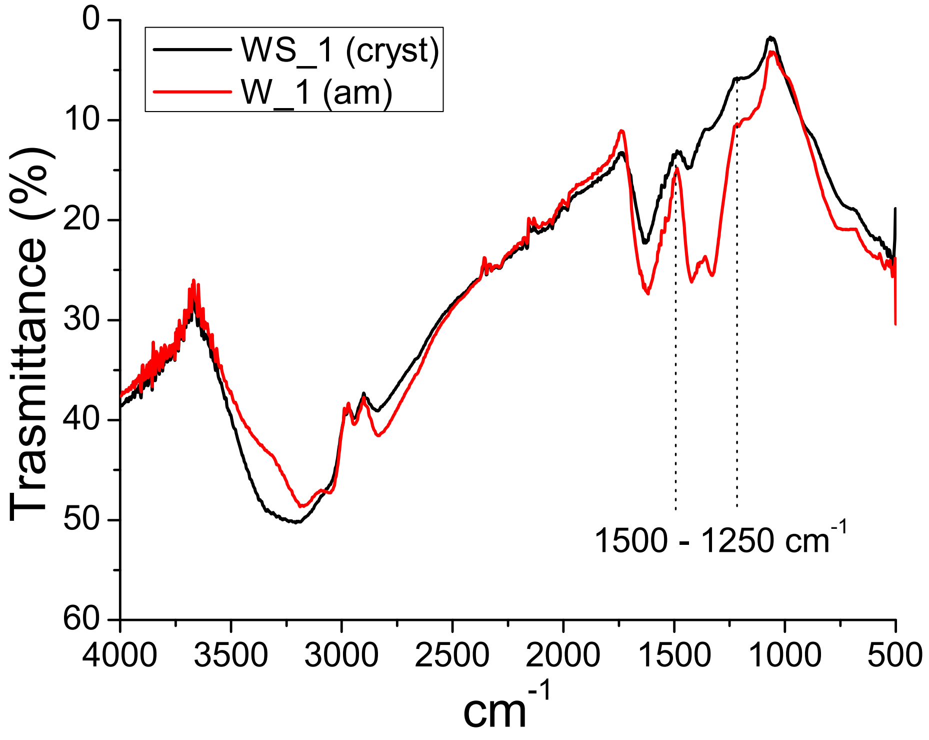

Figure 58: As indicated by Darzi et al., peaks comprised between 1500 cm^{-1} *and 1250 cm* $^{-1}$*could be attributed to the presence of nitrogen embedded in the host* TiO_2 *matrix.*

4.2.2.1-Temperature effect

After NH_4OH addition, a fast increase of the reactor temperature was observed and the system warmed up at a variable temperature comprised between 65° and 70°C. Since the temperature was an important parameter that must be controlled to obtain reproducible samples, a study focused on the definition of the best process temperature was performed. Each sample synthesized at different temperatures was hydrothermally treated following the procedure S_1. The reaction was performed in a jacketed vessel connected to a thermostatic bath; the temperature of the thermostatic bath was changed from 45°C to 65°C.

In order to compare the produced samples, bandgap values were calculated on the Tauc plot showed in Fig.69 and in Tab.16.

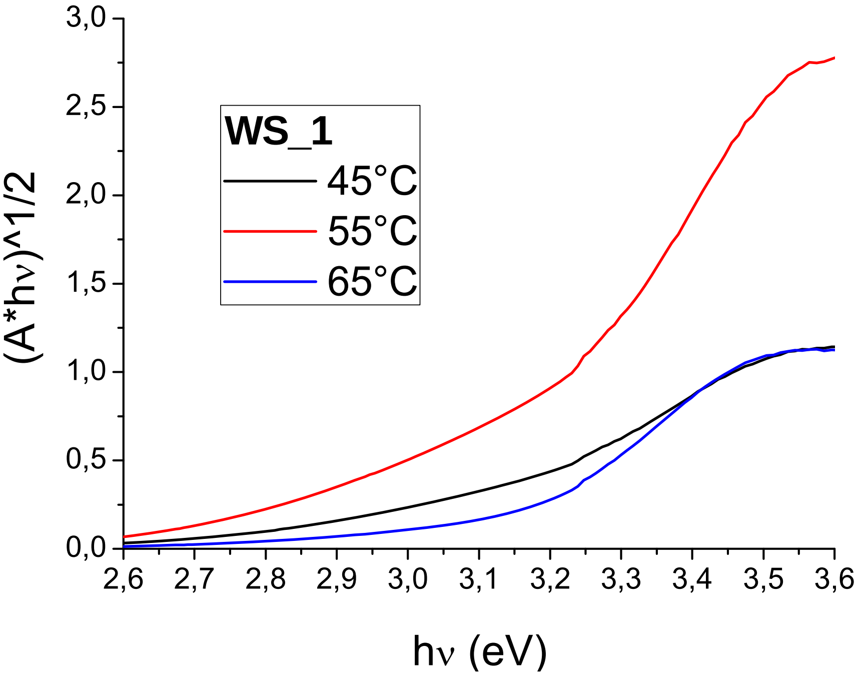

Figure59: Tauc plot of WS_1 samples synthesized at several temperatures; the two dot lines defined the linear range used to calculate the linear fit for the optical bandgap determination.

Best sample showed the lowest bandgap, which was related to the high nitrogen doping in the lattice. The linear interval used to calculate the bandgap was comprised between 3,24 and 3,43 eV.

Table 16: Calculation of the optical bandgap of each samples synthesized, and definition of the best synthesis temperature.

Treating T°	Linear fit	Y=0	Bandgap
45°C	Y= 2,32X - 7,04	X= 7,04/2,32	3,03 eV
55°C	Y= 5,79X - 17,76	X= 17,76/5,79	3,06 eV
65°C	Y= 3,17X - 9,92	X= 9,92/3,17	3,12 eV

Bandgaps reported in Tab.16, calculated on the plot represented in Fig.60, showed that synthesis at 45°C produced a sample with lower bandgap. In order to contrast the increasing temperature, and to maintain the right temperature during the process, all the synthesis was synthesized at 45°C

After the best temperature definition, the optical bandgap on WS_1 sample synthesized at 45° was measured. In order to check the quality of the instrumental apparatus, the bandgap of the sample SW_1 was compared with references samples TiO_2comm. (3,2 eV) and the P25 [295] (3,1 eV).

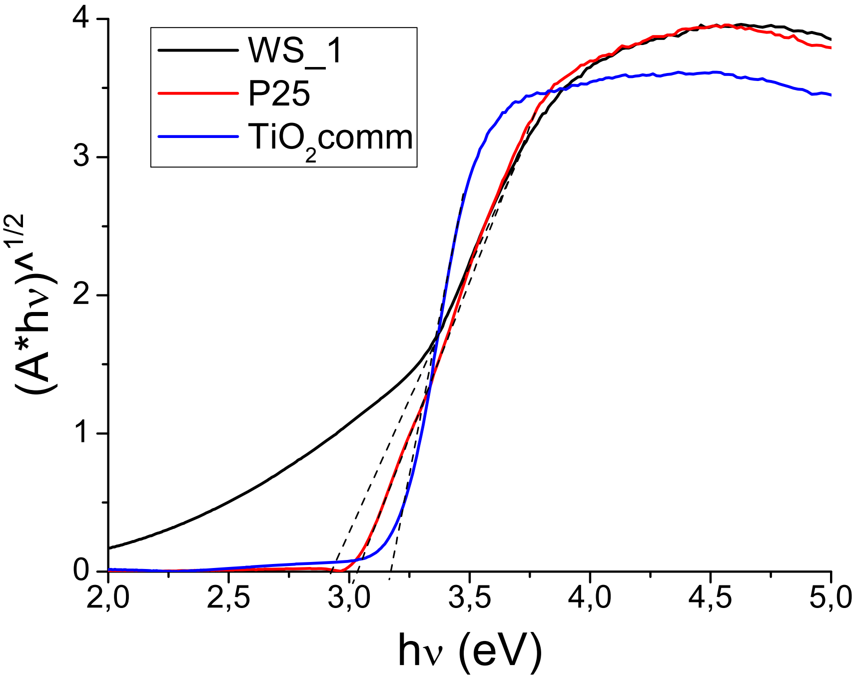

Figure 60: Tauc plot of commercial anatase TiO$_2$, Degussa P25 and a sample of WS_1. TiO$_2$comm and P25 are taken as reference in order to check the good response of the analysis.

In Fig. 60, the Tauc plot of the sample WS_1 showed some differences with the two commercial materials. Tauc plot of P25 and TiO$_2$ comm. presented well defined transition, while WS_1 showed a decreasing trend at lower energy values. Reference materials bandgap, which were reported in Tab.17, matched with values reported in literature. Therefore, we could assume that reflectance measurement were conducted in the right manner, and the calculated value for sample WS_1 was reliable.

Table 17: Calculation of the optical bandgap of each samples synthesized in order to define the best synthesis temperature.

Sample	Linear fit	Y=0	Optical bandgap	Reference Band Gap
P25	Y= 4,94x – 15,12	X= 15,12 / 4,94	3,06 eV	3,1 eV
TiO$_2$comm	Y= 9,66x – 30,84	X= 30,84 / 9,66	3,19eV	3,2 eV
WS_1	Y= 4,25x - 12,43	X= 12,43 / 4,25	2,92 eV	from 3,0 eV to 2,6 eV

To define the quality of WS_1, photocatalytic activity was performed under simulated solar light radiation. Here, the ability of the photocatalyst to degrade sacrificial material was plotted against the time of light exposition. As showed in the plot in Fig.61, WS_1 didn't produce any photocatalytic activity under solar light simulation. At this purpose, in Fig.57, wide X-Ray diffraction showed the baseline of the pattern. The baseline indicated the presence of a large amount of amorphous material. Since the photocatalityc activity was related to crystallinity, we changed hydrothermal process parameters in order to increase the crystallinity.

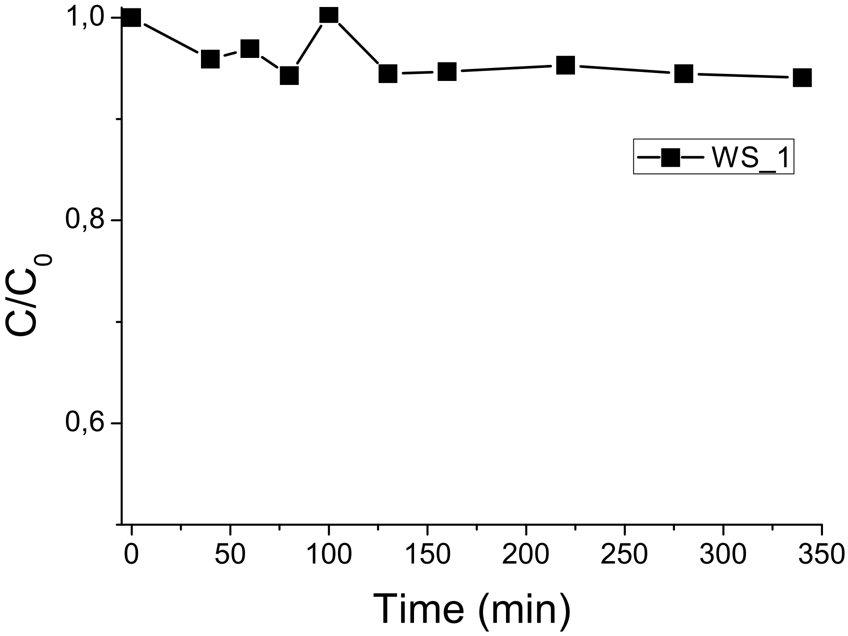

Figure 61: Photocatalityc degradation of methyl orange under visible light realized by the nitrogen doped titanium dioxide hydrothermally treated with S_1.

As summary of this paragraph, we can conclude that the sample WS_1 didn't possess enough crystallinity to perform good photocatalytic activity. At this purpose, optimization of the hydrothermal treatment is needed.

4.2.3- Hydrothermal process of the nitrogen doped titanium dioxide

XRD pattern of WS_1 sample was compared with the TiO_2 comm. and amorphous W_1. The wide halo presented in the WS_1 XRD pattern indicated the presence of a large amount of amorphous phase. Since the photocatalityc activity of a material was related to the crystallinity, we changed the hydrothermal process parameters in order to increase sample crystallinity. The hydrothermal process parameters were: i) the amount of amorphous material treated per unit volume; ii) ionic strength of the treating solution; iii) temperature of the process and iv) time of the process. We didn't change the pH of the solution because Sugimoto et al.[252] already defined the best pH values that allow the maximum conversion of amorphous gel in to anatase. The samples were labeled according to the parameters used during the process. WS_1 represented the synthesis of W_1 with the hydrothermal treatment of S_1. In a typical labeling, as for example WS_10_01_24_100, the first number represented the amount of amorphous material treated on milliliter of treating solution (mg/ml); the second number represented the ionic strength of the treating solution (mol/L); the third number represented the treating temperature during the hydrothermal treatment and, finally, the last number indicated the time of the treating process. The Tab. 18 reports all the parameters related to the percentage of the anatase phase produced during the hydrothermal treatment. Furthermore, amorphous W_1 and a sample of an annealed TiO_2 had been added to the table. W_1 was characterized after washing and without further treatment, while the other sample was annealed at 500°C for 2h. In the Tab.18 parameters of the hydrothermal process used for each sample are showed.

Table18: Treatment parameters optimization, and the resulting percentage of anatase phase obtained treating the amorphous nitrogen doped titanium dioxide.

Sample	**Amorph. Mat/ treat. Solution (mg/ml)**	**Ionic Strength (mol/L)**	**Treating T° (C°)**	**Treating time (h)**	**% Anatase**	**Diameter Crystallite (nm)**
W_1	- - -	- - -	- - -	- - -	0	- - -
WS_10_01_24_100	10	0,1	100	24	42	4,3
WS_5_01_24_100	5	0,1	100	24	47	5,5
WS_2_01_24_100	2	0,1	100	24	73	6,1
WS_2_1_24_100	2	1	100	24	84	4,7
WS_2_2_24_100	2	2	100	24	95	6,1
WS_2_2_24_150	2	2	150	24	97	6,9
WS_2_2_24_200	2	2	200	24	98	10,4
WS_2_2_15_200	2	2	200	15	98	9,2
WS_2_2_8_200	2	2	200	8	98	9,6
Annealed	- - -	- - -	- - -	- - -	100	- - -

In Fig. 62 patterns comparison of the most representative samples are showed. When crystallinity increased, patterns were more defined. Sample WS_10_01_24_100 showed high amount of amorphous phase, and both the low definition of the peaks and the amorphous halos indicated a sample with low crystallinity. Optimization of hydrothermal parameters, such as the sample dilution in the treating solution, the increase of the ionic strength solution and the temperature, produced higher crystalline phase and sharper peaks.

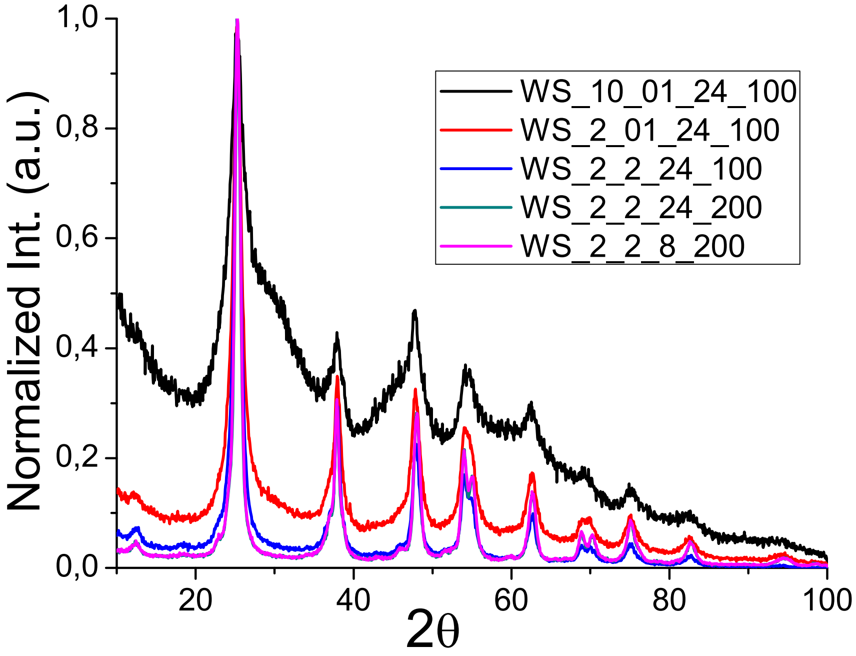

Figure 62: X-ray diffraction patterns of the more representative samples related to the optimization of the hydrothermal process. Increasing ionic strength, processing temperature, treatments time and reducing the amount of treated material, enhance the crystallinity.

The histogram presented in Fig. 63 summarizes the amount of crystallinity in all the samples. The increase of crystallinity was related to the amount of anatase phase determined for each sample. With respect to the analysis of the XRD patterns, in this histogram was easier to notice the crystallinity growth and the formation of a plateau. The plateau was reached when ionic strength was increased from 1mol/L to 2mol/L. The temperature variation restricted the crystallinity development. After temperature variation, was possible to reduce the treating time from 24h to 8h. Despite the optimization, the 100% of crystallinity was not reached, but the 98%.

In conclusion, WS_2_2_8_200 was the sample with the best crystallinity obtained with the best conditions.

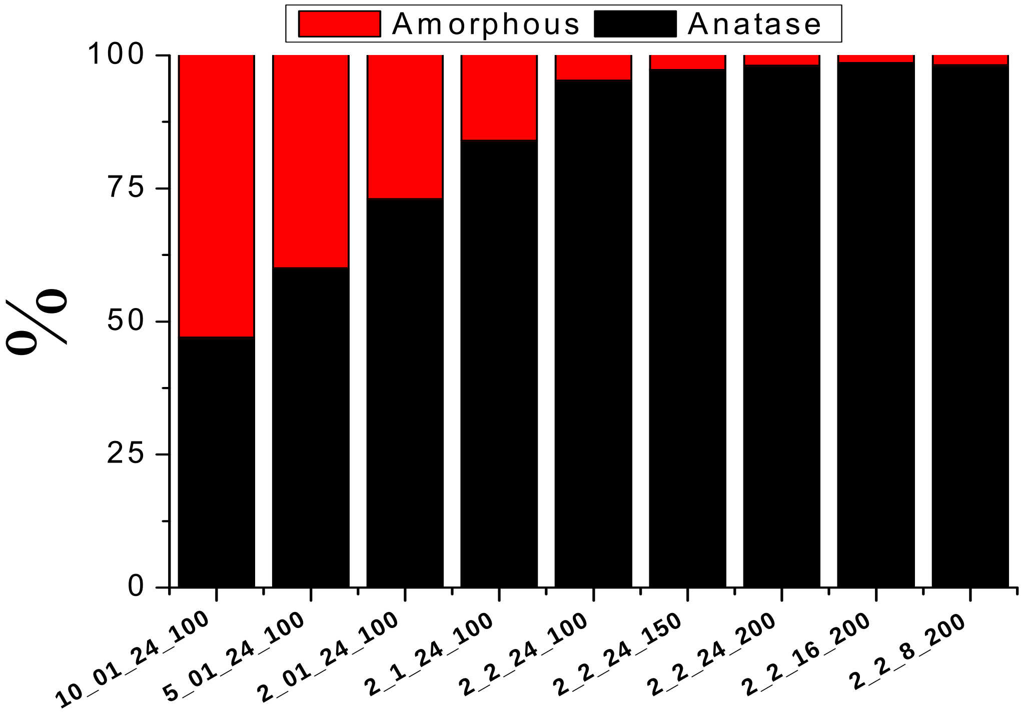

Figure 63: Histogram showing the increase of crystallinity thanks to the optimization of the hydrothermal process. The optimization started from parameters indicated by Sugimoto et al. with crystallinity of 42% and increase until 98% after optimization.

To understand the effects of the hydrothermal process, and how the dissolution and re-crystallization can change the sample structure, SEM analysis was performed. At this purpose, amorphous W_1 was compared with WS_1 and WS_2_2_8_200.

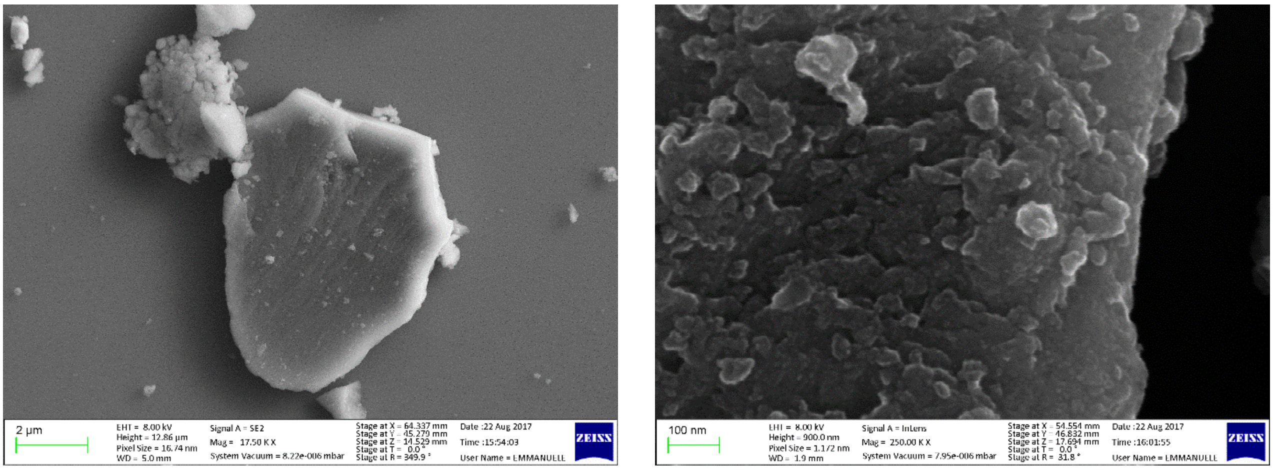

A **B**

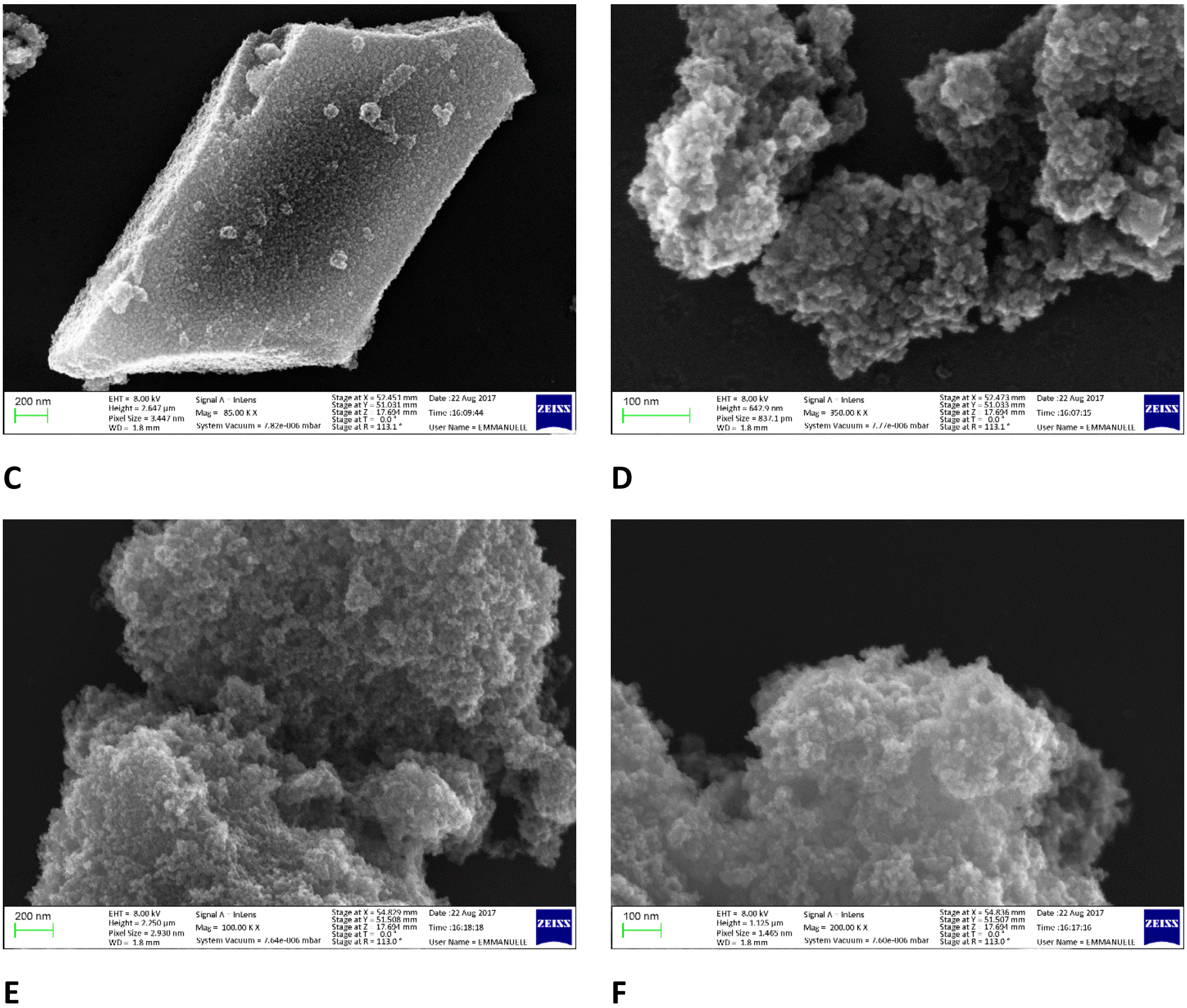

Figure 64 morphological study of A) and B) amorphous W1, C) and D) WS_1, while in E) and F) WS_2_2_8_200 is showed.

In the Fig. 64A and 64B, the amorphous nitrogen doped TiO_2 (W_1) presented a homogeneous aspect. The sample showed compact body, without substructures. As it is showed in the next images, hydrothermal treatment was able to change radically the shape and the morphology of the sample. If the treated WS_1 maintained a bulk shape (fig.64C), at greater magnification (Fig.64D) was noticeable the dissolution and re-crystallization effect produced during the hydrothermal treatment. A great number of nano-sized globular particles, with an average size of 18±2nm constituted the bulk material. The globular particles were strongly bonded each other. A strong sonication was not able to disaggregate the solid in to particles. In Fig. 64 E and F, sample WS_2_2_8_200 showed characteristics very similar to the WS_1. The solid was still composed by small globular particles, with an average size of 12±1nm. From the size comparison of the globular particle, was noticeable how increasing crystallinity is related with smaller nanoparticles.

From the morphological analysis of amorphous and differently treated samples, was noticeable how hydrothermal process obtained crystalline material. The dissolution and re-crystallization process evolving in hydrothermal treatment produced small and crystalline particles which group together in bulk materials. Changing hydrothermal process parameters to produce more crystalline material led a production of smaller particles.

In order to explain the behavior of the different samples, the photocatalytic activity of WS_2_2_8_200 was compared with WS_10_01_24_100. To evidence the real improvement of the optimized hydrothermal treatment, photocatalytic activity of sample S_1 and $NTiO_2$ ann. were added for comparison. Photocatalytic study conducted on different hydrothermally treated samples, compared with the photocatalytic activity of amorphous S_1 and reference $NTiO_2$ann. have been showed in Fig.65.

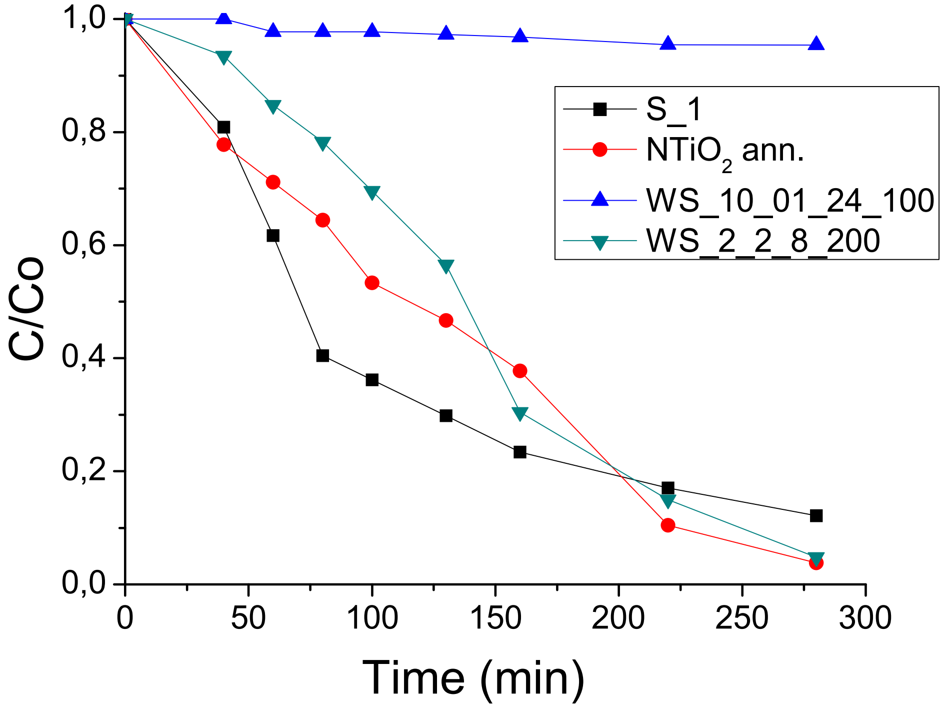

Figure 65: Photocatalityc activity of WS_10_01_24_100 and WS_2_2_8_200 against S_1 and reference $NTiO_2$ann.

We would like to remember that sample S_1 and sample WS_10_01_24_100 were processed with the same hydrothermal treatment, but they were synthesized with different path. Moreover, WS_10_01_24_100 was doped with nitrogen, it was orange colored and it was able to absorb more visible light instead of the white and un-doped S_1. Despite this feature, WS_10_01_24_100 showed a lower photocatalytic activity than S_1. Optimizing the hydrothermal process permited to produce a system such as the sample WS_2_2_8_200, which showed similar photocatalytic activity to S_1. Despite the optimization of the hydrothermal process, the reference sample $NTiO_2$ ann. still possessed the best photocatalytic activity.

The reading of the Tauc plot represented in Fig.66 must consider two factors: the slope of the linear transition of the absorption, used to calculate the bandgap; and the adsorption tail in visible region. If W_1 showed small bandgap and great absorption in the visible range (hv> 3,26eV), the increase of crystallinity in WS_10-01-24-100 reduced the absorption. WS_10-01-24-100 still showed absorption in visible light and an appreciable reduced bandgap, but the WS_2-2-24-200 and WS_2-2-8-200 showed an increased bandgap. This increment was associated to an absorbance loss in visible region, due to a loss of nitrogen. Indeed, these two samples showed a behavior typical of an un-doped TiO_2.

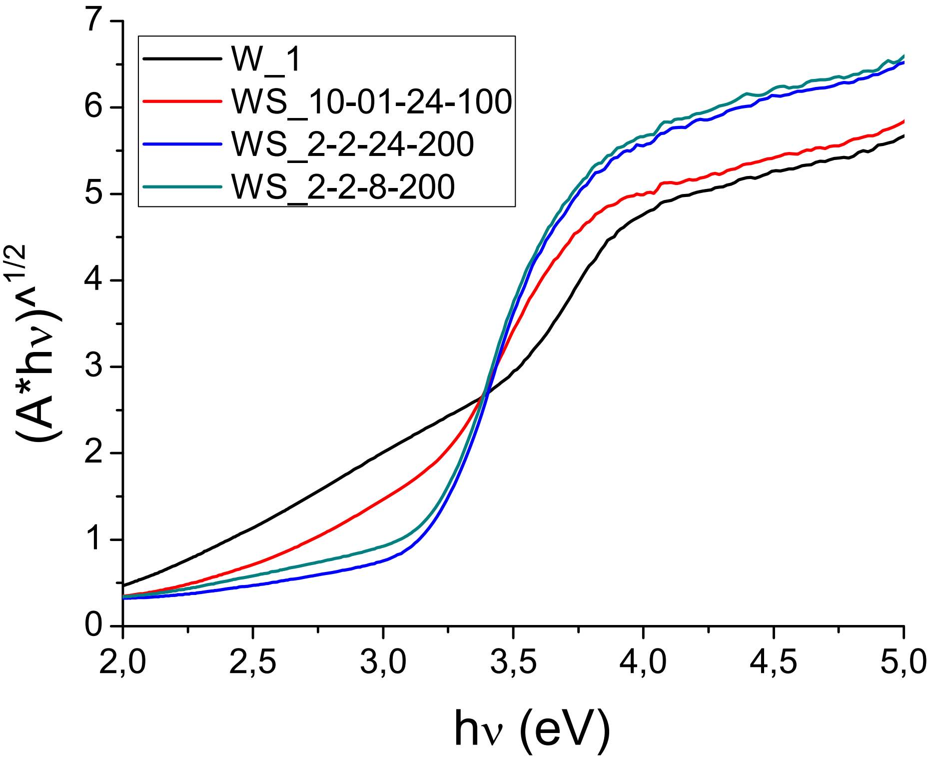

Figure 66: Comparison of Tauc plot of different optimization step. Starting from the amorphous material, the optimization of the hydrothermal process reduce the amount of nitrogen and, at the same time, reduce the ability to absorb in visible region and increase the bandgap.

In Tab.19 bandgap comparison of the most representative samples of the hydrothermal treatment optimization have been showed. As underlined for the comparison of the Tauc plot in Fig.66, the optimization produced a system with a bandgap typical of un-doped samples.

Table19: calculated bandgap of the most representative sample, synthesized during the optimization step.

Sample	W_1	WS_10-01-24-100	WS_2-2-24-200	WS_2-2-8-200
Bandgap (eV)	2,8	2,9	3,1	3,1

Hydrothermal treatment permitted to improve the crystallinity, but also produced a narrower bandgap. To understand if the amount of doping nitrogen depended on the treating parameters, it was necessary to analyze samples elemental composition.

To define if the bandgap narrowing was due to the nitrogen loss, elemental analysis was performed on the most representative samples obtained by the optimization process. In Fig. 67 the $\%_w$ of carbon, hydrogen and nitrogen of these samples have been showed.

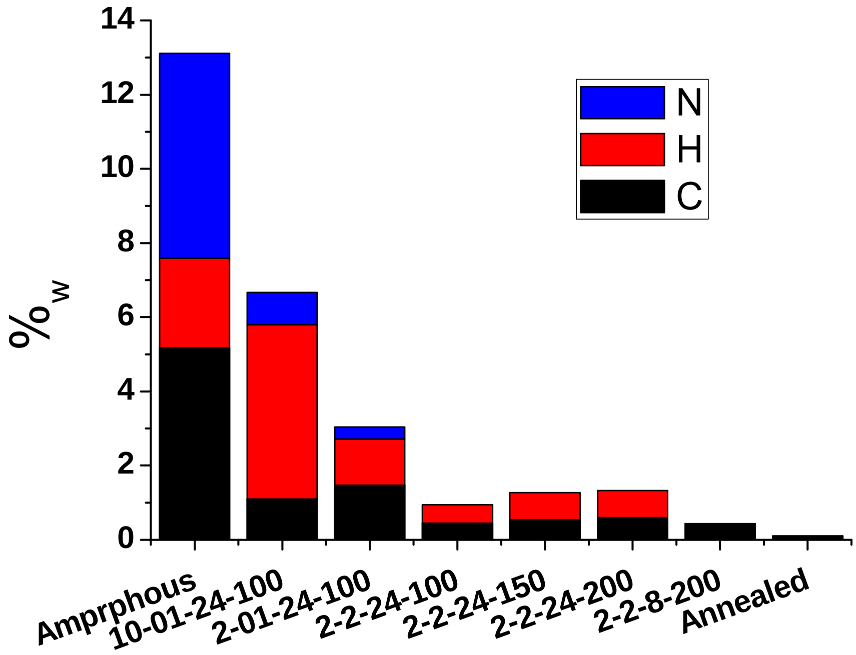

Figure 67: Histogram representing the $\%_w$ of carbon, hydrogen and nitrogen measured for the most representative samples of the optimization process. After the hydrothermal treatment, the amount of nitrogen falls and completely disappear.

W_1 posses the 5,52$\%_w$ of nitrogen, but in WS_10_01_24_100 the nitrogen amount falled at 0,87$\%_w$. Reducing the amount of treated amorphous material from 10mg/ml to 2mg/ml the $\%_w$ of nitrogen decreased to 0,32$\%_w$. Finally, the increase of the treating solution concentration, represented by WS_2_2_24_100, determined the complete nitrogen removal. From the elemental analysis emerged also that the annealing treatment at 500°C for 2h removed all the nitrogen present in the material.

In Fig.68, the crystalline phase fraction have been compared with the nitrogen $\%_w$ for the most representative samples.

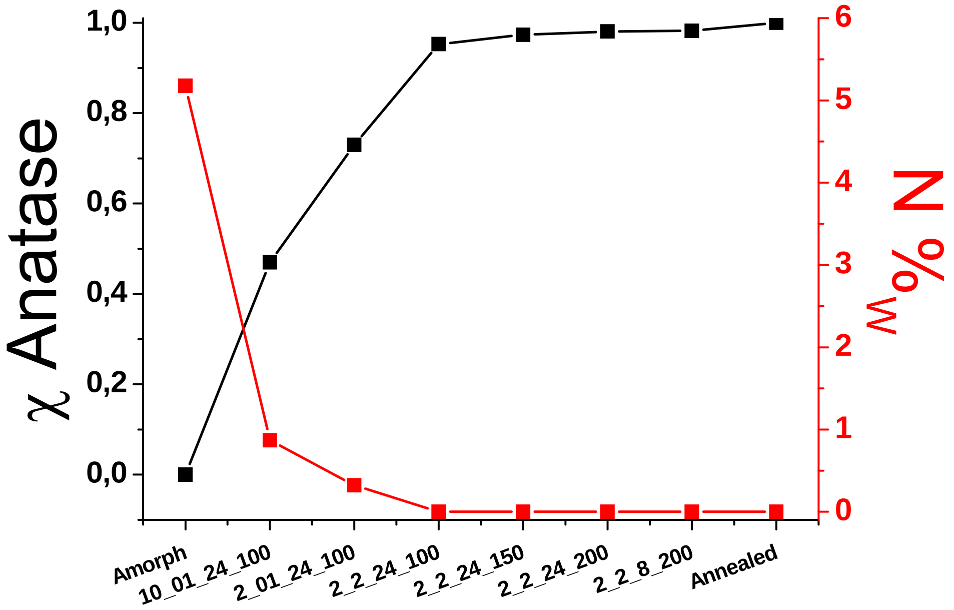

Figure 68: comparison of the crystalline phase fraction with the nitrogen %won the most representative samples of the hydrothermal process optimization.

As it is showed in the Fig.68, W_1 possessed $5{,}18\%_w$ of nitrogen and, obviously, no crystalline phase. When the material was treated under a mild hydrothermal condition it was possible to obtain the 47% of crystalline phase with the $0{,}87\%_w$ of nitrogen. Reducing the amorphous material an additional increase of the crystallinity was reached, but more nitrogen was lost. The 73% of crystallinity matched with an amount of nitrogen equal to $0{,}32\%_w$. Unlikely, appreciable amount of anatase was reached only when last nitrogen traces are lost. The increase of the concentration of the treatment solution from 0,1mol/L to 2mol/L led an increase of the crystallinity until 95%, but no nitrogen was detected.

4.2.4- Results

A procedure to obtain $NTiO_2$ to host CDs was investigated . At this purpose, the synthesis proposed by Wang et al. was adopted to produce $NTiO_2$. After synthesis definition, previously selected hydrothermal process was applied, followed by the determination with FTIR of the presence of nitrogen in the host lattice. Once confirmed the presence of nitrogen, the optimization of the amorphous $NTiO_2$ was carried out defining the best synthesis temperature, using material bandgap as discriminating factor. After that, the hydrothermal treatment optimization was conducted focusing on the production of the maximum fraction of crystalline anatase phase. The optimization progress was followed calculating the crystallinity on XRD patterns. Elemental analysis and photocatalityc activity were associated to their crystallinity for the most representative samples of the hydrothermal optimization. Despite these great improvements, all the intra-crystalline and inter-crystalline nitrogen was lost. The decrease of absorbance detected in Tauc plots could derive from the decrease of defects that produce absorbance, but certainly, they were due to the removal of the nitrogen from the crystal lattice. The suppression of the nitrogen from the material removed the absorption ability in visible range, as for the samples without nitrogen. The loss of the nitrogen content increased the bandgap from 2.9eV of the sample WS_1-10-01-24-100 to 3,1eV of the sample WS_1-2-2-8-200. The achievement of the 98% of crystalline phase was an important aspect, especially if obtained with alternative method than annealing processes. Despite the complete loss of nitrogen in the crystal lattice, this method produced a photoactive and crystalline material with conditions able to maintain unaltered CDs. In this way, during the synthesis could be possible to insert CDs in the matrix. So, the obtained composite amorphous material could be processed with the hydrothermal treatment instead of annealing. Synthesis and crystallization in presence of CDs avoided the impregnation, with the risk to lose them in the solution during the application of the photocatalytic material. If the process developed above didn't fit for the production of nitrogen doped titanium dioxide, it could be applied for un-doped titania loaded with CDs. These experiments were focused on the characterization of samples with different CDs loading and with different doped CDs. Not to be confuse with complex sample labels, WS_2_2_8_200 was labeled as WS_2.

4.3- Enhanced photocatalytic materials

As Described in Fig. 69, the aim of this part of the thesis was the study of the effect of selected CDs on TiO_2- based photocatalytic systems. At this purpose, WS_2@CDs samples were synthesized loading the best selected CDs on optimized WS_2 photocatalytic material.

During the WS_2 synthesis, defined amount of NCDs had been loaded in the amorphous material and reproducibility was studied with a focus on the sample bandgap. Successively, a study on CDs loading was performed. WS_2 samples loaded with different CDs% were characterized by their elemental analysis, photocatalytic activity and bandgap properties. Due to their low performances, WS_2-based samples was compared with a standard material loaded with CDs. This experiment allowed to define the real origin of the low quality of the sample: or the synthesis of the amorphous or the hydrothermal treatment. This experiment excluded CDs nature because their positive interaction with TiO_2 was widely described in literature.

The standard material loaded with CDs was synthesized and characterized with XRD, elemental analysis, SEM, optical bandgap and photocatalytic activity.

Finally photocatalytic activity studies were used to compare WS_2-based samples and the standard material loaded with CDs.

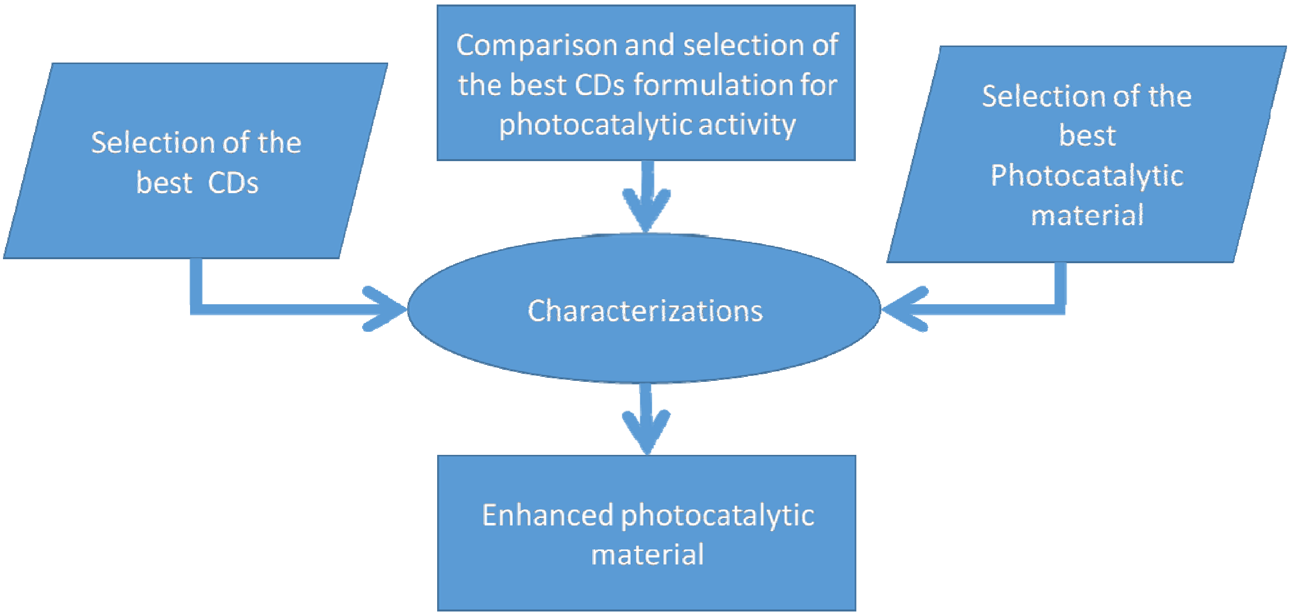

Figure 69:Scheme of the research topic investigated on the development of the best enhanced photocatalytic material.

4.3.1- Reproducibility

To study the CDs loading effect during the WS_2 synthesis, defined amounts of NCDs were added during the third step of the synthesis showed in Fig. 70. To the amorphous material, a theoretical percentage in weight equal to $0,01\%_w$; $0,1\%_w$ and $1\%_w$ was loaded. The right amount of NCDs was reached adding 10mg/ml NCDs suspension to the HNO_3 solution (Tab.18). All the synthesis were performed with optimized hydrothermal treatment.

With the aim to assess the reproducibility of the CDs loading, three synthesis of WS_2 with different loaded CDs were produced. To define if the addition of different amount of CDs could change the reliability to reproduce the material, optical bandgap was considered.

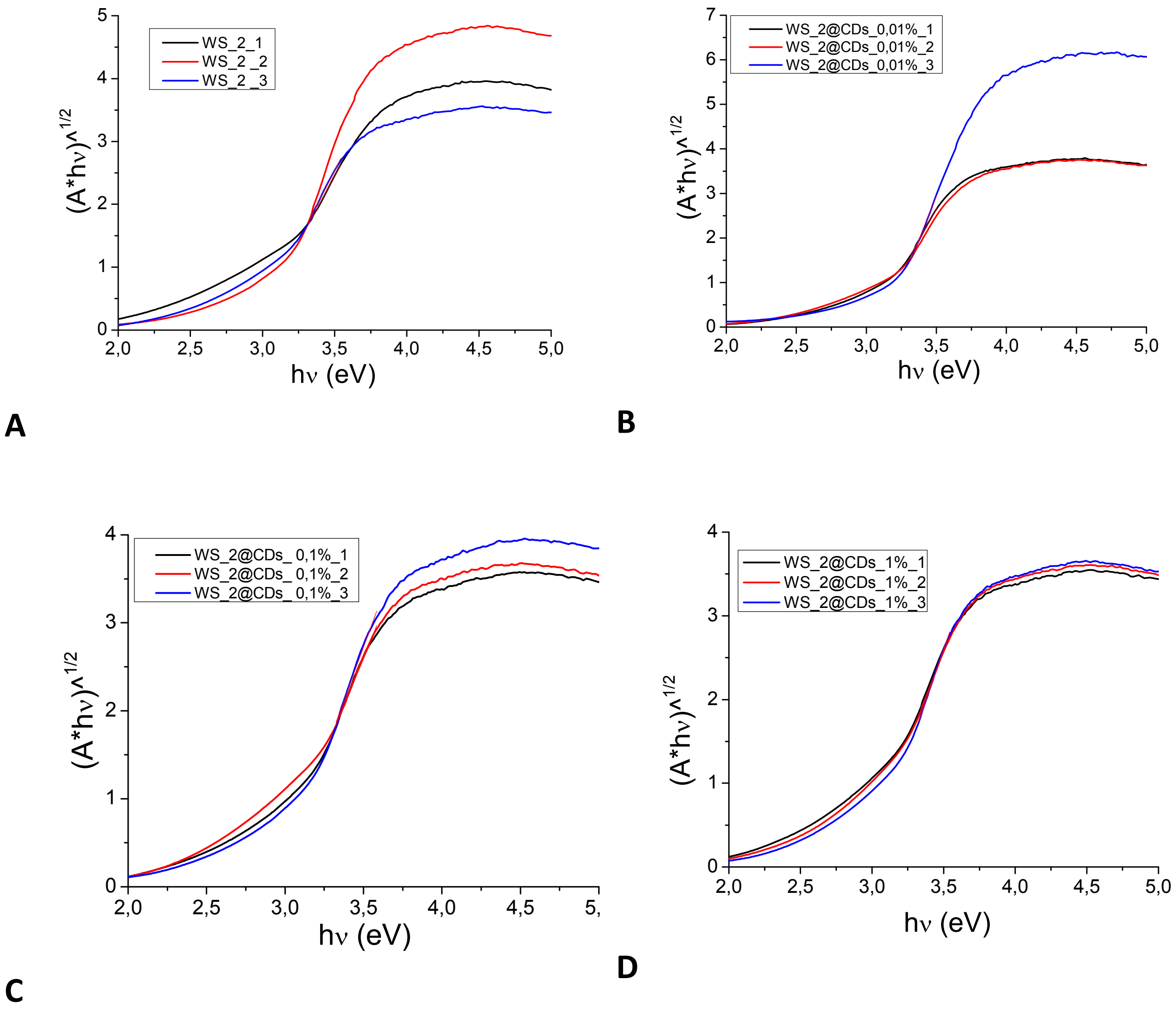

Figure 70: A) Tauc plot of the three repeated synthesis of WS_2. B) Tauc plot of the three repeated synthesis of WS_2 doped with the theoretical 0,01% in weight on NCDs. C) Tauc plot of the three repeated synthesis of WS_2 doped with the theoretical 0,1% in weight on NCDs. D) Tauc plot of the three-repeated synthesis of WS_2 doped with the theoretical 1% in weight on NCDs.

Fig. 70A showed the Tauc plot of three-repeated WS_2. It was noticeable how two of the three samples showed similar behavior. This difference was reported in the Tab. 20, where bandgaps of WS_2_1 and WS_2_3 were similar. Same consideration could be done for the three repeated WS_2 @CDs_0,01% in Fig. 70B. Considering Tauc plots in Fig. 70C and in Fig.70D, repeatability increased with CDs loading. In Tab.20, samples were presented with their associated linear fit and the calculated optical bandgap. For each series of repeated sample, semidispersion on bandgap was calculated.

Table20: Calculation of the optical bandgap of each samples synthesized in order to define the repeatability of the synthesis with different percentages of CDs. The presence of CDs do not heavily alter the reproducibility of the bandgap.

Sample	Linear fit	Y=0	Bandgap	Mean
WS_2 _1	Y= 4,25x - 12,43	X= 12,43 / 4,25	2,92 eV	2,97 ± 0,07
WS_2 _2	Y= 6,83x - 20,09	X= 20,09 / 6,83	3,06 eV	
WS_2 _3	Y= 4,5x - 13,2	X= 13,2 / 4,5	2,93 eV	
WS_2 @CDs_0,01%_1	Y= 5,26x - 15,91	X= 15, 91 / 5,26	3,02 eV	3,05 ± 0,06
WS_2 @CDs_0,01%_2	Y= 5,70x - 17,20	X= 17,20 /5,70	3,01 eV	
WS_2 @CDs_0,01%_3	Y= 7,91x - 24,75	X= 24,75 / 7,91	3,13 eV	
WS_2 @CDs_0,1%_1	Y= 4,19x - 12,1	X= 12,1 / 4,19	2,89 eV	2,90 ± 0,02
WS_2 @CDs_0,1%_2	Y= 4,35x - 12,61	X= 12,61 /4,35	2,90 eV	
WS_2 @CDs_0,1%_3	Y= 4,88x - 14,34	X= 14,34 / 4,88	2,93 eV	
WS_2 @CDs_1%_1	Y= 4,92x - 14,61	X= 14,61 /4,92	2,93 eV	2,92 ± 0,02
WS_2 @CDs_1%_2	Y= 4,37x- 12, 73	X= 12,73 / 4,37	2,91 eV	
WS_2 @CDs_1%_3	Y= 4,26x - 12,32	X= 12,32 /4,26	2,89 eV	

For a better understanding of the meaning of these results, the calculated mean was plotted. As showed in Fig.71, was clear that the increasing amount of NCDs didn't condition reproducibility and bandgap of the material, because all the values were inscribed in the semidispersion of the other samples. Considering that the mean of the all calculated bandgap was 2,96± 0,02 eV, we could assume that the synthesis process, with or without NCDs, showed a discrete reproducibility. Of course, small bandgap values variations corresponded to appreciable differences in the ability of adsorbing light. For that reason, these values must be considered sufficient, but not excellent.

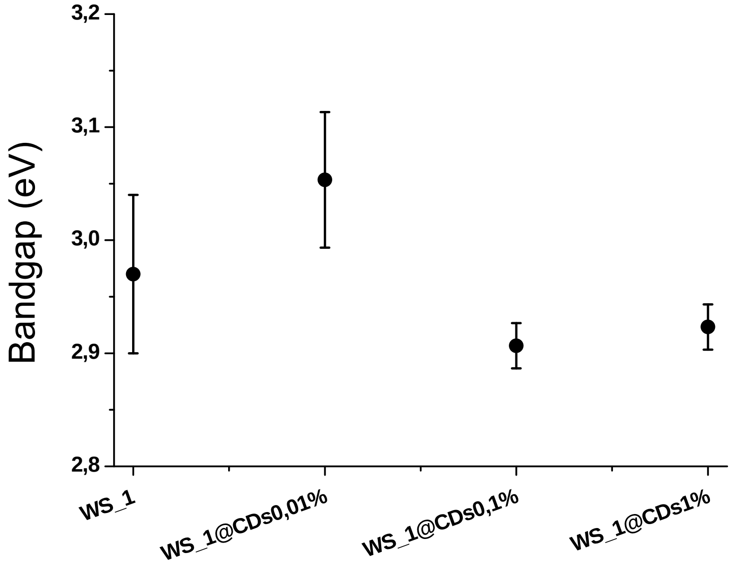

Figure 71: Comparison of the mean bandgap value calculated on the three-repeated synthesis of the samples WS_2, WS_2 @CDs_0,01%, WS_2 @CDs_0,1% and WS_2 @CDs_1% respectively.

4.3.2- CDs loading and type study

In order to define the effective CDs loading, elemental analysis was performed to define the carbon%$_w$ loaded on samples WS_2.

Table 21: Elemental analysis of sample WS_2 loaded with different amount of NCDs

Sample	C(%$_w$)	H(%$_w$)	N(%$_w$)
WS_2	0,3	0,4	0,1
WS_2@NCDs 0,1%	0,2	0,5	<0,1
WS_2@NCDs 1%	1,1	0,62	<0,1
WS_2@NCDs 5%	4,2	1,4	<0,1

In the Tab.21, carbon, hydrogen and nitrogen %$_w$ were showed. Considering the carbon % increase, was possible to state that the loading process took place. In samples WS_2 and WS_2@NCDs 0,1% carbon detected might derived from contaminations, but carbon content in WS_2@NCDs 1% and WS_2@NCDs 5% unequivocally derived from NCDs. Nitrogen content in NCDs was too low to be detected with elemental analysis.

In order to define if the NCDs loading can change photocatalytic properties, and to define the best CDs percentage, photocatalytic activity of WS_2 samples loaded with different NCDs% were studied.

In Fig.72 photocatalytic activities of WS_2 and WS_2 loaded with increasing % of NCDs had been presented. $NTiO_2$ann. was compared as reference material.

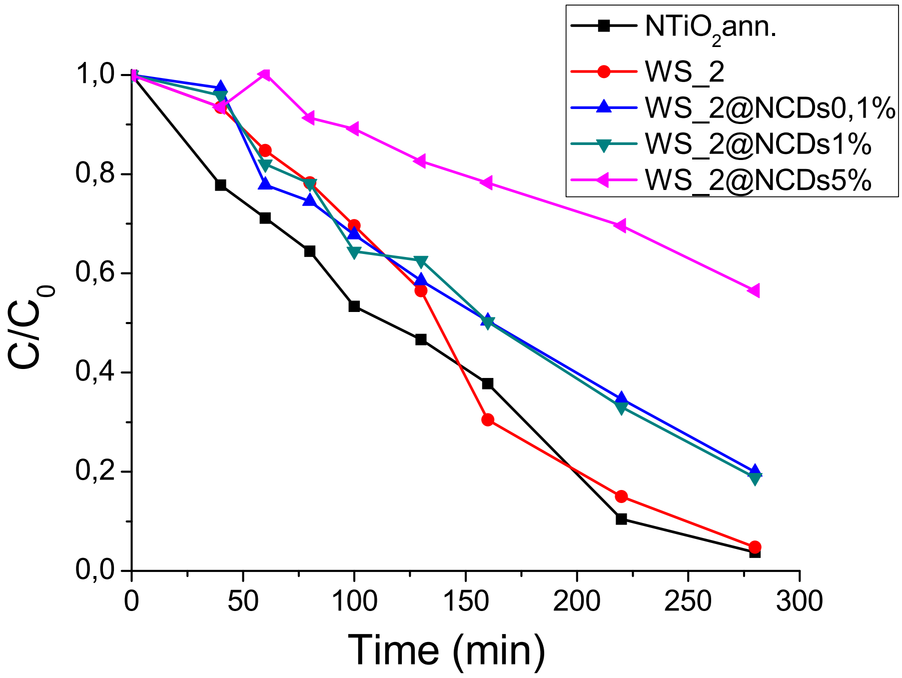

Figure 72: Photocatalytic activity of $NTiO_2$ann. compared withWS_2 with increasing amount of NCDs.

From the comparison emerged that WS_2@NCDs_5% was the only sample with evident different photocatalytic activity. In addition, when CDs changed the behavior of the system, photocatalytic activity was reduced. Samples with less percentage of NCDs showed photocatalytic activity comparable with $NTiO_2$ann.

To study if different CDs loading could change sample bandgaps, Tauc plot-based study was performed.

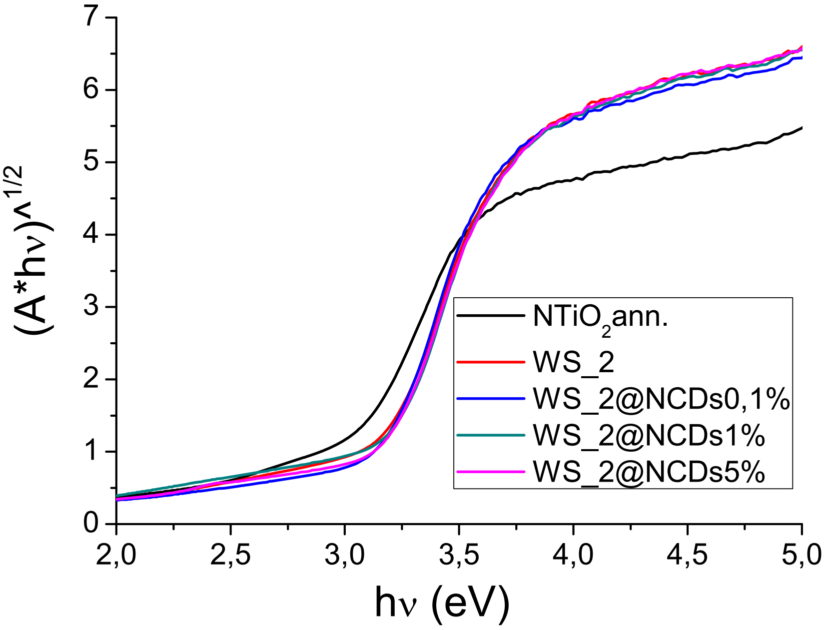

Figure 73: Tauc plot of NTiO$_2$ann. compared with WS_2 with increasing percentage of NCDsweight.

As is possible to understand from the Tauc plot in Fig.73 increasing the percentage of NCDs don't change semiconductor bandgap. Indeed Tauc plots of the samples are completely overlapped.

Similar conclusion could be done from the calculated band gap showed in Tab.22.

Table.22: calculated bandgap for sample WS_2 and samples with increasing amount of NCDs.

Sample	TiO$_2$ann.	WS_2	WS_2@NCDsN0,1%	WS_2@NCDsN1%	WS_2@NCDsN5%
Bandgap (eV)	2,9	3,1	3,1	3,1	3,1

Calculated bandgap was similar for all the samples. In comparison with TiO$_2$ann. all WS_2 samples showed greater bandgap. The bandgap value regularity was also significant on the type of interaction between CDs and titania. This was indicative that CDs didn't contaminate the crystal lattice with carbon atoms, and didn't reduce the bandgap introducing intragap layers typical of carbon-doped titania.

The loading of different quantities of CDs couldn't improve photocatalytic activity neither reduce bandgap. The only changes from the photocatalytic point of view derived from WS_2@NCDsN5%. Due to this consideration, even if several NSCDs-doped WS2 were produced, only WS_2@NSCDs5% was taken in consideration. In this experiment WS_2 samples were, firstly, loaded with 5% of NCDs and NSCDs and, secondly, characterized. At this purpose, the photocatalytic activity and bandgap determination of the two samples were compared.

In Fig.74, photocatalytic activity conducted on WS_2, WS_2@NCDs5% and WS_2@NSCDs5% had been showed.

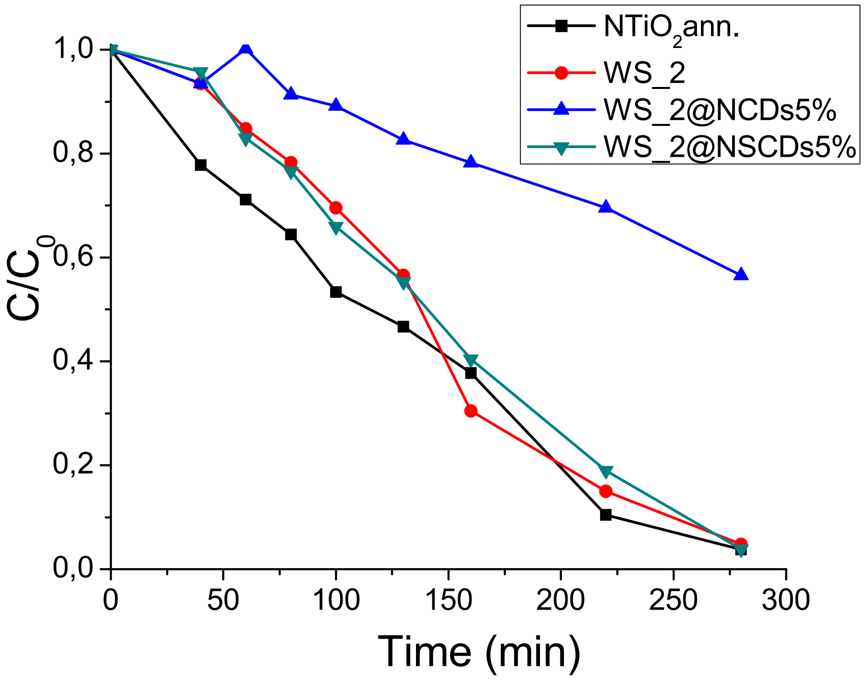

Figure74: Photocatalytic activity of samplesTiO$_2$ann., WS_2 and WS_2 loaded with 5%w of NCDs and NSCDs.

Comparing WS_2@NCDs and WS_2@NSCDs, some differences with equivalent samples loaded with corresponding 1%$_w$ could be noticed. WS_2@CDsN5% shows smaller photocatalytic activity, while WS_2@CDsNS5% showed activity comparable with WS_2 and TiO$_2$ann. Probably the interaction of NSCDs with the host material didn't produce any effect on photocatalytic activity.

To study if the CDs co-doping with sulphur could change sample bandgaps, Tauc plot-based study was performed. At this purpose, Tauc plot of unloaded WS_2 and reference samples as NTiO$_2$ ann. were added in the comparison.

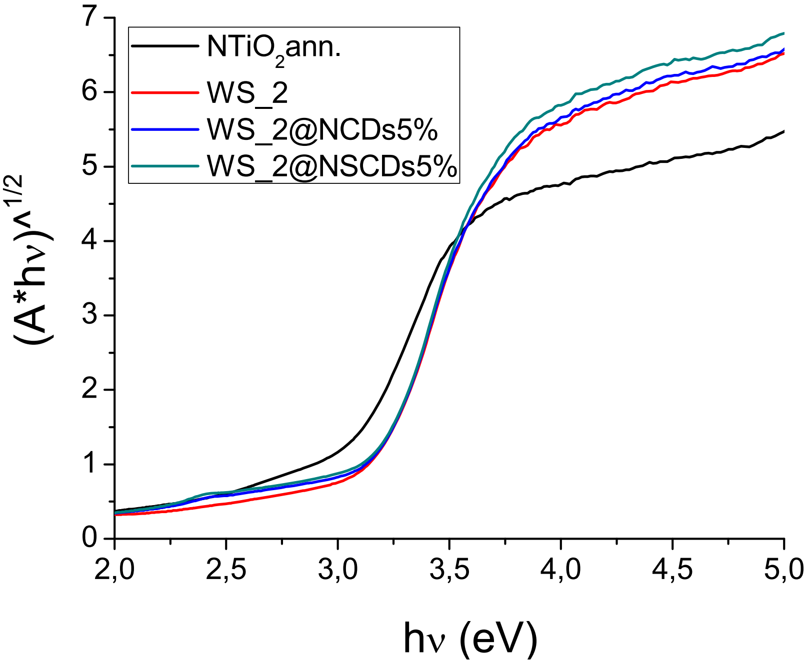

Figure 75: Tauc plot of WS_2 samples loaded with theoretical 5%$_w$ NCDs and co-doped NSCDs.

Tauc plot in Fig.75 showed that the loading of 5%$_w$ of different doped CDs didn't change samples bandgap. Tauc plots of the samples were completely overlapped. Similar conclusion could be done from the calculated bandgap showed in Tab.23.

Table23: Bandgap values of reference annealed NTiO$_2$ and samples WS_2 unloaded and loaded with 5%$_w$ of different doped NCDs, calculated from Tauc Plot showed in Fig.76.

Sample	NTiO$_2$ ann.	WS_2	WS_2@NCDs5%	WS_2@NSCDs5%
Bandgap (eV)	2,9	3,1	3,1	3,1

Calculated bandgap was similar for all the samples. In comparison with TiO$_2$ann. all WS_2 based samples showed greater bandgap. Optimized hydrothermal treatment was applied to produce high crystalline WS_2 samples loaded with increasing amount of NCDs. In this way, was defined the minimum CDs% able to produce differences in sample properties.

Samples were characterized from the optical and photocatalytic point of view. From the analysis, emerged that despite the increasing amount of loaded CDs, in calculated bandgap no change were noticed. Photocatalytic activities of different loaded WS_2 samples were not increased. To obtain different photocatalytic activity, 5%$_w$ of NCDs must be loaded. In this case, in comparison to the unloaded WS_2, the catalytic behavior decreased.

At this regard, in order to explicate the poor activity of these materials, new amorphous TiO_2 based material was loaded with NCDs and NSCDs, and processed with the optimized hydrothermal treatment. In this way was possible to understand if the low activity derived from the low quality of the amorphous material or from the optimized hydrothermal treatment.

4.3.3- Comparison with standard material

In order to define if the bad quality of the WS_2 based samples derived from the amorphous material or from the hydrothermal treatment, new TiO_2 based samples were studied. The synthesis of these samples were proposed in the paragraph 3.4. These new samples were loaded with NCDs and NSCDs and processed with hydrothermal treatment used for WS_2 samples.

As first characterization, XRD pattern of the basic TiO_2, loaded with 1% of NCDs and NSCDs, was studied. The three samples were compared with a reference titania annealed at 500°C for 1h. the results of this study was showed in Fig. 76.

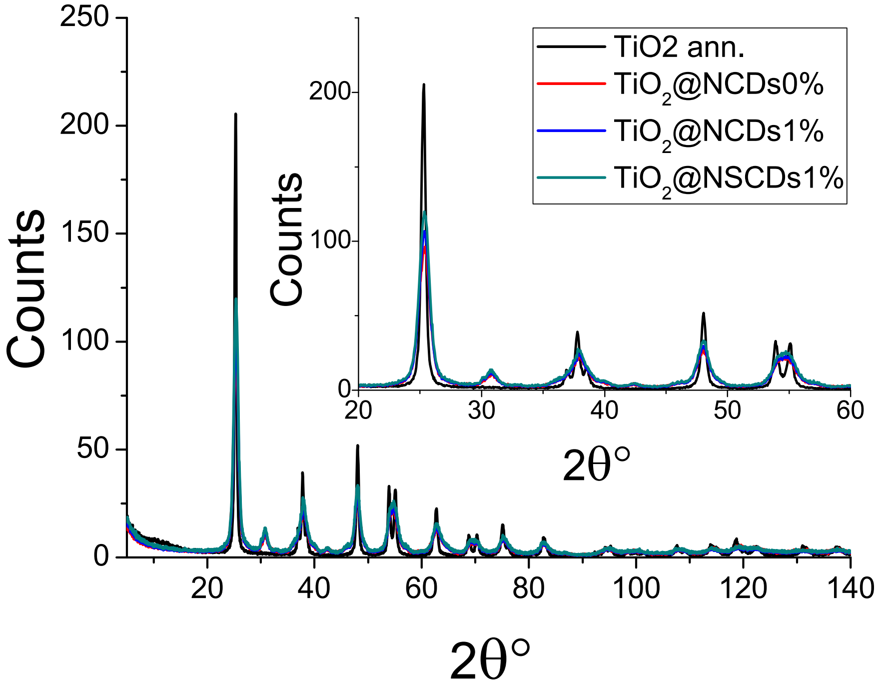

Figure 76: XRD pattern of the TiO_2@ and loaded with 1% of NCDs and NSCDs. The three samples are compared with a reference sample of titania annealed at 500°C for 1h.

XRD patterns of treated samples presented in Fig.76, showed re-arrangement from amorphous to crystalline material. All the three samples denoted broaden peak patterns. This characteristic derived from nano-sized dimension of the material. From pattern analysis resulted that samples were not completely constituted by anatase. Quantification of the different peaks assigned approximately 10% of the samples to brookite phase. In the Tab.24, calculated quantities of the two phases and crystallite dimensions were reported.

Table24: Phase quantification and crystallite dimension calculated on patterns showed in Fig.77.

Sample	**Anatase %**	<L> (nm)	**Brookite %**	<L> (nm)
TiO_2 ann.	100	22	-	-
TiO_2@CDs 0%	90,3	7,6	9,7	6,1
TiO_2@NCDs 1%	90,5	8,2	9,5	6,9
TiO_2@NSCDs 1%	90,7	8,5	9,3	6,6

In comparison with TiO_2ann., hydrothermal treatment produced smaller crystallites than an annealed material. Comparing TiO_2 based samples with WS_2 based samples showed in Tab.8, the hydrothermal treatment produced similar crystallite dimension.

In order to study the effective CDs loading in TiO2@NCDs1% and TiO2@NSCDs1%, elemental analysis was performed.

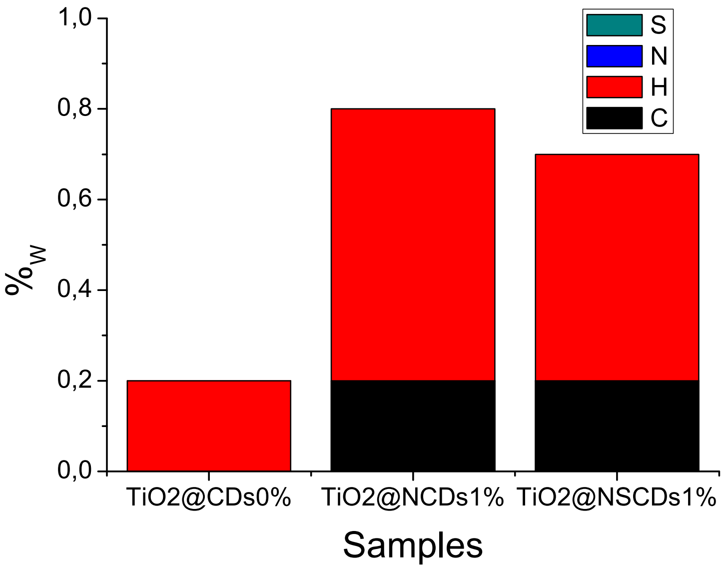

Figure 77: Histogram representing the $\%_w$ of carbon, hydrogen, nitrogen and sulphur measured for the samples of loaded and unloaded TiO_2 with NCDs and NSCDs.

As is noticeable from the elemental analysis showed in Fig. 77, a fraction of carbon was detected in samples loaded with CDs. In comparison, the unloaded sample didn't show presence of carbon, and this difference allow to argue that the detected carbon arised from CDs loading. Since during the synthesis of the amorphous TiO_2@NCDS and TiO_2@NSCDS, an amount of $1\%_W$ of CDs was added, the detection of 0,2% induce to assure that $\frac{1}{5}$ of the added CDs was effectively loaded in TiO_2@CDs samples.

In order to define the morphology and the size of the samples of un-doped titania, SEM images were performed on unloaded TiO_2@CDs0%, TiO_2@NCDs_1% and TiO_2@NSCDs_1%.

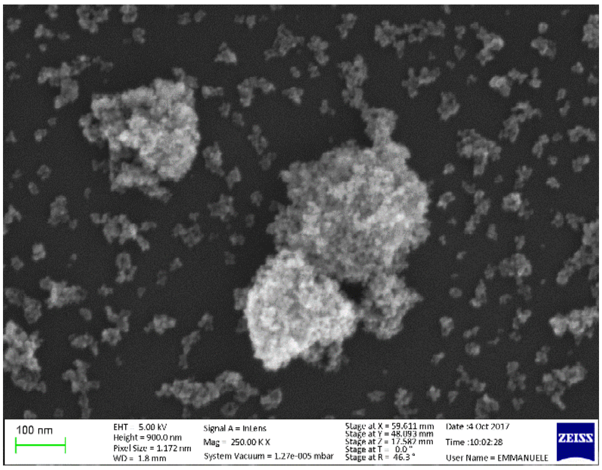

A

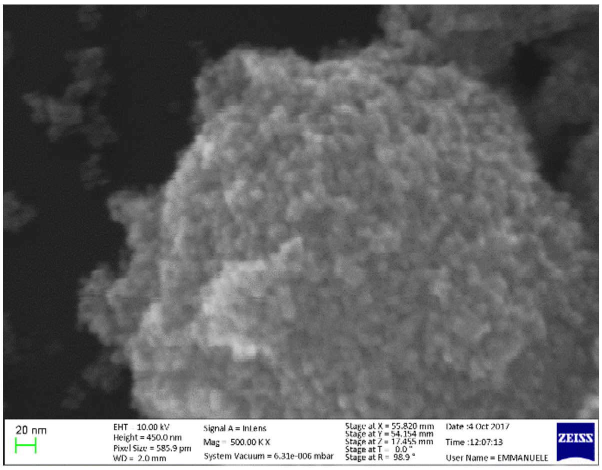

B

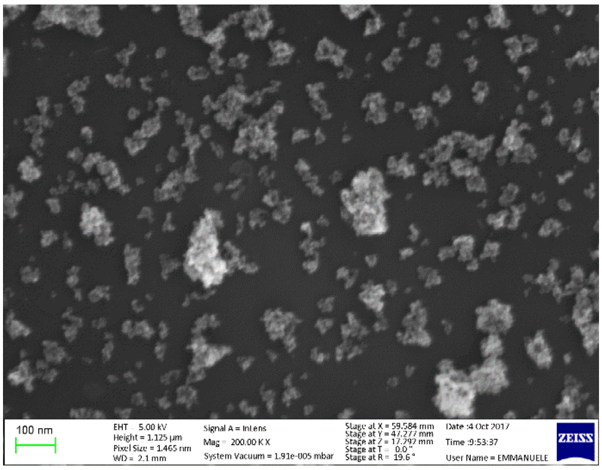

C

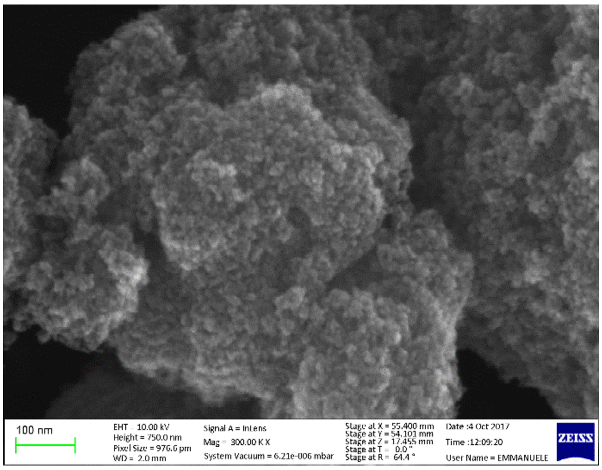

D

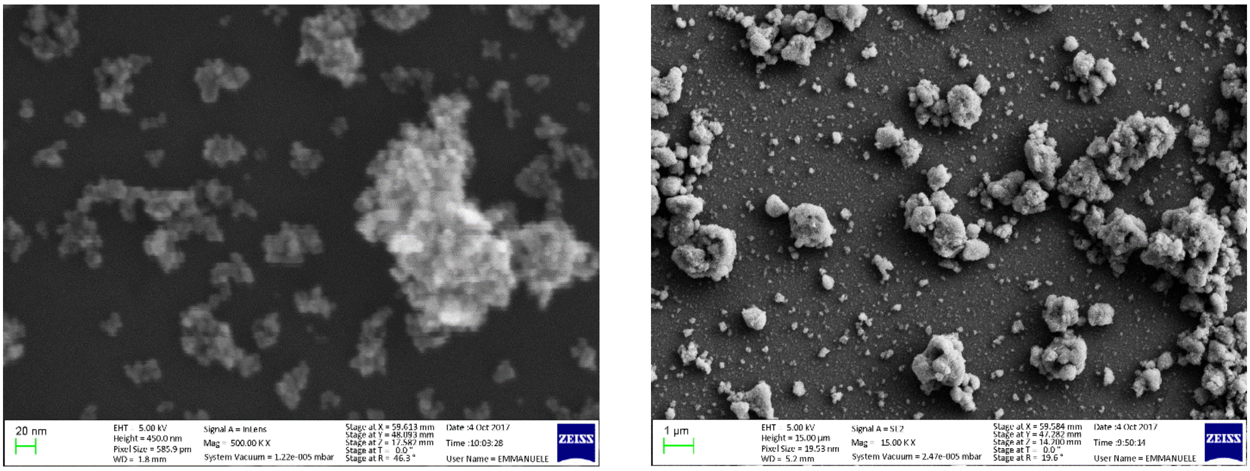

E **F**

Figure 78: A) and B) SEM images of the sample of unloaded TiO_2@CDs_0%. C) and D) SEM images of the sample of TiO_2@NCDs_1%. E) and F) SEM images of the sample of TiO_2@NSCDs_1%.

From the morphological study, emerged that TiO_2@CDs_0% showed in Fig.78A and B was composed by 10nm globular nanoparticles. A wide range of agglomerated nanoparticles composed the material, with objects constituted by few nanoparticles since micron-sized aggregates. As TiO_2@CDs_0%, TiO_2@NCDs_1%, presented in Fig.78 C and D, was composed by 10nm globular nanoparticles. Here, the addition of NCDs suspension during the amorphous synthesis didn't produce substantial variations from the unloaded sample. In addition, nanoparticles aggregates varied from few gathered nanoparticles to big micro-sized objects. As the unloaded sample, TiO_2@NSCDs_1%,presented in Fig. 78 E and F, was composed by globular nanoparticles of 10nm. Here, the addition of NSCDs suspension during the amorphous synthesis didn't produce substantial variations from the unloaded sample. Also in this case, nanoparticles aggregates varied from few gathered nanoparticles to big micro-sized objects.

Therefore, from the morphological analysis conducted on the group of standard materials emerged that during the synthesis, the addition of CDs suspension didn't produce morphological variations.

To define optical bandgap and the possible correspondence with bandgap and CDs loading, Tauc plot from reflectance measurements was studied in fig 79.

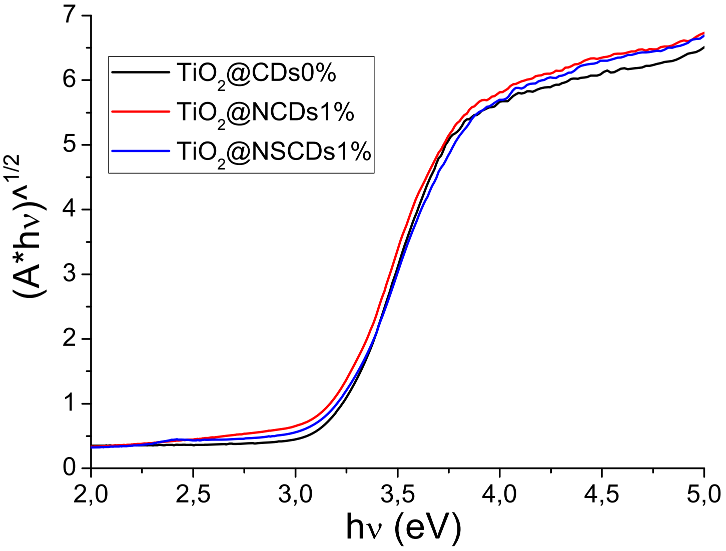

Figure 79: Tauc plot of TiO_2@CDs_0%, TiO_2@NCDs_1% and TiO_2@NSCDs_1%

As for the previous loaded materials, new samples of titania loaded with different doped NCDs didn't present bandgap differences from the unloaded sample. In addition, loaded CDs didn't condition the optical bandgap. Similar consideration could be taken from the Tab. 25.

Table 25: Bandgap values of TiO_2 samples unloaded and loaded with 1%$_w$ of different doped NCDs, calculated from Tauc Plot showed in Fig.80.

Sample	TiO_2@CDs0%	TiO_2@NCDs1%	TiO_2@NSCDs1%
Bandgap (eV)	3,1	3,1	3,1

As final consideration, in Fig. 80 photocatalytic activity of the samples TiO2@CDs_0%, TiO2@NCDs_1% and TiO2@NSCDs_1% was compared with reference samples as such as P25 and TiO_2ann.

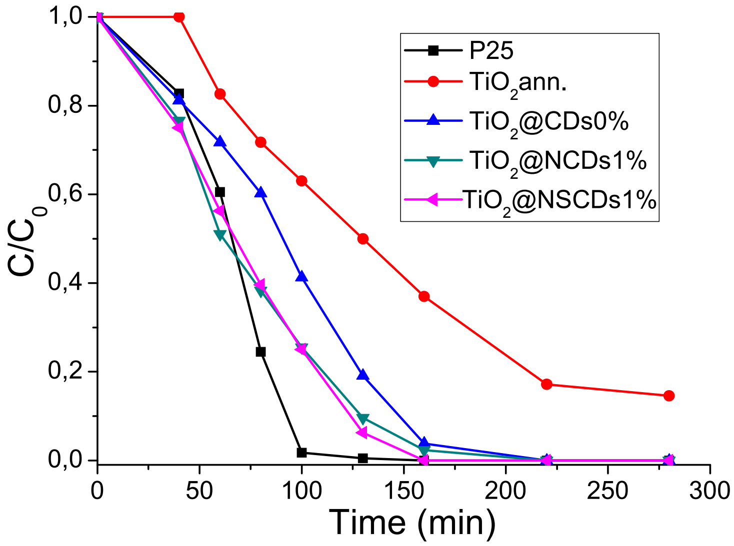

Figure 80: Photocatalytic activity of TiO$_2$@CDs_0%, TiO$_2$@NCDs_1% and TiO$_2$@NSCDs_1% compared with P25, TiO$_2$ ann. reference materials.

Comparing TiO$_2$@NCDs and TiO$_2$@NSCDs with reference materials clarified how the loading of CDs could really improve the photocatalytic activity. Despite the implementation derived from the CDs, P25 still showed the best photocatalytic performances.

After the definition of the photocatalytic activity of the WS_2-based and TiO$_2$-based group of samples, emerged that the quality of the amorphous material strongly conditioned the properties of the photocatalytic material. Considering also that the hydrothermal process was the same used for the treatment of the two kind of amorphous materials, we concluded that the hydrothermal treatment produced a good quality of photocatalytic material. Therefore, the low photocatalytic activity of the WS_2 based group of samples was due to the synthesis of the amorphous material.

To better understand how the photocatalytic activity was related to the synthesis of a good amorphous starting material, a comparison between photocatalytic activity of TiO$_2$@ and WS_2@ based systems was presented in Fig. 81.

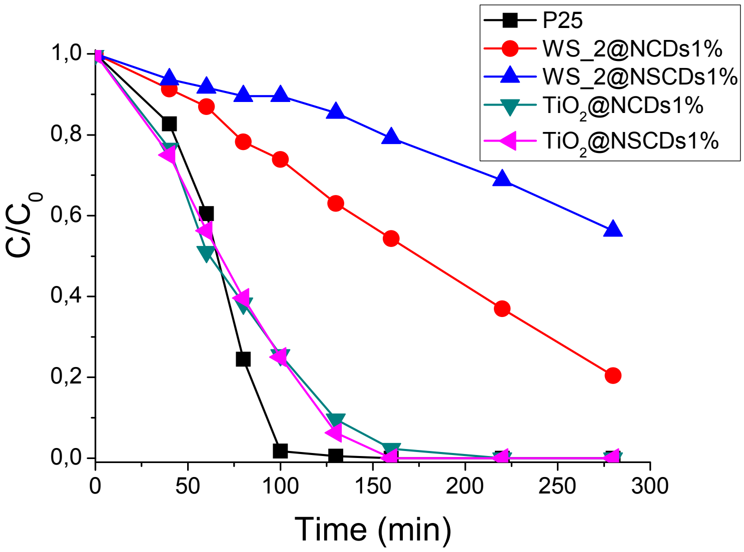

Figure 81: *Photocatalytic activity of the samples*, WS_2@NCDs1%, WS_2@NSCDs1%, TiO_2@NCDs1% and TiO_2@NSCDs1%

From the comparison of the two group of samples, was clear that the TiO_2@ based samples offer the best performances. This comparison clarified the good efficacy of the optimized hydrothermal treatment to produce high crystalline materials with good photocatalytic activity. Moreover, Fig.81 showed how the good quality of the starting amorphous material conditioned the performances of the final product.

4.3.4- Results

Despite the effect of carbon nanoparticles, the low performances of WS_2 based samples, underlined the problem of which step determined their low quality. Therefore, to verify the responsibility of the low quality to the synthesis of the amorphous material or to the hydrothermal treatment, additional samples were synthesized. At this purpose, un-doped TiO_2 loaded with 1% of different doped NCDs was produced. To synthesize these samples, the production of the starting material of TiO_2 ann. was used. During the gelation step CDs water suspension was added and instead of annealing, the amorphous material was processed with optimized hydrothermal treatment. After crystallinity and bandgap characterization, photocatalytic activity was determined. Then, WS_2-based and TiO_2-based samples were compared. From this study emerged that the quality of the amorphous material strongly conditioned the properties of the sample. Considering also that the hydrothermal process was the same used for the treatment of the two kind of amorphous materials, was possible to conclude that the hydrothermal treatment allowed producing good quality photocatalytic material.

Usually, photocatalytic material was firstly synthesized and annealed, secondly, was loaded through impregnation with CDs. Now, hydrothermal treatment draw up for crystalline titania production permitted the CDs loading during the synthesis of the amorphous material. This process allowed better interaction between CDs and photocatalytic material but, mostly important, allowed to not lose CDs in reaction environment.

5-Conclusions

Nanotechnologies are massively present in our everyday life. Electronics, pharmaceutics and agriculture are just few fields in which nanotechnologies are present and active. For this reason, the design of new technologies has to take care even to its entire lifecycle and the respect environmental interactions. Carbon dots (CDs) are a recent family of materials in the nano systems universe, and since their discovery in 2004, they have attracted great attention due to their physical and chemical properties and their versatility in a wide range of applications, such as lighting and theragnostic materials.

In this chapter, most important conclusion are presented following the adopted research line.
As reported in results and discussion chapter, three main issues were considered and studied in this thesis: 1) Carbon dots, 2) Titanium dioxide and 3) Enhanced photocatalytic materials.

1) Carbon dots.

The study and application of CDs was developed to assess their viability in the field of treatment of polluted water and the related cytotoxicity for a possible application in nanomedicine. From this perspective, many efforts have been made to understand if CDs could be used for enhanced advanced oxidation systems, and how they could be able to produce UPCL phenomena.
As reported in this work, we demonstrated that the CDs emission was due to the second order of diffraction of the main excitation light, and it is not derived by UPCL. Indeed, further studies will be focused on deeply understand this issue.
Heteroatoms doping in CDs allowed to insert intragap layers in the CDs energetic structures, useful to delocalize charges in advanced oxidation systems and able to improve their efficiency. In order to study possible doped-CDs candidates, different samples have been produced via hydrothermal process. This kind of synthesis was chosen because it is easy to control and it has great synthesis reproducibility. Preliminary group of different doped CDs was synthesized using a receipt reported by Barman et al[123].
Optical studies carried out in this research, photoluminescence showed independence from the λ_{ex}, but different Stoke-shift between NCDs and the other co-doped samples. The independence from the λ_{ex} is due to the passivation of the CDs surface with high content of amine. Indeed, the role of amine is to substitute the surface functional groups, of different energies, with an

homogeneous functionalization, that has the same surface energy. The morphological investigations showed the small sizes of the co-doped and doped samples. This result permitted to understand that the dialysis is an inadequate purification method. Indeed, this kind of CDs pass through membrane and is lost in washing solution. With the aim to avoid the CDs lose, another purification process based on different chemical affinity of solvents with un-reacted material have been developed. The use of this process permitted to partially remove reacted materials, and obtain clean samples rich in CDs.

The CDs with greater dimension produced with the changed procedure of hydrothermal synthesis, as reported in Materials and methods chapter, were characterized in order to select the best CDs to apply in enhanced photocatalytic materials. The characterization considered the optical properties, cytotoxicity, CDs size/surface functionalization ratio, morphological features and elemental analysis. The obtained results showed that DETA-based group is the most suitable samples for the enhancement in advanced oxidation processes and for their potentially use in nanomedicine. Elemental analysis results showed that in the DETA-based samples, only NCDs and NSCDs are doped with the right heteroatoms (N and S) as we attended. These results allowed to select DETA NCDs and NSCDs as the best samples to apply in enhanced photocatalytic processes.

The cytotoxicity investigation unlighted that the use of DETA allow to produce non-toxic compounds. Furthermore, from our results it can be noted that CDs cytotoxicity can be independent on the toxicity of the starting reagent and dependent to the toxicity of degradation products, which contribute at the CDs formation.

2) Titanium dioxide.

The aim of the study was to develop a procedure to produce crystalline $NTiO_2$ able to host CDs and be activated under solar light radiation.

The experiments carried out following the procedure proposed by Sugimoto et al. was able to produce small crystallites and photoactive material. Its application on different amorphous materials, as the selected $NTiO_2$, produced a crystalline material but without photocatalytic activity, probably due to the low crystalline amount. Furthermore, the hydrothermal procedure was modified and it produced sample with better photocatalytic activity but the new material lost all its nitrogen content. The nitrogen loss reduced the ability of the material to be activated under solar light. Concluding, the developed material does not satisfy the required properties. However, the developed material (S_1-2-2-8-200) was loaded with CDs to study enhanced photocatalytic materials.

3) Enhanced photocatalytic material

Combining the CDs selected to enhance advanced oxidation processes photocatalytic activity with the selected S_1-2-2-8-200 material produced with the Sugimoto-modified procedure, we obtained a new composite which has lower photocatalytic activity. This disadvantage can be due to the low capability of the amorphous material (NTiO_2) used in the hydrothermal procedure, to obtain a crystalline material without crystal defects. This aspect is demonstrated by experiments carried out on obtained samples in comparison with reference samples loaded with CDs.

Concluding, synthesis and crystallization in presence of CDs should preserve CDs properties. However, has to be taken into consideration the use of an amorphous photocatalytic material able to rearrange the structure into a system free of defects.

The world of CDs has just discovered, and despite great efforts are spent, several aspects must to be clarified.

The efforts spent in this study showed several necessities, as a standardization of the CDs characterization. Each study considered in literature shows a partial characterization that not allow a complete knowledge on CDs system. A complete and systematic characterization, should include optical studies, cytotoxicity analysis, morphological investigation, elemental composition and surface functionalization. The purpose is to obtain a data-set useful to optimize the research and to finally use CDs for the technologic development.

The example of the CDs toxicity is a case in point. Usually CDs are considered safety ex-ante. The conclusion of this study, demonstrates that CDs safety must not be taken as granted taking in consideration CDs size and their membrane permeability.

Another point of interest emerged in this thesis, is that electrophoresis can be used to study in detail CDs superficial charge and size distribution. In order to make the use of electrophoresis unquestionably effective for CDs study, a charge/size reference is needed. In our opinion, the development of a reference system with well-defined charge and size objects may permit to the electrophoresis analysis to be a quantitative technique for the CDs study.

Finally, the experience developed in this study underline the necessity to study the ions which support functional groups decorating the CDs surface. If in literature the CDs surface is customized with defined functional groups, the ions that balance functional group charges are often not studied. A greater knowledge of these negligible aspects may permit to develop CDs with higher ability to load defined compounds, and may base new studies focused on carrier-CDs able to release defined compounds in defined environmental conditions. These studies may allow the developing of new drug delivery materials generation.

6-Appendix

List of the samples

Table 1: List of all the samples reported in this thesis.

<table>
<tr><td colspan="60">Carbon Dots</td></tr>
<tr><td colspan="60">Upconversion study samples</td></tr>
<tr><td colspan="12"><i>CD_A</i></td><td colspan="12"><i>CD_B</i></td><td colspan="12"><i>CD_C</i></td><td colspan="12"><i>CD_D</i></td><td colspan="12"><i>CD_E</i></td></tr>
<tr><td colspan="60">Preliminary codoped NCDs</td></tr>
<tr><td colspan="15"><i>N_CDs</i></td><td colspan="15"><i>N_P_CDs</i></td><td colspan="15"><i>N_B_CDs</i></td><td colspan="15"><i>N_S_CDs</i></td></tr>
<tr><td colspan="60">Codoped NCDs with different nitrogen sources (synthesis #1 and #2)</td></tr>
<tr><td colspan="15"><i>UREA_NCDs</i>
<i>UREA _NPCDs</i>
<i>UREA _NBCDs</i>
<i>UREA _NSCDs</i></td><td colspan="15"><i>ETIDI_NCDs</i>
<i>ETIDI_NPCDs</i>
<i>ETIDI_NBCDs</i>
<i>ETIDI_NSCDs</i></td><td colspan="15"><i>DETA_NCDs</i>
<i>DETA_NPCDs</i>
<i>DETA_NBCDs</i>
<i>DETA_NSCDs</i></td><td colspan="15"><i>TRITETRA-NCDs</i>
<i>TRITETRA-NPCDs</i>
<i>TRITETRA-NBCDs</i>
<i>TRITETRA-NSCDs</i></td></tr>
<tr><td colspan="60">Titanium Dioxide</td></tr>
<tr><td colspan="60">Reference samples</td></tr>
<tr><td colspan="15">TiO_2 <i>ann.</i></td><td colspan="15">$NTiO_2$ <i>ann.</i></td><td colspan="15">TiO_2<i>comm</i></td><td colspan="15"><i>P25</i></td></tr>
<tr><td colspan="60">Hydrothermal study samples</td></tr>
<tr><td colspan="20"><i>S_1</i></td><td colspan="20"><i>S_2</i></td><td colspan="20"><i>B_1</i></td></tr>
<tr><td colspan="60">Crystal phase optimization</td></tr>
<tr><td colspan="30"><i>W_1</i></td><td colspan="30"><i>WS_1</i></td></tr>
<tr><td colspan="20"><i>WS_1 45°C</i></td><td colspan="20"><i>WS_1 55°C</i></td><td colspan="20"><i>WS_1 65°C</i></td></tr>
<tr><td colspan="60">Hydrothermal process of the nitrogen doped titanium dioxide</td></tr>
<tr><td colspan="12"><i>WS_10_01_24_100</i></td><td colspan="12"><i>WS_5_01_24_100</i></td><td colspan="12"><i>WS_2_01_24_100</i></td><td colspan="12"><i>WS_2_1_24_100</i></td><td colspan="12"><i>WS_2_2_24_100</i></td></tr>
<tr><td colspan="12"><i>WS_2_2_24_150</i></td><td colspan="12"><i>WS_2_2_24_200</i></td><td colspan="12"><i>WS_2_2_15_200</i></td><td colspan="12"><i>WS_2_2_8_200</i></td><td colspan="12"><i>Annealed</i></td></tr>
<tr><td colspan="60"><i>WS_2_2_8_200 = WS_2</i></td></tr>
<tr><td colspan="60">Enhanced Photocatalytic Materials</td></tr>
<tr><td colspan="60">Repeatability</td></tr>
<tr><td colspan="15"><i>WS_2_1</i></td><td colspan="15"><i>WS_2@CDs_0,01%_1</i></td><td colspan="15"><i>WS_2@CDs_ 0,1%_1</i></td><td colspan="15"><i>WS_2@CDs_1%_1</i></td></tr>
<tr><td colspan="15"><i>WS_2_2</i></td><td colspan="15"><i>WS_2@CDs_0,01%_2</i></td><td colspan="15"><i>WS_2@CDs_ 0,1%_2</i></td><td colspan="15"><i>WS_2@CDs_1%_2</i></td></tr>
<tr><td colspan="15"><i>WS_2_3</i></td><td colspan="15"><i>WS_2@CDs_0,01%_3</i></td><td colspan="15"><i>WS_2@CDs_ 0,1%_3</i></td><td colspan="15"><i>WS_2@CDs_1%_3</i></td></tr>
<tr><td colspan="60">CDs loading and type of study</td></tr>
<tr><td colspan="12"><i>WS_2</i></td><td colspan="12"><i>WS_2@NCDs 0,1%</i></td><td colspan="12"><i>WS_2@NCDs 1%</i></td><td colspan="12"><i>WS_2@NCDs 5%</i></td><td colspan="12"><i>WS_2@NSCDs 5%</i></td></tr>
<tr><td colspan="60">Comparison with standard material</td></tr>
<tr><td colspan="20">TiO_2<i>@CDs 0%</i></td><td colspan="20">TiO_2<i>@NCDs 1%</i></td><td colspan="20">TiO_2<i>@NSCDs 1%</i></td></tr>
</table>

4.1.1-Upconversion studies

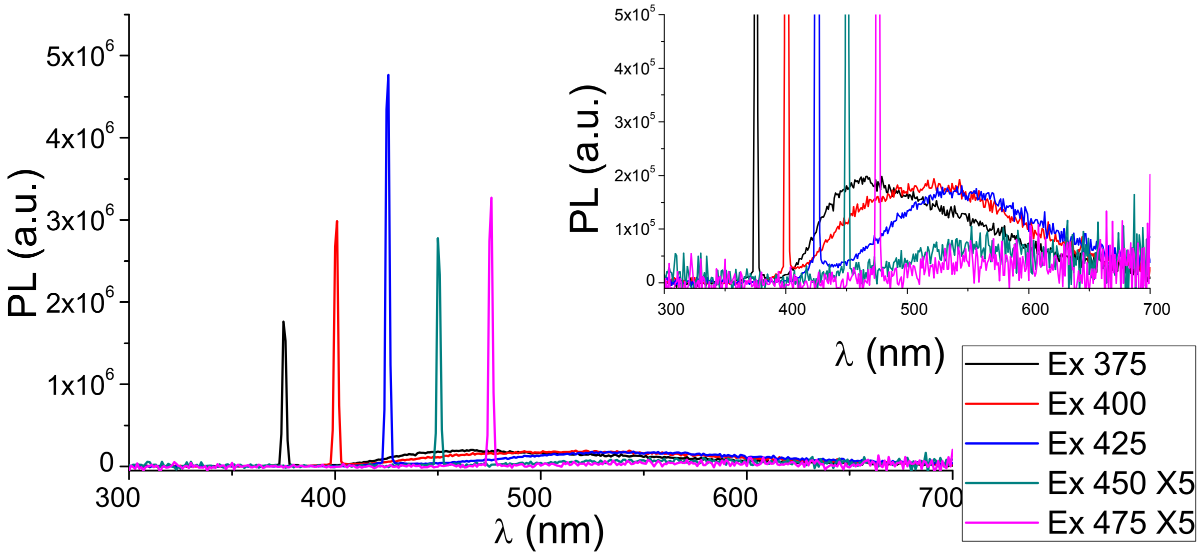

Figure 1: CD_B PL spectra excited at the same wavelength of the second harmonic. In the inset, magnification of the emission is proposed. PL recorded at 470nm and 475nm are magnified x5.

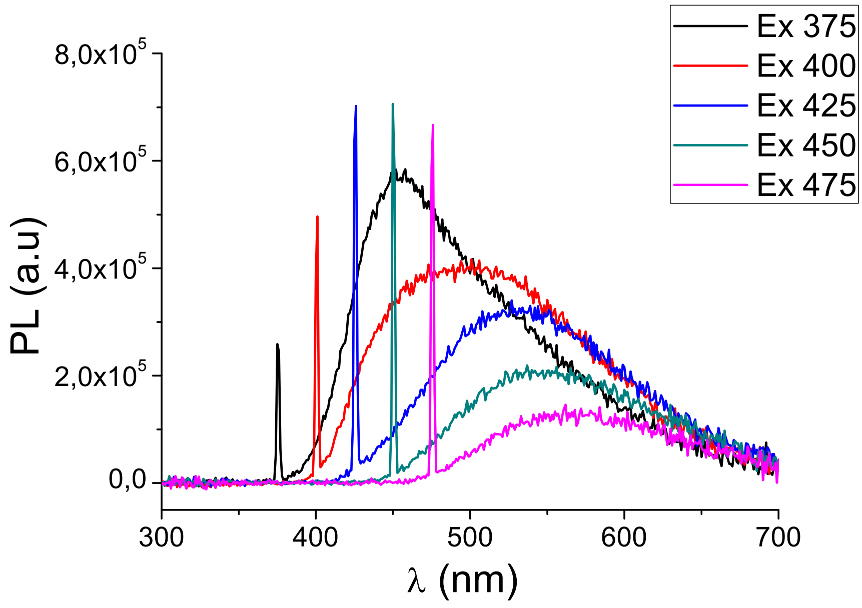

Figure 2: CD_C PL spectra excited at the same wavelength of the second harmonic.

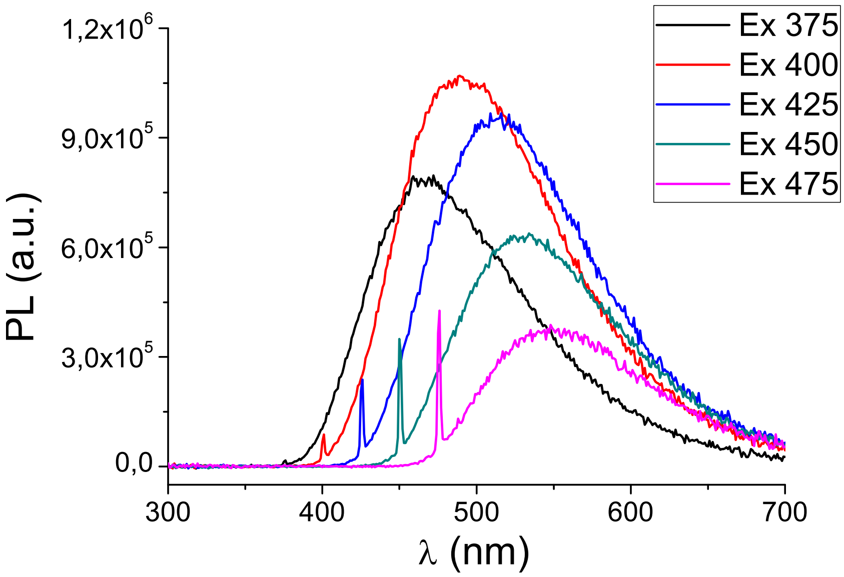

Figure 3: CD_D PL spectra excited at the same wavelength of the second harmonic.

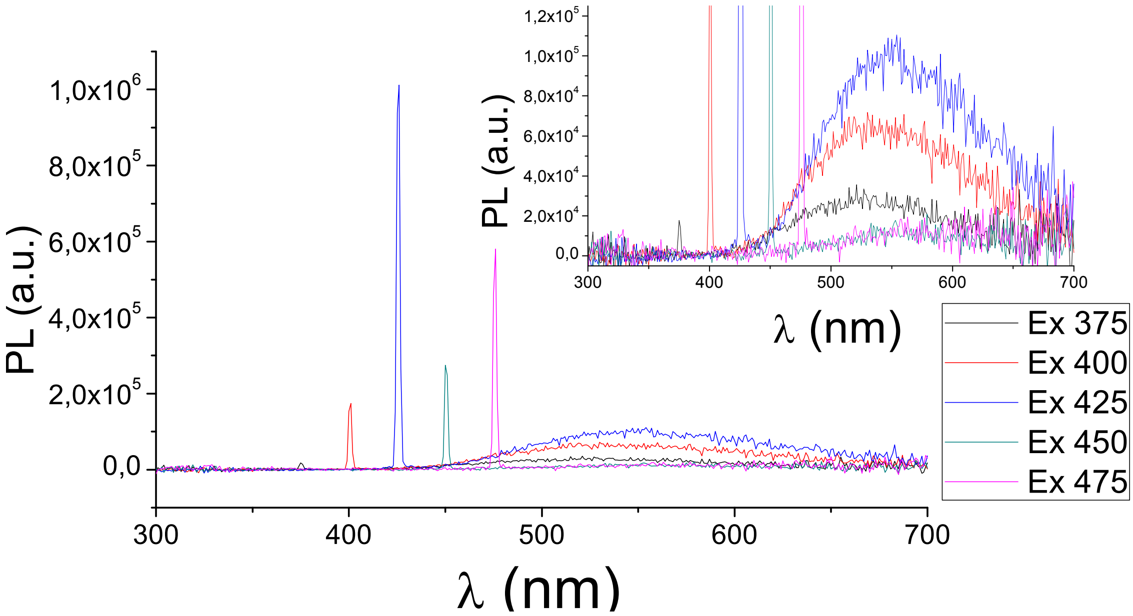

Figure 4: CD_E PL spectra excited at the same wavelength of the second harmonic. In the inset, magnification of the emission is proposed.

4.1.3.2- Cytotoxicity

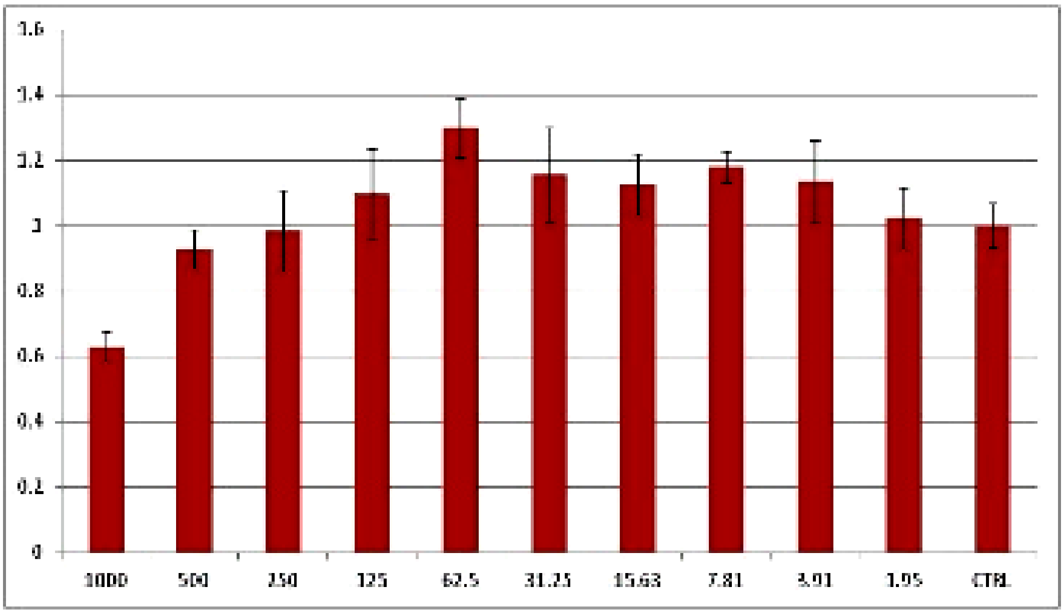

Figure 5: cytotoxicity study on UREANCDs#1

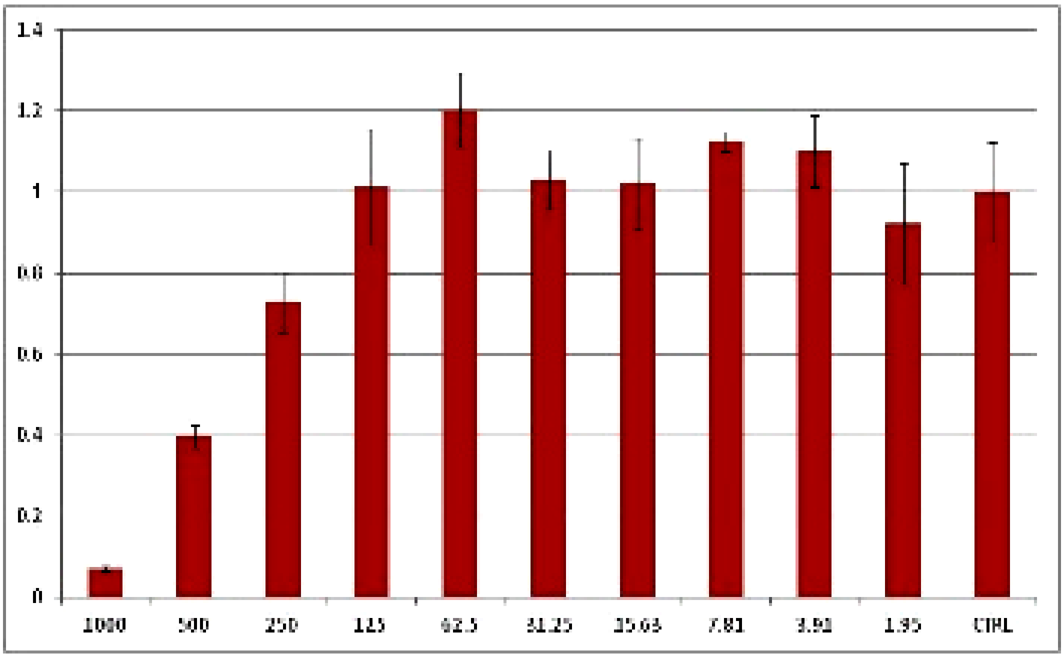

Figure 6: cytotoxicity study on UREANCDs#2

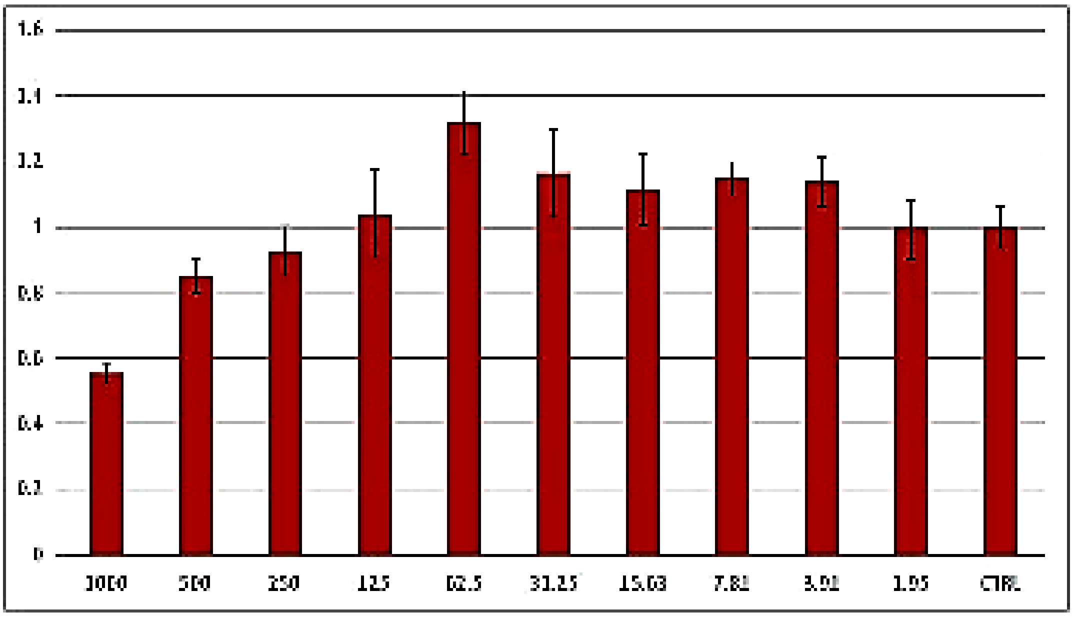

Figure 7: cytotoxicity study on UREA NPCDs#1

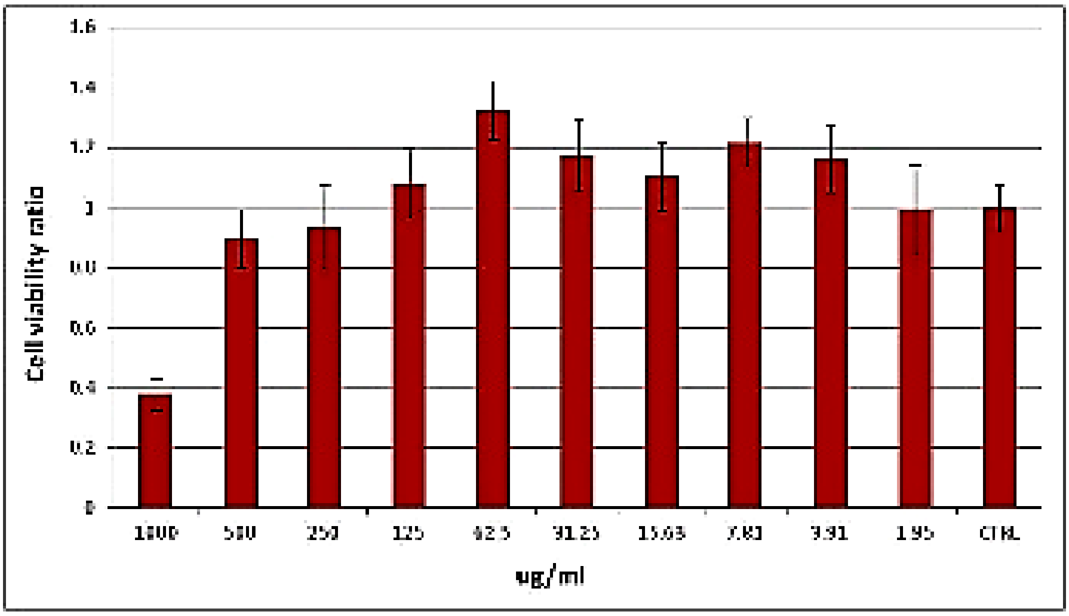

Figure 8: cytotoxicity study onUREA_NPCDs#2

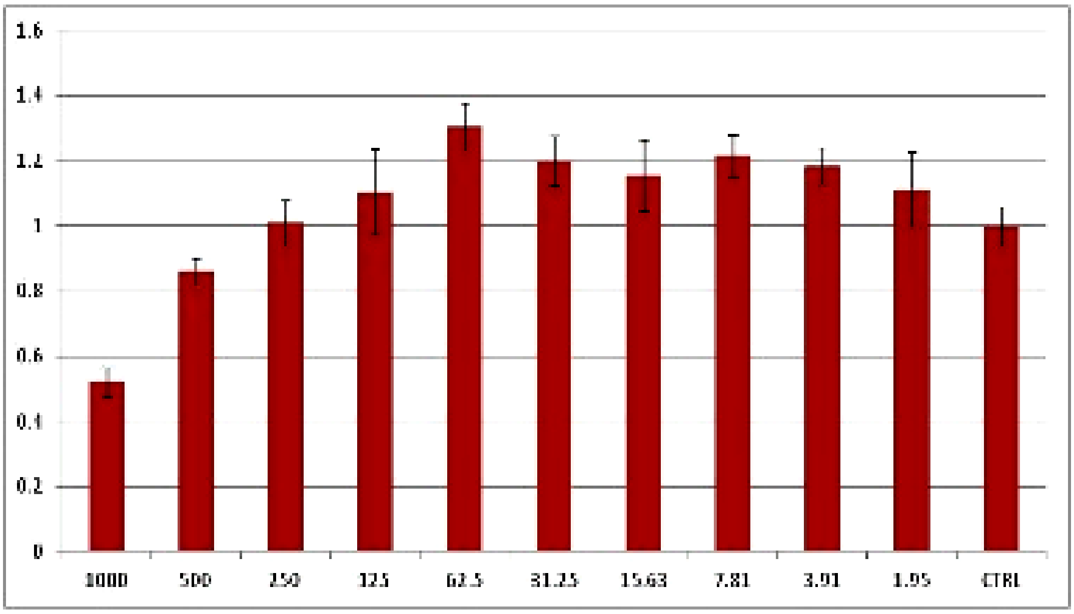

Figure 9: cytotoxicity study onUREA_NBCDs#1

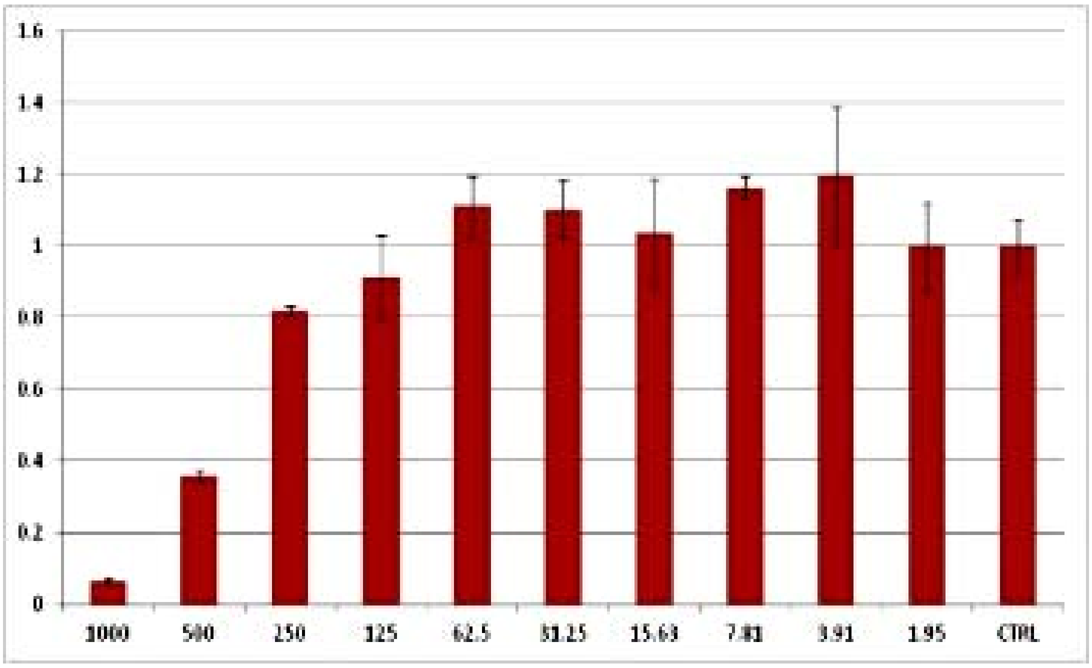

Figure 9: cytotoxicity study onUREA_NBCDs#2

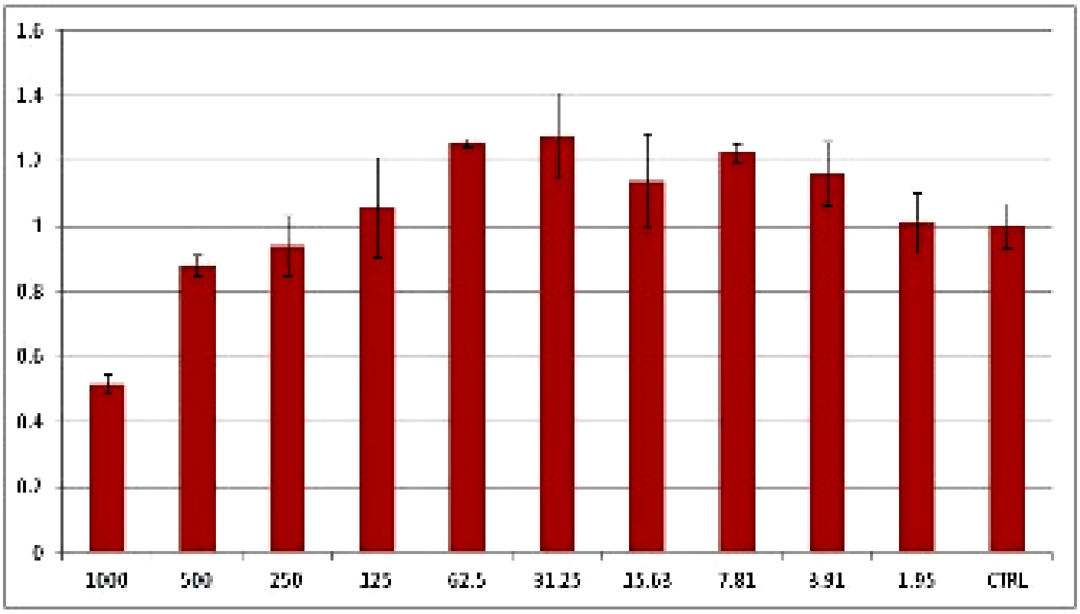

Figure 10: cytotoxicity study onUREA_NSCDs#1

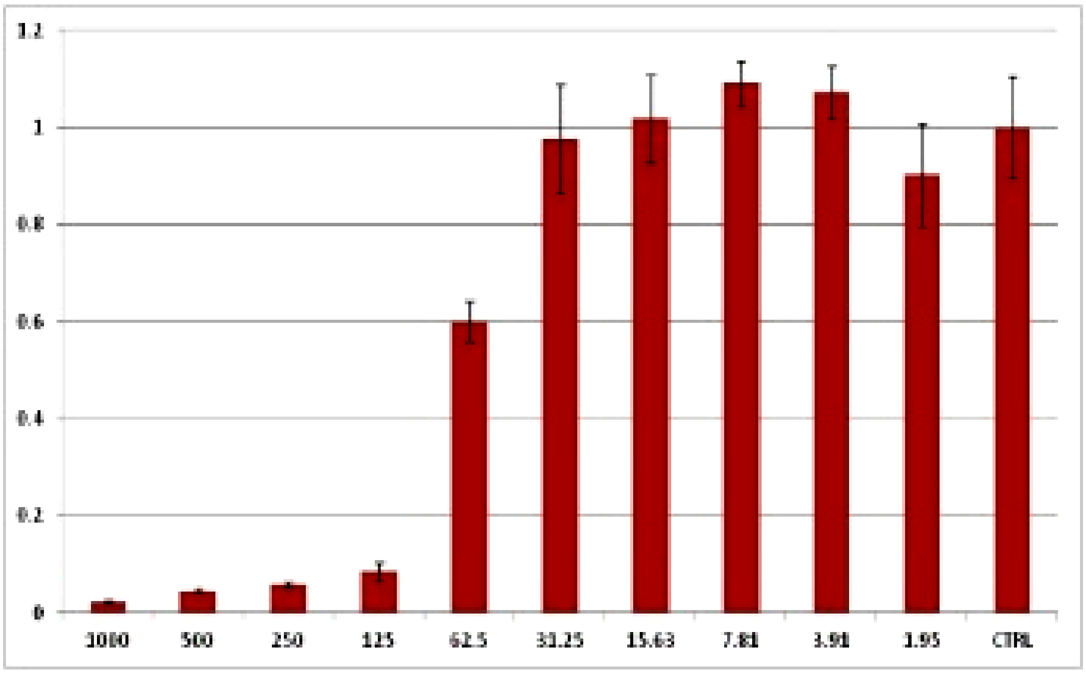

Figure 11: cytotoxicity study onUREA_NSCDs#2

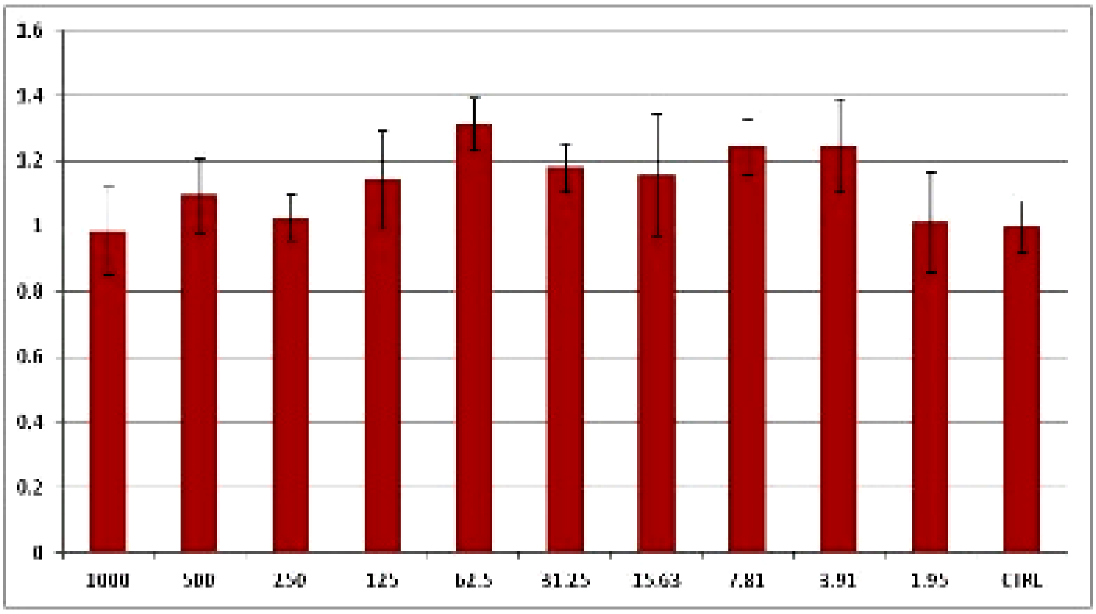

Figure 12: cytotoxicity study onETIDI_NCDs#1

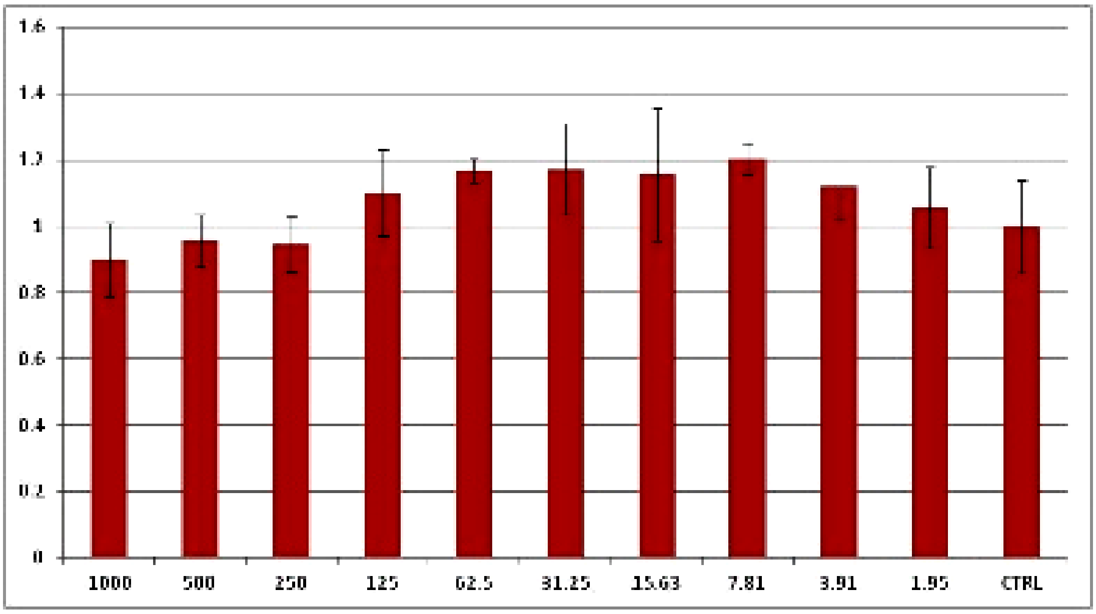

Figure 13: cytotoxicity study onETIDI_NCDs#2

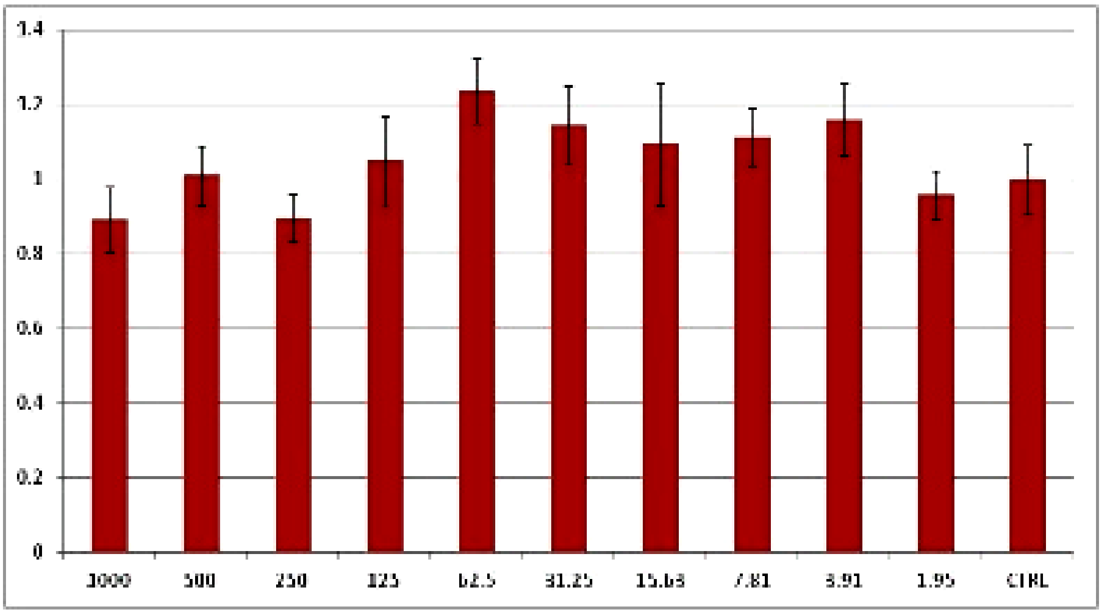

Figure 14: cytotoxicity study onETIDI_NPCDs#1

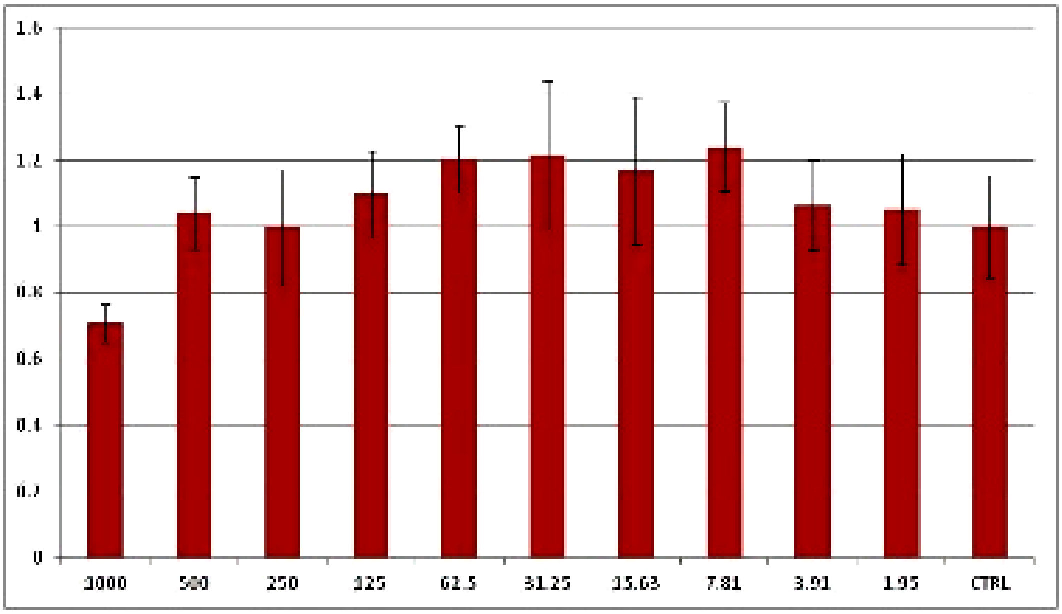

Figure 15: cytotoxicity study onETIDI_NPCDs#2

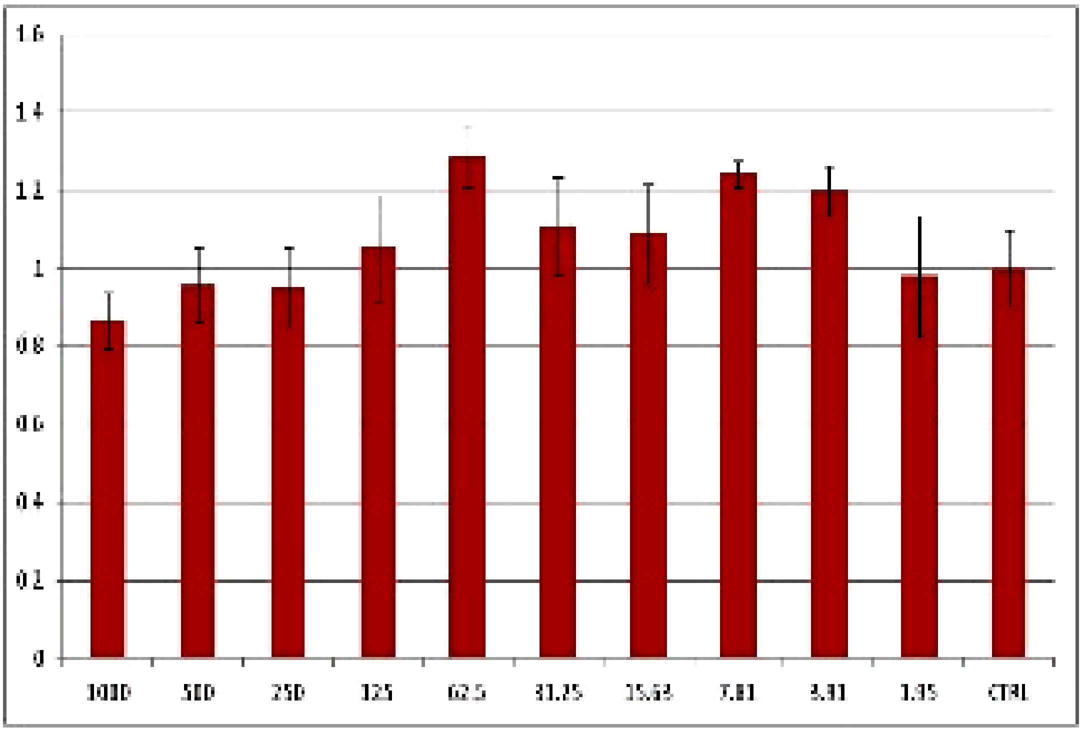

Figure 16: cytotoxicity study onETIDI_NBCDs#1

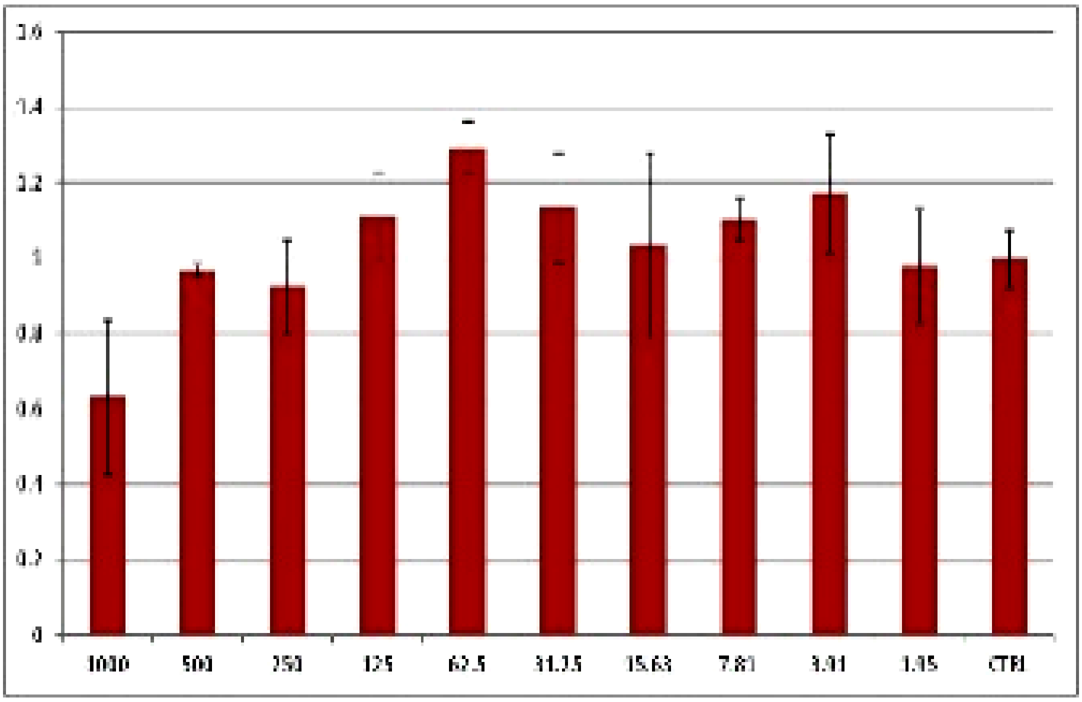

Figure 17: cytotoxicity study onETIDI_NBCDs#2

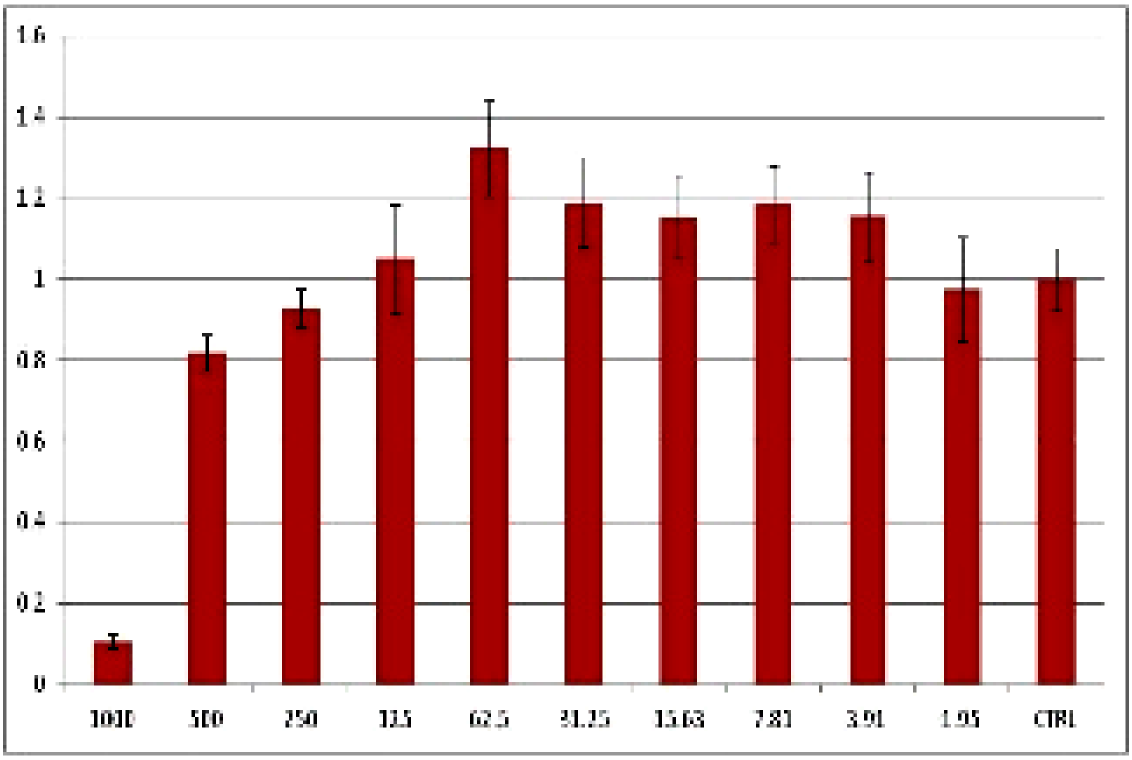

Figure 18: cytotoxicity study onETIDI_NSCDs#1

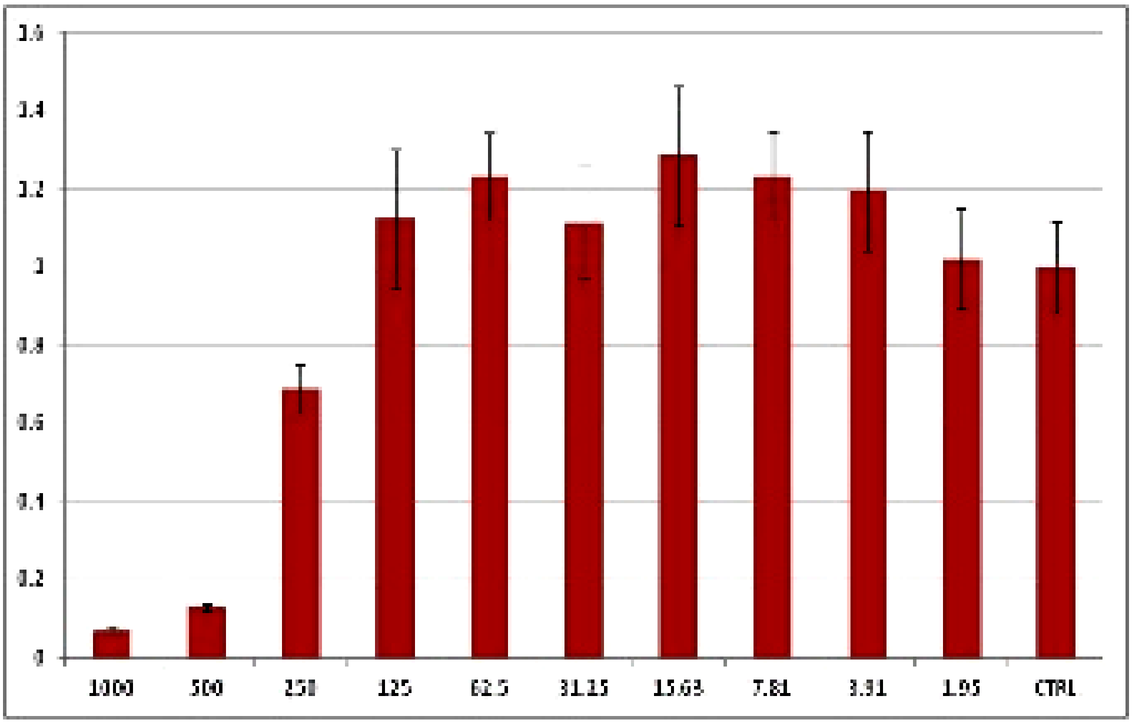

Figure 19: cytotoxicity study onETIDI_NSCDs#2

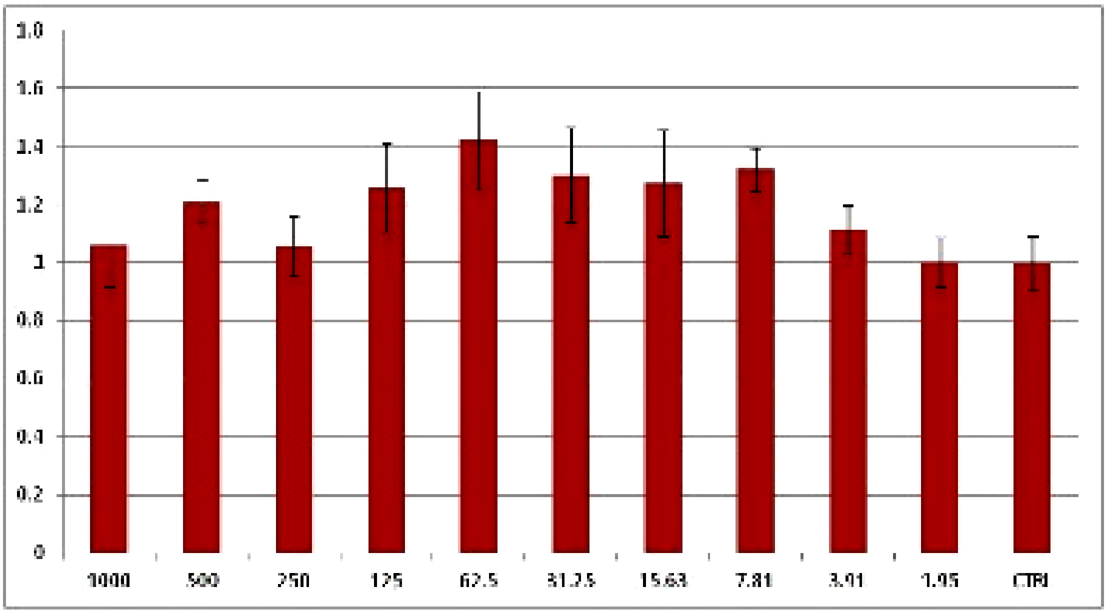

Figure 20: cytotoxicity study onDETA_NCDs#1

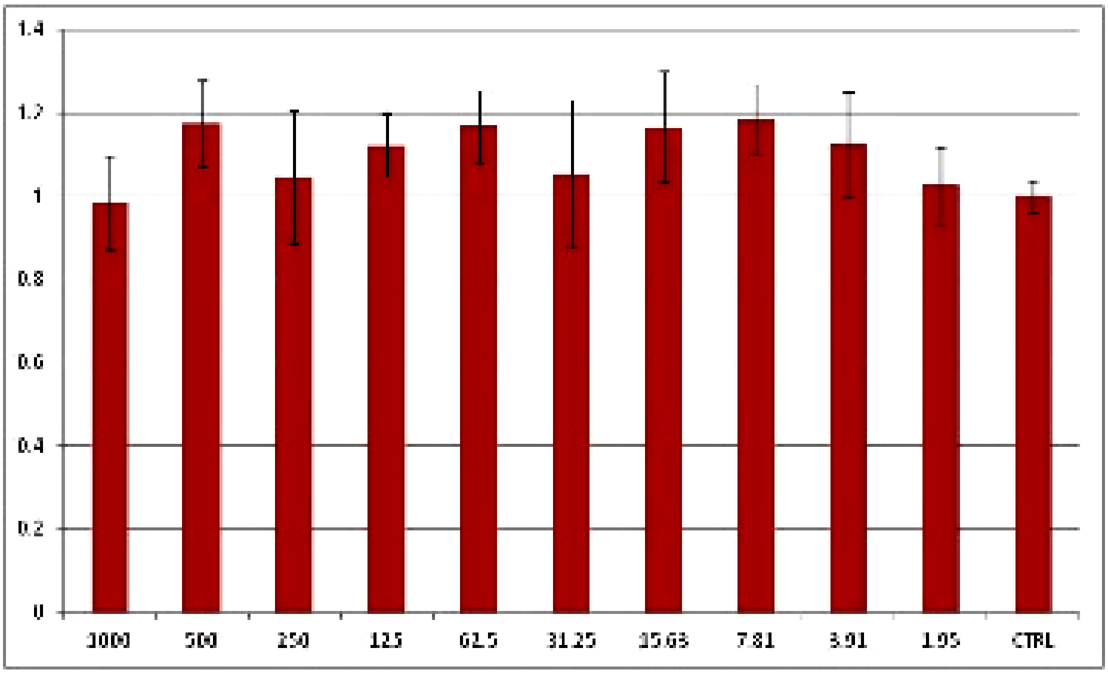

Figure 21: cytotoxicity study onDETA_NCDs#2

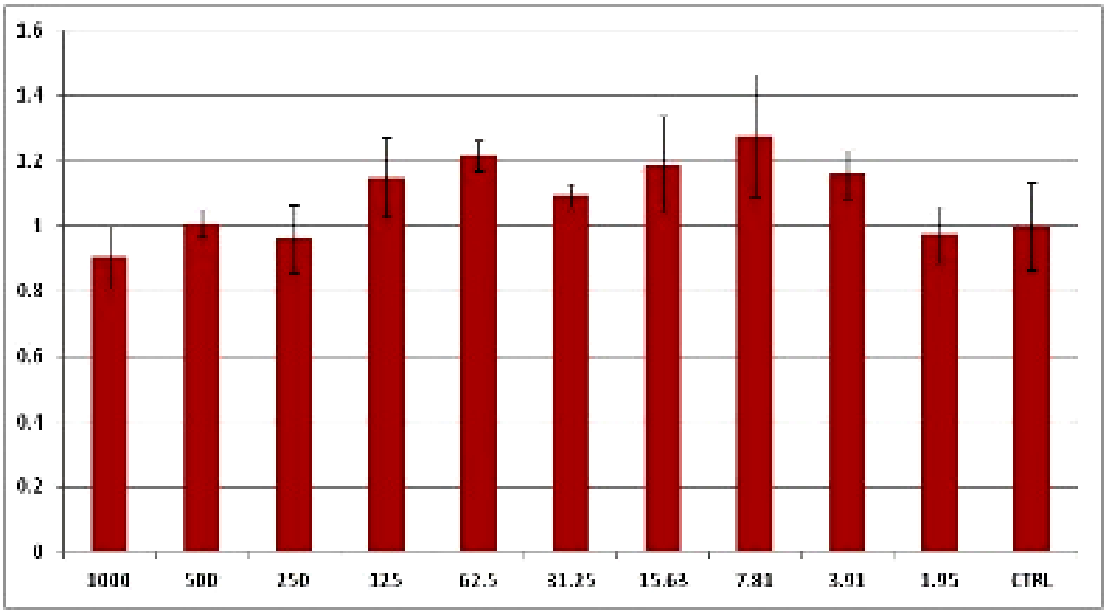

Figure 22: cytotoxicity study onDETA_NPCDs#1

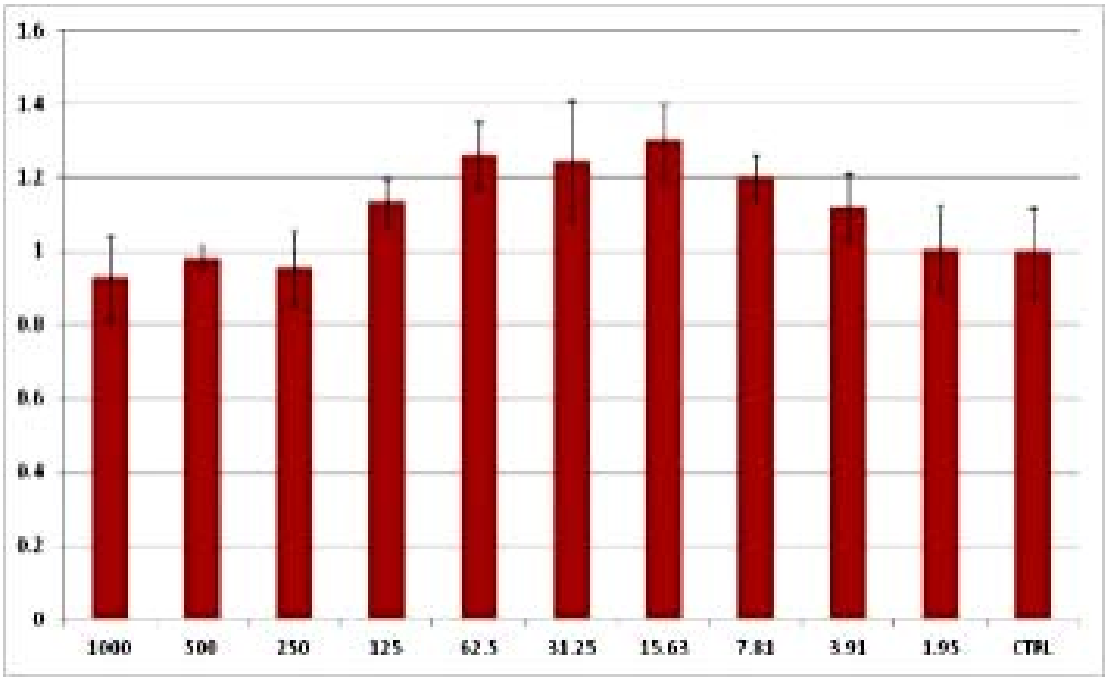

Figure 23: cytotoxicity study onDETA_NPCDs#1

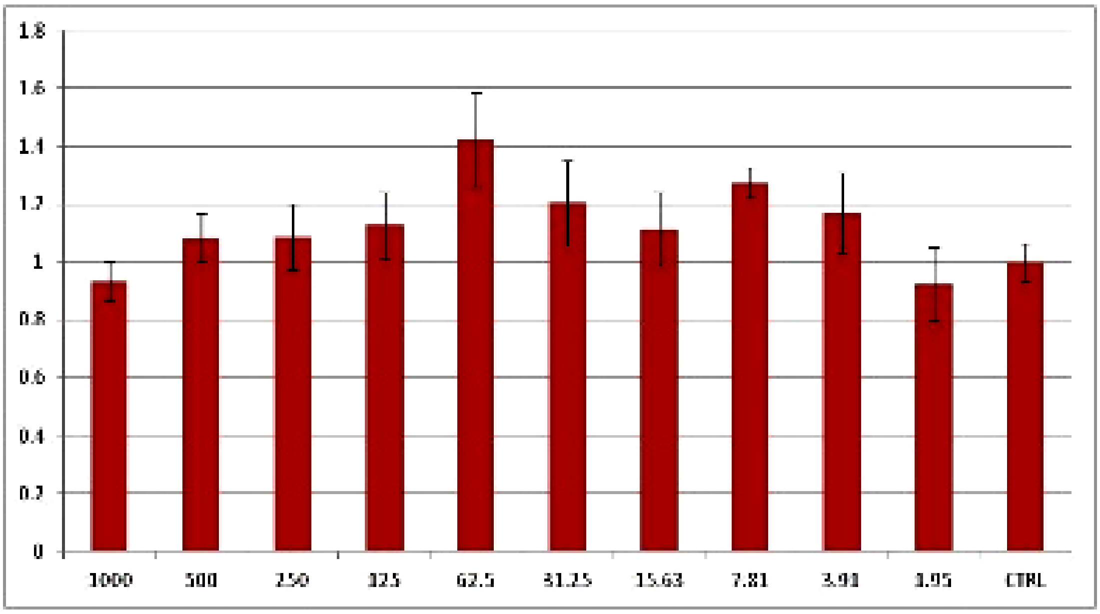

Figure 24: cytotoxicity study onDETA_NBCDs#1

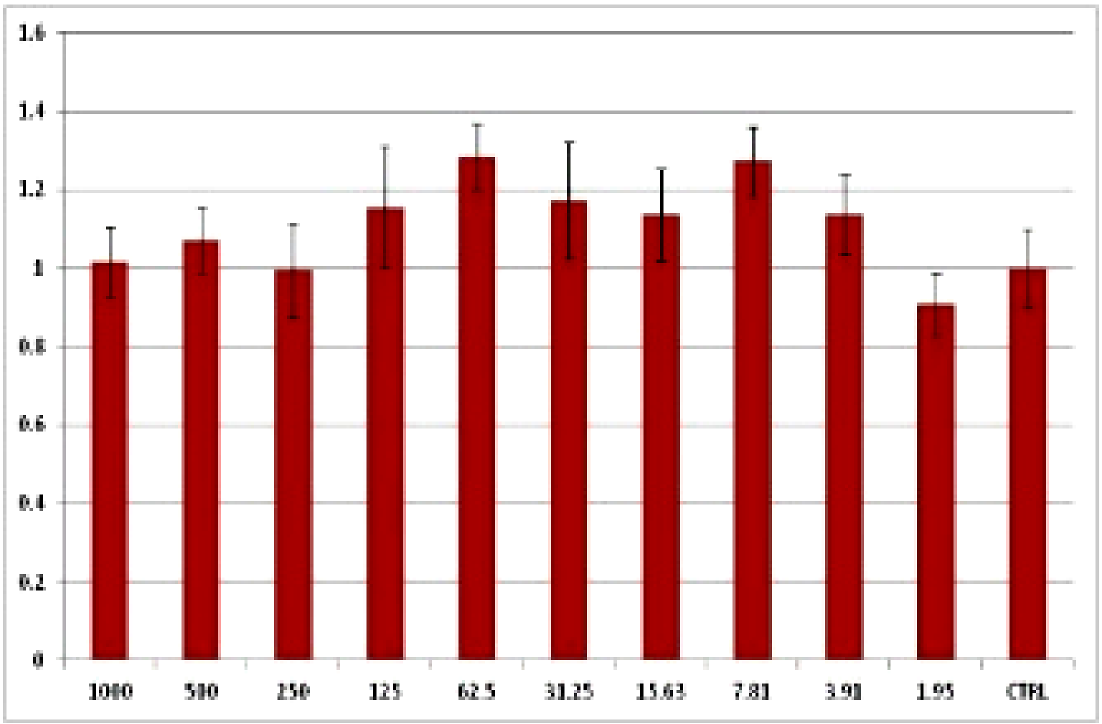

Figure 25: cytotoxicity study onDETA_NBCDs#2

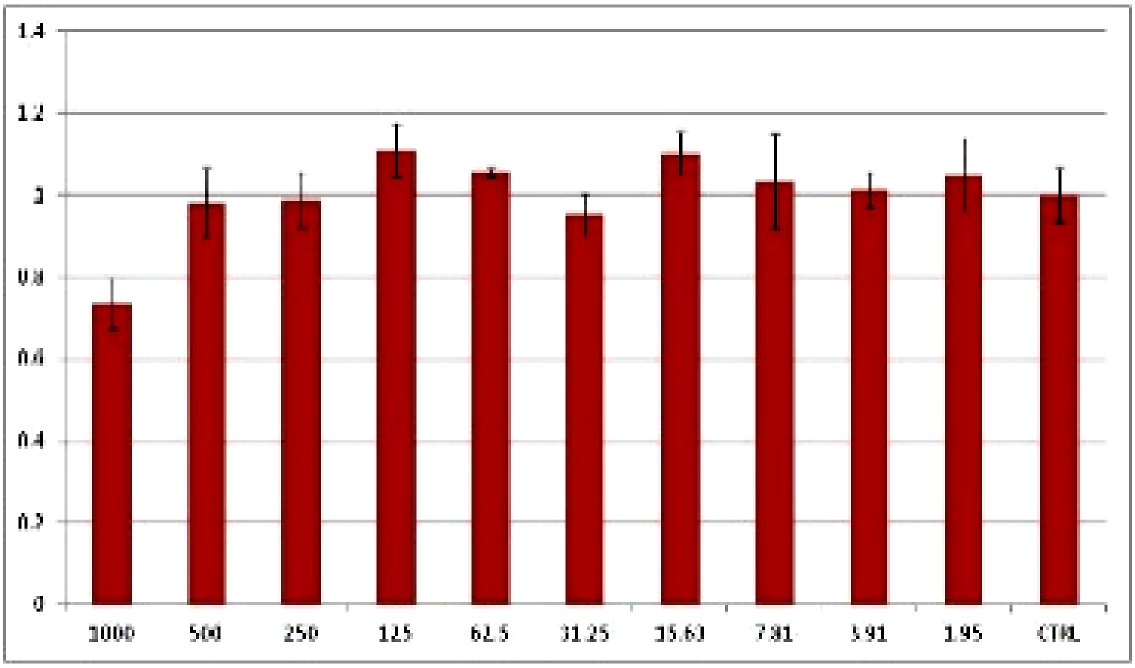

Figure 26: cytotoxicity study onDETA_NSCDs#1

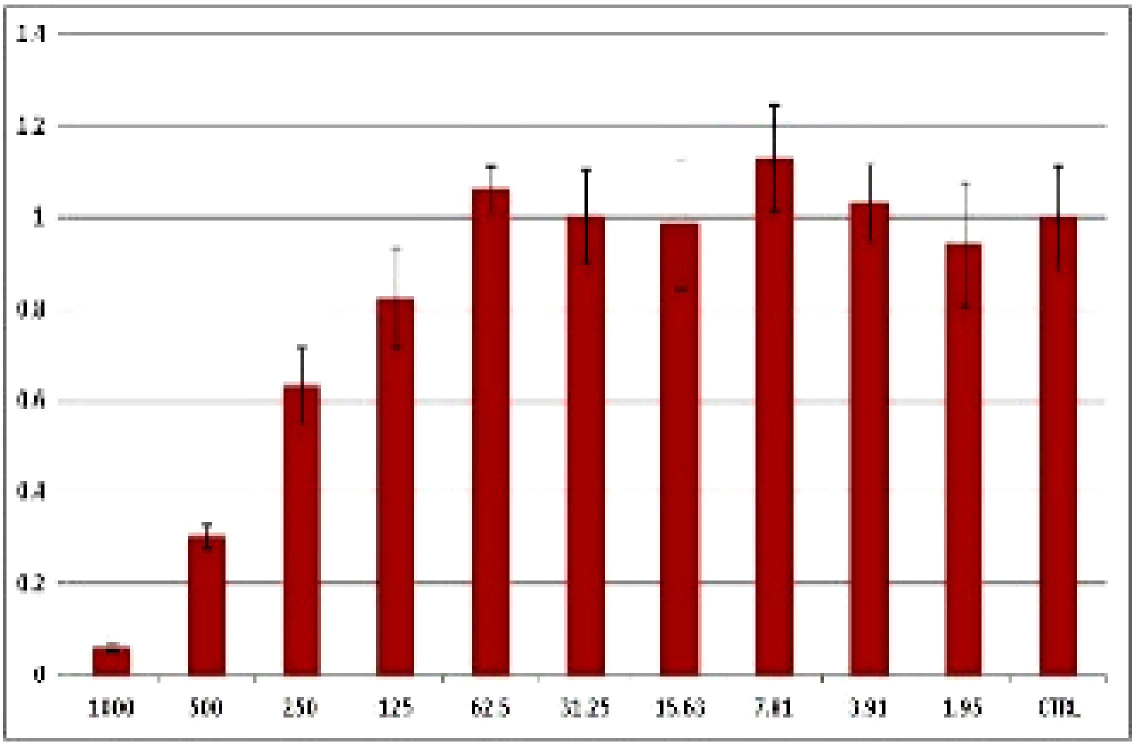

Figure 27: cytotoxicity study onDETA_NSCDs#2

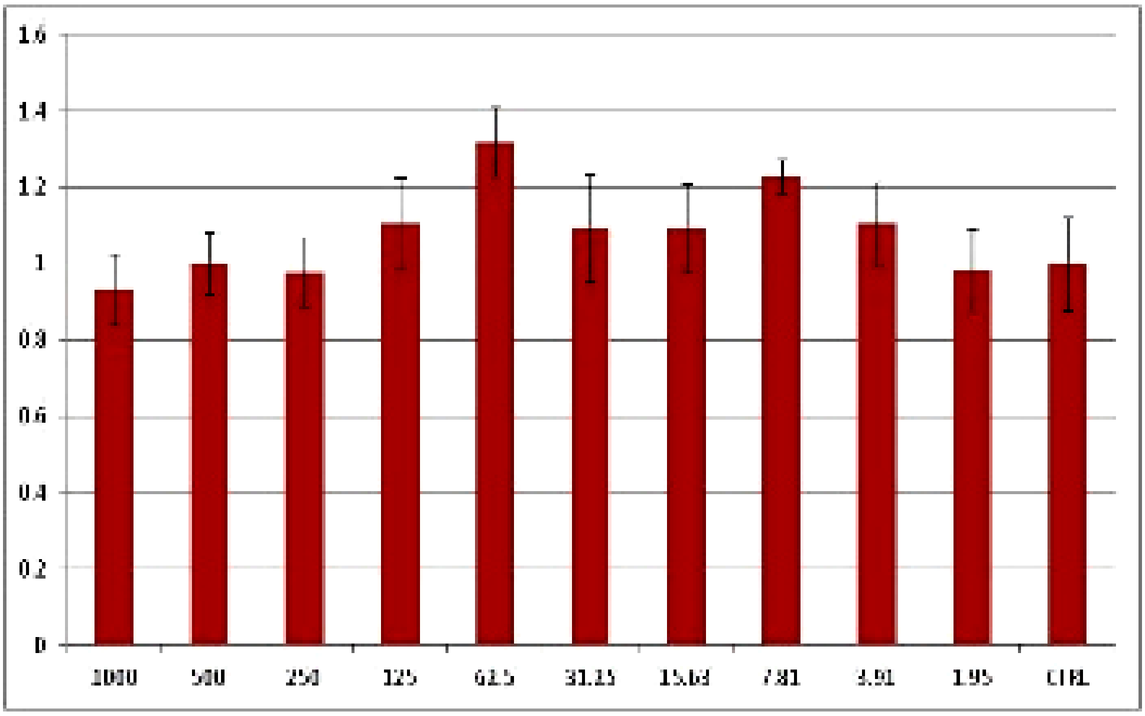

Figure 28: cytotoxicity study onTRITETRA_NCDs#1

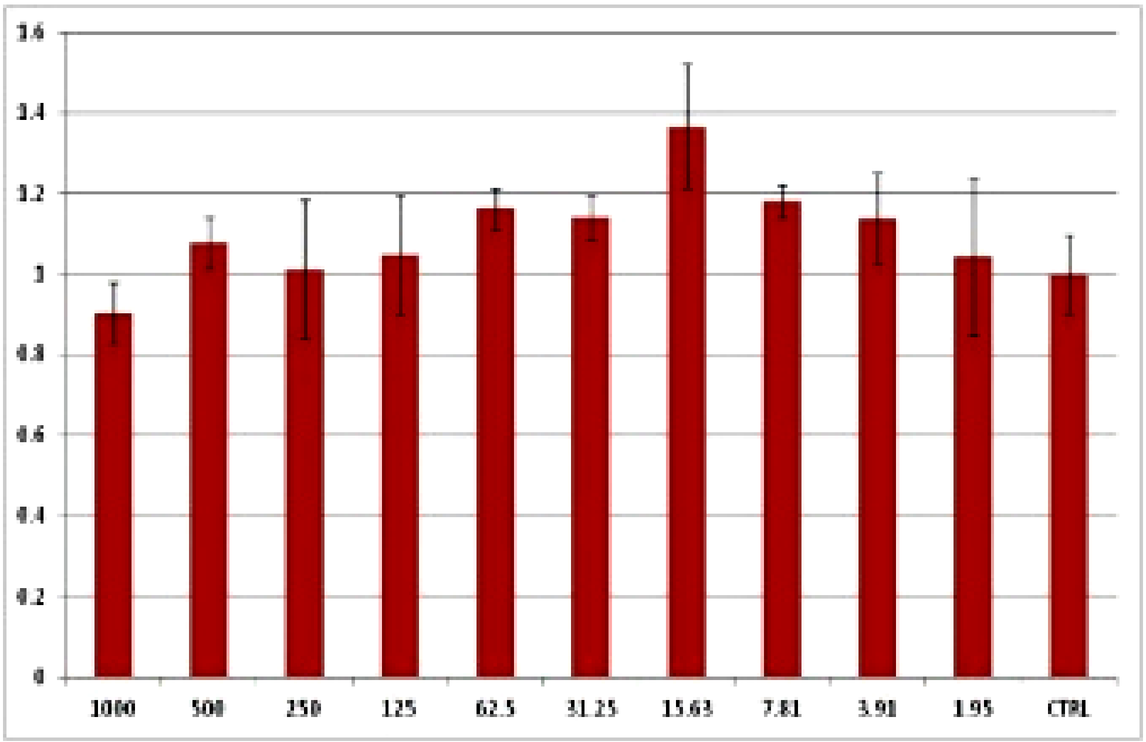

Figure 29: cytotoxicity study onTRITETRA_NCDs#2

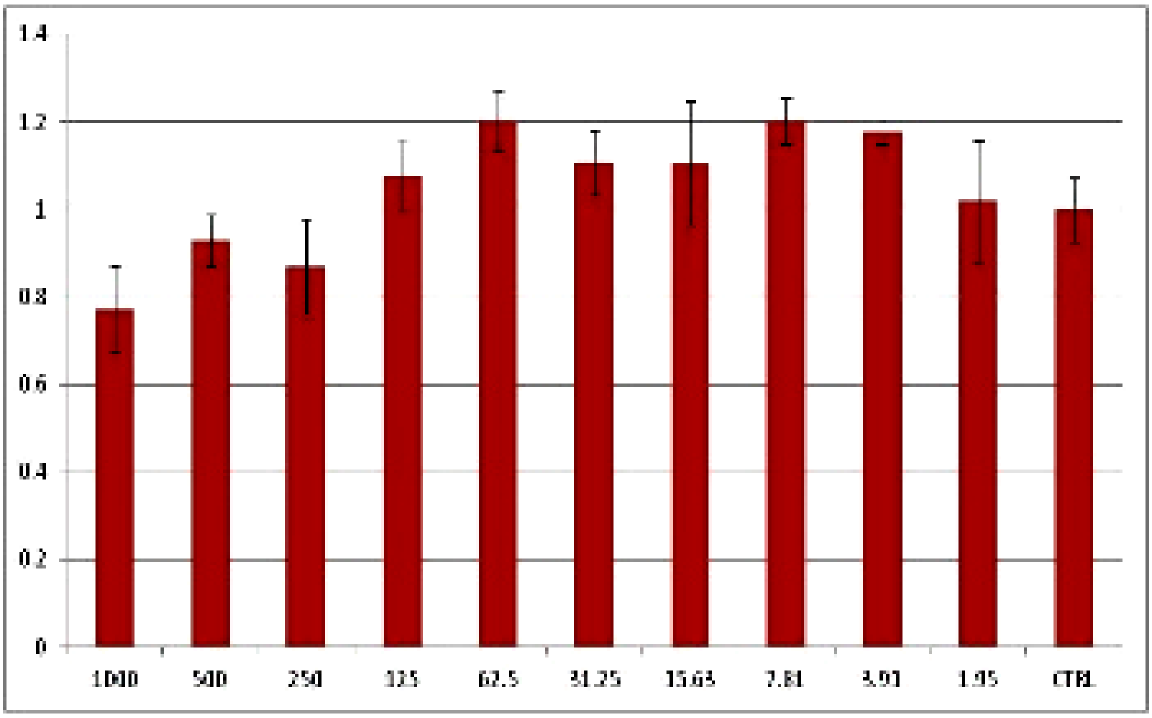

Figure 30: cytotoxicity study onTRITETRA_NPCDs#1

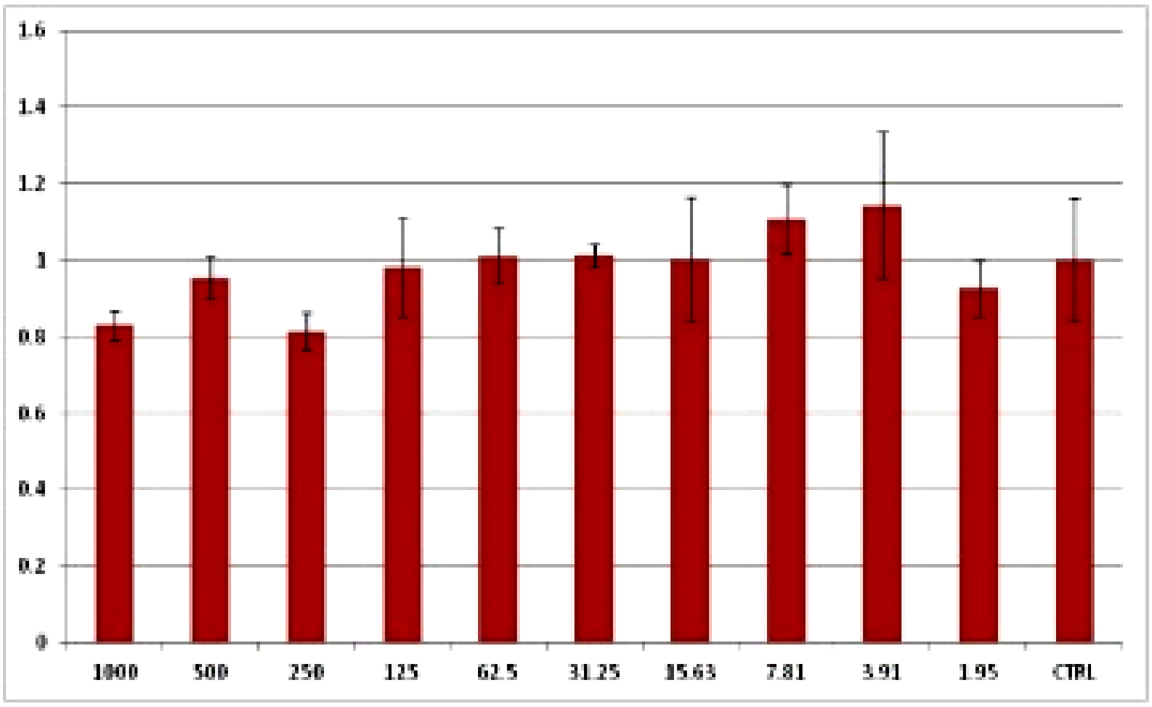

Figure 31: cytotoxicity study onTRITETRA_NPCDs#2

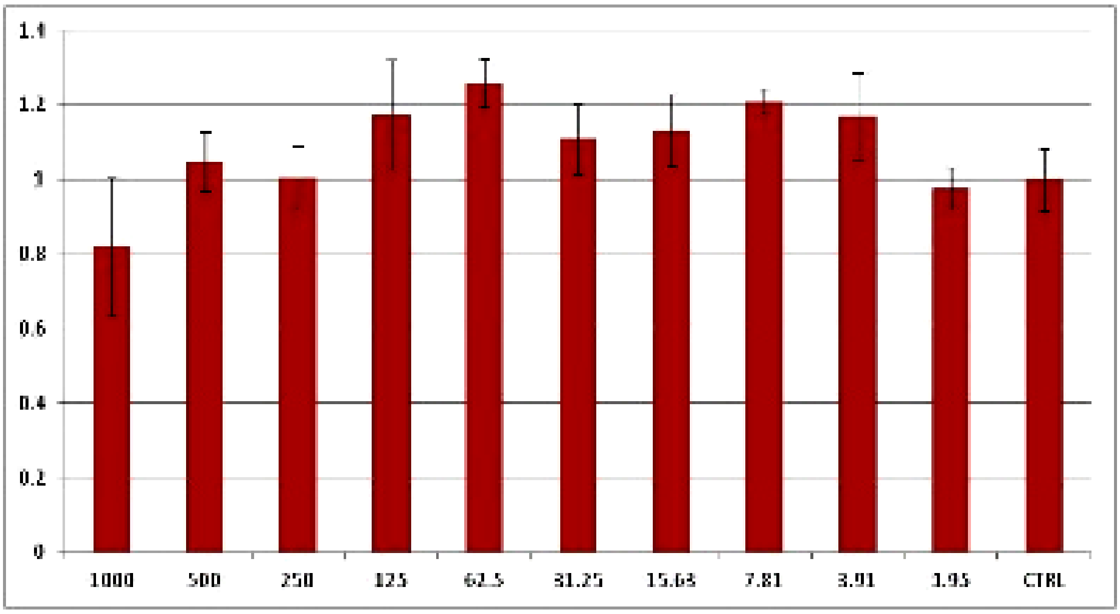

Figure 32: cytotoxicity study onTRITETRA_NBCDs#1

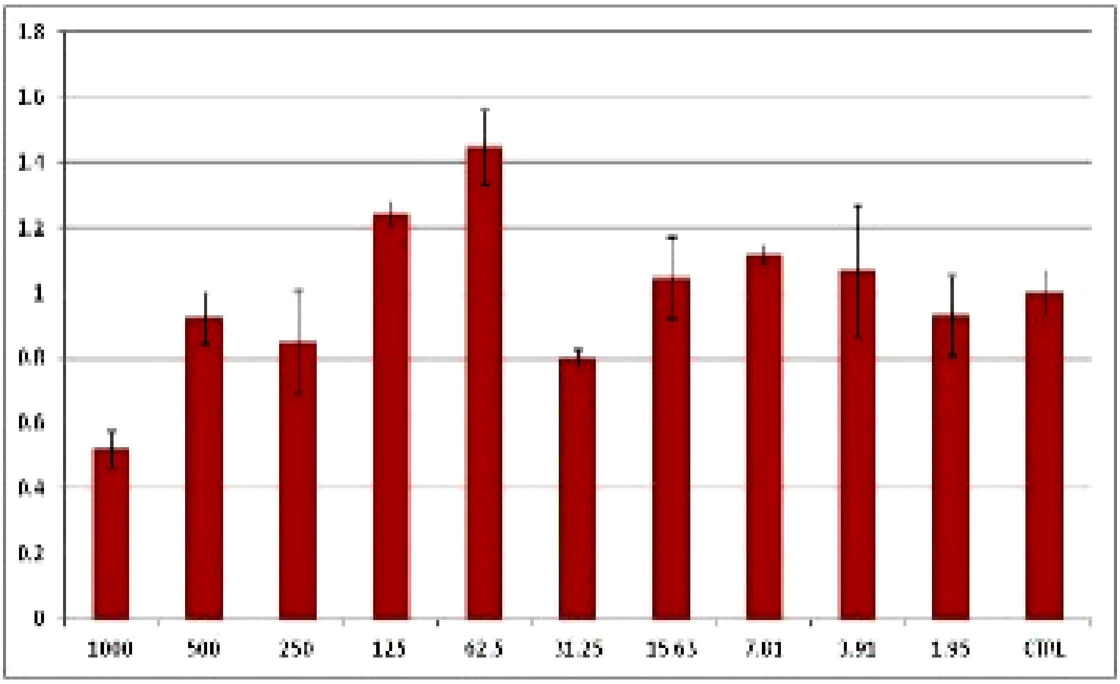

Figure 33: cytotoxicity study onTRITETRA_NBCDs#2

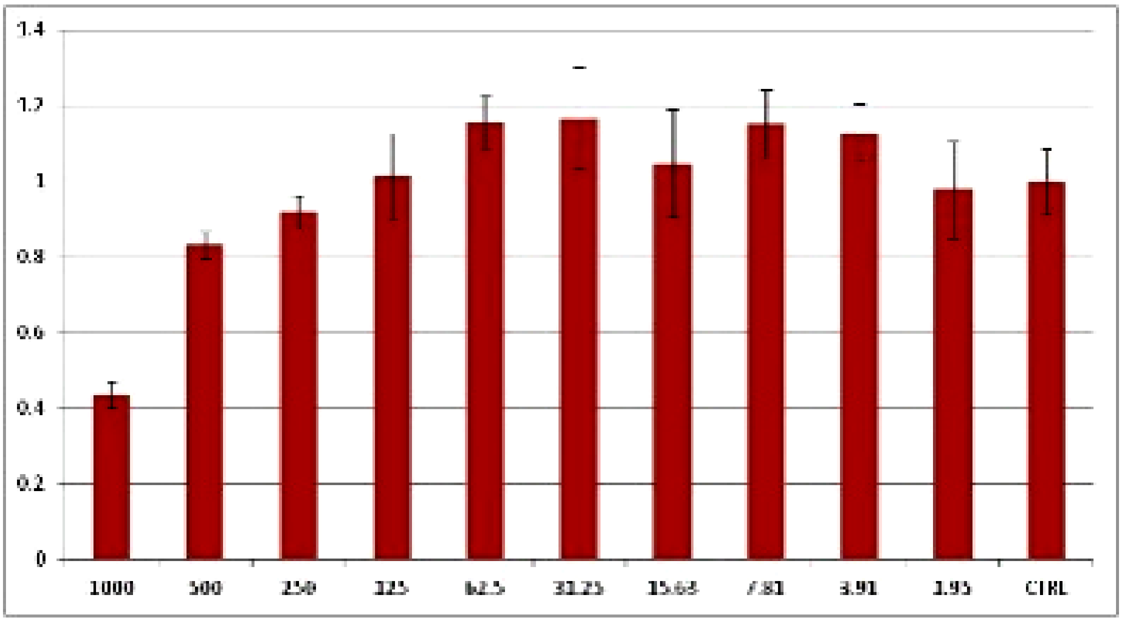

Figure 34: cytotoxicity study onTRITETRA_NSCDs#1

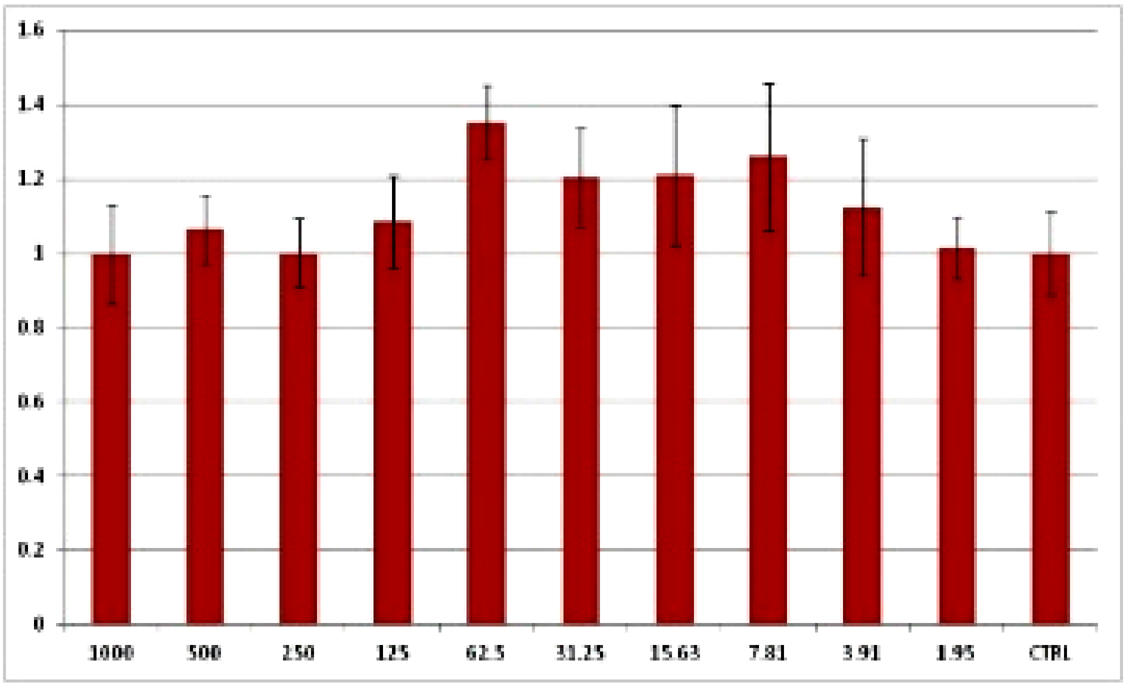

Figure 35: cytotoxicity study onTRITETRA_NSCDs#2

4.1.3.3- Electrophoresys studies

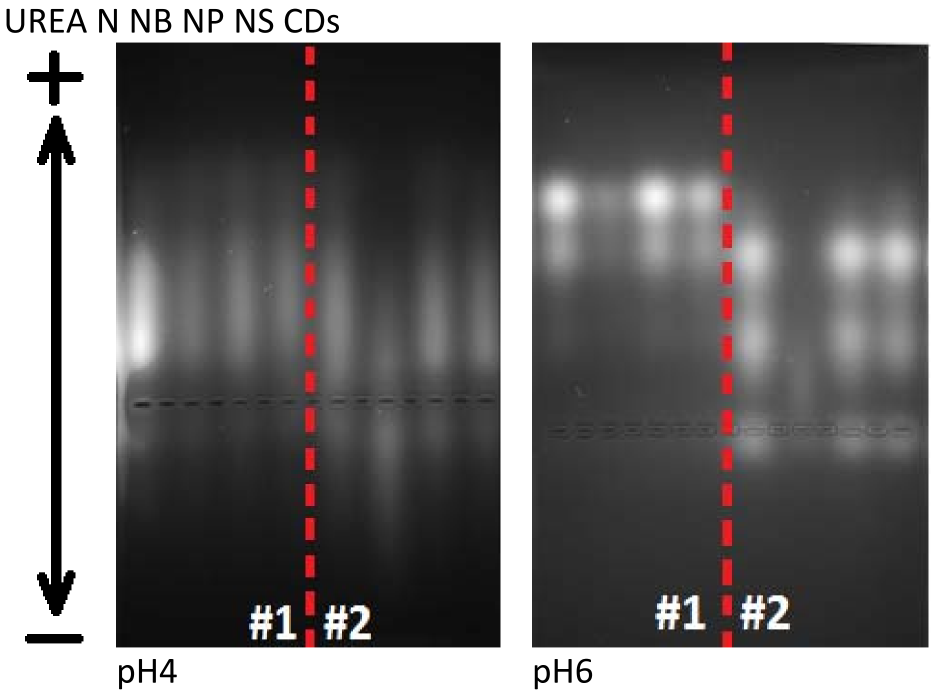

Figure 36 A)and B): Electrophoretic gel at pH 4 and pH6 respectively, performed on repeated synthesis of UREA_NCDs, UREA_NBCDs, UREA_NPCDs and UREA_NSCDs.

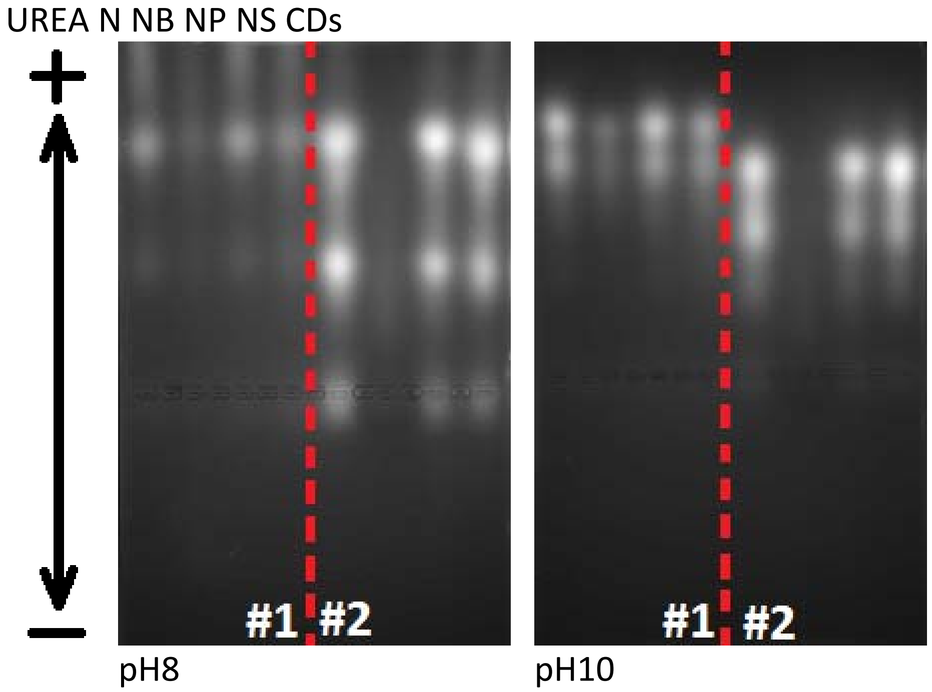

Figure 37 A)and B): Electrophoretic gel at pH 8 and pH10 respectively, performed on repeated synthesis of UREA_NCDs, UREA_NBCDs, UREA_NPCDs and UREA_NSCDs.

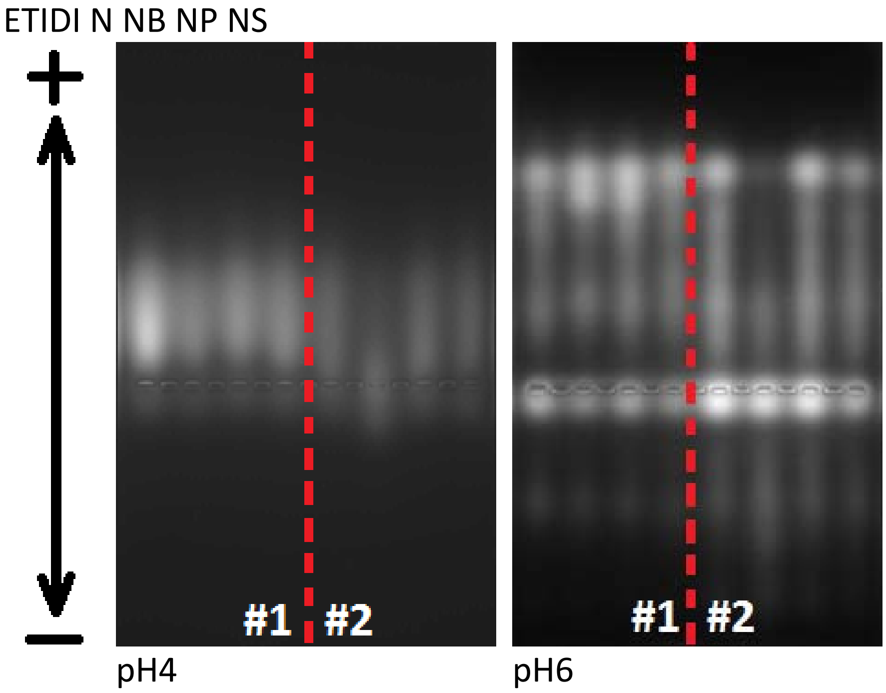

Figure 38 A)and B): Electrophoretic gel at pH 4 and pH6 respectively, performed on repeated synthesis of ETIDI_NCDs, ETIDI_NBCDs, ETIDI_NPCDs and ETIDI_NSCDs.

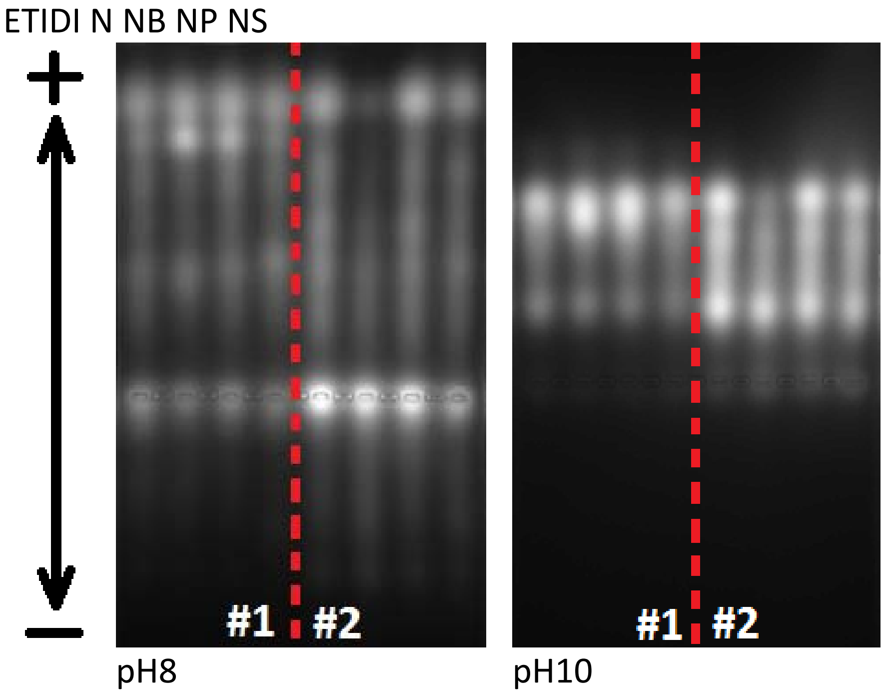

Figure 39 A)and B): Electrophoretic gel at pH 8 and pH10 respectively, performed on repeated synthesis of ETIDI_NCDs, ETIDI_NBCDs, ETIDI_NPCDs and ETIDI_NSCDs.

DETA N NB NP NS

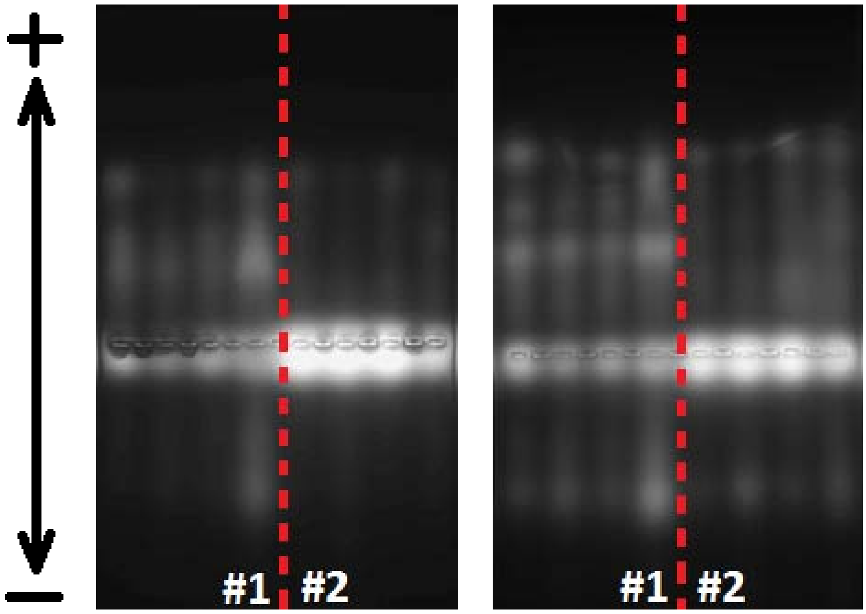

pH4 pH6

Figure 40 A)and B):Electrophoretic gel at pH 4 and pH6 respectively, performed on repeated synthesis DETA_NCDs, DETA _NBCDs, DETA _NPCDs and DETA _NSCDs.

DETA N NB NP NS

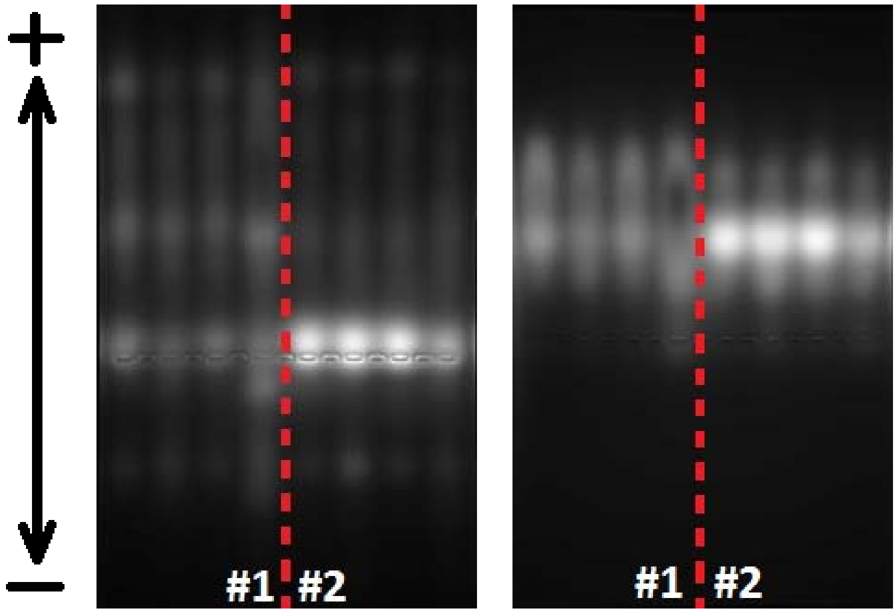

pH8 pH10

Figure 41 A)and B): Electrophoretic gel at pH 8 and pH10 respectively, performed on repeated synthesis of DETA_NCDs, DETA _NBCDs, DETA _NPCDs and DETA _NSCDs.

TRITETRA N NB NP NS

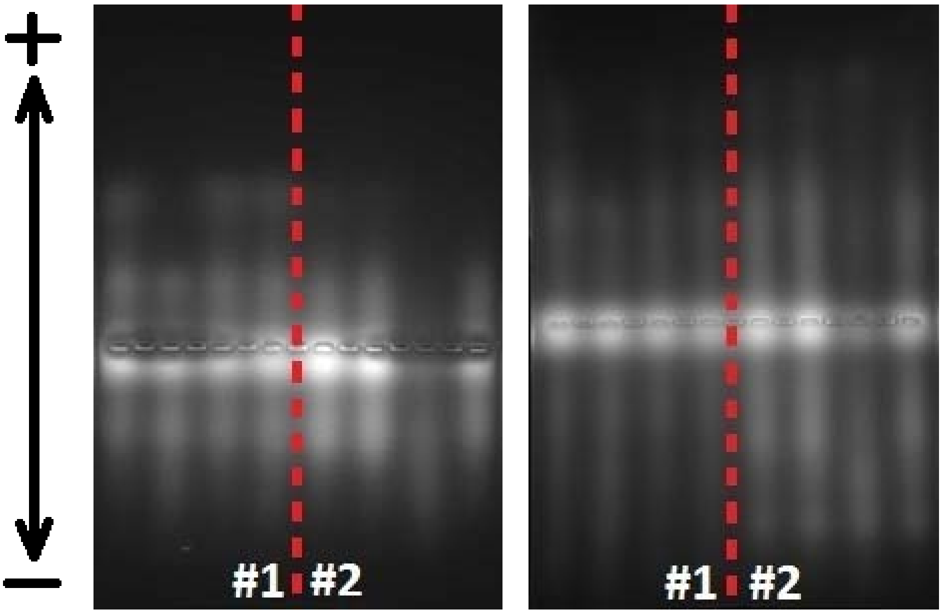

pH4 pH6

Figure 42 A)and B): Electrophoretic gel at pH 4 and pH6 respectively, performed on repeated synthesis TRITETRA_NCDs, TRITETRA_NBCDs, TRITETRA_NPCDs and TRITETRA_NSCDs.

TRITETRA N NB NP NS

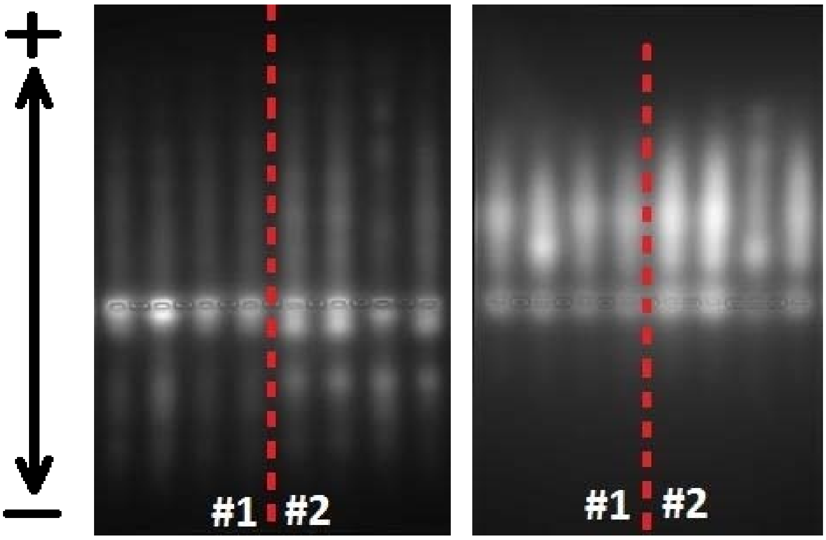

pH8 pH10

Figure 43 A)and B): Electrophoretic gel at pH 8 and pH10 respectively, performed on repeated synthesis of TRITETRA_NCDs, TRITETRA_NBCDs, TRITETRA_NPCDs and TRITETRA_NSCDs.

7-Bibliography

1. Shang, J. *et al.* The Origin of Fluorescence from Graphene Oxide. *Sci. Rep.* **2,** 792 (2012).
2. Wang, J., Choi, H. S. & Wáng, Y. X. J. Exponential growth of publications on carbon nanodots by Chinese authors. *J. Thorac. Dis.* **7,** E201–E205 (2015).
3. Islam, S., Nagpure, S., Kim, D. & Rankin, S. Synthesis and Catalytic Applications of Non-Metal Doped Mesoporous Titania. *Inorganics* **5,** 15 (2017).
4. Fujishima, A. & Honda, K. Electrochemical Evidence for the Mechanism of the Primary State of Photosynthesis. *Bulletin of the Chemical Society of Japan* **44,** 1148–1150 (1971).
5. Kyzas, G. Z. & Matis, K. A. Electroflotation process: A review. *J. Mol. Liq.* **220,** 657–664 (2016).
6. Munter, R. Advanced Oxidation Processes - Current Status and Prospect. *Proc. Est. Acad. Sci. Chem.* **50,** 59–80 (2001).
7. Sharma, S., Ruparelia, J. & Patel, M. A general review on advanced oxidation processes for waste water treatment. *Int. Conf. Curr.* 8–10 (2011).
8. Fawell, J. K., Lund, U. & Mintz, B. Chlorine in Drinking-water Background document for development of WHO Guidelines for Drinking-water Quality. *World Heal. Organ. Geneva* **2,** 6 (1996).
9. Georgakilas, V., Perman, J. A., Tucek, J. & Zboril, R. Broad Family of Carbon Nanoallotropes: Classification, Chemistry, and Applications of Fullerenes, Carbon Dots, Nanotubes, Graphene, Nanodiamonds, and Combined Superstructures. *Chem. Rev.* **115,** 4744–4822 (2015).
10. Gu, J. *et al.* High-yield synthesis of graphene quantum dots with strong green photoluminescence. *RSC Adv.* **4,** 50141–50144 (2014).
11. Chen, W., Hu, C., Yang, Y., Cui, J. & Liu, Y. Rapid synthesis of carbon dots by hydrothermal treatment of lignin. *Materials (Basel).* **9,** (2016).
12. Zhao, Y. *et al.* Carbon Dots: From Intense Absorption in Visible Range to Excitation-Independent and Excitation-Dependent Photoluminescence. *Fullerenes Nanotub. Carbon Nanostructures* **23,** 922–929 (2015).
13. Jiang, K. *et al.* Red, green, and blue luminescence by carbon dots: Full-color emission tuning and multicolor cellular imaging. *Angew. Chemie - Int. Ed.* **54,** 5360–5363 (2015).
14. Tian, L., Song, Y., Chang, X. & Chen, S. Hydrothermally enhanced photoluminescence of carbon nanoparticles. *Scr. Mater.* **62,** 883–886 (2010).
15. Hu, L. *et al.* Multifunctional carbon dots with high quantum yield for imaging and gene delivery. *Carbon N. Y.* **67,** 508–513 (2014).
16. Yang, Z. *et al.* Controllable Synthesis of Fluorescent Carbon Dots and Their Detection Application as Nanoprobes Citation. *Nano-Micro Lett* **5,** 247–259 (2013).
17. Sahu, S., Behera, B., Maiti, T. K. & Mohapatra, S. Simple one-step synthesis of highly luminescent carbon dots from orange juice: application as excellent bio-imaging agents. *Chem. Commun.* **48,** 8835 (2012).

18. Chandra, S. *et al.* Luminescent S-doped carbon dots: an emergent architecture for multimodal applications. *J. Mater. Chem. B* **1,** 2375 (2013).

19. Zeng, Y. W. *et al.* N, S co-doped carbon dots with orange luminescence synthesized through polymerization and carbonization reaction of amino acids. *Appl. Surf. Sci.* **342,** 136–143 (2015).

20. Bhattacharjee, L., Manoharan, R., Mohanta, K. & Bhattacharjee, R. R. Conducting carbon quantum dots – a nascent nanomaterial. *J. Mater. Chem. A* **3,** 1580–1586 (2015).

21. Dong, Y. *et al.* Blue luminescent graphene quantum dots and graphene oxide prepared by tuning the carbonization degree of citric acid. *Carbon N. Y.* **50,** 4738–4743 (2012).

22. Luk, C. M. *et al.* An efficient and stable fluorescent graphene quantum dot–agar composite as a converting material in white light emitting diodes. *J. Mater. Chem.* **22,** 22378 (2012).

23. Li, H. Water-Soluble Fluorescent Carbon Quantum Dots and Photocatalyst Design. *Angew. Chem Int. Ed.* **49,** 4430–4434 (2010).

24. Deng, J. *et al.* Electrochemical synthesis of carbon nanodots directly from alcohols. *Chem. - A Eur. J.* **20,** 4993–4999 (2014).

25. Huang, X., Li, Y., Zhong, X., Rider, A. E. & Ostrikov, K. Fast microplasma synthesis of blue luminescent carbon quantum dots at ambient conditions. *Plasma Process. Polym.* **12,** 59–65 (2015).

26. Kim, J. & Suh, J. S. Size-controllable and low-cost fabrication of graphene quantum dots using thermal plasma jet. *ACS Nano* **8,** 4190–4196 (2014).

27. Mao, L. H. *et al.* Facile access to white fluorescent carbon dots toward light-emitting devices. *Angew. Chem. Int. Ed.* **53,** 6417–6425 (2014).

28. Park, S. Y. *et al.* Photoluminescent green carbon nanodots from food-waste-derived sources: Large-scale synthesis, properties, and biomedical applications. *ACS Appl. Mater. Interfaces* **6,** 3365–3370 (2014).

29. Li, H. *et al.* Carbon quantum dots/Cu2O composites with protruding nanostructures and their highly efficient (near) infrared photocatalytic behavior. *J. Mater. Chem.* **22,** 17470 (2012).

30. Kwon, W. & Rhee, S.-W. Facile synthesis of graphitic carbon quantum dots with size tunability and uniformity using reverse micelles. *Chem. Commun.* **48,** 5256 (2012).

31. Fang, Y. *et al.* Easy synthesis and imaging applications of cross-linked green fluorescent hollow carbon nanoparticles. *ACS Nano* **6,** 400–409 (2012).

32. Yang, Y. *et al.* Fluorescent N-Doped Carbon Dots as in Vitro and in Vivo Nanothermometer. *ACS Appl. Mater. Interfaces* **7,** 27324–27330 (2015).

33. Wen, X., Yu, P., Toh, Y. R., Hao, X. & Tang, J. Intrinsic and Extrinsic Fluorescence in Carbon Nanodots: Ultrafast Time-Resolved Fluorescence and Carrier Dynamics. *Adv. Opt. Mater.* **1,** 173–178 (2013).

34. Zong, J., Zhu, Y., Yang, X., Shen, J. & Li, C. Synthesis of photoluminescent carbogenic dots using mesoporous silica spheres as nanoreactors. *Chem. Commun.* **47,** 764–766 (2011).

35. Shi, L. *et al.* Carbon dots with high fluorescence quantum yield: the fluorescence originates from organic fluorophores. *Nanoscale* **8,** 14374–14378 (2016).

36. Krysmann, M. J., Kelarakis, A., Dallas, P. & Giannelis, E. P. Formation mechanism of carbogenic nanoparticles with dual photoluminescence emission. *J. Am. Chem. Soc.* **134,** 747–750 (2012).

37. Zhu, S. *et al.* The photoluminescence mechanism in carbon dots (graphene quantum dots, carbon nanodots, and polymer dots): current state and future perspective. *Nano Res.* **8,** 355–381 (2015).

38. Gan, Z., Xu, H. & Hao, Y. Mechanism for excitation-dependent photoluminescence from graphene quantum dots and other graphene oxide derivates: consensus, debates and challenges. *Nanoscale* **8,** 7794–7807 (2016).

39. Xu, X. *et al.* Electrophoretic Analysis and Purification of Fluorescent Single-Walled Carbon Nanotube Fragments. *J. Am. Chem. Soc.* **126,** 12736–12737 (2004).

40. Pan, D., Zhang, J., Li, Z. & Wu, M. Hydrothermal route for cutting graphene sheets into blue-luminescent graphene quantum dots. *Adv. Mater.* **22,** 734–738 (2010).

41. Tang, L. *et al.* Deep ultraviolet photoluminescence of water-soluble self-passivated graphene quantum dots. *ACS Nano* **6,** 5102–5110 (2012).

42. Li, Y. Y. *et al.* Nanotechnology Applications for Clean Water. *J. Am. Chem. Soc.* **5,** 1–6 (2013).

43. Zhu, S. *et al.* Graphene quantum dots with controllable surface oxidation, tunable fluorescence and up-conversion emission. *RSC Adv.* **2,** 2717 (2012).

44. Wang, D., Wang, L., Dong, X., Shi, Z. & Jin, J. Chemically tailoring graphene oxides into fluorescent nanosheets for Fe 3+ ion detection. *Carbon N. Y.* **50,** 2147–2154 (2012).

45. Ming, H. *et al.* Large scale electrochemical synthesis of high quality carbon nanodots and their photocatalytic property. *Dalt. Trans.* **41,** 9526 (2012).

46. Zhou, X. *et al.* Photo-Fenton reaction of graphene oxide: A new strategy to prepare graphene quantum dots for DNA cleavage. *ACS Nano* **6,** 6592–6599 (2012).

47. Li, Y. *et al.* An electrochemical avenue to green-luminescent graphene quantum dots as potential electron-acceptors for photovoltaics. *Adv. Mater.* **23,** 776–780 (2011).

48. Gupta, V. *et al.* Luminscent graphene quantum dots for organic photovoltaic devices. *J. Am. Chem. Soc.* **133,** 9960–9963 (2011).

49. Tetsuka, H. *et al.* Optically tunable amino-functionalized graphene quantum dots. *Adv. Mater.* **24,** 5333–5338 (2012).

50. Nie, H. *et al.* Carbon dots with continuously tunable full-color emission and their application in ratiometric pH sensing. *Chem. Mater.* **26,** 3104–3112 (2014).

51. Hernandez, Y. *et al.* High-yield production of graphene by liquid-phase exfoliation of graphite. *Nat. Nanotechnol.* **3,** 563–568 (2008).

52. Lu, J. *et al.* One-Pot Synthesis of Fluorescent Carbon Graphene by the Exfoliation of Graphite in Ionic Liquids. *ACS Nano* **3,** 2367–2375 (2009).

53. Li, L. L. *et al.* A facile microwave avenue to electrochemiluminescent two-color graphene quantum dots. *Adv. Funct. Mater.* **22,** 2971–2979 (2012).

54. Sun, H., Wu, L., Gao, N., Ren, J. & Qu, X. Improvement of photoluminescence of graphene quantum dots with a biocompatible photochemical reduction pathway and its bioimaging application. *ACS Appl. Mater. Interfaces* **5,** 1174–1179 (2013).

55. Kozawa, D. *et al.* Excitonic photoluminescence from nanodisc states in graphene oxides. *J. Phys. Chem. Lett.* **5,** 1754–1759 (2014).

56. Sun, Y. P. *et al.* Quantum-sized carbon dots for bright and colorful photoluminescence. *J. Am. Chem. Soc.* **128,** 7756–7757 (2006).

57. Zhou, L., Lin, Y., Huang, Z., Ren, J. & Qu, X. Carbon nanodots as fluorescence probes for rapid, sensitive, and label-free detection of Hg $^{2+}$ and biothiols in complex matrices. *Chem. Commun.* **48,** 1147–1149 (2012).

58. Jeong, J. *et al.* Color-tunable photoluminescent fullerene nanoparticles. *Adv. Mater.* **24,** 1999–2003 (2012).

59. Bhattacharya, A., Chatterjee, S., Prajapati, R. & Mukherjee, T. K. Size-dependent penetration of carbon dots inside the ferritin nanocages: evidence for the quantum confinement effect in carbon dots. *Phys. Chem. Chem. Phys.* **17,** 12833–12840 (2015).

60. Aloshyna, M., Kozankiewicz, B., Hadad, C. M., Snoonian, J. R. & Platz, M. S. Spectroscopic studies of 12-oxo-5(12H)-naphthacenylidene and 7H-benz[de]anthracen-7-ylidene in shpolskii matrixes at 5 K. *J. Phys. Chem. A* **104,** 3391–3397 (2000).

61. Lingam, K., Podila, R., Qian, H., Serkiz, S. & Rao, A. M. Evidence for edge-state photoluminescence in graphene quantum dots. *Adv. Funct. Mater.* **23,** 5062–5065 (2013).

62. Lin, L. & Zhang, S. Creating high yield water soluble luminescent graphene quantum dots via exfoliating and disintegrating carbon nanotubes and graphite flakes. *Chem. Commun.* **48,** 10177 (2012).

63. Liu, H., Ye, T. & Mao, C. Fluorescent carbon nanoparticles derived from candle soot. *Angew. Chemie - Int. Ed.* **46,** 6473–6475 (2007).

64. Wang, L. *et al.* Common origin of green luminescence in carbon nanodots and graphene quantum dots. *ACS Nano* **8,** 2541–2547 (2014).

65. Tan, D., Zhou, S., Shimotsuma, Y., Miura, K. & Qiu, J. Effect of UV irradiation on photoluminescence of carbon dots. *Opt. Mater. Express* **4,** 213 (2014).

66. Zheng, H. *et al.* Enhancing the luminescence of carbon dots with a reduction pathway. *Chem. Commun.* **47,** 10650 (2011).

67. Bao, L. *et al.* Electrochemical tuning of luminescent carbon nanodots: From preparation to luminescence mechanism. *Adv. Mater.* **23,** 5801–5806 (2011).

68. Sonkar, S. K., Ghosh, M., Roy, M., Begum, A. & Sarkar, S. Carbon Nano-Onions as Nontoxic and High-Fluorescence Bioimaging Agent in Food Chain—A Study from Unicellular E. coli to Multicellular C. elegans; *Mater. Express* **2,** 105–114 (2012).

69. Bayda, S. *et al.* Bottom-up synthesis of carbon nanoparticles with higher doxorubicin efficacy. *J. Control. Release* **248,** 144–152 (2017).

70. Das, S. K., Liu, Y., Yeom, S., Kim, D. Y. & Richards, C. I. Single-particle fluorescence intensity fluctuations of carbon nanodots. *Nano Lett.* **14,** 620–625 (2014).

71. Lim, S. Y., Shen, W. & Gao, Z. Carbon quantum dots and their applications. *Chem. Soc. Rev.* **44,** 362–381 (2015).

72. Li, H., Kang, Z., Liu, Y. & Lee, S.-T. Carbon nanodots: synthesis, properties and applications. *J. Mater. Chem.* **22,** 24230 (2012).

73. Baker, S. N. & Baker, G. A. Luminescent carbon nanodots: Emergent nanolights. *Angew. Chemie - Int.*

Ed. **49,** 6726–6744 (2010).

74. Khan, S., Gupta, A., Verma, N. C. & Nandi, C. K. Time-Resolved Emission Reveals Ensemble of Emissive States as the Origin of Multicolor Fluorescence in Carbon Dots. *Nano Lett.* **15,** 8300–8305 (2015).

75. Chattopadhyay, A. & Mukherjee, S. Fluorophore Environments in Membrane-Bound Probes: A Red Edge Excitation Shift Study. *Biochemistry* **32,** 3804–3811 (1993).

76. Demchenko, A. P. The red-edge effects: 30 years of exploration. *Luminescence* **17,** 19–42 (2002).

77. Zhai, X. *et al.* Highly luminescent carbon nanodots by microwave-assisted pyrolysis. *Chem. Commun.* **48,** 7955 (2012).

78. Ghosh, S. *et al.* Photoluminescence of carbon nanodots: Dipole emission centers and electron-phonon coupling. *Nano Lett.* **14,** 5656–5661 (2014).

79. Hu, S. *et al.* Chemical regulation of carbon quantum dots from synthesis to photocatalytic activity. *Chem. - An Asian J.* **8,** 1035–1041 (2013).

80. Bachmatiuk, A. *et al.* Few-layer graphene shells and nonmagnetic encapsulates: A versatile and nontoxic carbon nanomaterial. *ACS Nano* **7,** 10552–10562 (2013).

81. Sachdev, A., Matai, I. & Gopinath, P. Implications of surface passivation on physicochemical and bioimaging properties of carbon dots. *RSC Adv.* **4,** 20915–20921 (2014).

82. Sachdev, A. *et al.* A novel one-step synthesis of PEG passivated multicolour fluorescent carbon dots for potential biolabeling application. *RSC Adv.* **3,** 16958 (2013).

83. Li, X., Zhang, S., Kulinich, S. A., Liu, Y. & Zeng, H. Engineering surface states of carbon dots to achieve controllable luminescence for solid-luminescent composites and sensitive Be2+ detection. *Sci. Rep.* **4,** 4976 (2015).

84. Wang, C. *et al.* Upconversion fluorescent carbon nanodots enriched with nitrogen for light harvesting. *J. Mater. Chem.* **22,** 15522 (2012).

85. He, X. *et al.* Water soluble carbon nanoparticles: Hydrothermal synthesis and excellent photoluminescence properties. *Colloids Surfaces B Biointerfaces* **87,** 326–332 (2011).

86. Jia, X., Li, J. & Wang, E. One-pot green synthesis of optically pH-sensitive carbon dots with upconversion luminescence. *Nanoscale* **4,** 5572 (2012).

87. Shen, J., Zhu, Y., Chen, C., Yang, X. & Li, C. Facile preparation and upconversion luminescence of graphene quantum dots. *Chem. Commun.* **47,** 2580–2582 (2011).

88. Yu, X., Liu, J., Yu, Y., Zuo, S. & Li, B. Preparation and visible light photocatalytic activity of carbon quantum dots/TiO2 nanosheet composites. *Carbon N. Y.* **68,** 718–724 (2014).

89. Zhu, C., Zhai, J. & Dong, S. Bifunctional fluorescent carbon nanodots: green synthesis via soy milk and application as metal-free electrocatalysts for oxygen reduction. *Chem. Commun.* **48,** 9367 (2012).

90. Joubert, M.-F. Photon avalanche upconversion in rare earth laser materials. *Opt. Mater. (Amst).* **11,** 181–203 (1999).

91. Auzel, F. Upconversion and Anti-Stokes Processes with f and d Ions in Solids. *Chem. Rev.* **104,** 139–173 (2004).

92. Ogawa, T., Yanai, N., Monguzzi, A. & Kimizuka, N. Highly Efficient Photon Upconversion in Self-Assembled Light-Harvesting Molecular Systems. *Sci. Rep.* **5,** 10882 (2015).

93. Baluschev, S. *et al.* Two pathways for photon upconversion in model organic compound systems. *J. Appl. Phys.* **101,** (2007).

94. Zhao, J., Wu, W., Sun, J. & Guo, S. Triplet photosensitizers: from molecular design to applications. *Chem. Soc. Rev.* **42,** 5323 (2013).

95. Bhawalkar, J. D., He, G. S. & Prasad, P. N. 3-Photon Induced up-Converted Fluorescence from an Organic-Compound - Application to Optical Power Limiting. *Opt. Commun.* **119,** 587–590 (1995).

96. Li, M. *et al.* Synthesis and upconversion luminescence of N-doped graphene quantum dots. *Appl. Phys. Lett.* **101,** 10–13 (2012).

97. Zhuo, S., Shao, M. & Lee, S. T. Upconversion and downconversion fluorescent graphene quantum dots: Ultrasonic preparation and photocatalysis. *ACS Nano* **6,** 1059–1064 (2012).

98. Zheng, L., Chi, Y., Dong, Y., Lin, J. & Wang, B. Electrochemiluminescence of water-soluble carbon nanocrystals released electrochemically from graphite. *J. Am. Chem. Soc.* **131,** 4564–4565 (2009).

99. Cao, L. *et al.* Carbon dots for multiphoton bioimaging. *J. Am. Chem. Soc.* **129,** 11318–11319 (2007).

100. Gan, Z., Wu, X., Zhou, G., Shen, J. & Chu, P. K. Is There Real Upconversion Photoluminescence from Graphene Quantum Dots? *Adv. Opt. Mater.* **1,** 554–558 (2013).

101. Barati, A., Shamsipur, M. & Abdollahi, H. A misunderstanding about upconversion luminescence of carbon quantum dots. *J. Iran. Chem. Soc.* **12,** 441–446 (2015).

102. Shujuan, Z., Mingwang, S. & Lee, S.-T. Upconversion and dowconversion fluorescent graphene quantum dots: ultrasonnic preparation and photocatalysis. *ACS Nano* **6,** 6530–6531 (2012).

103. Eaton, D. F. International Union of Pure and Applied Chemistry Organic Chemistry Division Commission on Photochemistry. Reference materials for fluorescence measurement. *J Photochem Photobiol B* **2,** 523–531 (1988).

104. Liu, X. *et al.* N-Doped carbon dots: Green and efficient synthesis on a large-scale and their application in fluorescent pH sensing. *New J. Chem.* **41,** 10607–10612 (2017).

105. Qu, D. *et al.* Formation mechanism and optimization of highly luminescent N-doped graphene quantum dots. *Sci. Rep.* **4,** 5294 (2015).

106. Wang, C. Y. *et al.* Facile synthesis of nitrogen-doped carbon dots from COOH-functional ionic liquid and their sensing application in selective detection of free chlorine. *Mater. Res. Express* **3,** 11 (2016).

107. Carrara, S., Arcudi, F., Prato, M. & De Cola, L. Amine-Rich Nitrogen-Doped Carbon Nanodots as a Platform for Self-Enhancing Electrochemiluminescence. *Angew. Chemie - Int. Ed.* **56,** 4757–4761 (2017).

108. Zhao, S., Li, C., Huang, H., Liu, Y. & Kang, Z. ScienceDirect Carbon nanodots modified cobalt phosphate as efficient electrocatalyst for water oxidation. *J. Mater.* **1,** 236–244 (2015).

109. Mondal, T. K. *et al.* Highly luminescent N-doped carbon quantum dots from lemon juice with porphyrin-like structures surrounded by graphitic network for sensing applications. *RSC Adv.* **6,** 59927–59934 (2016).

110. Wang, H. *et al.* Nitrogen-Doped Carbon Dots for ‘green’ Quantum Dot Solar Cells. *Nanoscale Res.*

Lett. **11,** 27 (2016).

111. Karfa, P. *et al.* Amino acid derived highly luminescent, heteroatom-doped carbon dots for label-free detection of Cd $^{2+}$ /Fe $^{3+}$, cell imaging and enhanced antibacterial activity. *RSC Adv.* **5,** 58141–58153 (2015).

112. Cheng, H. J. *et al.* Amino acid derivatized carbon dots with tunable selectivity as logic gates for fluorescent sensing of metal cations. *Microchim. Acta* **184,** 3179–3187 (2017).

113. Yang, Z. *et al.* Nitrogen-doped, carbon-rich, highly photoluminescent carbon dots from ammonium citrate. *Nanoscale* **6,** 1890–1895 (2014).

114. Zhou, J. *et al.* Cationic carbon quantum dots derived from alginate for gene delivery: One-step synthesis and cellular uptake. *Acta Biomater.* **42,** 209–219 (2016).

115. Liu, H., Li, R. S., Zhou, J. & Huang, C. Z. Branched polyethylenimine-functionalized carbon dots as sensitive and selective fluorescent probes for N-acetylcysteine via an off–on mechanism. *Analyst* (2017). doi:10.1039/C7AN01136A

116. Bourlinos, A. B. *et al.* Luminescent surface quaternized carbon dots. *Chem. Mater.* **24,** 6–8 (2012).

117. Shi, B. *et al.* Nitrogen and Phosphorus Co-Doped Carbon Nanodots as a Novel Fluorescent Probe for Highly Sensitive Detection of Fe3+ in Human Serum and Living Cells. *ACS Appl. Mater. Interfaces* **8,** 10717–10725 (2016).

118. Chandra, S. *et al.* Synthesis of highly fluorescent nitrogen and phosphorus doped carbon dots for the detection of Fe3+ ions in cancer cells. *Luminescence* **31,** 81–87 (2016).

119. Nabid, M. R., Bide, Y. & Fereidouni, N. Boron and nitrogen co-doped carbon dots as a metal-free catalyst for hydrogen generation from sodium borohydride. *New J. Chem.* **40,** 8823–8828 (2016).

120. Tian, T., He, Y., Ge, Y. & Song, G. One-pot synthesis of boron and nitrogen co-doped carbon dots as the fluorescence probe for dopamine based on the redox reaction between Cr(VI) and dopamine. *Sensors Actuators, B Chem.* **240,** 1265–1271 (2017).

121. Amjadi, M., Manzoori, J. L., Hallaj, T. & Azizi, N. Sulfur and nitrogen co-doped carbon quantum dots as the chemiluminescence probe for detection of Cu2+ ions. *J. Lumin.* **182,** 246–251 (2017).

122. Zhuo, K. *et al.* Green synthesis of sulfur- and nitrogen-co-doped carbon dots using ionic liquid as a precursor and their application in Hg2+ detection. *J. Lumin.* **187,** 227–234 (2017).

123. Barman, M. K., Jana, B., Bhattacharyya, S. & Patra, A. Photophysical Properties of Doped Carbon Dots (N, P, and B) and Their In fl uence on Electron/Hole Transfer in Carbon Dots − Nickel (II) Phthalocyanine Conjugates. *J. Phys. Chem. C* **118,** 20034–20041 (2014).

124. Wang, J. *et al.* High Performance Photoluminescent Carbon Dots for in Vitro and in Vivo Bioimaging: Effect of Nitrogen Doping Ratios. *Langmuir* **31,** 8063–8073 (2015).

125. Han, Y. *et al.* Non-metal single/dual doped carbon quantum dots: a general flame synthetic method and electro-catalytic properties. *Nanoscale* **7,** 5955–5962 (2015).

126. Zhou, R., Zheng, Y., Jaroniec, M. & Qiao, S.-Z. Determination of the Electron Transfer Number for the Oxygen Reduction Reaction: From Theory to Experiment. *ACS Catal.* **6,** 4720–4728 (2016).

127. Renz, C. Zur Photochemie des Thallochlorids. *Helv. Chim. Acta* **2,** 704–717 (1919).

128. Goodeve, C. F. & Kitchener, J. A. Photosensitisation by titanium dioxide. *Trans. Faraday Soc.* **34,** 570

(1938).

129. Markham, M. C. & Laidler, K. J. Kinetic Study of Photo-oxidations on the Surface of Zinc Oxide in Aqueous Suspensions. *J. Phys. Chem.* **57,** 363–389 (1953).

130. Kennedy, D. R., Ritchie, M. & Mackenzie, J. The photosorption of oxygen and nitric oxide on titanium dioxide. *Trans. Faraday Soc.* **54,** 119 (1958).

131. Gupta, S. M. & Tripathi, M. A review of TiO2 nanoparticles. *Chinese Sci. Bull.* **56,** 1639–1657 (2011).

132. McLintock, I. S. & Ritchie, M. Reactions on titanium dioxide; photo-adsorption and oxidation of ethylene and propylene. *Trans. Faraday Soc.* **61,** 1007 (1965).

133. FUJISHIMA, A. & HONDA, K. Electrochemical Photolysis of Water at a Semiconductor Electrode. *Nature* **238,** 37–38 (1972).

134. Frank, S. N. & Bard, A. J. Heterogeneous Photocatalytic Oxidation of Cyanide Ion in Aqueous Solutions at TiO2 Powder. *J. Am. Chem. Soc.* **99,** 303–304 (1977).

135. Janusz, J. M. & Berson, J. A. Heterogeneous Photocatalytic Synthesis of Methane from Acetic Acid—New Kolbe Reaction Pathway. *J. Am. Chem. Soc.* **100,** 2239–2240 (1978).

136. Pelaez, M. *et al.* A review on the visible light active titanium dioxide photocatalysts for environmental applications. *Appl. Catal. B Environ.* **125,** 331–349 (2012).

137. Fujishima, A., Rao, T. N. & Tryk, D. A. Titanium dioxide photocatalysis. *J. Photochem. Photobiol. C Photochem. Rev.* **1,** 1–21 (2000).

138. Lazar, M., Varghese, S. & Nair, S. Photocatalytic Water Treatment by Titanium Dioxide: Recent Updates. *Catalysts* **2,** 572–601 (2012).

139. Li, Z., Cong, S. & Xu, Y. Brookite vs anatase TiO_2 in the photocatalytic activity for organic degradation in water. *ACS Catal.* **4,** 3273–3280 (2014).

140. Shklover, V. *et al.* Structure of Nanocrystalline TiO_2 Powders and Precursor to Their Highly Efficient Photosensitizer. *Chem. Mater.* **9,** 430–439 (1997).

141. Morgan, B. J. & Watson, G. W. Intrinsic n-type defect formation in TiO_2: A comparison of rutile and anatase from GGA+U calculations. *J. Phys. Chem. C* **114,** 2321–2328 (2010).

142. Feng, T., Feng, G. S., Yan, L. & Pan, J. H. One-Dimensional Nanostructured TiO_2 for Photocatalytic Degradation of Organic Pollutants in Wastewater. *Int. J. Photoenergy* **2014,** 1–14 (2014).

143. Zhang, Y., Zhou, Z., Chen, T., Wang, H. & Lu, W. Graphene TiO_2 nanocomposites with high photocatalytic activity for the degradation of sodium pentachlorophenol. *J. Environ. Sci. (China)* **26,** 2114–2122 (2014).

144. Fujishima, A., Zhang, X. & Tryk, D. A. TiO_2 photocatalysis and related surface phenomena. *Surf. Sci. Rep.* **63,** 515–582 (2008).

145. Colón, G., Hidalgo, M. C. & Navío, J. A. Photocatalytic behaviour of sulphated TiO_2 for phenol degradation. *Appl. Catal. B Environ.* **45,** 39–50 (2003).

146. Yoshihara, T. *et al.* Identification of Reactive Species in Photoexcited Nanocrystalline TiO_2 Films by Wide-Wavelength-Range (400−2500 nm) Transient Absorption Spectroscopy. *J. Phys. Chem. B* **108,** 3817–3823 (2004).

147. Serpone, N., Lawless, D. & Khairutdinov, R. Size Effects on the Photophysical Properties of Colloidal Anatase TiO_2 Particles: Size Quantization versus Direct Transitions in This Indirect Semiconductor. *J. Phys. Chem.* **99,** 16646–16654 (1995).

148. Ishibashi, K., Fujishima, A., Watanabe, T. & Hashimoto, K. Quantum yields of active oxidative species formed on TiO2 photocatalyst. *J. Photochem. Photobiol. A Chem.* **134,** 139–142 (2000).

149. Draper, R. B. & Fox, M. A. Titanium Dioxide Photosensitized Reactions Studied by Diffuse Reflectance Flash Photolysis in Aqueous Suspensions of TiO2 Powder. *Langmuir* **6,** 1396–1402 (1990).

150. Tachikawa, T., Tojo, S., Fujitsuka, M. & Majima, T. Influences of Adsorption on TiO_2 Photocatalytic One-Electron Oxidation of Aromatic Sulfides Studied by Time-Resolved Diffuse Reflectance Spectroscopy. 5859–5866 (2004).

151. Daimon, T. & Nosaka, Y. Formation and behavior of singlet molecular oxygen in TiO_2 photocatalysis studied by detection of near-infrared phosphorescence. *J. Phys. Chem. C* **111,** 4420–4424 (2007).

152. Salvador, P. & Gutierrez, C. On the Nature of Surface States Involved in the Photo- and Electroluminescence Spectra of N-TiO_2 Electrodes. *J. Phys. Chem.* **88,** 3696–3698 (1984).

153. Nakato, Y. *et al.* Photoluminescence from a bulk defect near the surface of an N-TiO_2 (rutile) electrode in relation to an intermediate of photooxidation reaction of water. *J. Phys. Chem. B* **101,** 4934–4939 (1997).

154. Munuera, G., Navio, A. & Rives-Arnau, V. Photogeneration of singlet oxygen from TiO_2 surfaces. *J. Chem. Soc. Faraday Trans. 1* **77,** 2747 (1981).

155. Nosaka, Y., Daimon, T., Nosaka, A. Y. & Murakami, Y. suspension. 2917–2918 (2004).

156. Hirakawa, K. & Hirano, T. Singlet Oxygen Generation Photocatalyzed by TiO_2 Particles and Its Contribution to Biomolecule Damage. *Chem. Lett.* **35,** 832–833 (2006).

157. Berger, T., Sterrer, M., Diwald, O. & Knözinger, E. Charge trapping and photoadsorption of O_2 on dehydroxylated TiO_2 nanocrystals - An electron paramagnetic resonance study. *ChemPhysChem* **6,** 2104–2112 (2005).

158. Ikeda, K., Sakai, H., Baba, R., Hashimoto, K. & Fujishima, A. Photocatalytic reactions involving radical chain reactions using microelectrodes. *J. Phys. Chem. B* **101,** 2617–2620 (1997).

159. Ikeda, K., Hashirnoto, K. & Fujishirna, A. Comparative studies on the photocatalytic decomposition of ethanol and acetaldehyde in water containing dissolved oxygen using a microelectrode technique. *Journal of electroanalytical chemstry*. **437,** 241–244 (1997).

160. Li, X. & Jenks, W. S. Isotope studies of photocatalysis: Dual mechanisms in the conversion of anisole to phenol. *J. Am. Chem. Soc.* **122,** 11864–11870 (2000).

161. Muggli, D. S. & Falconer, J. L. Role of Lattice Oxygen in Photocatalytic Oxidation on TiO_2. *J. Catal.* **191,** 318–325 (2000).

162. Schneider, J. *et al.* Understanding TiO_2 Photocatalysis: Mechanisms and Materials. *Chem. Rev.* **114,** 9919–9986 (2014).

163. Irie, H., Washizuka, S., Yoshino, N. & Hashimoto, K. Visible-light induced hydrophilicity on nitrogen-substituted titanium dioxide films. *Chem. Commun.* 1298–9 (2003).

164. Emeline, A. V., Kuznetsov, V. N., Rybchuk, V. K. & Serpone, N. Visible-Light-Active Titania Photocatalysts: The Case of N-Doped Properties and Some Fundamental Issues. *Int. J. Photoenergy*

2008, 1–19 (2008).

165. Devi, L. G. & Kavitha, R. A review on non metal ion doped titania for the photocatalytic degradation of organic pollutants under UV/solar light: Role of photogenerated charge carrier dynamics in enhancing the activity. *Appl. Catal. B Environ.* **140–141,** 559–587 (2013).

166. Zhao, A., Masa, J. & Xia, W. Oxygen-deficient titania as alternative support for Pt catalysts for the oxygen reduction reaction. *J. Energy Chem.* **23,** 701–707 (2014).

167. Sarkar, D. *et al.* Oxygen-Deficient Titania with Adjustable Band Positions and Defects; Molecular Layer Deposition of Hybrid Organic-Inorganic Thin Films as Precursors for Enhanced Photocatalysis. *J. Phys. Chem. C* **120,** 3853–3862 (2016).

168. Hardin, B. E. *et al.* Energy and hole transfer between dyes attached to titania in cosensitized dye-sensitized solar cells. *J. Am. Chem. Soc.* **133,** 10662–10667 (2011).

169. Vamvounis, G., Glasson, C. R., Bieske, E. J. & Dryza, V. Modulating electron injection from an organic dye to a titania nanoparticle with a photochromic energy transfer acceptor. *J. Mater. Chem. C* **4,** 6215–6219 (2016).

170. Jia, C. *et al.* Photoluminescence and energy transfer of terbium doped titania film. *Thin Solid Films* **496,** 555–559 (2006).

171. Kay, A. & Graetzel, M. Artificial photosynthesis. 1. Photosensitization of titania solar cells with chlorophyll derivatives and related natural porphyrins. *J. Phys. Chem.* **97,** 6272–6277 (1993).

172. Liu, B. *et al.* Low temperature fabrication of V-doped TiO_2 nanoparticles, structure and photocatalytic studies. *J. Hazard. Mater.* **169,** 1112–1118 (2009).

173. Koh, P. W., Hatta, M. H. M., Ong, S. T., Yuliati, L. & Lee, S. L. Photocatalytic degradation of photosensitizing and non-photosensitizing dyes over chromium doped titania photocatalysts under visible light. *J. Photochem. Photobiol. A Chem.* **332,** 215–223 (2017).

174. Lin, C. Y. W., Nakaruk, A. & Sorrell, C. C. Mn-doped titania thin films prepared by spin coating. *Prog. Org. Coatings* **74,** 645–647 (2012).

175. Zhao, W. *et al.* Direct microwave-hydrothermal synthesis of Fe-doped titania with extended visible-light response and enhanced H_2 production performance. *Chem. Eng. J.* **283,** 105–113 (2016).

176. Ohwada, M., Kimoto, K., Ebina, Y. & Sasaki, T. EELS tudy of Fe- or Co-doped titania nanosheets. *Microscopy* **64,** 77–85 (2015).

177. Yue, X. *et al.* Facile synthesis of metal-doped titania nanospheres with tunable size exhibiting highly efficient photoactivity for degradation. *Mater. Chem. Phys.* 1–9 (2015).

178. Ganesh, I. *et al.* Preparation and characterization of Cu-doped TiO_2 materials for electrochemical, photoelectrochemical, and photocatalytic applications. *Appl. Surf. Sci.* **293,** 229–247 (2014).

179. Benjwal, P.,Kar, K. K. One-step synthesis of Zn doped titania nanotubes and investigation of their visible photocatalytic activity. *Mater. Chem. Phys.* **160,** 279–288 (2015).

180. Rao, J. *et al.* Synthesis of Yttrium doped TiO_2 nanotubes by a microwave refluxing method and their photoluminescence properties and photocatalytic properties. *Int. J. Electrochem. Sci.* **11,** 2408–2418 (2016).

181. Kanattukara, V. B., Dong-Kyu, K., Dae-Won, P. Synthesis and characterization of zirconium-doped mesoporous nano-crystalline TiO_2.*Nanoscale* **2,** 1057 (2010).

182. Ismail, A. A., Bahnemann, D. W., Robben, L., Yarovyi, V. & Wark, M. Palladium doped porous titania photocatalysts: Impact of mesoporous order and crystallinity. *Chem. Mater.* **22,** 108–116 (2010).

183. Thiel, J. *et al.* Antibacterial properties of silver-doped titania. *Small* **3,** 799–803 (2007).

184. Karunakaran, C., Vijayabalan, A., Manikandan, G., Gomathisankar, P. Visible light photocatalytic disinfection of bacteria by Cd-TiO_2. *Catal. Commun.* **12,** 826–829 (2011).

185. Lorret, O., Francová, D., Waldner, G. & Stelzer, N. W-doped titania nanoparticles for UV and visible-light photocatalytic reactions. *Appl. Catal. B Environ.* **91,** 39–46 (2009).

186. Vijayan, B. K., Dimitrijevic, N. M., Wu, J. & Gray, K. A. The effects of Pt doping on the structure and visible light photoactivity of titania nanotubes. *J. Phys. Chem. C* **114,** 21262–21269 (2010).

187. Seabra, M. P., Salvado, I. M. M. & Labrincha, J. A. Pure and (zinc or iron) doped titania powders prepared by sol-gel and used as photocatalyst. *Ceram. Int.* **37,** 3317–3322 (2011).

188. Bodson, C. J. *et al.* Efficient P- and Ag-doped titania for the photocatalytic degradation of waste water organic pollutants. *J. Alloys Compd.* **682,** 144–153 (2016).

189. Han, T. Y., Wu, C.. Hydrothermal synthesis and visible light photocatalysis of metal-doped titania nanoparticles. *J. Vac. Sci. Technol. B Microelectron. Nanom. Struct.* **25,** 430 (2007).

190. Dunnill, C. W., Kafizas, A. & Parkin, I. P. CVD production of doped titanium dioxide thin films. *Chem. Vap. Depos.* **18,** 89–101 (2012).

191. Pandiyan, R., Delegan, N., Dirany, A., Drogui, P. & El Khakani, M. A. Probing the Electronic Surface Properties and Bandgap Narrowing of in situ N, W, and (W,N) Doped Magnetron-Sputtered TiO_2 Films Intended for Electro-Photocatalytic Applications. *J. Phys. Chem. C* **120,** 631–638 (2016).

192. Sanchez-Dominguez, M. *et al.* Synthesis of Zn-doped TiO_2 nanoparticles by the novel oil-in-water (O/W) microemulsion method and their use for the photocatalytic degradation of phenol. *J. Environ. Chem. Eng.* **3,** 3037–3047 (2015).

193. Osada, M. *et al.* Gigantic magneto-optical effects induced by (FeCo) -cosubstitution in titania nanosheets. *Appl. Phys. Lett.* **92,** 2006–2009 (2008).

194. Lee, S., Yun, C. Y., Hahn, M. S., Lee, J. & Yi, J. Synthesis and characterization of carbon-doped titania as a visible-light-sensitive photocatalyst. *Korean J. Chem. Eng.* **25,** 892–896 (2008).

195. Gorska, P., Zaleska, a, Suska, a & Hupka, J. Photocatalytic Activity and Surface Properties of Carbon-Doped Titanium Dioxide. *Physicochem. Probl. Miner. Process.* **43,** 21–30 (2009).

196. Venditti, F. *et al.* Visible light caffeic acid degradation by carbon-doped titanium dioxide. *Langmuir* **31,** 3627–3634 (2015).

197. Reyes-Garcia, E. A., Sun, Y., Reyes-Gil, K. R. & Raftery, D. Solid-state NMR and EPR analysis of carbon-doped titanium dioxide photocatalysts (TiO2-xCx). *Solid State Nucl. Magn. Reson.* **35,** 74–81 (2009).

198. Li, N. *et al.* High quality sulfur-doped titanium dioxide nanocatalysts with visible light photocatalytic activity from non-hydrolytic thermolysis synthesis. *Inorg. Chem. Front.* **1,** 521–525 (2014).

199. Rockafellow, E. M., Stewart, L. K. & Jenks, W. S. Is sulfur-doped TiO_2 an effective visible light photocatalyst for remediation? *Appl. Catal. B Environ.* **91,** 554–562 (2009).

200. Qin, H. L., Gu, G. B. & Liu, S. Preparation of nitrogen-doped titania with visible-light activity and its application. *Comptes Rendus Chim.* **11,** 95–100 (2008).

201. Gole, J. L., Stout, J. D., Burda, C., Lou, Y. B. & Chen, X. B. Highly efficient formation of visible light tunable $TiO_{2-x}N_x$ photocatalysts and their transformation at the nanoscale. *J. Phys. Chem. B* **108,** 1230–1240 (2004).

202. Kisch, H., Sakthivel, S., Janczarek, M. & Mitoraj, D. A Low-Band gap, nitrogen-modified titania visible-light photocatalyst. *J. Phys. Chem. C* **111,** 11445–11449 (2007).

203. Dozzi, M. V., D'Andrea, C., Ohtani, B., Valentini, G. & Selli, E. Fluorine-Doped TiO_2 Materials: Photocatalytic Activity vs Time-Resolved Photoluminescence. *J. Phys. Chem. C* **117,** 25586–25595 (2013).

204. Li, D., Haneda, H., Hishita, S., Ohashi, N. & Labhsetwar, N. K. Fluorine-doped TiO_2 powders prepared by spray pyrolysis and their improved photocatalytic activity for decomposition of gas-phase acetaldehyde. *J. Fluor. Chem.* **126,** 69–77 (2005).

205. Grabowska, E., Zaleska, A., Sobczak, J. W., Gazda, M. & Hupka, J. Boron-doped TiO_2: Characteristics and photoactivity under visible light. *Procedia Chem.* **1,** 1553–1559 (2009).

206. Chen, D., Yang, D., Wang, Q. & Jiang, Z. Effects of boron doping on photocatalytic activity and microstructure of titanium dioxide nanoparticles. *Ind. Eng. Chem. Res.* **45,** 4110–4116 (2006).

207. Iwase, M. *et al.* Visible-light photocatalysis with phosphorus-doped titanium(IV) oxide particles prepared using a phosphide compound. *Appl. Catal. B Environ.* **132–133,** 39–44 (2013).

208. Sato, S. Photocatalytic activity of NOx-doped TiO2 in the visible light region. *Chem. Phys. Lett.* **123,** 126–128 (1986).

209. Asahi, R. Visible-Light Photocatalysis in Nitrogen-Doped Titanium Oxides. *Science.* **293,** 269–271 (2001).

210. Ou, H., Lo, S. & Liao, C. Prepared from Microwave-Assisted Titanate Nanotubes ($Na_x H_{2-x} Ti_3O_7$): The Effect of Microwave Irradiation during TNT Synthesis on the Visible Light Photoactivity. *J. Phys. Chem. C* **115,** 4000–4007 (2011).

211. Zhou, X. *et al.* Simple fabrication of N-doped mesoporous TiO_2 nanorods with the enhanced visible light photocatalytic activity. *Nanoscale Res. Lett.* **9,** 34 (2014).

212. Dong, C. X., Xian, A. P., Han, E. H. & Shang, J. K. Acid-mediated sol-gel synthesis of visible-light active photocatalysts. *J. Mater. Sci.* **41,** 6168–6170 (2006).

213. Ruzmanova, Y., Stoller, M., Bravi, M. & Chianese, A. A Novel Approach for the Production of Nitrogen Doped TiO_2 Nanoparticles. *Chem. Eng. Trans.* **43,** 721–726 (2015).

214. Kachina, A. *et al.* A new approach to the preparation of nitrogen doped titania visible light photocatalyst. *Chem. Mater.* 120206060614009 (2012).

215. Zhou, X., Peng, F., Wang, H., Yu, H. & Yang, J. Preparation of nitrogen doped TiO_2 photocatalyst by oxidation of titanium nitride with H_2O_2. *Mater. Res. Bull.* **46,** 840–844 (2011).

216. Wu, Z., Dong, F., Zhao, W. & Guo, S. Visible light induced electron transfer process over nitrogen doped TiO_2 nanocrystals prepared by oxidation of titanium nitride. *J. Hazard. Mater.* **157,** 57–63 (2008).

217. Shen, H., Mi, L., Xu, P., Shen, W. & Wang, P. N. Visible-light photocatalysis of nitrogen-doped TiO_2 nanoparticulate films prepared by low-energy ion implantation. *Appl. Surf. Sci.* **253,** 7024–7028 (2007).

218. Ghicov, A. *et al.* Ion implantation and annealing for an efficient N-doping of TiO_2 nanotubes. *Nano Lett.* **6,** 1080–1082 (2006).

219. Lindgren, T. *et al.* Photoelectrochemical and Optical Properties of Nitrogen Doped Titanium Dioxide Films Prepared by Reactive DC Magnetron Sputtering. *J. Phys. Chem. B* **107,** 5709–5716 (2003).

220. Lynch, J. *et al.* Substitutional or interstitial site selective nitrogen doping in TiO_2 nanostructures. *J. Phys. Chem. C* **119,** 7443–7452 (2015).

221. Di Valentin, C. *et al.* N-doped TiO_2: Theory and experiment. *Chem. Phys.* **339,** 44–56 (2007).

222. Kuroda, Y. *et al.* Preparation of Visible-Light-Responsive $TiO_{2-x}N_x$ Photocatalyst by a Sol - Gel Method : Analysis of the Active Center on TiO_2 that Reacts with NH 3. *Langmuir* **21,** 8026–8034 (2005).

223. Peng, F., Cai, L., Yu, H., Wang, H. & Yang, J. Synthesis and characterization of substitutional and interstitial nitrogen-doped titanium dioxides with visible light photocatalytic activity. *J. Solid State Chem.* **181,** 130–136 (2008).

224. Nakamura, R., Tanaka, T. & Nakato, Y. Mechanism for Visible Light Responses in Anodic Photocurrents at N-Doped TiO_2 Film Electrodes. *J. Phys. Chem. B* **108,** 10617–10620 (2004).

225. Livraghi, S. *et al.* Origin of Photoactivity of Nitrogen-Doped Titanium Dioxide under Visible Light Origin of Photoactivity of Nitrogen-Doped Titanium Dioxide under Visible Light. *J. Am. Chem. Soc.* **128,** 15666–15671 (2006).

226. Taga, T. M. and R. A. and T. O. and K. A. and Y. Band-Gap Narrowing of Titanium Dioxide by Nitrogen Doping. *Jpn. J. Appl. Phys.* **40,** 561–563 (2001).

227. Irie, H., Watanabe, Y. & Hashimoto, K. Nitrogen-Concentration Dependence on Photocatalytic Activity of TiO_{2-x} N_x Powders. *J. Phys. Chem. B* **107,** 5483–5486 (2003).

228. Djega-mariadassou, G. Preparation and Characterization of Titanium Oxynitrides with Specific Surface Areas.*Journal of solid state chemistry* **155,** 145–155 (1991).

229. Irie, H., Watanabe, Y. & Hashimoto, K. Nitrogen-Concentration Dependence on Photocatalytic Activity of $TiO_{2-x}N_x$ Powders. *J. Phys. Chem. B* **107,** 5483–5486 (2003).

230. Bellardita, M., Addamo, M., Di Paola, A., Palmisano, L. & Venezia, A. M. Preparation of N-doped TiO_2: characterization and photocatalytic performance under UV and visible light. *Phys Chem Chem Phys* **11,** 4084–4093 (2009).

231. Bacsa, R., Kiwi, J., Ohno, T., Albers, P. & Nadtochenko, V. Preparation, testing and characterization of doped TiO_2 active in the peroxidation of biomolecules under visible light. *J. Phys. Chem. B* **109,** 5994–6003 (2005).

232. Yin, S., Zhang, Q., Saito, F. & Sato, T. Preparation of Visible Light-Activated Titania Photocatalyst by Mechanochemical Method. *Chem. Lett.* **32,** 358–359 (2003).

233. Tang, Y. C., Huang, X. H., Yu, H. Q. & Tang, L. H. Nitrogen-doped TiO_2 photocatalyst prepared by mechanochemical method: Doping mechanisms and visible photoactivity of pollutant degradation. *Int. J. Photoenergy* **2012,** (2012).

234. Graham, T. On the Properties of Silicic Acid and other Analogous Colloidal Substances. *Chem. Soc.* **17,** 318–327 (1864).

235. Zuas, O. & Budiman, H. Synthesis of Nanostructured Copper-doped Titania and Its Properties. **5,** 26–

33 (2013).

236. Navío, J. a *et al.* Iron-doped titania semiconductor powders prepared by a sol-gel method. Part I : synthesis and characterization. *Appl. Catal. A Gen.* **177,** 111–120 (1999).

237. Lv, K. *et al.* (Bi, C and N) codoped TiO_2 nanoparticles. *J. Hazard. Mater.* **161,** 396–401 (2009).

238. Jaiswal, R. *et al.* Efficient Co-B-codoped TiO_2 photocatalyst for degradation of organic water pollutant under visible light. *Appl. Catal. B Environ.* **183,** 242–253 (2016).

239. Yan, Y., Chaudhuri, S. R., Chen, D.-G. & Sarkar, A. Sol-Gel Synthesis of Titania Thin-Film-Stabilized Porous Silica Coating. *Chem. Mater.* **7,** 2007–2009 (1995).

240. Nassoko, D. *et al.* Nitrogen-doped TiO_2 nanoparticles by using EDTA as nitrogen source and soft template: Simple preparation, mesoporous structure, and photocatalytic activity under visible light. *J. Alloys Compd.* **540,** 228–235 (2012).

241. Dunnill, C. W. & Parkin, I. P. Nitrogen-doped TiO_2 thin films: photocatalytic applications for healthcare environments. *Dalt. Trans.* **40,** 1635–1640 (2011).

242. Sauthier, G., Ferrer, F. J., Figueras, A. & Gyorgy, E. Growth and characterization of nitrogen-doped TiO_2 thin films prepared by reactive pulsed laser deposition. *Thin Solid Films* **519,** 1464–1469 (2010).

243. Tian, L. *et al.* Undoped TiO_2 and nitrogen-doped TiO_2 thin films deposited by atomic layer deposition on planar and architectured surfaces for photovoltaic applications. *J. Vac. Sci. Technol. A Vacuum, Surfaces, Film.* **33,** 01A141 (2015).

244. Kollbek, K. *et al.* Study of N-doped TiO_2 thin films for photoelectrochemical hydrogen generation from water. *Open Chem.* **13,** 857–868 (2015).

245. Livage, J., Henry, M. & Sanchez, C. Sol-gel chemistry of transition metal oxides. *Prog. Solid State Chem.* **18,** 259–341 (1988).

246. Bao, N., Niu, J. J., Li, Y., Wu, G. L. & Yu, X. H. Low-temperature hydrothermal synthesis of N-doped TiO_2 from small-molecule amine systems and their photocatalytic activity. *Environ. Technol.* **34,** 2939–2949 (2013).

247. Li, H. *et al.* A systematic study on visible-light N-doped TiO_2 photocatalyst obtained from ethylenediamine by sol-gel method. *Appl. Surf. Sci.* **344,** 112–118 (2015).

248. Spadavecchia, F. *et al.* Solar photoactivity of nano-N-TiO_2 from tertiary amine: role of defects and paramagnetic species. *Appl. Catal. B Environ.* **96,** 314–322 (2010).

249. Peng, F., Cai, L., Huang, L., Yu, H. & Wang, H. Preparation of nitrogen-doped titanium dioxide with visible-light photocatalytic activity using a facile hydrothermal method. *J. Phys. Chem. Solids* **69,** 1657–1664 (2008).

250. Gole, J. L., Stout, J. D., Burda, C., Lou, Y. & Chen, X. Highly Efficient Formation of Visible Light Tunable $TiO_{2-x}N_x$ Photocatalysts and Their Transformation at the Nanoscale. *J. Phys. Chem. B* **108,** 1230–1240 (2004).

251. Sugimoto, T. Formation Mechansm of Monodisperse Pseudocubic a-Fe_2O_3 particles from Condensed Ferric Hydroxide Gel. *J. Colloid Interface Sci.* **159,** 372–382 (1993).

252. Sugimoto, T. & Zhou, X. Synthesis of Uniform Anatase TiO_2 Nanoparticles by the Gel–Sol Method. *J. Colloid Interface Sci.* **252,** 347–353 (2002).

253. Sugimoto, T., Zhou, X. & Muramatsu, A. Synthesis of uniform anatase TiO2 nanoparticles by gel-sol method. 1. Solution chemistry of $Ti(OH)_{(4-n)+(n)}$ complexes. *J. Colloid Interface Sci.* **252,** 339–46 (2002).

254. Sugimoto, T. & Zhou, X. Synthesis of uniform anatase TiO2 nanoparticles by the gel-sol method 2. Adsorption of OH- Ions to $Ti(OH)_4$ gel and TiO_2 particles. *J. Colloid Interface Sci.* **252,** 347–53 (2002).

255. Sugimoto, T., Zhou, X. & Muramatsu, A. Synthesis of uniform anatase TiO_2 nanoparticles by gel–sol method. *J. Colloid Interface Sci.* **259,** 43–52 (2003).

256. Hong, G., Diao, S., Antaris, A. L. & Dai, H. Carbon Nanomaterials for Biological Imaging and Nanomedicinal Therapy. *Chem. Rev.* **115,** 10816–10906 (2015).

257. Joseph, J. & Anappara, A. A. White light emission of carbon dots by creating different emissive traps. *J. Lumin.* **178,** 128–133 (2016).

258. Kwon, W., Do, S., Kim, J.-H., Seok Jeong, M. & Rhee, S.-W. Control of Photoluminescence of Carbon Nanodots via Surface Functionalization using Para-substituted Anilines. *Sci. Rep.* **5,** 12604 (2015).

259. Zhang, X. *et al.* Color-switchable electroluminescence of carbon dot light-emitting diodes. *ACS Nano* **7,** 11234–11241 (2013).

260. Sun, X. & Lei, Y. Fluorescent carbon dots and their sensing applications. *TrAC - Trends Anal. Chem.* **89,** 163–180 (2017).

261. Yu, B. Y. & Kwak, S.-Y. Carbon quantum dots embedded with mesoporous hematite nanospheres as efficient visible light-active photocatalysts. *J. Mater. Chem.* **22,** 8345 (2012).

262. Yu, H. *et al.* ZnO/carbon quantum dots nanocomposites: one-step fabrication and superior photocatalytic ability for toxic gas degradation under visible light at room temperature. *New J. Chem.* **36,** 1031 (2012).

263. Zhang, H. *et al.* Fe_2O_3/carbon quantum dots complex photocatalysts and their enhanced photocatalytic activity under visible light. *Dalt. Trans.* **40,** 10822 (2011).

264. Yu, H. *et al.* Carbon quantum dots/TiO_2 composites for efficient photocatalytic hydrogen evolution. *J. Mater. Chem. A* **2,** 3344 (2014).

265. Martindale, B. C. M., Hutton, G. A. M., Caputo, C. A. & Reisner, E. Solar Hydrogen Production Using Carbon Quantum Dots and a Molecular Nickel Catalyst. *J. Am. Chem. Soc.* **137,** 6018–6025 (2015).

266. Mirtchev, P., Henderson, E. J., Soheilnia, N., Yip, C. M. & Ozin, G. a. Solution phase synthesis of carbon quantum dots as sensitizers for nanocrystalline TiO2 solar cells. *J. Mater. Chem.* **22,** 1265 (2012).

267. Zhang, Y. Q., Ma, D. K., Zhang, Y. G., Chen, W. & Huang, S. M. N-doped carbon quantum dots for TiO_2-based photocatalysts and dye-sensitized solar cells. *Nano Energy* **2,** 545–552 (2013).

268. Tian, Y. & Tatsuma, T. Mechanisms and applications of plasmon-induced charge separation at TiO_2 films loaded with gold nanoparticles. *J. Am. Chem. Soc.* **127,** 7632–7637 (2005).

269. Hirakawa, T. & Kamat, P. V. Charge separation and catalytic activity of Ag@TiO_2 core-shell composite clusters under UV-irradiation. *J. Am. Chem. Soc.* **127,** 3928–3934 (2005).

270. Awazu, K. *et al.* A plasmonic photocatalyst consisting of silver nanoparticles embedded in titanium dioxide. *J. Am. Chem. Soc.* **130,** 1676–1680 (2008).

271. Réti, B., Mogyorósi, K., Dombi, A. & Hernádi, K. Substrate dependent photocatalytic performance of

TiO_2/MWCNT photocatalysts. *Appl. Catal. A Gen.* **469,** 153–158 (2014).

272. Guo, W., Zhang, F., Lin, C. & Wang, Z. L. Direct growth of TiO_2 nanosheet arrays on carbon fibers for highly efficient photocatalytic degradation of methyl orange. *Adv. Mater.* **24,** 4761–4764 (2012).

273. Yao, Y., Li, G., Ciston, S., Lueptow, R. M. & Gray, K. a. Photoreactive TiO_2 /Carbon Nanotube Composites: Synthesis and Reactivity. *Environ. Sci. Technol.* **42,** 4952–4957 (2008).

274. Yu, C., Fan, L., Yang, J., Shan, Y. & Qiu, J. Phase-reversal emulsion catalysis with CNT-TiO2 nanohybrids for the selective oxidation of benzyl alcohol. *Chem. - A Eur. J.* **19,** 16192–16195 (2013).

275. Cong, Y. *et al.* Anchoring a uniform TiO_2 layer on graphene oxide sheets as an efficient visible light photocatalyst. *Appl. Surf. Sci.* **282,** 400–407 (2013).

276. Lei, M., Wang, N., Zhu, L., Xie, C. & Tang, H. A peculiar mechanism for the photocatalytic reduction of decabromodiphenyl ether over reduced graphene oxide-TiO_2 photocatalyst. *Chem. Eng. J.* **241,** 207–215 (2014).

277. Lu, T. *et al.* TiO_2–graphene composites with exposed {001} facets produced by a one-pot solvothermal approach for high performance photocatalyst. *Phys. Chem. Chem. Phys.* **15,** 12963 (2013).

278. Yang, J. *et al.* Photocatalytic activities of heterostructured TiO_2-graphene porous microspheres prepared by ultrasonic spray pyrolysis. *J. Alloys Compd.* **584,** 180–184 (2014).

279. Lui, G. *et al.* Graphene-wrapped hierarchical TiO_2 nanoflower composites with enhanced photocatalytic performance. *J. Mater. Chem. A* **1,** 12255–12262 (2013).

280. Luk, C. M., Tsang, M. K., Chan, C. F. & Lau, S. P. Two-Photon Fluorescence in N-Doped Graphene Quantum Dots. *Int. Sch. Sci. Res. Innov.* **8,** 1310–1313 (2014).

281. Di Valentin, C., Pacchioni, G., Selloni, A., Livraghi, S. & Giamello, E. Characterization of paramagnetic species in N-doped TiO 2 powders by EPR spectroscopy and DFT calculations. *J. Phys. Chem. B* **109,** 11414–11419 (2005).

282. Junwei, W., Wei, Z., Yinqing, Z. & Shuangxi, L. An efficient two-step technique for nitrogen-doped titanium dioxide synthesizing: Visible-light-induced photodecomposition of methylene blue. *J. Phys. Chem. C* **111,** 1010–1014 (2007).

283. FLETCHER, A. N. Quinine Sulfate As a Fluorescence Quantum Yield Standard. *Photochem. Photobiol.* **9,** 439–444 (1969).

284. Li, H. *et al.* Water-soluble fluorescent carbon quantum dots and photocatalyst design. *Angew. Chemie - Int. Ed.* **49,** 4430–4434 (2010).

285. Brandt, U., Deters, A. & Steinbüchel, A. A jack-of-all-trades: 2-mercaptosuccinic acid. *Appl. Microbiol. Biotechnol.* **99,** 4545–4557 (2015).

286. Nie, S. *et al.* Effect of pH, temperature and heating time on the formation of furan in sugar–glycine model systems. *Food Sci. Hum. Wellness* **2,** 87–92 (2013).

287. Zhang, H. & Banfield, J. F. Thermodynamic analysis of phase stability of nanocrystalline titania. *J. Mater. Chem.* **8,** 2073–2076 (1998).

288. Nosaka, Y., Matsushita, M., Nishino, J. & Nosaka, A. Y. Nitrogen-doped titanium dioxide photocatalysts for visible response prepared by using organic compounds. *Sci. Technol. Adv. Mater.* **6,** 143–148 (2005).

289. Sakthivel, S., Janczarek, M. & Kisch, H. Visible light activity and photoelectrochemical properties of nitrogen-doped TiO2. *J. Phys. Chem. B* **108,** 19384–19387 (2004).

290. Cong, Y., Zhang, J., Chen, F. & Anpo, M. Synthesis and characterization of nitrogen-doped TiO_2 nanophotocatalyst with high visible light activity. *J. Phys. Chem. C* **111,** 6976–6982 (2007).

291. Darzi, S., Mahjoub, A. & Sarfi, S. Visible lignht active nitrogen doped TiO_2 nanoparticles prepared by sol-gel acid catalyzed reaction. *Iran. J. Mater. Sci.* **9,** 17–23 (2012).

292. Vasconcelos, D. C. L. *et al.* Infrared Spectroscopy of Titania Sol-Gel Coatings on 316L Stainless Steel. *Mater. Sci. Appl.* **2,** 1375–1382 (2011).

293. Izutsu, H., Nair, P. & Maeda, K. Structure and properties of TiO_2-SiO_2 prepared by sol-gel method in the presence of tartaric acid. *Mater. Res.* **32,** 1303–1311 (1997).

294. Darzi, S. J., Mahjoub, a R. & Sarfi, S. Visible light activated nitrogen dopedi TiO_2 nanoparticles prepared by sol-gel acid catalyzed reaction. *Iran. J. Mater.* **9,** 17–23 (2012).

295. Swetha, S., Santhosh, S. M. & Geetha Balakrishna, R. Synthesis and comparative study of nano-TiO_2 over degussa P-25 in disinfection of water. *Photochem. Photobiol.* **86,** 628–632 (2010).

Acknowledgements

I would like to thank all the people who contributed in some way to the work described in this thesis. First and foremost, I thank my academic advisor, professor Alvise Benedetti, for accepting me into his group and for his support and incitement during these three years. Additionally, I would like to thank professor Pietro Riello for his interest in my work, and professor Flavio Rizzoglio for his support. Every result described in this thesis was accomplished with the help and support of fellow lab mates and collaborators. In particular I would like to thank Dr. Emanuele Ambrosi, for his fundamental help in electrophoresis studies and for the beautiful SEM images. Thanks to Tiziano Finotto and Davide Cristofori, the technician of our lab. Thanks to the people of the ETA building, you have been my second family in this years.

I would also like to thank professor Xavier Sala Roman and professor Jordi García-Antón Aviñó of the Universitat Autonoma de Barcelona to host me in the wonderful SelOxCat research group. They provided a friendly and cooperative atmosphere at work and also useful feedback and insightful comments on my work. In particular I should like to thank Jordi Creus Casanovas and Dr. Nuria Romero Fernández for their friendship, and for their support during my stay in Barcellona.

Special thanks to Dr. Giulio Rosati, Dr. Giulia Ricci, and Giulio Bellocchio for their fundamental help, and for their true friendship.

Finally, I would like to acknowledge my family who supported me during my PhD. First and foremost I would like to thank mom, dad, Vera and Alessandro for their affection. Special thanks to Lucia who daily supported me, inciting me with her love and help, even in the most difficult moments.